



**HAL**  
open science

## Roadmap on Label-Free Super-Resolution Imaging

Vasily N Astratov, Yair Ben Sahel, Yonina C Eldar, Luzhe Huang, Aydogan Ozcan, Nikolay Zheludev, Junxiang Zhao, Zachary Burns, Zhaowei Liu, Evgenii Narimanov, et al.

► **To cite this version:**

Vasily N Astratov, Yair Ben Sahel, Yonina C Eldar, Luzhe Huang, Aydogan Ozcan, et al.. Roadmap on Label-Free Super-Resolution Imaging. *Laser and Photonics Reviews*, 2023, 17 (12), pp.2200029. 10.1002/lpor.202200029 . hal-04355087

**HAL Id: hal-04355087**

**<https://univ-rennes.hal.science/hal-04355087v1>**

Submitted on 20 Dec 2023

**HAL** is a multi-disciplinary open access archive for the deposit and dissemination of scientific research documents, whether they are published or not. The documents may come from teaching and research institutions in France or abroad, or from public or private research centers.

L'archive ouverte pluridisciplinaire **HAL**, est destinée au dépôt et à la diffusion de documents scientifiques de niveau recherche, publiés ou non, émanant des établissements d'enseignement et de recherche français ou étrangers, des laboratoires publics ou privés.



Distributed under a Creative Commons Attribution 4.0 International License

# Roadmap on Label-Free Super-Resolution Imaging

Vasily N. Astratov,\* Yair Ben Sahel, Yonina C. Eldar, Luzhe Huang, Aydogan Ozcan, Nikolay Zheludev, Junxiang Zhao, Zachary Burns, Zhaowei Liu, Evgenii Narimanov, Neha Goswami, Gabriel Popescu, Emanuel Pfizner, Philipp Kukura, Yi-Teng Hsiao, Chia-Lung Hsieh, Brian Abbey, Alberto Diaspro, Aymeric LeGratiet, Paolo Bianchini, Natan T. Shaked, Bertrand Simon, Nicolas Verrier, Matthieu Debailleul, Olivier Haeberlé, Sheng Wang, Mengkun Liu, Yeran Bai, Ji-Xin Cheng, Behjat S. Kariman, Katsumasa Fujita, Moshe Sinvani, Zeev Zalevsky, Xiangping Li, Guan-Jie Huang, Shi-Wei Chu, Omer Tzang, Dror Hershkovitz, Ori Cheshnovsky, Mikko J. Huttunen, Stefan G. Stanciu, Vera N. Smolyaninova, Igor I. Smolyaninov, Ulf Leonhardt, Sahar Sahebdivan, Zengbo Wang, Boris Luk'yanchuk, Limin Wu, Alexey V. Maslov, Boya Jin, Constantin R. Simovski, Stephane Perrin, Paul Montgomery, and Sylvain Lecler

Label-free super-resolution (LFSR) imaging relies on light-scattering processes in nanoscale objects without a need for fluorescent (FL) staining required in super-resolved FL microscopy. The objectives of this Roadmap are to present a comprehensive vision of the developments, the state-of-the-art in this field, and to discuss the resolution boundaries and hurdles that need to be overcome to break the classical diffraction limit of the label-free imaging. The scope of this Roadmap spans from the advanced interference detection techniques, where the diffraction-limited lateral resolution is combined with unsurpassed axial and temporal resolution, to techniques with true lateral super-resolution capability that are based on understanding resolution as an information science problem, on using novel structured illumination, near-field scanning, and nonlinear optics approaches, and on designing superlenses based on nanoplasmonics, metamaterials, transformation optics, and microsphere-assisted approaches. To this end, this Roadmap brings under the same umbrella researchers from the physics and biomedical optics communities in which such studies have often been developing separately. The ultimate intent of this paper is to create a vision for the current and future developments of LFSR imaging based on its physical mechanisms and to create a great opening for the series of articles in this field.

## Foreword

Imaging is one of the central services that the physical sciences supply to the biosciences. As well as optical microscopy, the subject of this Roadmap, we can add magnetic resonance imaging, X-ray computer tomography, electron microscopy (EM), atomic force microscopy (AFM), and scanning near field optical microscopy (SNOM). It is not an exaggeration to say that the physical sciences are the handmaiden of the biosciences a hugely important function often hidden by more newsworthy aspects such as astronomy. This is a message worth emphasising to our political masters when making the case for supporting our discipline.

Optical microscopy is by far the most venerable of the imaging techniques in use. Its convenience of use and benign treatment of specimens often make it the tool of choice. Frustratingly much of biology, particularly the more modern aspects, exists on a length scale beyond the reach of conventional microscopes but


the virtues alluded to above mean that over the past decades there has been huge effort overcome the resolution problem. Although EM, AFM, and SNOM are capable of high resolution they all have drawbacks relative to the optical microscope, whether it be of speed, convenience, or specimen damage.

The Abbé diffraction limit which restricts resolution to the threshold of many of the treasures of the biosciences, was broken first by exploitation of fluorescent dye markers. Label free imaging is more challenging but hopes were raised when the shibboleth of the Abbé law was shown to be a practical limit, not an absolute one. This was a consequence of detailed investigation of the strange properties of materials with negative refractive

\*E-mail: astratov@charlotte.edu

#The complete list of author affiliations can be found in the Addendum, at the end of the manuscript.

†Deceased

 The ORCID identification number(s) for the author(s) of this article can be found under <https://doi.org/10.1002/lpor.202200029>

© 2023 The Authors. Laser & Photonics Reviews published by Wiley-VCH GmbH. This is an open access article under the terms of the Creative Commons Attribution License, which permits use, distribution and reproduction in any medium, provided the original work is properly cited.

DOI: 10.1002/lpor.202200029

indices. First raised by Veselago as a theoretical possibility, negative refraction became a reality with the advent of metamaterials at the turn of the century. Subsequent refinement of our understanding of lenses based on negative refraction revealed their potential for super-resolution. Key to their properties are the permittivity and permeability which must both be negative: this creates a strange but transparent material contrasted with metals which have only a negative permittivity and are not transparent. However both support surface states: an electrical one in the case of metals, known as a surface plasmon. For negative refraction there are two surface states: one with predominantly electrical character like a metal and the other with predominantly magnetic character which is rarely if ever seen in naturally occurring materials. It is the surface states that give rise to the super-resolution characteristics of negative refracting materials. In fact as many of the articles in this Roadmap show, metals can sometimes substitute for a truly negatively refracting material in super resolving systems.

The close relationship of negative refraction to plasmonic materials connects with a wider interest in plasmonics and the abil-

ity of plasmons formed on suitably structured surfaces to focus light into an area whose size is determined by the plasmon wavelength rather than that of the free space wavelength. Early work by Ebbesen demonstrated how light can be gathered into such a small area as to be able to squeeze through holes in silver a mere tens of nanometres across. As our understanding of negative refraction and its connection to surface resonances grew exploitation for imaging was natural consequence. Application of these ideas is reported in this Roadmap in the form of structured illumination and the development of hyperbolic materials with their positive/negative hybrid structure and their unique ability to propagate sub-wavelength radiation.

The several areas explored in this Roadmap (see **Table 1**) have rich potential that has more to give and it is our hope that in laying out the current state of affairs further progress will be catalysed adding to the remarkable achievements made so far.

Sir John B. Pendry  
Imperial College London  
2023

**Table 1.** The list of topics and authors in this roadmap.

Section No.	Title	Authors
1	Introduction to Roadmap	Vasily N. Astratov
<i>Theme I: Information Science And Novel Structured Illumination</i>		
2	Deep Unrolled Image Restoration in Super-Resolution Microscopy	Yair Ben Sahel, Yonina C. Eldar
3	Deep Learning-Enabled Super-Resolution Microscopy	Luzhe Huang, Aydogan Ozcan
4	The Future of Super-Resolution Optical Microscopy at the Age of Big Data	Nikolay I. Zheludev
5	Label-Free Plasmonic/Metamaterial Structured Illumination Microscopy	Junxiang Zhao, Zachary Burns, Zhaowei Liu
6	Fundamental Limits to the Resolution of Label-free Far-field Microscopy	Evgenii Narimanov
<i>Theme II: Interferometric And Holographic Approaches</i>		
7	Current Trends In Quantitative Phase Imaging	Neha Goswami, Gabriel Popescu
8	The Present and Future of Scattering Microscopy for Studying Biomolecular Mechanisms	Emanuel Pfizner, Philipp Kukura
9	Coherent Brightfield Microscopy	Yi-Teng Hsiao, Chia-Lung Hsieh
10	Plasmon-Enhanced Optical Ptychography and Phase Imaging	Brian Abbey
11	Circular Intensity Differential Scattering Microscopy	Alberto Diaspro, Aymeric LeGratiet, Paolo Bianchini
12	Super-Resolved Off-Axis Holographic Multiplexing	Natan T. Shaked
13	Tomographic Diffractive Microscopy	Bertrand Simon, Nicolas Verrier, Matthieu Debailleul, Olivier Haerberlé
14	Scanning Near-Field Optical Microscope for Quantitative Nano-Imaging and Nano-Spectroscopy	Sheng Wang, Mengkun Liu
<i>Theme III: Nonlinear Optics Approaches</i>		
15	Absorption-Based Super-Resolution Imaging	Yeran Bai, Ji-Xin Cheng
16	Pump-Probe Super-Resolution Microscopy	Paolo Bianchini, Behjat S. Kariman, Alberto Diaspro
17	Super-Resolution Raman Microscopy	Katsumasa Fujita
18	Silicon Non-Linearity Based Super-Resolved Pump-Probe Imaging	Moshe Sinvani, Zeev Zalevsky
19	The Rise of Mie-Tronics-Based Nonlinear Scattering Imaging	Xiangping Li, Guan-Jie Huang, Shi-Wei Chu
20	Label-Free Super-Resolution Microscopy by Non-Linear Photomodulated Reflectivity	Omer Tzang, Dror Hershkovitz, Ori Cheshnovsky
21	Structured Illumination-Based Nonlinear Label-Free Super-Resolution Microscopy	Mikko J. Huttunen, Stefan G. Stanciu
<i>Theme IV: Advanced Superlens Designs</i>		
22	Surface Electromagnetic Wave Lenses and Transformation Optics	Vera N. Smolyaninova, Igor I. Smolyaninov
23	Perfect Imaging	Ulf Leonhardt, Sahar Sahebdivan
24	Microsphere Superlens and Metamaterial Solid Immersion Lens	Zengbo Wang, Boris Luk'yanchuk, Limin Wu
25	Microspherical Superlens Imaging: Fundamental Origins of Super-Resolution	Alexey V. Maslov, Vasily N. Astratov
26	Smartphone Ball Lens Microscopy	Vasily N. Astratov, Boya Jin
27	Imaging Beams for Subwavelength Resolution	Constantin R. Simovski
28	Microsphere-Assisted Interference Microscopy	Stephane Perrin, Paul Montgomery, Sylvain Lecler

## 1. Introduction to Roadmap

(Vasily N. Astratov)

Label-free imaging does not rely on the use of fluorescent markers and it has been a historically first and primary method of observational microbiology since the discovery of various microorganisms (“animalcules”) by Antonie van Leeuwenhoek in the 17<sup>th</sup> century. In this Roadmap, we address a development of label-free super-resolution (LFSR) imaging aimed at overcoming the classical diffraction limit introduced in the late 19<sup>th</sup> century by Abbe,<sup>[1]</sup> Helmholtz,<sup>[2]</sup> and Rayleigh.<sup>[3]</sup> According to the Abbe limit the far-field resolution of optical systems is limited to  $\lambda/(2n \times \sin\theta) = \lambda/(2 \times \text{NA})$ , where  $\lambda$  is the operating wavelength,  $n$  is the refractive index of the surrounding medium,  $\theta$  is the half-angle of the objective acceptance cone,  $\text{NA} = n \times \sin\theta$  is the numerical aperture of the imaging system. This corresponds to about 0.2  $\mu\text{m}$  in lateral direction and about 0.6  $\mu\text{m}$  in the direction of the optical axis for visible light. The beginning of the 20<sup>th</sup> century was a period of extraordinary developments in physics, but at that time it might seem almost impossible that the diffraction limit would be overcome.

This introduction, however, would be incomplete without mentioning the remarkably successful super-resolved fluorescence (FL) microscopy based on staining biomedical samples with organic dyes (linked to labeling agents) or by tagging proteins of interest with fluorescent proteins. Due to its unrivaled contrast, FL imaging has emerged as one of the dominant light microscopy methods in modern biology. It allows one to “highlight” the structures inside a living cell and it became widespread since the discovery of green FL protein in the 1960s. More recent developments aimed at achieving FL-based far-field super-resolution can be divided into deterministic methods using certain nonlinear properties of such emitters and stochastic methods using their statistical single-molecule FL detection properties, while the distinction between these methods is also related to the way fluorescence is induced and read out. We refer the interested reader to a roadmap,<sup>[4]</sup> topical reviews,<sup>[10, 5–9]</sup> and books<sup>[11–13]</sup> in this area based on the following methods which all, in one way or another, address the problem of the limited spatial resolution in far-field microscopy: stimulated emission depletion (STED),<sup>[14, 15]</sup> ground state depletion (GSD),<sup>[16, 17]</sup> reversible saturated optical (fluorescence) transitions (RESOLFT),<sup>[18, 19]</sup> photoactivation localization microscopy (PALM),<sup>[20, 21]</sup> stochastic optical reconstruction microscopy (STORM),<sup>[22, 23]</sup> super-resolution optical fluctuation imaging (SOFI),<sup>[24, 25]</sup> structured illumination microscopy (SIM),<sup>[26–29]</sup> or saturated structured illumination microscopy (SSIM).<sup>[30]</sup> While SIM achieves a two-fold improvement in spatial resolution compared to conventional optical microscopy, STED, RESOLFT, PALM/STORM, or SSIM have all gone beyond this, pushing the limits of optical image resolution to the nanometer scale.<sup>[4]</sup> An additional development is represented by the 4Pi laser scanning FL microscope with an improved axial resolution.<sup>[31–33]</sup> The 2014 Nobel Prize in Chemistry awarded to Eric Betzig, Stefan W. Hell, and William E. Moerner “for the development of superresolved fluorescence microscopy” can be seen as a combined prize for single-molecule detection and superresolution FL imaging. While FL microscopy is a separate area from LFSR imaging, and it is generally beyond

the scope of this Roadmap, the fast progress in this area was inspirational for the recent developments in LFSR imaging.

In contrast to super-resolved FL microscopy, the development of LFSR area was a slow gradual process based on introducing novel physical mechanisms or interdisciplinary concepts symbolically represented in the tree diagram in **Figure 1** explained later in this Introduction. Since the label-free imaging does not rely on using FL markers, it promises practically unlimited applications spanning from visualization of subcellular structures to nanostructure characterization in materials science. However, label-free super-resolution (LFSR) microscopy has to rely on subtler light-scattering processes in nanoscale objects, resulting in lower image contrasts. The problem of overcoming the far-field diffraction limit is extremely challenging in view of the limited photon budgets offered by unstained nanoscale objects.

Our motivation to create the Roadmap on LFSR imaging stems from three major conceptual breakthroughs in this area which took place mainly in the last two decades. The first one is recognizing imaging as an information science problem based on using different forms of prior knowledge about objects, training of imaging systems considered as deep-learning networks, and, finally, using artificial intelligence for recognizing images and improving resolution of optical instruments. The second one is the development of structured illumination microscopy (SIM) where different forms of structured illumination such as interference patterns, superoscillatory optical beams, plasmonic hot spots, photonic nanojets, vortices, or hyperstructured beams were used to shift high spatial frequencies into the bandpass of the microscope. The third one is the appearance of novel concepts such as “perfect” lens, superlens, hyperlens, superoscillatory lens, and transformation optics in the context of development of nanoplasmonics and metamaterials. Each of these three areas has some history of development by the early pioneers in the 20<sup>th</sup> century, however they were transformed into new frontiers in optics and photonics research due to their explosive growth during the last two decades. Although these three advancements represent cornerstones of the ongoing revolution in LFSR imaging, they do not represent the entire LFSR field. There are other important approaches which have a long and distinguished history of development. They are based on near-field scanning, nonlinear optics, and interference-based detection techniques. *Thus, this Roadmap represents an attempt to combine under the same umbrella research efforts of many groups working on all these directions, create a comprehensive vision of the entire LFSR field, present current state-of-the-art in LFSR imaging, and predict future progress in this field.*

The history of development of LFSR imaging and genealogical connections between different areas are illustrated by a tree diagram in **Figure 1**. The stem of the tree diagram, indicated as “4 - Mainstream”, represents two types of advancements: i) major factors impacting microscopy such as invention of lasers as well as contributions of great pioneers in the field, and ii) development of interferometric and holographic approaches. The stem (4) of the tree represents the mainstream microscopy which became more powerful, advanced, and probably most widely used in today’s biomedical research. Although, technically, most of these methods have a diffraction-limited resolution, they really became a powerhouse for all other methods with the true super-resolution capability illustrated by the branches of the tree (1–3, 5–7), each branch representing a particular mechanism



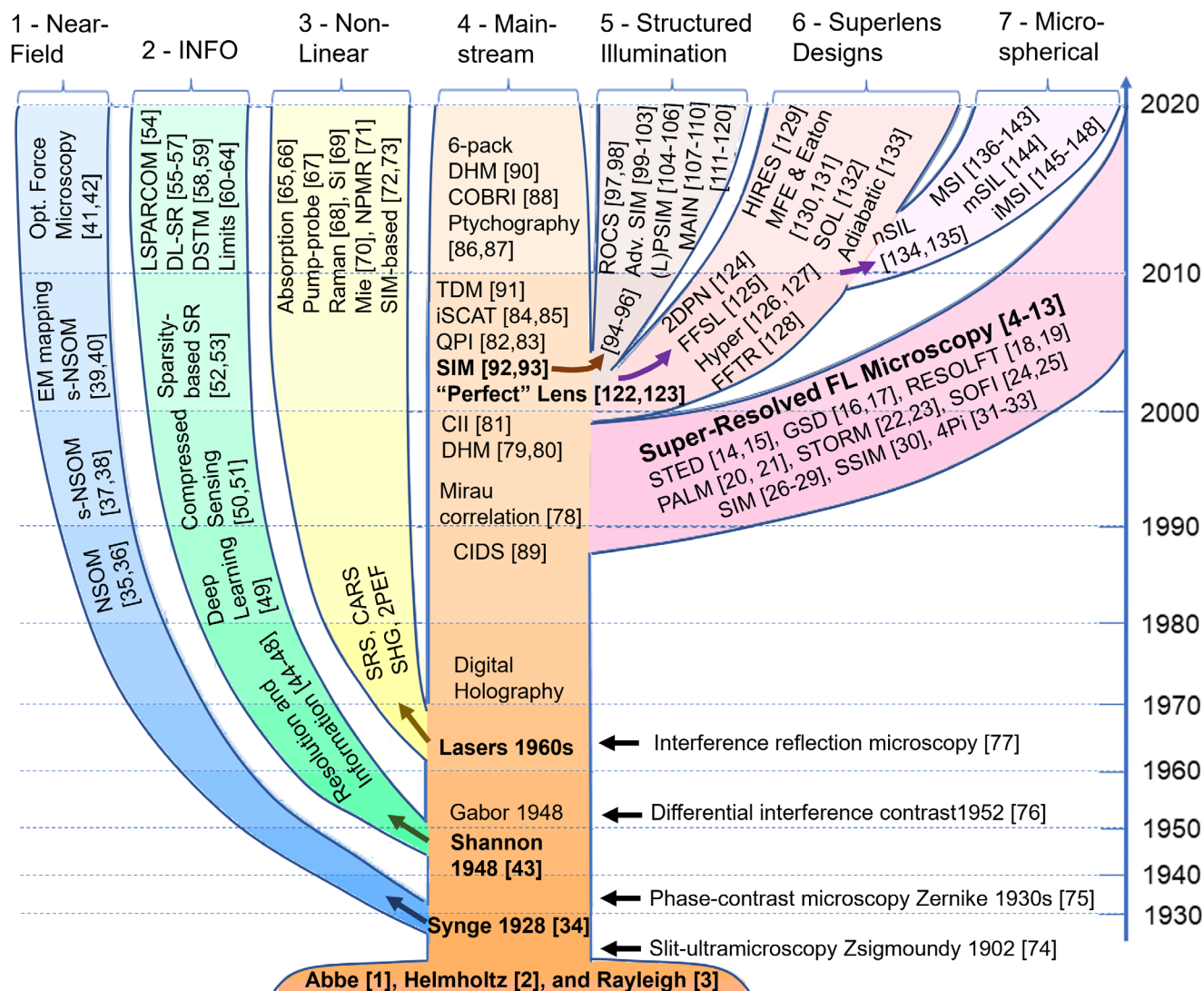


**Figure 1.** Tree diagram of evolutionary development of LFSR subjects and methods. The tree is rooted in a classical diffraction limit introduced by Abbe, Helmholtz, and Rayleigh. The stem (4) represents development of *Mainstream* diffraction-limited microscopy due to incorporation of interferometric and holographic approaches. The branches represent different LFSR imaging mechanisms: 1 – *Near-field* scanning, 2 – *Information (INFO)* approach, 3 – *Nonlinear* optics approach, 5 – *Structured Illumination*, 6 – advanced *Superlens Designs*, 7 – *Microspherical* superlens imaging (MSI). *Super-Resolved FL Microscopy* is illustrated, but it does not belong to LFSR methods. Notation: NSOM, near-field scanning optical microscopy; s-NSOM, scattering NSOM; EM, electromagnetic; SR, super-resolution; LSPARCOM, learned sparsity based super-resolution microscopy; DL-SR, deep learning-enabled image super-resolution; DSTM, deeply subwavelength topological microscopy; SRS, stimulated Raman scattering; CARS, coherent anti-Stokes Raman scattering; SHG, second harmonic generation; 2PEF, two-photon excitation fluorescence; NPMR, nonlinear photo-modulated reflectivity; SIM, structured illumination microscopy; DHM, digital holographic microscopy; CII, computational integral imaging; QPI, quantitative phase imaging; iSCAT, interferometric detection of scattering; COBRI, coherent brightfield imaging; CIDS, circular intensity differential scattering; DHM, digital holographic microscopy; TDM, tomographic diffractive microscopy; ROCS, rotating coherent scattering; Adv. SIM, advanced SIM; PSIM, plasmonic structured illumination microscopy; LPSIM, localized PSIM; MAIN, metamaterial-assisted illumination nanoscopy; 2DPN, 2-D plasmonic nanoscopy; FFSL, far-field superlens; “Hyper”, short for “hyperlens”; FFTR, far-field time reversal; HIRES, high-index resolution enhancement by scattering; MFE, Maxwell fisheye; SOL, super-oscillatory lens; nSIL, nano solid immersion lens; mSIL, metamaterial SIL; MSI, microspherical superlens imaging; iMSI, interferometric MSI.

or approach to the LFSR imaging: 1 – near-field scanning, 2 – information (INFO) approach, 3 – nonlinear optics approach, 5 – structured illumination, 6 – advanced superlens designs, and 7 – microspherical superlens imaging (MSI). The main methods of LFSR imaging with the key references are indicated on the tree diagram. More complete lists of publications devoted to different LFSR mechanisms can be found in the Topical Review articles.

We also illustrated super-resolved FL microscopy as an additional branch with the corresponding key references.<sup>[10–33, 4–9]</sup>

This tree diagram is a useful image for representing the entire LFSR field and its evolution in time, but it is rather difficult to follow the order of the tree diagram for creating the organizational structure of this Roadmap. Ideally, it could have been done by presenting Topical Review sections (called “Topics” for briefly)

either from bottom up or from left to right branches of the tree diagram. Each Topic, however, focuses on the present and future of a given field which means that the Topics tend to aggregate towards the top of the tree diagram. In addition, different branches of the tree are populated unevenly. As an example, the left-most “near-field” branch (1) of the tree is represented by a single Topic 14. At the same time, each Topic is in some sense a mini-review addressing several different developments inside each branch of the tree and sometimes involving an interplay between different branches. For these reasons, an attempt to closely follow the order of the tree diagram is rather difficult to implement and, perhaps, it would not be a natural approach in this situation.

To create an organizational structure for this Roadmap containing an Introductory section and 27 Topical Review sections, we used a somewhat simplified approach which still has a strong relevance to the tree diagram in Figure 1. In this Roadmap, the Topics are divided into four broad Themes. We begin this Roadmap with Theme I devoted to the information science and structured illumination directions (Topics 2–6) as areas at the forefront of research in this field today. Theme I can be mapped to combined second and fifth branches of the tree diagram. Theme II combines more traditional interferometric and holographic approaches (Topics 7–14) corresponding to the stem (4) of the tree diagram. Theme III describes the nonlinear optics approaches (Topics 15–21) corresponding to the third branch of the tree. The novel advanced superlens designs are combined in Theme IV (Topics 22–28) which corresponds to combined sixth and seventh branches of the tree diagram.

In this Introduction, we provide a brief account of history and developments of the LFSR imaging field following the order of branches (1–7) on the tree diagram with the references to the corresponding Topical Review sections.

### 1.1. Near-Field Scanning

The onset of the super-resolution era was marked by a proposal of microscopy based on scanning of optical near fields in 1928 by Synge<sup>[34]</sup> who was encouraged by Albert Einstein. Much later, in the 1980s and 1990s, this idea gave rise to near-field scanning optical microscope (NSOM)<sup>[35, 36]</sup> and scattering-NSOM (s-NSOM).<sup>[37, 38]</sup> Further development of these methods made possible electromagnetic field mapping in plasmonic and photonic nanostructures.<sup>[39, 40]</sup> It also led to the development of the optical force microscopy.<sup>[41, 42]</sup> The timeline of these developments is represented by the leftmost 1<sup>st</sup> branch on the Roadmap tree. Although this approach was historically significant and providing one of the highest, almost atomic-scale resolutions published to date, its representation in this Roadmap is rather limited since these methods are based on a relatively slow point-by-point near field scanning by nanoapertures or nanoprobes. An account of NSOM developments for quantitative nano-imaging and nanospectroscopy can be found in Topic 14 and in a review.<sup>[38]</sup>

### 1.2. Information Approach

In traditional optical imaging systems, the spatial resolution is limited by the physics of diffraction, which acts as a low-pass filter

attenuating high spatial frequencies and retaining low frequencies unchanged. In the information approach, however, the spatial frequencies have to be transmitted by sampling as a result of converting a signal into discrete numbers. This means that to transmit the spatial “cut-off” frequency which determines the resolution, one has to transmit its coordinates at a series of points spaced with the double frequency.<sup>[7]</sup> Imaging can be viewed as an information communication problem where achieving higher resolution requires higher channel capacity in a spirit of the information theory developed by Shannon in 1948.<sup>[43]</sup> Application of the information approach to optics was prepared by the early work of Toraldo di Francia who proposed in 1952 that the spatial frequency cut-off of an imaging system can be extended.<sup>[44]</sup> It was followed by introducing the mathematical framework for the informational capacity of two-dimensional optical system,<sup>[45]</sup> the formulation of invariance theorem by Lukosz,<sup>[46, 47]</sup> and incorporation of a noise factor in the theorem of invariance of the information capacity of an optical image by Cox and Sheppard.<sup>[48]</sup> The central concept is represented by the theorem of invariance of information capacity which states that it is not the spatial bandwidth but the information capacity of an imaging system that is constant. The expression for the information capacity has been derived based on three spatial dimensions, temporal dimension, and two independent states of polarization.<sup>[48]</sup> This means that if the object belongs to a restricted class, it is in principle possible to extend the spatial bandwidth (spatial resolution) by encoding-decoding the additional information onto the independent (unused) parameter(s) of the imaging system.<sup>[48]</sup> This early work came to two revelations about the nature of super-resolution which laid out the foundation for the future development in this area. The first was that the invariance theorem shows that the resolution can be enhanced by incorporating a priori knowledge about the object. The second was that from a purely informational point of view there are no bounds to achievable resolution, but the practical bound is imposed by the signal-to-noise ratio (SNR) of the resulting image.<sup>[48]</sup>

Meanwhile computational imaging has been developing since the emergence of machine learning in the 1960s. The most important advancements were the use of multi-layered computational geometries such as deep neural and backpropagation<sup>[49]</sup> networks as well as the development of compressed sensing.<sup>[50, 51]</sup> The latter showed that with a prior knowledge (assumption of sparsity), the signal may be reconstructed with fewer samples than it is required by the Nyquist–Shannon sampling theorem. It directly stimulated application of similar principles to achieving super-resolution imaging.<sup>[52, 53]</sup>

In the past few years, the information approach sparked a wealth of ideas where deep learning is directly applied to multi-layer imaging networks for achieving super-resolution. Initially, the applications were developed for FL microscopy. Topic 2 describes the development of FL single-molecule localization microscopies such as PALM, STORM, and SPARCOM (sparsity-based super-resolution correlation microscopy, which exploits the sparse nature of the fluorophores distribution, alongside a statistical prior of uncorrelated emissions) towards incorporating algorithms with trained neural networks via a process known as algorithmic unrolling that gave rise to Learned SPARCOM (LSPARCOM).<sup>[54]</sup> The latter method enables efficient, accurate, and robust imaging well below the diffraction limit, without any

prior knowledge of the imaging setup's physical parameters. It is proposed that algorithmic unrolling can become a powerful resource in label-free interferometric microscopy. Topic 3 is based on the first report on deep learning-enabled image super-resolution (DL-SR) in FL optical microscopy<sup>[55, 56]</sup> and on applications to label-free microscopy such as digital staining of label-free high-resolution images.<sup>[57]</sup> Topic 4 is devoted to deeply subwavelength topological microscopy (DSTM) which is a truly label-free method based on using a deep learning neural network that has been trained on scattering events from a large set of a priori known objects.<sup>[58]</sup> This method provided measurements of the width of sub-wavelength slits on an opaque screen with an extraordinary accuracy of  $\approx\lambda/130$  for a single-shot measurement or  $\approx\lambda/260$  (i.e., 2.4 nm) when combining measurements of diffraction patterns at different distances from the object, thus challenging the accuracy of scanning electron microscopy and ion beam lithography.<sup>[59]</sup> Resolution analysis based on the Shannon's theory of information transmission in linear systems in the presence of noise<sup>[60]</sup> can be found in Topic 6. It develops earlier work<sup>[48]</sup> and incorporates both SNR and a priori knowledge about the object (in the form of sparsity) into the resolution limit determined by the information theory.

The conclusion of classical information theory that the noise factor determines the resolution of an imaging system is consistent with the Feynman's perspective that "Rayleigh's criterion is a rough idea in the first place", and a better resolution can be achieved "if sufficiently careful measurements of the exact intensity distribution over the diffracted image spot can be made".<sup>[61]</sup> It should be noted that the quantum physics approach based on quantum photon correlation allows increasing the resolution of images by the factor of two beyond the diffraction limit.<sup>[62–64]</sup> This approach considers anti-bunching photon statistics or quantum entanglement for photons sharing common location information. In principle, it can be interpreted as a form of using a *prior knowledge* about the sample or as a form of optical nonlinearity due to multiphoton nature of interaction with the sample, however, this approach is not included in this Roadmap.

### 1.3. Nonlinear Optics

The Abbe resolution limit is formulated for linear optical systems, however in special situations it can be surpassed even in this limit with the example given by the interference-based FL SIM where the two-fold resolution increase beyond the classical diffraction limit is still diffraction-limited.<sup>[26–29]</sup> The axial resolution can be enhanced severalfold compared to that of the standard FL confocal microscopy using a 4Pi microscope.<sup>[31–33]</sup> Optical nonlinearity opens new ways of achieving super-resolution imaging. The photoswitching and saturation (depletion) are nonlinear effects used in super-resolved FL microscopy. Another possibility is offered by the multiphoton microscopy, where the nonlinear processes provide novel, label-free contrast mechanism. Multiphoton microscopy can also increase the penetration depth by using longer excitation wavelengths and enhance resolution, contrast, and molecular specificity. It should be noted, however, that higher photoexcitation intensities intrinsic for nonlinear methods can limit their applications for studying biomedical samples. However, they can become a tool of choice for nanostructure

characterization in material science with many examples such as imaging single-walled carbon nanotubes, nanodiamonds, gold nanoparticles, graphene, silicon, etc. The development of nonlinear optical microscopy began with the broad application of lasers in the 1960s that resulted in the creation of stimulated Raman scattering (SRS), coherent anti-Stokes Raman scattering (CARS), second harmonic generation (SHG), two-photon excitation fluorescence (2PEF), and many other types of microscopy techniques.

This Roadmap contains several Topics where various optical nonlinearities are exploited to increase the resolution of optical microscopy beyond the classical diffraction limit using a label-free contrast mechanism. As shown in Topic 15, absorption-based imaging can be performed in two modalities (without using near-field probes): a) optical photothermal detection<sup>[65]</sup> which can provide resolution up to  $\approx\lambda/10$  and b) ground-state depletion in transient absorption processes for imaging.<sup>[66]</sup> Pump-probe methods described in Topic 16 provide an experimental basis for many imaging modalities including transient absorption, SRS, CARS, SHG, 2PEF, etc. Nonlinear light-matter interactions in these methods involve the second  $\chi^{(2)}$  and third  $\chi^{(3)}$  order of susceptibilities. In particular, imaging on graphene with pulse powers about  $7.0 \text{ MW cm}^{-2}$  allows achieving a resolution of the order of  $\approx\lambda/10$ .<sup>[67]</sup> Topic 17 is devoted to imaging based on Raman scattering that include coherent methods such as CARS, SRS, and surface enhanced Raman scattering (SERS). High-resolution coherent Raman imaging based on CARS and SRS have been demonstrated based on saturation excitation (SAX) microscopy.<sup>[68]</sup> Topic 18 considers super-resolution imaging based on material nonlinearity due to plasma dispersion nonlinearity in silicon.<sup>[69]</sup> Topic 19 develops a nonlinear Rayleigh scattering microscopy based on plasmonic or dielectric particles with resonant properties (Mie-resonators) which provide a novel super-resolution contrast mechanism.<sup>[70]</sup> Topic 20 introduces LFSR imaging based on nonlinear photo-modulated reflectivity (NPMR) which takes place due to the nonlinear changes in the reflectance of materials induced by an ultra-short pump pulse.<sup>[71]</sup> Topic 21 is devoted to a combination of SIM with the optical nonlinear detection,<sup>[72]</sup> where SIM illumination can be understood broadly similar to that in the pixel reassignment<sup>[73]</sup> or image scanning microscopies.

### 1.4. Mainstream Microscopy: Interferometric and Holographic Approaches

Despite all the successes of FL microscopy which became a major tool in cell biology, the mainstream label-free microscopy remained very attractive because it does not require cells (or other structures) to be stained, thus avoiding associated phototoxicity and photobleaching effects. Although being diffraction-limited, these methods (especially the modern interference detection techniques) offer an unsurpassed precision of axial resolution combined with high temporal resolution that explains the widespread and high popularity of these methods in biomedical imaging applications. In addition, the resolution of these label-free methods can be increased beyond the classical diffraction limit by combining them with near-field scanning, information-based or superlens-based approaches. The development of mainstream label-free methods has a distinguished

history in the 20<sup>th</sup> century and it is actively developing in the last two decades, as symbolically represented by stem (4) in the Roadmap tree diagram in Figure 1.

The first notable step was observation of gold particles with diameters less than 4 nm in solid material in 1902<sup>[74]</sup> and silver particles with estimated sizes 50–77 nm in a colloidal solution in 1905 by Richard Zsigmondy using his *ultramicroscope* (1925 Nobel Prize in Chemistry). This breakthrough result can be viewed as an early sign of emerging era of nanotechnology. The second step based on introduction of phase-contrast microscopy (PCM) in 1930s by Frits Zernike (1953 Nobel Prize in Physics)<sup>[75]</sup> made a profound impact on label-free imaging. It was followed by the development of a large family of interferometric detection techniques such as differential interference contrast (DIC) microscopy proposed in 1952 by Georges Nomarski,<sup>[76]</sup> interference reflection microscopy,<sup>[77]</sup> and Mirau correlation microscopy.<sup>[78]</sup> The third step began with the invention of holography by Dennis Gabor in 1948 that stimulated ideas about combining holography and microscopy aimed at highly sensitive measurements of the thickness and refractive index of biological samples. In the 1990s, increasing power of digital image sensors and computers facilitated development of digital holographic microscopy (DHM).<sup>[79]</sup> Application of DHM to 3D objects with complicated shapes allowed obtaining their extended focused images without any mechanical scanning or using special phase plates.<sup>[80]</sup> Another form of 3D volumetric object reconstruction is based on using computational integral imaging (CII) where sensing of the 3D scene is carried out by a microlens array.<sup>[81]</sup> More recently, quantitative phase imaging (QPI) provided the enhanced stability of imaging by locking of the incident field with the scattered light.<sup>[82]</sup> An interesting development of QPI for label-free, high-resolution discrimination of live stem cells is based on its combination with the total internal reflection microscopy.<sup>[83]</sup> The fourth step was developing methods of interferometric detection of scattering (iSCAT) from single nanoparticles,<sup>[84]</sup> viruses,<sup>[85]</sup> and proteins. One more important step was developing visible-light super-resolution ptychography where a specimen is stepped through a localized coherent “probe” wavefront, generating a series of diffraction patterns at the plane of a detector.<sup>[86, 87]</sup>

This Roadmap contains several Topics descending from the phase-contrast microscopy pioneered by Frits Zernike and showing the past, present, and future of the interferometric detection methods. Topic 7 presents current trends in QPI including imaging of strongly scattering structures, imaging with computational specificity, and improved resolution using deep learning. Topic 8 is devoted to iSCAT microscopy for studying biomolecular mechanisms. Topic 9 introduces coherent brightfield imaging (COBRI)<sup>[88]</sup> which can be considered as a transmission counterpart of iSCAT. Topic 10 describes the current status and future prospects of plasmon-enhanced optical ptychography.<sup>[87]</sup> Topic 11 is devoted to circular intensity differential scattering (CIDS) method<sup>[89]</sup> originated in the 1980s as a differential measurement of the circular right and left polarized light scattered by a specimen outside the absorption bands that separates this method from the circular dichroism. Although the mechanism of this effect is different from that used in interferometric or holographic microscopy approaches, Topic 11 represents potential of polarization microscopy based on using non-conventional detection modalities. Topic 12 is devoted to off-axis

DHM where holographic multiplexing of up to six simultaneous wave-front channels can be reconstructed to an extended synthetic aperture and the super-resolved image.<sup>[90]</sup> Topic 13 introduces tomographic diffractive microscopy (TDM, also referred to as synthetic aperture microscopy, tomographic phase microscopy, phase nanoscopy, optical diffraction tomography, etc.; see Ref. [91] for a general introduction to these techniques) and its modern challenges. Topic 14 generally covers near-field scanning methods such as NSOM, however, the interferometric schemes that simultaneously retrieve the near-field optical signal amplitude and phase are also widely used in NSOM.

## 1.5. Structured Illumination

Structured illumination microscopy (SIM) is a widefield method in which a series of periodic illumination patterns are superimposed onto an object resulting in a twofold increase in resolution.<sup>[26–29]</sup> SIM was developed mainly in the context of FL imaging based on using multiple incoherent point-like sources emitting light at mutually random phase. This “loss of phase” in FL microscopy allows understanding image formation due to the superposition of the individual intensity distributions created by the point-like sources rather than their amplitudes. It also underlines the mathematical apparatus of SIM method based on the fact that product of functions (object and its illumination pattern) in real space leads to a convolution of these functions in the reciprocal space. Due to this property, the information about higher spatial frequencies (larger  $k$ -vectors) of the object can be projected into an escape cone of the microscope objective accessible for the far-field imaging. Thus, such “loss of phase” in FL imaging as opposed to elastic scattering “is the reason that fluorescence structured illumination microscopy is able to shift out-of-band information<sup>[27]</sup> into the detection passband”.<sup>[92, 93]</sup> An increase of resolution beyond the factor of two requires one of the following: nonlinear sample response, prior knowledge about the sample and its properties, or near-field excitation or emission.<sup>[92]</sup> Nonlinear SIM can be realized using saturation effects in fluorophores,<sup>[30]</sup> which can lead to photobleaching and therefore limit the applications in biomedical imaging. Alternatively, some possibilities of further enhancing the SIM resolution without invoking any nonlinearity were proposed based on the proximity projection grating scheme.<sup>[94]</sup> It should be noted, however, that label-free imaging involves scattered light, and due to a coherent nature of scattering, the resolution advantage is limited.<sup>[92, 93]</sup> A twofold increase in lateral resolution can be achieved by oblique, coherent illumination. Averaging several high-contrast and high-resolution images in combination with near-field excitation lays the foundations of synthetic aperture microscopy<sup>[95, 96]</sup> and rotating coherent scattering (ROCS) microscopy.<sup>[97, 98]</sup> It should be noted that due to its high imaging speed, wide field-of-view, and low photodamage in FL biomedical applications there is currently a significant interest in exploring the resolution benefits of both FL<sup>[99]</sup> and label-free versions of SIM.<sup>[100–103]</sup> A common feature of these advanced SIM schemes is based on using a near-field excitation/illumination typically combined with the use of high-index substrates such as GaP.<sup>[103]</sup>

Another way of increasing the resolution is based on using periodically patterned nanoplasmonic or metamaterial sub-



strates which can create higher spatial frequency illumination patterns. As shown in Topic 5, plasmonic structured illumination microscopy (PSIM) shows 2.6-fold resolution advantage<sup>[104]</sup> and localized plasmonic structured illumination microscopy (LP-SIM) shows threefold resolution advantage with biomedical samples.<sup>[105, 106]</sup> PSIM and LP-SIM use interference patterns from counter-propagating surface plasmon polaritons and localized surface plasmon waves, respectively. They originate in metallic nano-disc arrays to generate illuminations structured at the scale beyond the traditional diffraction-limit. Metamaterial-assisted illumination nanoscopy (MAIN) can achieve much higher resolution than the standard SIM methods due to a hyper-structured illumination theoretically proposed in<sup>[107]</sup> and experimentally studied in various hyperbolic metamaterials.<sup>[108–110]</sup> A 6-fold resolution improvement over the diffraction limit has been reported for hyper-structured illumination with label-free imaging, resolving features down to  $\approx 80$  nm.<sup>[110]</sup>

A different approach to ultra-sharp focusing of beams is represented by the optical superoscillation phenomenon reviewed in a recently published Roadmap on Superoscillations.<sup>[111]</sup> Mathematically, this phenomenon is rooted in a fact that a band-limited function can vary arbitrarily faster than its fastest Fourier component, over arbitrarily long intervals.<sup>[112]</sup> Experimentally, the sub-diffraction hot spots produced by array of nanoholes illuminated with coherent light and by binary zone plates were observed and applied for super-resolution imaging.<sup>[113–116]</sup> Superoscillatory “needles” extending for tens of wavelengths along the axis can be explored for high-density data storage,<sup>[117]</sup> light-induced magnetic holography,<sup>[118]</sup> planar diffractive lenses,<sup>[119]</sup> and countersurveillance metaoptics.<sup>[120]</sup>

## 1.6. Advanced Superlens Designs

The information on sub-wavelength features is carried by evanescent waves which exponentially decay in the out-of-plane direction, thus precluding reconstruction of an object in the far field with resolution better than the diffraction limit. The general principle of superlens designs is to preserve the information about high spatial frequencies encoded in the objects' near-fields. In 1970, Nassenstein suggested an ingenious scheme in which the object is illuminated with evanescent waves, and a magnified image is obtained using a holographic technique.<sup>[121]</sup> This work paved the way to future superlens designs. The whole area of superlens designs stemmed from the inspirational proposal of a “perfect lens” by Sir John Pendry in 2000<sup>[122]</sup> based on using negative index materials. Previously, Victor Veselago realized that if a material had negative values for both the electric and magnetic permittivities, then its index of refraction would also be negative.<sup>[123]</sup> This lens, however, works only when the object and its image are located in the subwavelength proximity to the lens which is different from imaging a remote object. In addition, such “near-sighted” lens does not have an ability to magnify the image. It was followed by several advanced superlens designs which had a significant impact on emerging nanoplasmonics and metamaterials communities: (i) 2D plasmonic nanoscope (2DPN) with  $\approx \lambda/8$  resolution<sup>[124]</sup> using image magnification at much shorter plasmonic wavelengths compared to that in air, (ii) far-field superlens (FFSL) with  $\approx \lambda/6$  resolution<sup>[125]</sup> which en-

hances the evanescent waves and converts them into propagating waves, (iii) hyperlens<sup>[126, 127]</sup> represented by an anisotropic metamaterial with hyperbolic dispersion which can provide magnification in a cylindrical geometry, iv) design based the far-field time reversal (FFTR) for objects with near-field scatterers providing imaging with an up to  $\approx \lambda/30$  resolution,<sup>[128]</sup> v) high-index resolution enhancement by scattering (HIRES) lens<sup>[129]</sup> with  $\approx \lambda/6$  resolution in a visible regime, vi) broadband Maxwell fisheye (MFE) and inverted Eaton microlenses<sup>[130, 131]</sup> where the precondition for superresolution is a drain placed at the image position, vii) super-oscillatory lens (SOL) with  $\approx \lambda/6$  resolution in a visible regime<sup>[111–120, 132]</sup> represented by a nanostructured mask which focuses coherent beam into a subwavelength spot, and viii) adiabatic lens<sup>[133]</sup> which utilizes the interference of slowly decompressing far-field electromagnetic waves in plasmonic waveguides with gradient properties.

Topic 22 presents a review of surface electromagnetic wave lenses and transformation optics.<sup>[124–131]</sup> It also introduces a newly discovered class of surface electromagnetic waves which propagate along gradual interfaces of lossy optical media. Topic 23 is devoted to a “perfect” imaging by MFE and Eaton lenses<sup>[130, 131]</sup> as well as, more generally, to transformation optics. A particularly interesting observation is that curved surfaces like the surface of the sphere modify the resolution of imaging in a fundamental way due to modification of the uncertainty relation between position and momentum.

## 1.7. Microspherical Superlens Imaging (MSI)

Magnification of near-field image components has been suggested in experiments with self-assembled plano-spherical nano solid immersion lenses (nSILs).<sup>[134, 135]</sup> Due to micron-scale dimensions of nSILs, the resolution was found to be slightly improved compared to macroscopic SILs limit ( $\lambda/(2n)$ ), but it was still close to  $\approx \lambda/3$ .<sup>[135]</sup> In this regard, the observation of deeply subwavelength resolution by virtual imaging through microspheres in 2011<sup>[136]</sup> was a breakthrough result which stimulated a significant and prolonged interest of imaging community in this technology. To enable study of biomedical samples, MSI technology was developed by using liquid-immersed high-index microspheres.<sup>[137]</sup> Convolution-based resolution analysis revealed that the MSI resolution is typically limited at  $\approx \lambda/6$ - $\lambda/7$  level.<sup>[138]</sup> Exact numerical solutions of Maxwell equations, however, revealed that the maximal theoretical resolution is limited at  $\approx \lambda/4$  level.<sup>[139]</sup> It stimulated a deeper theoretical investigation of the resolution criteria and underlying MSI mechanisms.<sup>[140–142]</sup> Because of the limited field-of-view through individual microspheres, several MSI scanning schemes were proposed including use of movable coverslips with embedded microspheres,<sup>[138]</sup> integration with AFM system<sup>[143]</sup> and several other methods. A notable advancement in the field was the development of metamaterial SILs (mSILs) with the material of the lenses formed by densely packed nanoscale TiO<sub>2</sub> clusters<sup>[144]</sup> which are capable of potentially even higher resolution compared to conventional MSI techniques.

Topic 24 represents a history of development and state-of-the-art of MSI and mSIL methods. Topic 25 contains a review of theoretical factors which can be responsible for super-resolution



capability of MSI including the fundamental role of curvature of microsphere, resonant properties, and role of plasmonic contributions. Topic 26 describes designs of pocket-size smartphone-based microscopes aimed at maximizing their resolution capability. Topic 27 represents a theoretical analysis of resolving power of MSI method inspired by analogy with hyperlens imaging mechanisms where the super-resolution is achieved without involving evanescent fields. Topic 28 contains an account of integration of MSI technology with interferometry (iMSI) which can be realized in Linnik,<sup>[145]</sup> Mirau,<sup>[146, 147]</sup> and Mach-Zehnder<sup>[148]</sup> configurations to achieve surface topography reconstruction with a high axial sensitivity.

In conclusion, this Roadmap provides a snapshot of this rapidly evolving field ultimately intending to develop a systematic approach to this area based on classification of physical mechanisms of LFSR imaging and to create a vision for current and future developments in this field.

This Roadmap originated from a series of special sessions and workshops on Label-Free Super-Resolution Microscopy, which I organized at PQE-2016 and 2017, IEEE Photonics-2017, and ICTON-2017–2020 conferences. Many of the topics included in this Roadmap are represented by Chapters in a book “Label-Free Super-Resolution Microscopy” (Ed. Vasily Astratov) published in 2019.<sup>[149]</sup> For these Topics, the interested readers can potentially find more detailed information on the corresponding subjects in this book.

## Theme I: Information Science and Novel Structured Illumination

### 2. Deep Unrolled Image Restoration in Super-Resolution Microscopy

(Yair Ben Sahel\*, Yonina C. Eldar)

#### 2.1. Introduction

Inspection of sub-cellular features and organelles requires imaging tools with nanometer resolution. Until the development of super-resolution microscopy, the optical resolution limit was set by Abbe's diffraction limit, which is hundreds of nanometers at best for modern light microscopes. When dealing with labeled samples, like in fluorescence microscopy, it is possible to surpass the diffraction limit by distinguishing between light coming from two neighboring fluorophores.<sup>[150]</sup> Such distinction can be done by utilizing photo-activated or photo-switching fluorophores to separate light emission in time; this is the basic principle of single molecule localization microscopy (SMLM) techniques such as photo-activated localization microscopy (PALM) and stochastic optical reconstruction microscopy (STORM).<sup>[20, 22]</sup> These methods take a sequence of diffraction-limited images, generated by a sparse set of fluorophores with whose overlapping point-spread functions (PSFs) have minimal overlap, and produce emitter localizations with high precision. However, low emitter density requires lengthy imaging times to achieve full coverage and minimal overlap between PSFs, resulting in low temporal resolution.

To overcome the long acquisition times required for SMLM methods, a variety of techniques have emerged, which reduce

the number of frames required for reconstruction of the 2D super-resolved image.<sup>[151–153, 24]</sup> These techniques exploit prior knowledge regarding either the optical system, the geometrical structure of the sample, or the statistics of the emitters. One such technique is SPARCOM,<sup>[153, 154]</sup> which makes use of sparsity in the correlation domain, while assuming that the blinking emitters are uncorrelated over time and space. This allows to re-formulate the localization task as a sparse recovery problem which can be solved, for example, using the “Iterative Shrinkage and Thresholding Algorithm” (ISTA).<sup>[155]</sup> SPARCOM achieves similar spatial resolution compared to a standard STORM reconstruction with as few as 361 and even 60 frames, compared with the 12 000 frames for standard STORM recovery, corresponding to a 33- or 200-times faster acquisition rate. Thus, SPARCOM improves temporal resolution while maintaining the spatial resolution of PALM/STORM. However, these benefits also introduce some tradeoffs: SPARCOM requires prior knowledge of the PSF of the optical imaging system, which is not always available, and a careful choice of a regularization factor  $\lambda$ , which is generally done heuristically.

These disadvantages can be overcome by replacing iterative algorithms like SPARCOM with trained neural networks, where each block in the network corresponds to single iteration of the algorithm. This allows us to automatically learn parameters which would have to be specified explicitly or tuned, and relevant context that may have been ignored by the algorithm can be incorporated into the learned model. This process is known as algorithmic unrolling<sup>[156]</sup> (or alternatively, unfolding), and it enables model-based learning where we benefit from both the underlying structure and prior physical information, but at the same time learn from the data itself. Since its introduction a decade ago, a wide variety of techniques have been adapted using learned unrolling, enabling improvements in performance across a variety of settings.<sup>[157]</sup> Here, we briefly review how unrolling has been used to achieve fast, accurate super-resolution imaging in SMLM while training from even only a single image sequence and preserving interpretability. We then turn to discuss how algorithmic unrolling may be applied to data analysis problems in label-free microscopy, to achieve similar benefits.

#### 2.2. Unrolling in Single Molecule Localization Microscopy

The shortcomings of iterative algorithms like SPARCOM can be overcome by learning from data using an algorithm unrolling approach. This was recently demonstrated by Dardikman-Yoffe et al.,<sup>[54]</sup> which introduced Learned SPARCOM (LSPARCOM) - a deep network with 10 layers resulting from unrolling SPARCOM, trained on a single sequence of frames taken from one field-of-view (FOV) with a known underlying structure which was generated via simulation. LSPARCOM is derived by unrolling ISTA into a learned ISTA (LISTA) network,<sup>[156]</sup> yielding an efficient and interpretable neural network which does not require fine-tuning or prior knowledge of the regularization factor of the system's PSF.

The results shown in **Figures 2 and 3** illustrate that LSPARCOM outperforms its iterative counterpart, and the leading classical deep-learning based localization method for high emitter-density frames, Deep-STORM.<sup>[160]</sup> LSPARCOM is also

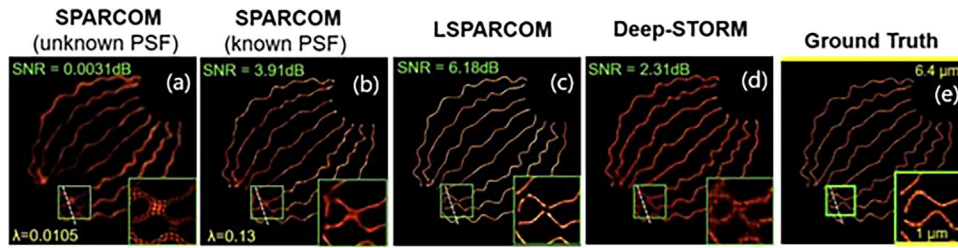


**Figure 2.** Super-resolved reconstruction of a simulated tubulins dataset,<sup>[158]</sup> composed of 361 high-density frames. a,b) SPARCOM reconstruction, executed over 100 iterations with a) unknown PSF (assuming a dirac delta PSF) and  $\lambda = 0.0105$ , b) the correct PSF and  $\lambda = 0.13$ . c) LSPARCOM reconstruction. d) Deep-STORM reconstruction. e) Ground truth position. Reproduced with permission<sup>[54]</sup> Copyright 2020, Optical Society of America.

faster to use, with approximately 5x improvement over SPARCOM in execution time. On the other hand, LSPARCOM is yet to provide us with fully accurate reconstructions. Its results tend to be somewhat fragmented, as can be seen by the missing connections between the artificial filaments in Figure 2d. Such impairments may be resolved by adjusting the unrolling scheme of LSPARCOM and expanding its training dataset to more than a single field-of-view, as suggested in.<sup>[54]</sup> Nonetheless, the improvement brought by unrolling in various imaging modalities,<sup>[161]</sup> and particularly by LSPARCOM in the context of SMLM, further suggests that unrolling may benefit other super-resolution imaging schemes, as we discuss in the next section.

### 2.3. Possible Extensions to Label-Free Microscopy

Learned unrolling has shown to achieve fast, highly accurate, interpretable results in SMLM. Thus, it is interesting to explore applications to other challenges in computational microscopy, and label-free microscopy in particular. Here we touch on two methods of label-free microscopy that may benefit from unrolling in particular: differential interference contrast (DIC) microscopy, and phase contrast microscopy. The image reconstruction task in each of these methods can be described using a linear image formation model<sup>[162, 163]</sup>:

$$g = Hf \quad (1)$$

with  $g$  being the observed image, and  $H$  representing the image formation process of the microscope (i.e., the microscope's PSF). The ideal object image that we want to retrieve - be it the optical

path length distribution in the object, or artifact-free phase contrast image - is denoted by  $f$ . This model allows for re-formulation of the restoration task as a regularized quadratic optimization problem,<sup>[162, 163]</sup> that can be iteratively solved using non-negative multiplicative updating<sup>[164]</sup>:

$$\hat{f} = \min_{\hat{f} \geq 0} \|g - H\hat{f}\|_2^2 + \gamma \|R\hat{f}\|_2^2 + \beta \|W\hat{f}\|_1 \quad (2)$$

where  $R$  is a Laplacian matrix defining the similarity between spatial pixel neighbors, and  $W$  is a diagonal matrix which defines the sparsity term. Their relative importance is controlled by the positive coefficients  $\gamma$  and  $\beta$ . The corresponding iterative algorithm for this problem is detailed in Algorithm 1 (full derivation of the algorithm is provided in<sup>[162]</sup>).

#### Algorithm 1 Iterative Multiplicative Updating

**Input:**  $Q, z, \alpha, \beta, \epsilon$

**Output:**  $\hat{f}$

- 1:  $\hat{f}^{(1)} = \mathbf{1}, w^{(1)} = \mathbf{1}, k = 1.$
- 2: **while**  $\|\hat{f}^{(k+1)} - \hat{f}^{(k)}\|_2^2 > \epsilon$  **do**
- 3:  $\hat{f}_i^{(k+1)} = \frac{-(z_i + \beta w_i^{(k)}) + \sqrt{(z_i + \beta w_i^{(k)})^2 + 4(Q + f^{(k)})_i(Q - f^{(k)})_i}}{2(Q + f^{(k)})_i} f_i^{(k)}$
- 4:  $w_i^{(k+1)} = \frac{1}{\hat{f}_i^{(k+1)} + \alpha}$
- 5:  $k \leftarrow k + 1$
- 6: **end while**
- 7:  $\hat{f} = \hat{f}^{(k)}$

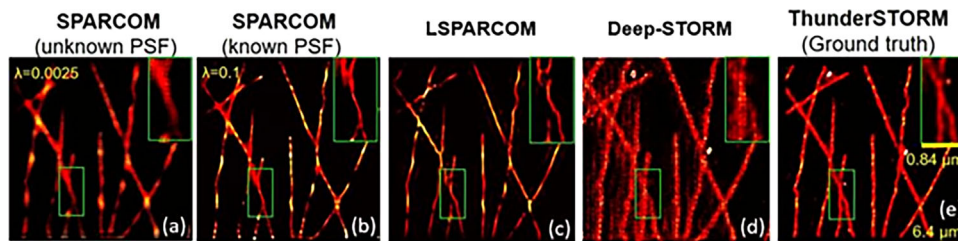


**Figure 3.** Super-resolved reconstruction of an experimental tubulins dataset,<sup>[158]</sup> composed of 15 000 low-density frames. The frames were summed in groups of 50, resulting in a high-density sequence of 300 frames, on which the super-resolved reconstructions were performed. a,b) SPARCOM reconstruction, executed over 100 iterations with a) unknown PSF (assuming a dirac delta PSF) and  $\lambda = 0.0025$ , b) the correct PSF and  $\lambda = 0.1$ . c) LSPARCOM reconstruction. d) Deep-STORM reconstruction. e) ThunderSTORM<sup>[159]</sup> reconstruction, using the original low-density sequence, which we refer to “ground truth” (there is no actual ground truth since this is an experimental dataset). Reproduced with permission<sup>[54]</sup> Copyright 2020, Optical Society of America.

where  $\alpha$  and  $\epsilon$  are positive constants,  $Q = H^T H + \gamma R^T R$ ,  $z = -H^T g$  and  $w = \text{diag}(W)$ . Note that as part of the algorithm, we express  $Q$  in terms of its positive and negative components:

$$Q_{ij}^+ = \begin{cases} Q_{ij} & \text{if } Q_{ij} > 0 \\ 0 & \text{otherwise} \end{cases} \quad Q_{ij}^- = \begin{cases} |Q_{ij}| & \text{if } Q_{ij} < 0 \\ 0 & \text{otherwise} \end{cases} \quad (3)$$

We can see that this method requires careful choice of several hyper-parameters ( $\alpha$ ,  $\beta$ ,  $\gamma$ ,  $\epsilon$ ), which can be highly time-consuming. In addition, estimation of the microscope's PSF ( $H$ ) and the Laplacian matrix ( $R$ ) are also required. This is where algorithm unrolling can come into play - by unfolding the iterative updates in Algorithm 1, a deep network can be formed. Instead of iterative computation with a stopping criteria, we will have a neural network with a set number of layers,  $L$ . Each layer will consist of trainable parameters  $\{Q^{(l)}, z^{(l)}, \beta^{(l)}, \alpha^{(l)}\}_{l=1, \dots, L}$  and perform the same update rules as in Algorithm 1 (lines 3,4) - only with learned scalars and matrices instead of predefined ones. The specifics of the network's architecture and training (exact number of layers, tied/untied weights across different layers and loss function) need to be chosen to complete the solution. Nonetheless, given the improvement brought by algorithm unrolling in the case of super-resolution microscopy, we believe that such an extension will result in an efficient and interpretable network that may outperform its iterative counterparts for image reconstruction in label-free microscopy.

## 2.4. Conclusion

Algorithm Unrolling is a powerful model-based approach to develop deep neural networks, based on iterative algorithms that are used widely in signal and image processing. We have described how unrolling allowed to combine SPARCOM, a recent high-performing classical method for SMLM image restoration, with model-based deep learning, resulting in LSPARCOM, a compact and interpretable neural network that outperforms its iterative counterpart and other learning-based methods. Given the success of applying algorithm unrolling in super-resolution, we propose to extend its application to label-free imaging schemes that can also benefit from it, such as DIC and phase contrast microscopy, and provided a general outline for such an application.

## 3. Deep Learning-Enabled Super-Resolution Microscopy

(Luzhe Huang, Aydogan Ozcan\*)

### 3.1. Introduction

Super-resolution (SR) has long been a hot topic in image processing field focusing on the reconstruction of a high resolution (HR) image from one or more low resolution (LR) image(s). Super-resolution imaging techniques have been widely used in various fields, including e.g., photography,<sup>[165]</sup> medical imaging<sup>[166]</sup> and microscopy.<sup>[167]</sup> For example, optical microscopy modalities, including bright-field and fluorescence microscopes,

are in general diffraction limited, which prevents standard microscopy systems to resolve objects separated by a distance that is closer than approximately half a wavelength, in other words,  $\approx 200\text{--}300$  nm for visible light. In order to overcome the diffraction limit, the last two decades have seen various advances in SR fluorescence microscopy techniques, e.g., stimulated emission depletion (STED)<sup>[14]</sup> microscopy, stochastic optical reconstruction microscopy (STORM),<sup>[22]</sup> photo-activated localization microscopy (PALM),<sup>[20]</sup> and structured illumination microscopy (SIM),<sup>[26]</sup> among others. These methods achieve SR following two basic principles: (1) by using illumination patterns that modulate the emission of fluorescent molecules such that closely-spaced molecules can be differentiated spatially, or (2) by modulating the temporal behavior of fluorescent molecules to resolve different molecules as a function of time. Through these advances, SR fluorescence microscopy has revolutionized our understanding of biology, including e.g., cellular and molecular structures, stoichiometric characterization of molecular complexes, and temporal dynamics within cells.<sup>[167]</sup>

In addition to these, deep learning-based computational methods have also enabled an unprecedented success in advancing microscopic imaging, with various new image reconstruction and enhancement tools. As illustrated in **Figure 4a**, one of the most widely explored applications of deep learning in optical microscopy has been image super-resolution. The first public report on deep learning-enabled image super-resolution in optical microscopy was introduced in May 2017,<sup>[168, 55]</sup> which also demonstrated an extended depth-of-field. Since then deep learning super-resolution (DL-SR) microscopy has been applied to various imaging modalities, including bright-field<sup>[169, 55]</sup> and wide-field fluorescence microscopy.<sup>[170–175]</sup> In addition to SR, deep learning has also been utilized for e.g., denoising low-quality microscopic images,<sup>[169, 171, 175]</sup> virtually refocusing microscopic images, on demand, to designated 3D surfaces,<sup>[176, 177]</sup> virtual staining of label-free microscopic images,<sup>[178, 179, 57]</sup> virtual re-staining of already-labeled microscopic images,<sup>[180]</sup> or prediction of microscopic fluorescent labels in label-free images.<sup>[181, 182]</sup>

In this section, we will focus on DL-SR microscopy and will first discuss the forward imaging model of optical microscopy in order to provide an introduction to some of the commonly employed deep neural network (DNN) architectures, also covering their applications in DL-SR microscopy. Finally, we will conclude with a discussion of some of the limitations of these emerging techniques, also exploring potential future directions of research.

### 3.2. Building Blocks of Deep Learning-Enabled SR Microscopy

Assuming  $f$  denotes the object function, the forward optical imaging process can be modeled by the following discrete model<sup>[56]</sup>

$$g = \mathcal{P}(Hf) + \epsilon \quad (4)$$

where  $g$  is the vectorized optical intensity collected on the image sensor plane of the microscope.  $\mathcal{P}$  represents a Poisson random process, modelling the shot noise and  $\epsilon$  stands for other noise terms in the system, including thermal noise and readout noise,

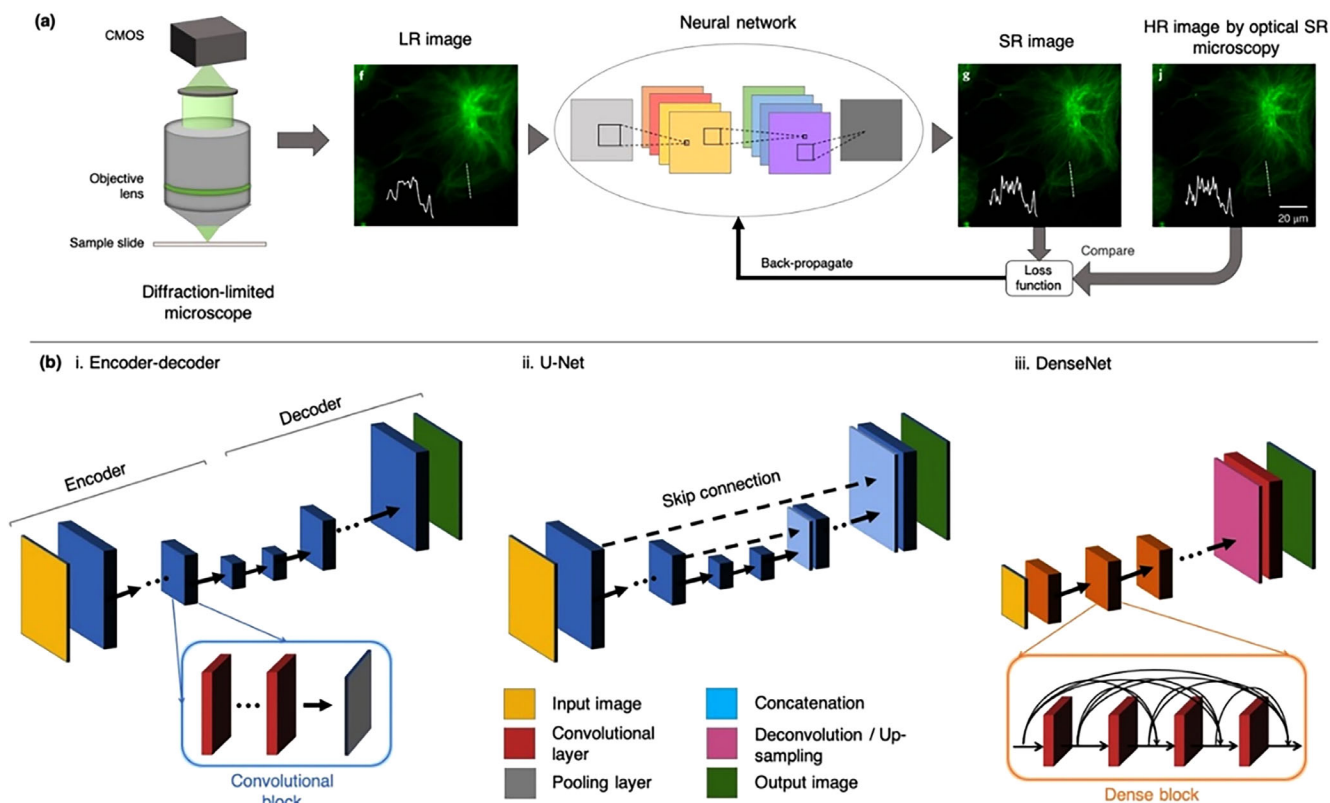


**Figure 4.** DL-SR microscopy and commonly employed DNN architectures. a) DL-SR microscopy digitally transforms a LR image obtained by a diffraction-limited microscope to match the corresponding HR image of the same specimen that is acquired by a SR microscopy modality.<sup>[172]</sup> b) Common DNN architectures frequently used for DL-SR microscopy, including encoder-decoder, U-Net and DenseNet.

which can be in general modeled as additive white Gaussian noise. For fluorescence microscopic imaging, as an example, the transfer function  $H$  can be generally modeled as a circulant matrix of the point spread function (PSF), which is determined by e.g., the numerical aperture of the objective lens of the microscope, the wavelength of light and potential aberrations in the imaging system. Super-resolution techniques focus on solving an inverse problem to retrieve the HR image  $f$  from LR measurement(s) set by  $g$ . However, due to the low-pass characteristics of the transfer function and the existence of measurement noise and aberrations, this problem is underdetermined and ill-posed.

Some of the earlier generations of optical super-resolution microscopy methods rely on special illumination patterns or controlling the temporal behavior of fluorophores in order to separate emitters in space or time, such that  $f$  becomes sparse and the inverse problem can be solved with adequate regularization and prior knowledge of  $H$ . However, limited by the space-bandwidth-product (SBP) of the microscopy system, multiple image acquisition steps are generally required for these SR microscopy methods, which prolong the imaging time and considerably increase total sample irradiation, which might introduce photo-bleaching and/or photo-toxicity.

Since the success of LeNet-5,<sup>[183]</sup> a 7-level convolutional neural network (CNN), in handwritten digit recognition in 1998, CNNs have gained massive popularity in various computer vision tasks

and have over time surpassed human experts in certain tasks. Convolutional layers share the same convolution kernels and biases such that the number of trainable parameters is significantly reduced compared to fully-connected layers. Another advantage of CNNs is that they permit variable-size input images, which is essential for processing sample images of different sizes. Two major types of CNN-based network architectures used in microscopic image super-resolution are U-Net<sup>[184]</sup> and DenseNet<sup>[185]</sup> (see Figure 4b). U-Net introduces skip-connections between the encoder-decoder layers to facilitate mapping of low-level and structural image features.<sup>[184]</sup> Although it was originally aimed at biomedical image segmentation, U-Net and its variants have been frequently used in various image transformation and reconstruction tasks in optical microscopic imaging, including super-resolution microscopy. As an example, Wang *et al.* employed a U-Net based architecture to realize cross-modality SR image transformations using diffraction-limited confocal images as input to match, at its output, the high-resolution images obtained by STED microscopy<sup>[172]</sup>; a similar success was also demonstrated by establishing a SR image transformation between diffraction-limited TIRF (total internal reflection fluorescence microscopy) and SIM, enabling the reconstruction of SIM equivalent images of live cells and embryos without the need for structured illumination, potentially reducing photo-toxicity and photo-bleaching on the samples.<sup>[172]</sup> Similar deep neural network architectures were also demonstrated to improve image resolution in wide-



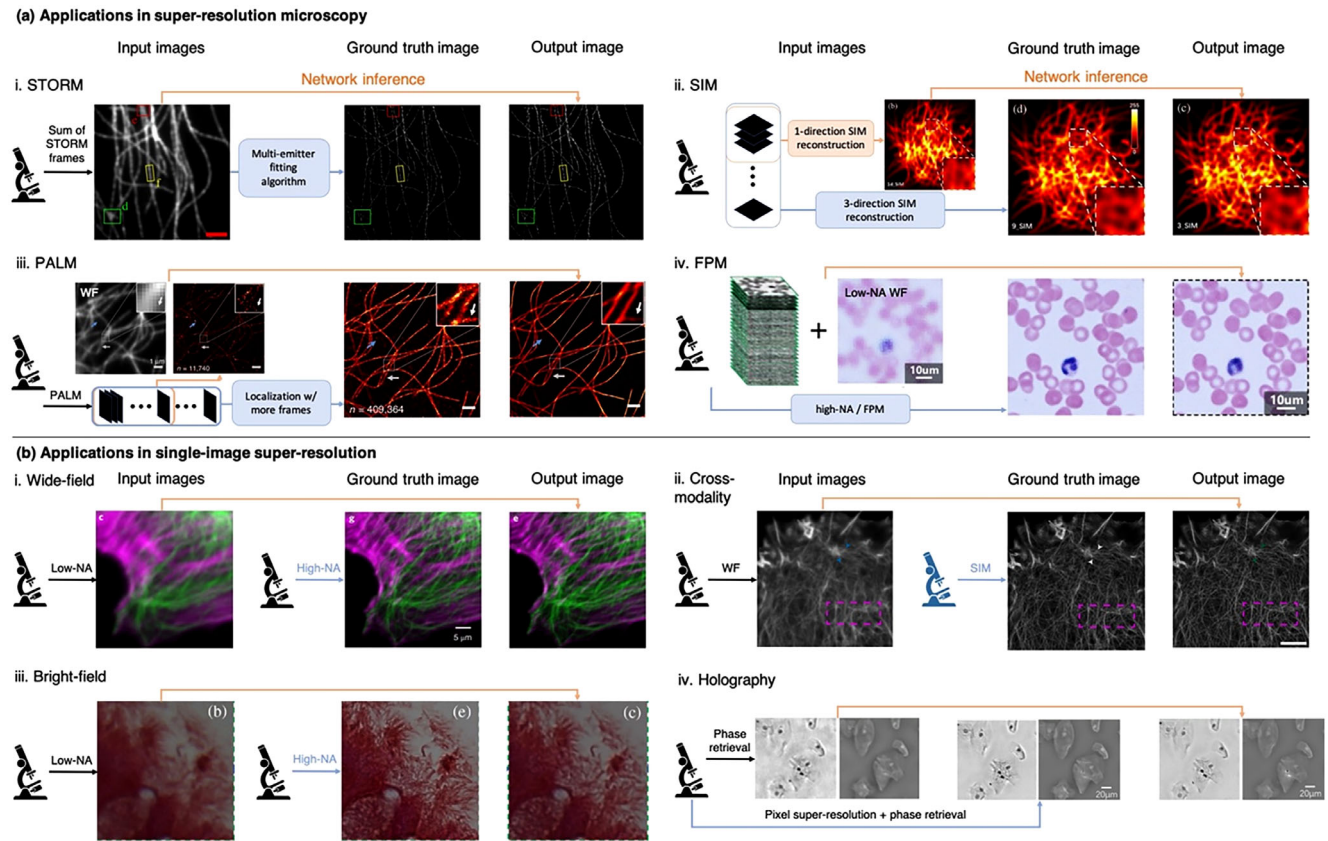


**Figure 5.** Applications of DL-SR optical microscopy. a) STORM,<sup>[160]</sup> SIM,<sup>[191]</sup> PALM,<sup>[187]</sup> and Fourier ptychographic microscopy (FPM).<sup>[194]</sup> b) Single-image super-resolution in wide-field fluorescence,<sup>[172, 174]</sup> bright-field,<sup>[55]</sup> and digital holographic microscopy.<sup>[195]</sup> Reproduced with permission.<sup>[55, 160]</sup> Copyright 2017 and 2018, The Optical Society.

field microscopy,<sup>[171, 172]</sup> STORM,<sup>[160]</sup> light-sheet microscopy<sup>[186]</sup> and PALM.<sup>[187]</sup>

Following the observation<sup>[188]</sup> that shorter connections between layers substantially improve the training of deeper CNNs, DenseNet<sup>[185]</sup> was constructed to connect every convolutional layer in each block with its preceding feature maps to alleviate diminishing gradients inside the network and strengthen the propagation and reuse of features within the deep network. The success of DenseNet in super-resolution optical microscopy has been demonstrated through transforming LR images obtained by a low numerical aperture (NA) objective lens, to match HR counterparts captured with a high-NA lens<sup>[173]</sup>; similarly, cross-modality SR imaging was also demonstrated using DenseNet, transforming diffraction-limited microscopy images to match HR images obtained by e.g., STED, SIM.<sup>[174, 175]</sup>

These earlier studies have mainly employed DL to solve the inverse imaging problem in two ways: (1) to enhance existing optical super-resolution microscopy modalities, and (2) to perform single image super-resolution (SISR) using a diffraction-limited microscope. As summarized in **Figure 5a**, DL has been successfully applied to advance various optical super-resolution microscopy modalities, including e.g., STORM,<sup>[160, 189, 190]</sup> PALM,<sup>[187]</sup> SIM,<sup>[191]</sup> FPM,<sup>[192–194]</sup> helping to reduce the total image acquisition time, accelerating the SR imaging speed as well as reducing photobleaching and

phototoxicity during the imaging process. For SISR, on the other hand, DNNs have been successfully demonstrated to transform a given LR image captured by a low-NA objective lens to match the ground truth labels generated by a high-NA objective lens,<sup>[172, 55]</sup> or to perform cross-modality image transformations by super-resolving a diffraction-limited microscopic image<sup>[172, 174]</sup> as shown in **Figure 5b**. Deep learning-enabled SISR and related techniques have been widely successful to improve the resolution of e.g., wide-field fluorescence microscopy,<sup>[172, 174]</sup> bright-field microscopy,<sup>[169, 55]</sup> digital holographic microscopy,<sup>[195]</sup> among others.

### 3.3. Conclusions and Future Prospects

Fueled by the rapid advances in DL, the massive availability of high-end computational hardware and GPUs, as well as the precision, repeatability, and high-speed of microscopic imaging systems have opened up a new set of exciting opportunities that are data-driven in solving inverse problems in optical microscopy through learning. Nevertheless, for wide-scale adoption of DL-SR microscopy techniques in e.g., biomedical and healthcare-related tasks, model generalizability, interpretability, and reliability are still open research questions for DNN models due to their “black-box” behavior stemming from the complexity of such



deep neural networks with millions of parameters. Modern neural networks have been shown to generalize well as long as the testing data distribution is close to that of the training data. Failure modes of DNNs when a distribution shift occurs in the testing phase need comprehensive investigation, demanding the development of new statistical tools that will routinely warn the users, as a watchdog, when such changes/drifts start to emerge. Model interpretability and reliability are especially critical for clinical, biomedical applications, where imprecise and unexplainable predictions can potentially lead to severe negative consequences. Further interpretation and better understanding of the underlying image features and the network models' statistical inference process may not only improve the reliability of DNN models, but also provide new insights regarding the optical forward model and the physics of the microscopic imaging process that are hard to model with our current understanding of light-matter interaction. An important example of this includes the recently demonstrated cross-modality image transformations from holography to brightfield microscopy,<sup>[196]</sup> reconstructing object features that are holographically imaged using a single wavelength, spatially-coherent illumination into brightfield equivalent images, with the color and spatial contrast of a brightfield microscope that uses broadband and spatially-incoherent light.

In addition to the choice of the network architecture, the training dataset quality and the image registration processes are critical factors influencing the network performance. Careful registration and matching between the input and ground truth data are generally required to produce high-quality training image datasets, and this can be realized by e.g., digitally generating training input images from ground truth images, or through rigid/non-rigid transformation-based image registration processes. As another very important factor that determines the success of a DNN-based SR model, the training loss function often consists of structural similarity metrics between the network's output and the ground truth images, including e.g., pixel-wise difference loss terms such as mean absolute error (L1-norm), mean squared error (L2-norm), BerHu loss,<sup>[197]</sup> and structural similarity index (SSIM) loss, among others. In addition to these loss terms, Generative Adversarial Network (GAN)<sup>[198]</sup> framework also provides another type of training loss (the discriminator loss) by optimizing an evaluation network, which adaptively helps the training of the generator network to produce accurate super-resolved and enhanced images. Other types of loss functions including perceptual loss<sup>[199]</sup> that are derived from pre-trained network models are also shown to be effective in microscopic image enhancement and SR tasks.

In the future, we believe that deep learning-based methods will play an increasingly important role in advancing optical microscopy techniques, and will find various practical applications, especially in areas where automation and high-throughput image analysis are required. Ultimately, the use of deep learning in super-resolution microscopy could create fundamentally new generations of optical instruments and measurement systems, designed by joint optimization of the optical front-end hardware (e.g., through trainable diffractive processors<sup>[200, 201]</sup>) and the back-end image processing workflow, achieving high-resolution imaging with low-cost and/or high-throughput microscopy systems.

## 4. The Future of Super-Resolution Optical Microscopy at the Age of Big Data

(Nikolay I. Zheludev\*)

We are at the verge of a new era of microscopy, the era of Deeply Subwavelength Optical Microscopy (Figure 6). This technology is based on the recovery of information on the shape and size of the object from its light scattering pattern using neural network-based artificial intelligence. Adding topologically structured illumination improves resolution that reaches molecular and even atomic levels. Imaging of soft-matter biological and solid-state nanotechnology samples will be equally possible in color and in two and three dimensions without labeling samples with luminescent material and at low intensities, without using nonlinear light-matter interactions. Training of the neural networks is a "Big Data" scale problem, but at the user end the optical part of the microscopy instrument is simple and only modest computer resources are required.

The label-free imaging is an ill-posed inverse light scattering problem, which can be reduced to solving the Fredholm integral equation.<sup>[204]</sup> Not so long ago, my close colleague Prof. Ilya Kuprov gave me a call saying: "Nikolay, I now know why your artificial intelligence-based high-resolution imaging techniques work so well. I found a paper<sup>[205]</sup> mathematically proving that the Fredholm integral equation can be accurately solved by a fully connected neural network!" This was exciting and very important news. We have been enthusiastically developing Deeply Subwavelength Optical Microscopy enabled by neural network-based artificial intelligence that can see far beyond the diffraction limit.<sup>[206–208, 59]</sup>

In conventional microscopy, the image of the object is constructed by a lens. Such imaging has a "diffraction limit" on resolution, which depends on the numerical aperture of the lens, but cannot exceed half of the wavelength of light. With artificial intelligence we beat the diffraction limit several orders of magnitude over by recording the intensity pattern of coherent light scattered from the sample into the far-field. In fact, we detect only the intensity of scattered light by an image sensor. This information is not sufficient to exactly reconstruct shape of the scattering object by analytical techniques. However, we retrieve information about the unknown object using a deep learning neural network that has been trained on scattering events from a large set of a priori known objects. Importantly, the network does not operate as correlator with a library of a priori known objects, but as a true solver of the inverse scattering problem. For instance, with a laser operating at 633nm, we retrieve the width of a randomly positioned sub-wavelength slits in opaque screen with accuracy of  $\approx \lambda/130$  for a single-shot measurement or  $\approx \lambda/260$  (i.e. 2.4nm), when combining measurements of diffraction patterns at different distances from the object. Such accuracy challenges the accuracy of scanning electron microscopy and ion beam lithography that were used to manufacture and measure the slits. In numerical experiments, we show that the technique could reach an accuracy beyond  $\lambda/1000$ , which brings it to the atomic scale.<sup>[59]</sup>

The use of artificial intelligence requires revising of what imaging and microscopy are in the age of big data. For centuries, imaging was a technique of representation of an object's shape by creating a light pattern resembling the object, in the way that a

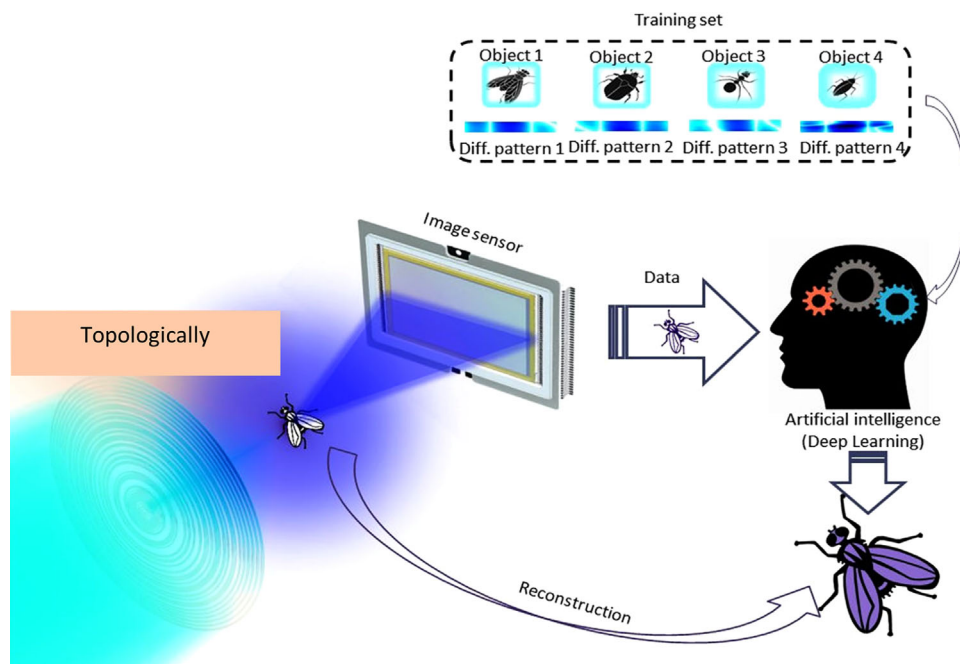


**Figure 6.** Deeply Subwavelength Topological Metrology and Microscopy with a topologically structured (e.g., superoscillatory) light field (following<sup>[202, 203]</sup>). The intensity profile of the diffraction pattern resulting from scattering of the topologically structured light field on the imaged object is mapped by the image intensity sensor. The artificial intelligence deconvolution program, trained on a large number of scattering events with a priori known object (numbered 1,2,3,4 ...) reconstructs/measures the object from the collected data with high resolution.

microscope creates it on the retina of the observer's eye, or projector at the cinema screen. Data processing techniques implemented on computers can enhance or completely replace the lens as the handler of optical information. Moreover, image analysis and mining data from the image do not necessarily involve projecting them on the screen as they can remain in the computer memory. Indeed, computer-enabled imaging is commonly used far- and near-field optical microscopies and the electron-beam imaging techniques. The artificial intelligence generated images also fall into this category. Broadly, imaging is the representation of an object's form and involves the generation, collection, duplication, analysis, modification, and visualization of images, including imaging things that the human eye cannot detect. The artificial intelligence-enabled imaging technique provide representations of the object's including its form, shape and dimensions and are true imaging techniques. As we have shown, they can be extremely useful in microscopy "to view objects ... that cannot be seen with the naked eye (objects that are not within the resolution range of the normal eye)."<sup>[209]</sup>

Reconstruction of the object shape from its far-field diffraction pattern shows that a lens is not the only tool for constructing the image. Moreover, the image may be constructed much more precisely than the lens can do. What does it makes the improved resolution possible? From the prospective of the information theory, multiple scattering patterns recorded during the training process provide more information for the image retrieval process than what is available in a lens-generated single image. Moreover, for some objects, the object's sparsity and the existence of prior knowledge about it significantly helps the retrieval process.

How can we best exploit the ability of artificial intelligence to handle complex stuttering patterns and to achieve higher resolution of optical imaging instruments?

We recently observed that the scattering of topologically structured light could be very sensitive to the placement and displacement in the field of an absorbing nanoparticle with a size of only  $\lambda/1000$  (about a covalent diameter of the caesium atom).<sup>[207]</sup> Complex monochromatic light fields are known to have deeply subwavelength structures, such as phase singularities, zones of energy backflow and rapid phase variation and energy hotspots.<sup>[210]</sup> This has already been used in metrology.<sup>[211]</sup> With such topologically structured illumination scattered field varies substantially when deeply subwavelength features of the light field overlaps with nanoscale features of the scatter. The reaction of topologically structured light field to the present of deeply subwavelength object could be two to three orders stronger compared to the plane wave illumination.

These works have resulted in developing the Deeply Subwavelength Topological Microscopy.<sup>[202, 207]</sup> It reveals the fine structure of an object through its far-field scattering pattern when it is illuminated with light containing deeply subwavelength singularity features. The object is reconstructed from such a pattern by a neural network that is trained on a large number of scattering events on known objects exposed to a number of different illumination conditions. From the prospective of Fourier optics, topologically structured superoscillatory illumination gives access to large local wavevectors and ensures that the scattering pattern of structured light is more sensitive to the small features of the imaged object than that of the unstructured light. In recent experiments, we show that with topologically structured illumination

an accuracy beyond  $\lambda/10\,000$  (a few tens of femto-meter), can be reached which brings it to the sub-atomic scale.<sup>[203]</sup>

Although so far, the deeply subwavelength topological microscopy has been demonstrated for 1D imaging, it can be readily extended to 2D and 3D objects, as well as objects of random shape by building the image from point-to-point scanning. It will be most efficient in microscopy of a priori known shapes, such as those found in routine tasks of biomedical research and machine vision. Furthermore, the technique does not require labeling of the sample with luminescent materials, nor intense laser illumination, and is resilient to noise.

As it has been realized,<sup>[206]</sup> in practical terms, the main challenge in the implementation of deep learning-enabled optical microscopy is creating a reliable and trustworthy training set for neural network training. Such a dataset can be either virtual or physical. The virtual training dataset of imaged objects and their diffraction scattering patterns can be generated by numerical modelling (Maxwell solving) on a random set of a priori defined large set of random or application-specific virtual training objects. Here, the main challenge is to ensure that the computer model is congruent with the physical realization of the microscope, which may be problematic. Alternatively, a physical dataset can be created by fabricating a number of real scattering elements followed by recording of their scattering patterns in the imaging instrument. Generating a physical set is labor-intensive, but such a set is naturally congruent with the imaging microscope. The choice of the training dataset (physical or virtual) shall be made with the desired resolution and complexity of the microscope optical tract, and, in general, higher resolution would require large training datasets. Neural networks can also be trained on hybrid data sets that are partially physical and partially virtual. An important direction for future research is the analysis of resolution limits of microscopies using prior knowledge of the sample and deep learning techniques that give access to the large amount of information accrued during the neural network training process with hybrid sets.

In conclusion, we are at the verge of a new era of microscopy, the era of Deeply Subwavelength Optical Microscopy. The diffraction limit and imaging lens will be the things of the past. The light scattered by the object will be the main source of information about it. Illumination with topologically structured light will make these diffraction patterns highly sensitive to the nanoscopic features of the sample. The microscopy will not require labeling of the samples and engaging the nonlinear regimes of light-matter interaction. The molecular and even atomic resolution will be routinely achievable. Imaging of soft-matter biological and solid-state nanotechnology samples will be equally possible in one, two, and three dimensions. Imaging at multiple laser frequencies will give access to microscopy in color and the wavelength range can be readily extended to any part of electromagnetic spectrum where coherent sources of light and detectors exist. Microscopy will be based on reconstructing shapes of the scattering object with artificial intelligence and will be limited in resolution only by size and quality of the training sets.

High throughput diffraction simulations and Maxwell solving will be used for creating the training data sets. Training sets with increased sophistication will be developed. At some level of finesse we will need to go beyond the effective medium approximation when material properties are described by their perme-

ability and permittivity, and ab initio modelling of light scattering on molecular structures will have to be developed to build the training sets.

It is likely that training of neural network will be application-specific for tasks such as, for example, protein folding or semiconductor chip fault diagnostics. The size of training sets can easily reach petabyte volumes and may require super-computers to generate. However, the end-user will not need to deal with Big Data, they will only need to be informed with the final results of training, which can be distributed as a file to set the neural network on the imaging instrument computer, a simple desktop PC. While the increase of resolution will require increased computer resources, the optical imaging act will remain simple: a single or multiple shot registration of the diffraction patterns.

## 5. Label-Free Plasmonic/Metamaterial Structured Illumination Microscopy

(Junxiang Zhao, Zachary Burns, Zhaowei Liu\*)

Structured illumination microscopy (SIM) doubles the resolution of a wide field fluorescent microscope and has seen many applications in biomedical studies. However, SIM provides no additional resolution enhancement over oblique illumination for label-free imaging due to the coherent nature of the scattering process. Meta-substrates using plasmonic structures and metamaterials provide a possibility to achieve illumination wave vectors beyond the limit of traditional optics, leading to a unique path for label-free super-resolution imaging. Here, we review the current super-resolution imaging techniques that combine SIM with meta-substrate assisted illuminations. We outline the challenges in achieving label-free super-resolution imaging and offer a set of directions for future work.

Optical microscopy has been an irreplaceable tool in biomedical research but has a limited resolution due to the wave nature of the light. According to the Abbe diffraction limit of  $\lambda/2NA$ , where  $\lambda$  is the light wavelength and NA is the numerical aperture of the optics, the maximum spatial resolution of a conventional lens-based microscope at visible frequencies is around 200nm.

Numerous super-resolution microscopy (SRM) techniques<sup>[14, 20, 22]</sup> has been developed for fluorescent microscopies to break the diffraction limit. Among these SRM techniques, structured illumination microscopy (SIM)<sup>[26]</sup> utilizes a series of periodic illumination patterns superimposed onto an object to improve the resolution by 2-fold. Compared to other SRM techniques, SIM's advantages are its high imaging speed, wide field-of-view (FOV) and low photodamage, representing a nice combination for many biomedical applications.<sup>[28]</sup> However, since the scattering process is coherent, label-free imaging using scattered light gains little from structured illumination.<sup>[93]</sup> The bandwidths for detection and excitation are both limited within the coherent transfer function (CTF) using conventional optics. Therefore, for coherent label-free imaging, the structured illumination scheme does not yield any more information than imaging with oblique illuminations, which has a resolution well defined by the Abbe diffraction limit.

SIM achieves super-resolution by frequency mixing the high spatial frequency components of the object into the detectable bandwidth of a microscope. The highest achievable resolution

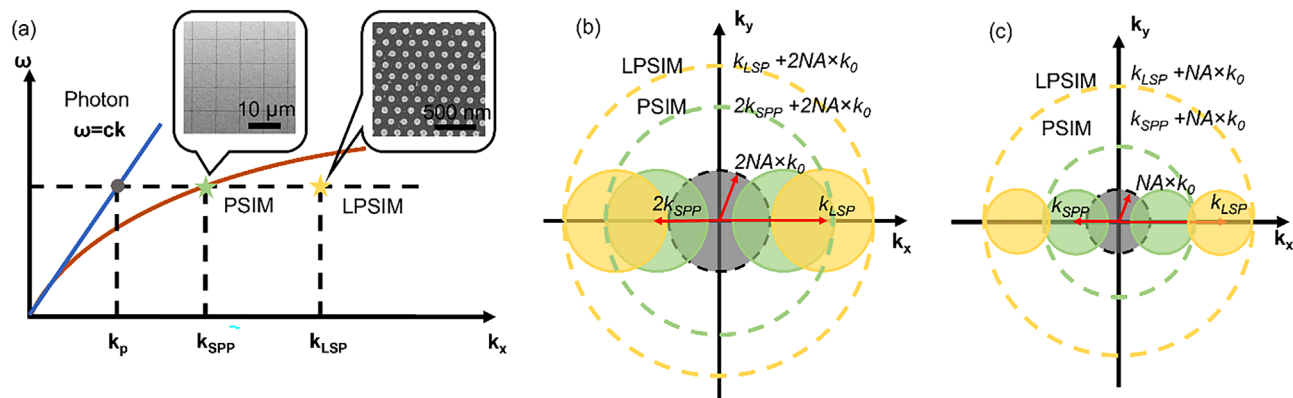


**Figure 7.** Concept of resolution enhancement with PSIM and LPSIM. a) The dispersion relation comparison of a propagating photon in dielectric media, a SPP at dielectric/metal interfaces, and the LSP field from a nanoantenna array. The wavevectors at the illumination frequency are denoted  $k_p$ ,  $k_{SPP}$ , and  $k_{LSP}$  respectively. Inset: SEM images of typical PSIM and LPSIM substrates. A PSIM substrate is constructed from thin Ag film with an array of patterned slits. A LPSIM substrate consists of a hexagonal silver disc array. Reproduced with permission.<sup>[104]</sup> Copyright 2014, American Chemical Society. b, c) Resolution improvement of PSIM and LPSIM for incoherent and coherent imaging system, respectively. The green circles and yellow circles correspond to the spatial frequency shift due to SPP and LSP illuminations. The dashed circles represent the total detectable Fourier components of the objects with PSIM and LPSIM.

is determined by the sum of illumination and detection spatial frequencies:  $f = f_{det} + f_{illum}$ . For a coherent imaging system with both illumination and detection cutoff frequency at  $NA/\lambda$ , the maximum attainable resolution is  $\lambda/2NA$ . Techniques like Fourier ptychography<sup>[96]</sup> use high angle oblique illumination combined with low NA objectives to achieve multiple fold resolution enhancement compared to the low NA resolution limit. But since the NA of oblique illuminations in free space cannot surpass 1, ultimately such methods cannot achieve higher resolution than the Abbe diffraction limit of high NA optics.

Since optical microscopes typically require far-field detection, the detection bandwidth cannot be further improved other than using objectives with the highest available NA. Therefore, creating higher spatial frequency illumination patterns is the most viable and crucial approach to achieving label-free super-resolution SIM. Plasmonic structures and hyperbolic metamaterials are known for supporting larger wavevector waves compared to dielectric medium and have seen many applications in sub-wavelength imaging and sensing.<sup>[212–214]</sup> By introducing a meta-substrate designed with a plasmonic nanostructure or metamaterial to generate illuminations, metamaterial assisted illumination nanoscopy (MAIN) can achieve much higher resolution than standard SIM methods.<sup>[215]</sup>

One way to create illuminations beyond the diffraction-limit is to use a meta-substrate containing plasmonic nanostructures. Plasmonic structured illumination microscopy (PSIM)<sup>[104]</sup> and localized plasmonic structured illumination microscopy (LPSIM)<sup>[105, 106]</sup> use interference patterns from counter propagating surface plasmon polaritons (SPP) and localized surface plasmon (LSP) waves from metallic nano-disc arrays to generate illuminations beyond the traditional diffraction-limit respectively. **Figure 7a** illustrates the lateral wavevector comparison for propagating light, PSIM illumination and LPSIM illumination. Contrary to traditional SIM, the maximum achievable bandwidths for PSIM and LPSIM with fluorescent imaging are described by  $k_{PSIM} = 2k_{SPP} + 2NA \times k_0$  and  $k_{LPSIM} = k_{LSP} + 2NA \times k_0$ , where  $k_{SPP}$  and  $k_{LSP}$  are the wavevectors of PSIM and LPSIM illumina-

tion patterns, and  $k_0$  is the free space wavevector of the illumination wavelength (Figure 7b). Compared to the diffraction-limit, PSIM has experimentally demonstrated  $\approx 2.6$ -fold resolution improvement<sup>[104]</sup> and LPSIM has demonstrated 3-fold resolution improvement for biological samples.<sup>[105, 106]</sup> For a coherent label-free imaging system with CTF cutoff frequency at  $NA/\lambda$ , the illuminations from PSIM and LPSIM are purely dependent on the nanostructures and thus can achieve higher resolution beyond the diffraction limit described by:  $k_{PSIM/LPSIM} = k_{SPP/LSP} + NA \times k_0$  (Figure 7c). At this moment, however, the experimental demonstration of label-free PSIM and LPSIM has yet to be done.

Hyperbolic metamaterials (HMM) have recently been used as meta-substrates for ultra-high resolution optical imaging.<sup>[108, 216, 217]</sup> **Figure 8a-b** show that an ideal HMM can support arbitrarily large lateral wavevectors as the isofrequency surface of an HMM is a two-sheet hyperboloid for a Type I HMM ( $\epsilon_{\perp} > 0, \epsilon_{\parallel} < 0$ ) or a one-sheet hyperboloid for a Type II HMM ( $\epsilon_{\perp} < 0, \epsilon_{\parallel} > 0$ ). HMMs are commonly implemented by two types of structures: a lattice of metallic nanorods embedded in a dielectric medium or a stack of deep subwavelength alternating metallic and dielectric layers. For imaging applications, the multilayer structures are the most practical methods to implement the HMMs. A practical HMM consists of multiples layers of metal and dielectric films can support extremely large lateral wavevectors<sup>[109]</sup> in the near field, thus they can create high resolution illumination patterns (Figure 8c). One implementation of HMM assisted illumination microscopy is hyper-structured illumination,<sup>[108, 217]</sup> which utilizes the highly dispersive nature of an HMM to project a series of deep-subwavelength illumination patterns which are tuned by the incident wavelength. A 6-fold resolution improvement over the diffraction limit has been reported for hyper-structured illumination with label-free imaging, resolving features down to  $\approx 80$  nm.<sup>[108]</sup> Another implementation of MAIN, named speckle-MAIN,<sup>[109]</sup> creates deep sub-wavelength speckle illumination patterns by taking advantage of the inherent material roughness within the multilayer HMM (Figure 8d) and achieves 40 nm resolution with a fluorescent microscope.



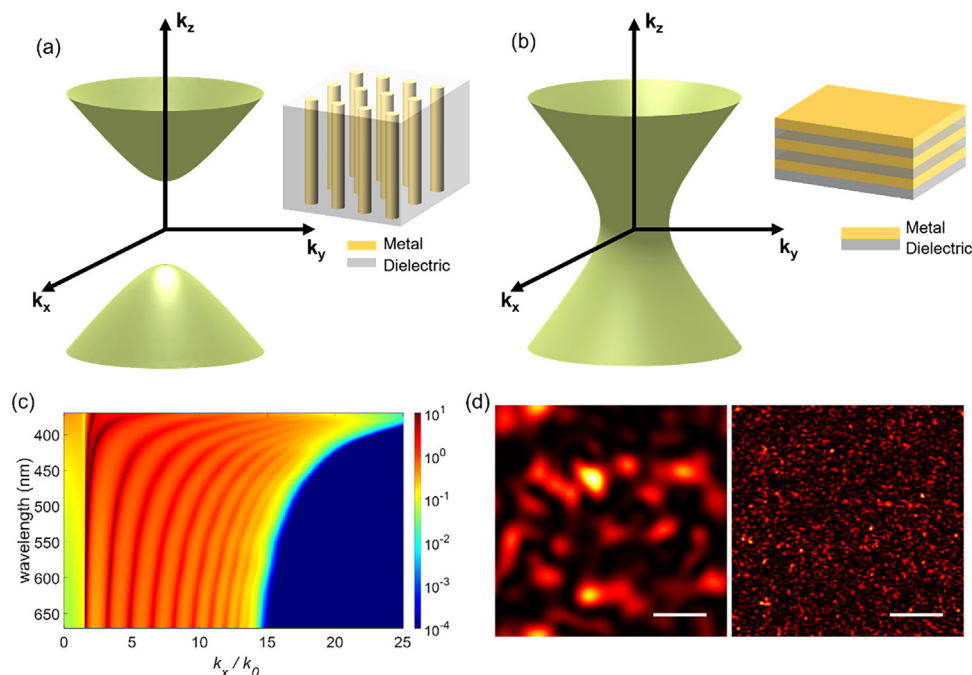


**Figure 8.** HMM for super-resolution imaging. a) The isofrequency surface for a Type I HMM ( $\epsilon_{\perp} > 0$ ,  $\epsilon_{\parallel} < 0$ ). Type I HMMs are commonly achieved with nanorod arrays. b) The isofrequency surface for a Type II HMM ( $\epsilon_{\perp} < 0$ ,  $\epsilon_{\parallel} > 0$ ). Type II HMMs are commonly fabricated with metal-dielectric multilayers. c) Transmission of a multilayer HMM with 12 pairs of 5 nm Ag and 5 nm SiO<sub>2</sub>. d) Calculated exemplary speckle patterns for a diffraction limited system (left) and HMM assisted speckles (right). Scale bar, 1  $\mu$ m.

Recently, novel organic hyperbolic metamaterials (OHM) fabricated by self-assembled regioregular poly(3-hexylthiophene-2,5-diyl) have been demonstrated to support remarkably large lateral wavevector in the visible frequencies.<sup>[218, 219]</sup> The OHM assisted MAIN produces ultra-high resolution of 30 nm while exhibiting superior biocompatibility and photostability due to its exceptionally large Purcell factor at the film surface.<sup>[219, 220]</sup>

One of the main challenges of label-free super-resolution imaging is the low photon budget due to the very weak scattering of sub-wavelength objects. The resulting low signal-to-noise ratio (SNR) causes significant loss of high-resolution information as higher spatial frequency components of an object typically have very low spatial spectrum density. Recently, plasmonic scattering imaging<sup>[221]</sup> demonstrated imaging of single proteins by using a thin gold film as the sample substrate. With a meta-substrate, significant enhancement of scattering from small objects greatly improves the SNR and allows for far-field detection. This is especially crucial for imaging tiny objects with a target resolution of sub-50 nm, as the scattering cross-section is too small to create a meaningful measurement with traditional imaging methods.

Image reconstruction has also been a major roadblock for realizing label-free MAIN. Fluorescent versions of MAIN that rely on intensity fluctuation based reconstruction methods<sup>[222, 223, 24]</sup> have shown promising imaging results. However, since scattering is a coherent process, the label-free imaging system is linear with respect to the electric field rather than the intensity. As we detect only the intensity with a camera, an ill-posed non-linear inverse problem must be solved to retrieve the object information. One method to overcome this problem is to use a meta-substrate made of turbid medium and record the transmis-

sion matrix of all near-field input modes at the cost of requiring near-field scanning of the entire FOV prior to imaging. The far-field scattered light of the object will be a linear combination of the basis transmission matrix such that a super-resolution image can be retrieved by time reversal reconstruction.<sup>[224]</sup>

Increasingly deep neural networks are being used for super resolution microscopy reconstruction<sup>[187, 225]</sup> to boost performance over traditional methods, for example by reducing the number of sub-frames and handling cases of low signal-to-noise ratio. Often there is knowledge of the physical system that could be incorporated into the network to reduce the training burden and improve results.<sup>[56]</sup> Recently there has been the development of “physics-based” or “untrained” neural networks that incorporate a physical forward model into the loss function for training. These methods have been applied to cases such as phase imaging and lensless imaging.<sup>[226–228]</sup> For label-free MAIN, where the illumination field and forward process is known, there is the potential to incorporate this knowledge into a physics-based network trained on a collection of data. Such a model could combine the benefits of a traditional physics-based model with those of statistical learning to create better reconstructions and alleviate some of the challenges of the ill-posed inverse problem.

Current label-free MAIN results are, at this point, mostly preliminary. Hyper-structured illumination has achieved label-free super-resolution for a 1D object, but its 2D imaging capability has not been demonstrated. PSIM, LPSIM and speckle-MAIN have only been experimentally demonstrated with fluorescent imaging and a robust image reconstruction scheme for coherent imaging has yet to be developed. Nevertheless, MAIN addresses the major difficulties in achieving super-resolution label-free



imaging with its exceptionally larger illumination bandwidth and SNR improvement over traditional optics.

## 6. Fundamental Limits to the Resolution of Label-free Far-field Microscopy

(Evgenii Narimanov\*)

### 6.1. Introduction

High resolution optical imaging is essential for the investigation of fundamental microscopic processes both in nature and in artificial systems – from the charge carrier dynamics in electronic nano-circuits<sup>[229]</sup> to the biological activity in cellular structures.<sup>[230]</sup> However, as optical diffraction prevents focusing the light into a spot with dimensions much smaller than its wavelength,<sup>[231]</sup> the resulting Abbe's diffraction limit<sup>[232–234]</sup> does not allow the conventional optical microscopy to directly image subwavelength structures such as cell membranes, individual viruses, or large protein molecules. As a result, there is now an increasing interest in “super-resolution” optical methods that allow to overcome this diffraction barrier – with a particular demand for a label-free approach that is inherently non-toxic and operates on the sample that is in the far-field from all elements of the imaging system.

Recent developments in label-free optical super-resolution imaging<sup>[132, 235–237, 52, 53]</sup> clearly demonstrate that Abbe's bound of half-wavelength (and its quarter-wavelength counterpart for structured illumination) is not a fundamental limit for optical imaging. Nevertheless, there is in fact a fundamental limit on the resolution of far-field optical imaging, but it is much less stringent than Abbe's criterion. While in a perfectly noise-free environment arbitrary resolution is possible,<sup>[238]</sup> the presence of any finite amount of noise in the system leads to a limit on the optical resolution, that has its origin in Shannon's theory of information transmission in linear systems.<sup>[239]</sup>

### 6.2. The Definition of the Resolution Limit

We define the resolution limit  $\Delta$  as the *shortest* spatial scale of the object whose geometry can still be reconstructed, *error-free*, from the far-field optical measurements in the presence of noise.<sup>[60]</sup> The essential “lower bound” nature of  $\Delta$  then allows to reduce the problem to the limiting case of an object that is composed of an arbitrary number of point scatterers of a priori unknown amplitudes located at the nodes of the grid with the period  $\Delta$ , as any additional structure in the sources (or scatterers) as well as any further variations in their positions, will only add to the information that needs to be recovered from the far-field image. Furthermore, the same argument allows to reduce the task of calculating  $\Delta$  to the case of an effectively one-dimensional target (formed by line, rather than point, sources) – since, as it was already known to M. André<sup>[240]</sup> and L. Raleigh,<sup>[241]</sup> line sources are “more easily resolvable” than point sources.

Note that, even within the original framework of “resolving” two point sources,<sup>[241]</sup> the resolution clearly depends on the difference of their amplitudes – with increasing disparity between

the two leading to progressively worse “performance”. The “ultimate” resolution limit  $\Delta$  therefore corresponds to the case of identical point sources/ scatterers, which are present only in an (unknown) fraction of the grid nodes.

For the definition of the fundamental resolution imaging, it is essential to assume *coherent* detection, as the phase information is generally available in the far field, and can always be measured even with an intensity only sensitive detector using e.g., optical heterodyne approach,<sup>[242]</sup> – so that any failure to obtain the phase information in a given experimental setup cannot be attributed to a *fundamental* limitation.

### 6.3. Information-Theoretical Framework

The fundamental limit on the resolution of optical imaging is reached when the total amount of information about the object that has been recovered in the far field, is equal to the amount of information that is necessary and sufficient to define the geometry of the object. Treating the optical point-spread function of the imaging system in the noisy environment as the input – output relation of a linear information channel, the amount of the actual information carried from the object to the far field detector, can be obtained using the standard methods of the information theory,<sup>[239]</sup> in terms of the mutual information functional, calculated between the statistical distributions of the object profile and of the far field scattering pattern, as described in detail in Ref. [60]. The resolution limit then follows from the requirement of the recovered information being sufficient to reconstruct the target:

$$\Delta = \frac{L}{T} \quad (5)$$

where  $L$  is the length of the object, and  $T$  is the information about the structure and geometry of the object that was successfully transmitted to the detector(s) at the far-field. Note that when the object is composed of  $M$  different materials (or is formed by an array of point sources with  $M$  different levels of amplitude), additional information is needed for its reconstruction, which leads to a more stringent bound on the spatial resolution,

$$\Delta_M = \frac{L \log_2 M}{T} = \Delta \cdot \log_2 M \geq \Delta \quad (6)$$

The transmitted information  $T$  can be obtained from the standard mutual information functional<sup>[239]</sup>

$$T = H - H_c \quad (7)$$

where  $H$  is the information entropy for the signal at the detector array. As the imaging system is noisy, for any output signal, there is some uncertainty of what was the originating optical field scattered (or emitted) by the object. The conditional entropy  $H_c$  of the signal at the detector array for a *fixed* optical field from the object, represents this uncertainty in Equation (7). Calculating the resulting analytical expressions<sup>[239]</sup> for  $H$  and  $H_c$  and substituting them into the mutual information functional  $T$  in Equation (7),

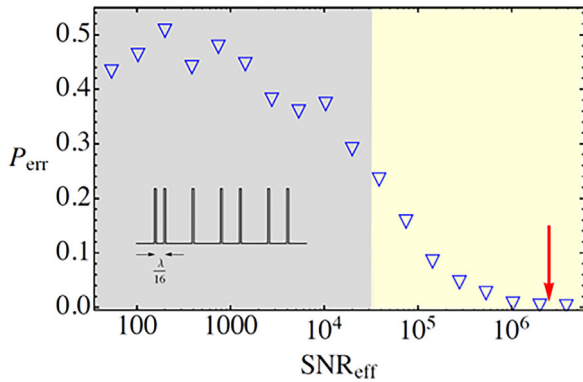


**Figure 9.** Super-resolution object reconstruction for a binary mask (with the profile shown in the inset), with the error probability of the recovered geometry  $P_{\text{err}}$  shown as a function of the effective signal-to-noise ratio,  $\text{SNR}_{\text{eff}}$ . The boundary separating the gray and light-yellow background, represents the value of the signal-to-noise ratio that according to Equation (8) is sufficient to resolve the  $\lambda/16$  spacing (see the inset). The red arrow indicates the minimum value of  $\text{SNR}_{\text{eff}}$  where the numerical reconstruction procedure implemented in<sup>[60]</sup> shows no errors.

for the resolution limit in the case of uniform illumination, we obtain<sup>[60]</sup>

$$\Delta = \frac{\lambda}{2} \frac{1}{\log_2 \sqrt{1 + 2 \text{SNR}_{\text{eff}}}} \quad (8)$$

Here  $\text{SNR}_{\text{eff}}$  is the effective signal-to-noise ratio<sup>[60]</sup> measured at the detector array, and  $\lambda$  is the wave-length. Similarly, in the case of conventional structured illumination<sup>[26]</sup> (where the illumination pattern is formed in the far-field of the light source(s) and is therefore subject to the diffraction constraints), for the resolution limit we find

$$\Delta^{\text{SE}} = \frac{\lambda}{4} \frac{1}{\log_2 \sqrt{1 + 2 \text{SNR}_{\text{eff}}}} \quad (9)$$

### 6.3.1. The Discussion

While Equation (8) allows for an unlimited resolution in a noise-free environment, even a relatively low noise dramatically alters this picture. With the weak logarithmic dependence of the resolution limit on the SNR in Equations (8), (9), to reduce the resolution limit by e.g., a factor of ten, the signal-to-noise ratio needs to be increased by six orders of magnitude.

The experimentally observed resolution can reach the value of  $\Delta$  in the case of imaging a binary mask or a pattern of identical subwavelength particles – leading to practical imaging well below the Abbe’s limit. However, this can only be achieved in the regime of extreme noise suppression, with the corresponding values of the SNR on the order of  $\approx 10^5$  and beyond.

This is illustrated in **Figure 9**, where the profile of a subwavelength binary mask (see the inset to Figure 9) is recovered from its image in the far-field. While a finite amount of noise in the far-field measurements inevitably leads to errors, with the increase of the effective signal-to-noise ratio SNR the corresponding error

probability  $P_{\text{err}}$  rapidly goes to zero. In particular, for the resolution of  $\lambda/16$  in the example of Figure 9, the numerical calculation with an ensemble of multiple ( $\approx 10^4$ ) different realizations,<sup>[60]</sup> showed no errors for SNR beyond the value indicated by the red arrow ( $\approx 10^6$ ).

However, for many practical imaging applications, especially in the field of biomedical imaging, the level of noise reduction that is needed for subwavelength resolution, is beyond the reach of current technology. For the signal-to-noise level of  $\approx 10$ – $10^2$  typical for a biological environment, we find the ultimate resolution of the order of  $\approx \lambda/10$ . As a result, any endeavor to push the observed resolution beyond this level in a conventional (direct rather than statistical, and single exposure) imaging, is akin to an attempt to develop a working example of a perpetual motion machine.

This situation is however dramatically reversed when additional information about the object is available a priori. This a priori knowledge reduces the amount of information about the object that must be obtained from its far-field image – which leads to the corresponding reduction of  $\Delta$  in the resolution limit of optical imaging. Furthermore, this effect is described by an *algebraic* rather than logarithmic function. For this reason, rather than improving the noise performance of the imaging set-up, the route to a practical implementation of far-field super-resolution lies in taking full advantage of the a priori information about the target.

Among different examples of a priori available information about the object, particularly important is the case of sparse objects, as this property is widely spread in both natural and artificial systems.<sup>[230]</sup> When the target is sparse, with the effective sparsity parameter  $\beta$  (which can be defined as the fraction of empty “slots” in the grid superimposed on the target), we find<sup>[60]</sup>

$$\Delta^{(\beta)} = \Delta \cdot |\beta \log_2 \beta + (1 - \beta) \log_2 (1 - \beta)| \quad (10)$$

For the numerical example studied in Ref. [52], with  $\beta \approx 0.03$  and  $\text{SNR} \approx 10^2$ , the resolution limit  $\Delta^{(\beta)} \approx 0.025\lambda$ . Accurate numerical reconstruction of the features on the scale of  $\approx \lambda/10$  demonstrated in Ref. [52], is therefore fully consistent with the fundamental resolution limit presented here.

Finally, we note that subwavelength resolution of statistical localization microscopy<sup>[22, 243, 244]</sup> also originates from this mechanism, as each of the multiple images that are assembled in this approach to reconstruct the topology of the target, are measured with extremely low values of the sparsity  $\beta$  (when only one or a few of the point light emitters introduced into the object, are currently active), thus according to Equation (10) leading to  $\Delta \approx \lambda\beta \ll \lambda$ .

## 6.4. Conclusions

In conclusion, we have presented the fundamental resolution limit for far-field optical imaging and demonstrated that it is generally well below the standard half-the-wavelength estimate. Our result also applies to other methods that rely on wave propagation and scattering – such as e.g., geophysical and ultrasound imaging.

## Theme II: Interferometric and Holographic Approaches

### 7. Current Trends In Quantitative Phase Imaging

(Neha Goswami\*, Gabriel Popescu†)

*Dedicated to the memory of Gabriel Popescu (deceased June 2022)*

#### 7.1. Introduction

With its 400-year-old history, optical microscopy has become the most widely used technology in biomedicine.<sup>[245]</sup> Fluorescence-based microscopy is currently dominant, as it provides microstructure information with chemical specificity. However, this capability often comes at a heavy price: chemical and phototoxicity affects the function and viability of live cellular systems and photobleaching drastically narrows down the temporal window of investigation. For these reasons, we have witnessed a renewed interest in label-free imaging, as evidenced by the various sections of this current Roadmap article. In this section, we describe quantitative phase imaging (QPI), an approach to label-free imaging that is rooted in holography and interferometric microscopy.<sup>[246]</sup>

In recent years, QPI has registered significant progress both in technology development and biomedical applications.<sup>[247]</sup> It is becoming an important tool in biomedicine due to its label-free and quantitative nature and has proved to be a valuable tool in many areas, including cell biology, blood testing, neuroscience, clinical diagnosis, fertility, and infectious diseases.<sup>[247]</sup> As a non-destructive technique, QPI enables long-term investigation of live systems. Due to the linear relationship between the phase shift map of a biospecimen and its dry mass density, QPI can report on cell growth and intercellular mass transport with very high sensitivity.<sup>[247]</sup> Importantly, knowledge of the complex image field is equivalent to that of the scattered field, which allows solving scattering inverse problems and tomographic reconstructions, based on QPI data.<sup>[248]</sup>

Despite tremendous progress in recent years, which resulted in robust instruments capable of user-friendly operation, we identified several current challenges that can turn into enormous opportunities in the field. These challenges are: achieving super-resolution QPI, performing QPI in thick, strongly scattering tissues, and performing QPI with chemical specificity. In addition to hardware developments to tackle these problems, an exciting, newly emerging solution is artificial intelligence. In this chapter, we review the QPI principles of operation, its figures of merit, applications, and these current challenges and opportunities.

In the 1930's, phase contrast (PC) microscopy was invented as an "intrinsic" method that allowed the visualization of transparent structures with high contrast.<sup>[249]</sup> The intensity distribution of an image can be described as an interferogram, following Abbe's insight from 1873.<sup>[11]</sup> Thus, the intensity of a PC image can be written as

$$I(x, y) = |a| I_0 + I_1(x, y) + 2\sqrt{|a| I_0 I_1(x, y)} \cos[\Delta\phi(x, y) + \gamma] \quad (11)$$

In Equation (11),  $I_0$  and  $I_1$  are the intensities of the incident and scattered light, respectively,  $\Delta\phi(x, y)$  is the phase difference between the two fields, while  $a = |a|e^{i\gamma}$  is a complex filter applied by Zernike to the incident light. The point of the filter is to make  $I$  more sensitive to  $\Delta\phi$ , i.e., to increase the contrast of the interferogram. First, the filter attenuates  $I_0$  ( $|a| < 1$ ), which otherwise is much stronger than  $I_1$  for transparent structures, resulting in low contrast interference. Second, the phase shift  $\gamma$  is set to a value of  $\pm\pi/2$ , which converts the slowly varying cosine into a rapidly varying sine, which, for small values of  $\Delta\phi$  approximates a linear function. With this simple filter, the contrast of the image is increased significantly, which allowed PC to become a broadly adopted technique, especially for visualizing unlabeled cell cultures. However, as can be seen from Equation (11), a single measurement of  $I(x, y)$  is insufficient for decoupling  $I_0$ ,  $I_1$  and  $\Delta\phi$ , which means that it cannot be used for quantitative measurements.

A decade later, Gabor invented holography to store phase information into a single intensity recording on a transparency, which can be further "read" with the same incident light and recreate the phase and amplitude information associated with the object field.<sup>[250]</sup> The equation for describing Gabor's "in-line" hologram is very similar to Equation (11), except  $I_1(x, y)$  corresponds to the scattered light at an out-of-focus-plane, described by Fresnel's formula, and there is no filter, i.e.,  $a = 1$ . Therefore, in-line holography cannot be used to extract quantitative phase information either. Furthermore, because the recorded signal  $I$  is real, the reconstructed signal, i.e., the complex field associated with the object is Hermitian, resulting in a pair of images along the optical axis, complex-conjugated of one another. This obstacle became known as the "twin image" problem and was solved later with the advancement of off-axis holography.<sup>[251]</sup> The goal in QPI is to eliminate all these ambiguities and measure quantitatively the phase shift at each point in the field of view. The main approaches to accomplish this are presented below.

#### 7.2. Principles of QPI

When choosing a certain method for QPI, one must be mindful of the figures of merit that are most important for the application at hand. There are four main parameters that describe the performance of a QPI system: spatial and temporal resolution, as well as spatial and temporal phase sensitivity.<sup>[246]</sup> Phase shifting interferometry (Figure 10a) is one solution for decoupling the phase and amplitude contributions in Equation (11). By controlling the phase difference between the two interfering fields, one records several independent interferograms, which solves for the phase uniquely. As a time-modulation technique, phase shifting preserves the space-bandwidth product of image, at the expense of the time resolution.

Conversely, off-axis interferometry (Figure 10b) isolates the cross-term in Equation (11) by spatial modulation and, as a result, provides high acquisition rates at the expense of space-bandwidth product.

The spatial and temporal sensitivity describe the smallest phase changes that an instrument can detect between two points, respectively, in space and time. The temporal sensitivity is affected by the stability of the instrument and techniques for

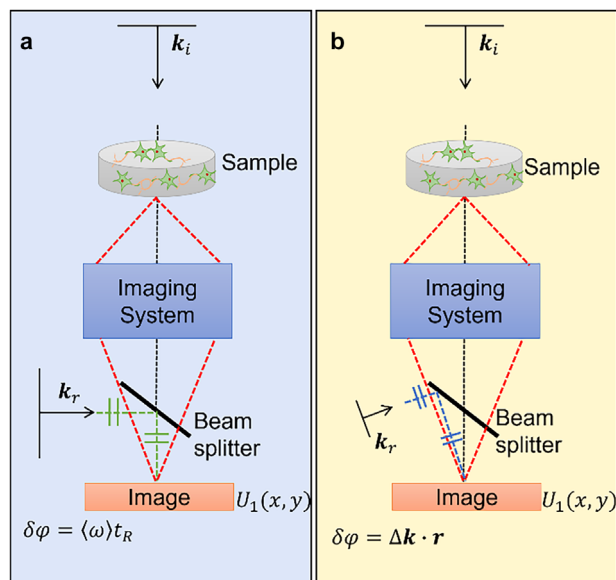


**Figure 10.** QPI modes of operation. a. Phase shifting interferometry b. Off-axis interferometry.  $k_i$  is the incident wavevector and  $k_r$  is the reference wavevector.  $U_1(x, y)$  is the scattered component of the complex field  $U(x, y)$  at the image plane.

noise cancellation. Common-path interferometers are intrinsically most stable. (see Chapter 8 in Ref. [246]) Spatial sensitivity is dictated by the nonuniformity within a field of view in the absence of a sample. Suppressing speckles by using both spatial and temporal frequency averaging via, respectively, a rotating diffuser or broadband illumination is critical in achieving high spatial sensitivity.<sup>[247]</sup>

### 7.3. Status: Applications of QPI

It has been discovered early on that a quantitative phase map  $\phi$  is linearly related to the surface dry mass density of the structure,  $\rho$ ,

$$\rho(x, y) = \frac{\lambda}{2\pi\alpha} \phi(x, y) \quad (12)$$

The proportionality constant,  $\alpha$ , referred to as the refractive increment, is relatively constant across a variety of molecular species within live cells,  $\alpha \approx 0.2 \text{ mL/g}$ .<sup>[246]</sup> This simple relationship allows researchers to “weigh” cells by simply imaging them and study cell growth and its modulation nondestructively, over many cell cycles.<sup>[252]</sup>

Time-lapse QPI data yields dynamic dry mass density maps,  $\rho(x, y, t)$ , which in turn can be used to understand the physics of the intracellular transport. This transport has diffusive (passive, random) and directed (active, deterministic) contributions, and is governed by the diffusion-advection equation,<sup>[253]</sup>

$$\left( Dq^2 - i\mathbf{q} \cdot \mathbf{v} + \frac{\partial}{\partial t} \right) \rho(x, y, t) = 0 \quad (13)$$

where  $D$  is the diffusion coefficient,  $\mathbf{v}$  is the velocity, and  $\mathbf{q}$  is the spatial frequency.

Assuming a distribution of velocities of width  $\Delta v$ , the dispersion relation associated with Equation (13) yields

$$\Delta\omega(q) = Dq^2 + \Delta vq \quad (14)$$

Equation (14) indicates that measuring the temporal bandwidth as a function of spatial frequency,  $\Delta\omega(q)$ , reveals the diffusion component as a quadratic dependence and the active one as a linear relation. It has been found that intracellular transport for most cells is characterized by a diffusive component at short distances (large  $q$ ) and a directed one over large distance (small  $q$  values) (Figure 11a).<sup>[253]</sup> This result indicates that cells optimize their energy consumption and involve the molecular motors to perform work only for transport at larger scales of several microns.

Highly sensitive QPI data has been shown to hold tremendous potential in cancer pathology.<sup>[257]</sup> Thus, phase maps of histology slides reveal not only the epithelial structure of tissues, which can be used for label-free diagnosis (Figure 11b),<sup>[247, 258]</sup> but also the tumor microenvironment, which can provide information about the disease aggressiveness, (Figure 11c).<sup>[254]</sup> QPI has been employed to quantify the alignment of collagen fibers, a task that previously was possible only by using specialized stains or second-harmonic generation microscopy. Collagen arrangement has been shown to be a valuable marker in predicting metastasis and patient survival outcome.<sup>[254]</sup>

Using QPI data, one can reconstruct the tomography of the refractive index distribution, as shown by Wolf’s classical paper in 1969.<sup>[248]</sup> Under the weakly scattering approximation, the scattering potential,  $F$ , is just the 3D Fourier transform of the scattered field,  $U$ ,  $F(\mathbf{q}) \propto U(\mathbf{q})$ , where  $q = (2\pi/\lambda) \sin(\theta/2)$  is the scattering wavevector and  $\theta$  is the scattering angle. Thus, the 3D reconstruction requires collecting QPI frames along a third dimension, whether direct z-axis, or equivalently, illumination angle or wavelength. The understanding that QPI data is entirely equivalent to those obtained via angular scattering, led to the development of tomographic methods that are robust and ready for wide adoption in the biomedical field [Figures 11d and e and Refs. [255, 256, 259–262]

### 7.4. Challenges and Advances in QPI

There is no doubt that the tremendous effort in the QPI field during recent years resulted in technology solutions to seemingly insurmountable problems. Achieving sub-nanometer pathlength stability over several days appeared out of reach in the early 2000’s. Now, many variants of such instruments exist and are also being commercialized globally. Developing an instrument so easy to use and robust that it would allow broad-scale use by non-engineers appeared far-fetched as well. Yet, today, we see commercially available QPI systems that are increasingly embraced by biologists and clinicians world-wide. The application range of this technology has been growing exponentially, branching out from cell biology into infectious diseases,<sup>[263]</sup> neuroscience,<sup>[264]</sup> tissue engineering,<sup>[265]</sup> fertility,<sup>[266]</sup> pathology<sup>[267]</sup> and beyond.<sup>[268]</sup> We anticipate that applications to non-biological field, such as materials and polymer science will also continue to grow.<sup>[269]</sup>



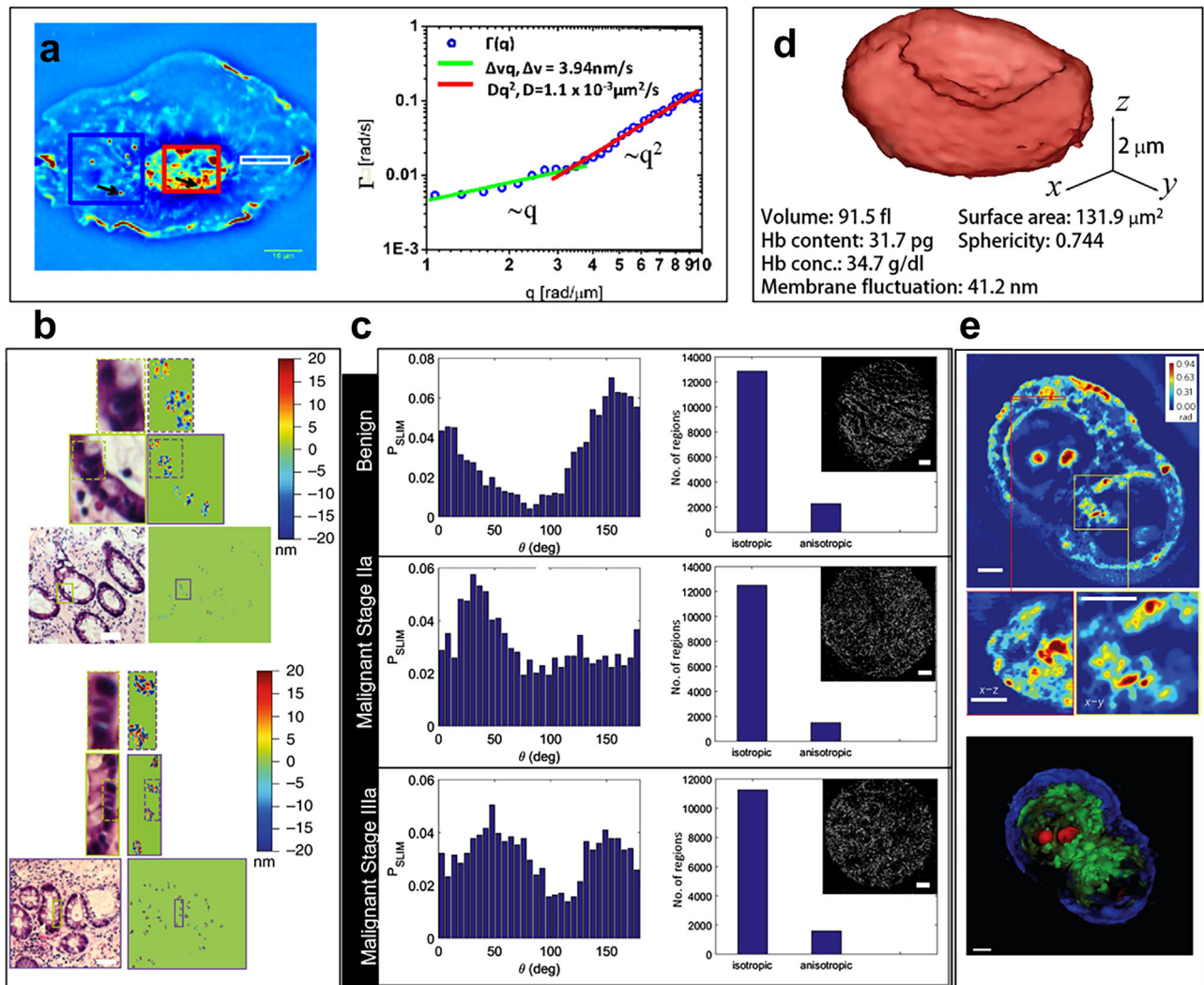


**Figure 11.** Applications of QPI. a) QPI reveals intracellular cell mass transport: Quantitative phase image of a culture of glia (left image) and Dispersion curves (right image),  $\Gamma(q)$ , in log-log scale, associated with the white box regions in left image, respectively. The green and red lines indicate directed motion and diffusion, respectively, with the results of the fit as indicated in the legend. Reproduced with permission.<sup>[253]</sup> Copyright 2011, Optica Publishing Group. b) Normal colon epithelial nuclei from an ulcerative colitis patient who did not develop colorectal cancer after seven years (low risk, top panel) and from an ulcerative colitis patient who developed colorectal cancer after seven years (high risk, bottom panel). Scale bars 20  $\mu\text{m}$ . Color bars indicate optical path length in nm. Reproduced under terms of the CC-BY license.<sup>[247]</sup> Copyright 2018, The Authors, published by Springer Nature. c) Collagen fiber orientation probability densities and bar charts with counts of isotropic and anisotropic regions for three different cores. Scale bar: 200  $\mu\text{m}$ . Reproduced with permission.<sup>[254]</sup> Copyright 2017, SPIE d) 3D rendered isosurfaces of RI maps of individual healthy RBC. Reproduced with permission.<sup>[255]</sup> Copyright 2014, The Authors, published by Springer Nature. e) Top: a deconvolved z-slice measured using a  $\times 63/1.4$  NA oil immersion objective. Middle: a cross-section at the area indicated by the red box and the yellow box. Bottom: false-color three-dimensional rendering of the deconvolution result. Scale bars in all panels, 5  $\mu\text{m}$ . Reproduced under terms of the CC-BY license.<sup>[256]</sup> Copyright 2014, The Authors, published by Springer Nature.

However, to continue this tremendous progress and eliminate further obstacles that may prevent QPI from becoming a routine method of investigation in biomedicine, we must assess critically the current limitations of the technology. In our opinion there are three major shortcomings of the QPI technology: 1) imaging strongly scattering tissues is extremely challenging, 2) as a label-free technique, QPI lacks chemical specificity, and 3) as a diffraction limited method, QPI has limited resolution. Solving these problems represent enormous opportunities in the field, as briefly described below.

#### 7.4.1. QPI of Strongly Scattering Structures

It has become increasingly clear that 3D cellular clusters better mimic the behavior of in-vivo tissue. Such systems are crucial not only in tissue engineering, but also for developing “biobots” and precision medicine.<sup>[270]</sup> As a label-free, nondestructive tool, QPI appears ideal for investigating such cellular systems in terms of function and viability. However, as these structures can range from 100s of microns to millimeters in size, they are significantly larger than the scattering mean-free path and thus, produce



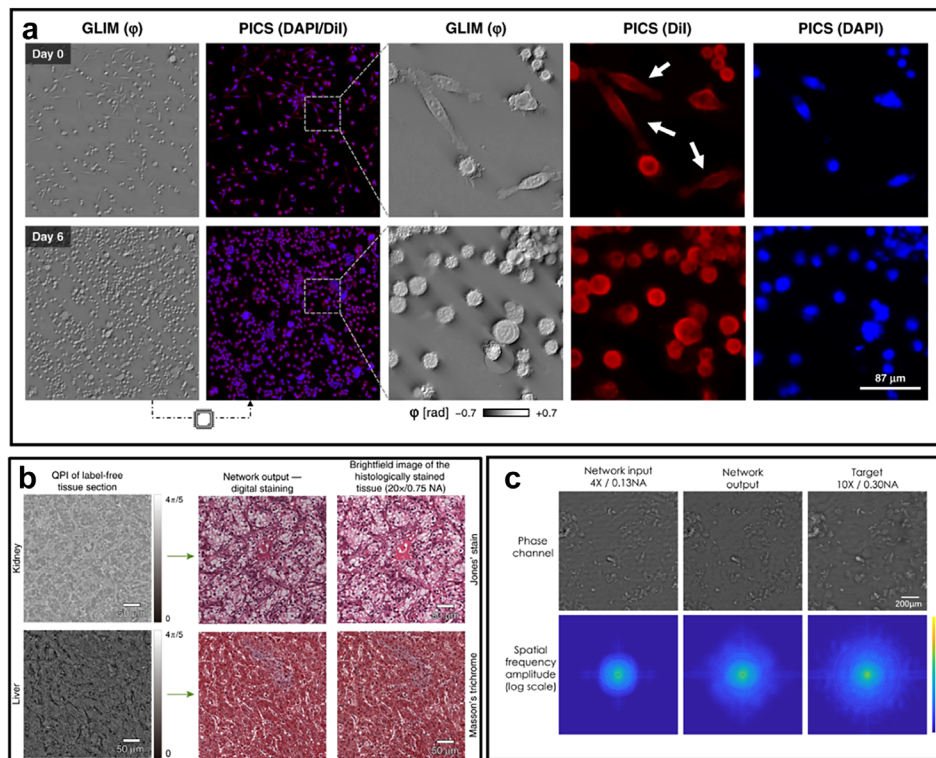


**Figure 12.** Current trends in QPI. a) Phase imaging with computational specificity (PICS)-To demonstrate time-lapse imaging and high-content screening capabilities, the authors of Ref. [272] seeded a multiwell with three distinct concentrations of SW cells ( $\times 20/0.8$ ). These conditions were imaged over the course of a week by acquiring mosaic tiles consisting of a  $2.5 \text{ mm}^2$  square area in each well using a  $\times 20/0.8$  objective. The machine learning classifier, trained at the final time point after paraformaldehyde fixation, is applied to the previously unseen sequence to yield a DII and DAPI equivalent image. Interestingly, the neural network was able to correctly reproduce the DII stain on more elongated fibroblast-like cells, even though few such cells are present when the training data was acquired (white arrows). Reproduced under terms of the CC-BY license.<sup>[272]</sup> Copyright 2020, The Authors, published by Springer Nature. b) Phase-stain for image-to-image translation-PhaseStain-based virtual staining of label-free kidney tissue (Jones' stain) and liver tissue (Masson's Trichrome). Reproduced under terms of the CC-BY license.<sup>[57]</sup> Copyright 2019, The Authors, published by Springer Nature. c) Resolution enhancement through deep learning-Spatial frequency analysis for the diffraction-limited system. Reproduced under terms of the CC-BY license.<sup>[273]</sup> Copyright 2019, The Authors, published by Springer Nature.

strong multiple scattering. The multiply scattered waves, characterized by a distribution of propagation direction and phase shifts, overlap at each point in the field of view creating in essence a strong incoherent background. As a result, the singly scattered light, carrying the phase image information, is subdominant, overwhelmed by the multiple scattering background. That is to say, the image recorded exhibits low contrast. Initial efforts to tackle this challenge already have been made: using a DIC geometry, in which the interfering fields are always equal in power and phase shifting that only modulates the single scattering light, GLIM has shown promise for imaging embryos and spheroids.<sup>[271]</sup> However, as a wide-field QPI method, GLIM still suffers from "spatial cross-talk", whereby scattered light from neighboring points overlaps in the same field of view.

This tremendous challenge is likely to generate new efforts in the field for the foreseeable future. While suppressing multiple scattering to increase penetration depth is a problem applicable to all optical techniques, label-free or otherwise, the separate access to amplitude and phase specific to QPI, may provide the path toward viable solutions. Along with new technology development, we anticipate that improved physical models coupled with computational algorithms will contribute towards suppressing or us-

ing multiple scattering for 3D tomography of thick objects. In particular, deep learning models may augment the physics-based descriptions for this purpose.

#### 7.4.2. Phase Imaging with Computational Specificity (PICS)

Image to image translation based on deep learning has shown enormous potential for converting computationally one form of contrast into another.<sup>[57]</sup> Using label-free data as input, it has been shown that specific fluorescence or stain maps can be inferred (Figures 12a-b).<sup>[272, 57]</sup> While still in its infancy, phase imaging with computational specificity (PICS)<sup>[272]</sup> has demonstrated its value in identifying subcellular and tissue compartments with high specificity but without the shortcomings associated with the fluorescence dyes. This approach virtually has an unlimited range of potential applications, where toxic dyes are replaced by harmless computational algorithms that can operate in real time, without concerns about photobleaching. Because the data is recorded via QPI instead of fluorescence, which often yields weak signals, the exposure and acquisition rate are significantly better. We envision that the ideal QPI device of the future will have its

seamless integration with fluorescence and enable “learning” of various chemical signatures automatically.

#### 7.4.3. Improving Resolution of QPI Systems

Existing QPI systems are diffraction limited, with a limited bandwidth coverage that is typically different in the axial vs. transverse direction. The resolution of a microscope is limited by the numerical aperture (NA) of the imaging optics. For a partially coherent illumination, the transverse resolution can be expressed as<sup>[274]</sup>

$$r = \frac{1.22\lambda}{(NA_{obj} + NA_{cond})} \Big|_{NA_{cond} \leq NA_{obj}} \quad (15)$$

where,  $NA_{obj}$  is the NA of the objective lens and  $NA_{cond}$  is the NA of the illumination condenser lens.

Resolution enhancement for QPI has been a subject of current research.<sup>[275]</sup> Resolution improvement utilizing partially coherent illumination and high NA optics has been reported in literature for 3D refractive index distribution measurement.<sup>[271, 276, 277]</sup>

Oblique illumination can synthetically increase the NA of the system and hence improve the resolution.<sup>[278]</sup> The resultant “synthetic aperture” can thus capture higher frequencies associated with the object thereby increasing the resolution.<sup>[279, 96]</sup> Enhancement in resolution by incrementing NA of the digital holographic microscopy (DHM) system using 2D hexagonal phase grating and recording holograms which are spatially multiplexed has been reported as another potential candidate in superresolution QPI.<sup>[280]</sup>

An important development is introduced in Ref. [279] where quantitative phase information is retrieved with improved resolution, directly from a set of intensity images by applying space Kramers-Kronig relationship and synthetic aperture approach using oblique illumination. This concept was also shown to be applicable to the optical diffraction tomography for estimating the 3D refractive index distribution.<sup>[279]</sup> QPI techniques based on Fourier ptychography<sup>[96]</sup> and intensity based diffraction tomography have also shown an increase in the resolution of 3D refractive index distribution by using an LED array as a source of illumination followed by phase recovery through an algorithm utilizing Born-approximation.<sup>[281]</sup> Another intensity based diffraction tomography method using annular LED illumination has reported gain in acquisition speed while maintaining near diffraction-limit spatial resolution in 3D.<sup>[282]</sup>

Resolution enhancement by structured illumination has been another popular method reported in literature.<sup>[283]</sup> Here, sample is illuminated with a structured light (for example, a sinusoidal pattern) which can then shift the higher frequencies of the object (which were originally outside the NA of the objective) into the existing aperture of the imaging system, thereby increasing the resolution.<sup>[284]</sup>

Phase deconvolution microscopy based on the principle of deconvolution of through focus stack of images by experimental/theoretical model of point spread function (PSF) has also been shown to increase the resolution and signal to noise ratio (SNR) in 3D QPI.<sup>[285, 286]</sup>

Highly desirable goal in this area of research is thus to achieve the definition of “superresolution”, which strictly refers

to diffraction-unlimited resolution, as achieved in fluorescence microscopy via nonlinear light-sample interactions.<sup>[287]</sup>

Recent efforts have shown that, again, deep learning may hold the potential for filling in the missing frequencies and extend the frequency range to super-resolution domain (Figure 12c).<sup>[273]</sup> The high signal to noise measurement of the complex field in QPI can increase the chances of this frequency extrapolation beyond what is currently achieved with deconvolution methods. This form of image-to-image translation, where the output consists of a super-resolved version of the input, will benefit from a new generation of instruments combining QPI and one of the established fluorescence super resolution techniques, such as a STED, PALM, or STORM.

#### 7.5. Conclusion

In this section we aimed to present a brief overview of the QPI field, its principles of operation and applications. While acknowledging the incredible progress that QPI has experienced in recent years, we also point out the three main challenges that we believe to hold the key to the next wave of opportunities in the field. It is very likely that, with new advances in computational specificity, thick tissue imaging, and resolution, QPI will be embraced by the biomedical community at large.

## 8. The Present and Future of Scattering Microscopy for Studying Biomolecular Mechanisms

(Emanuel Pfitzner, Philipp Kukura\*)

#### 8.1. Status

Proteins are the fundamental building blocks of life, involved in almost all biological processes. The underlying molecular mechanisms invariably rely on interactions between proteins. These interactions are analogous to chemical reactions, where covalent bonds between atoms are formed or broken. They range from simple protein-protein interactions, such as those between antibodies and antigens, to more complex biochemical reactions – like protein biosynthesis, G-protein coupled receptor (GPCR) signalling, and virus-cell interactions (Figure 13). Revealing the structural and dynamic aspects of these processes is key not only to our understanding of biomolecular function and regulation, but also to devise therapeutics for disease intervention<sup>[288]</sup> and to the creation of novel bio-inspired materials and processes.<sup>[289]</sup>

Our ability to study biomolecules has been revolutionised by the development of ever more powerful structural methods, which have recently been complemented by AI-based structure prediction.<sup>[290]</sup> However, our ability to observe and thus study biomolecular mechanisms at the molecular level is much less advanced; insights into mechanisms are generally extracted from a series of experiments involving biochemical and biophysical techniques, combined with structural information. Single molecule methods – predominantly based on single molecule fluorescence, atomic force microscopy or optical trapping – have contributed significantly to progress in this area. Nonetheless dynamics, and the choreography of protein-protein interactions

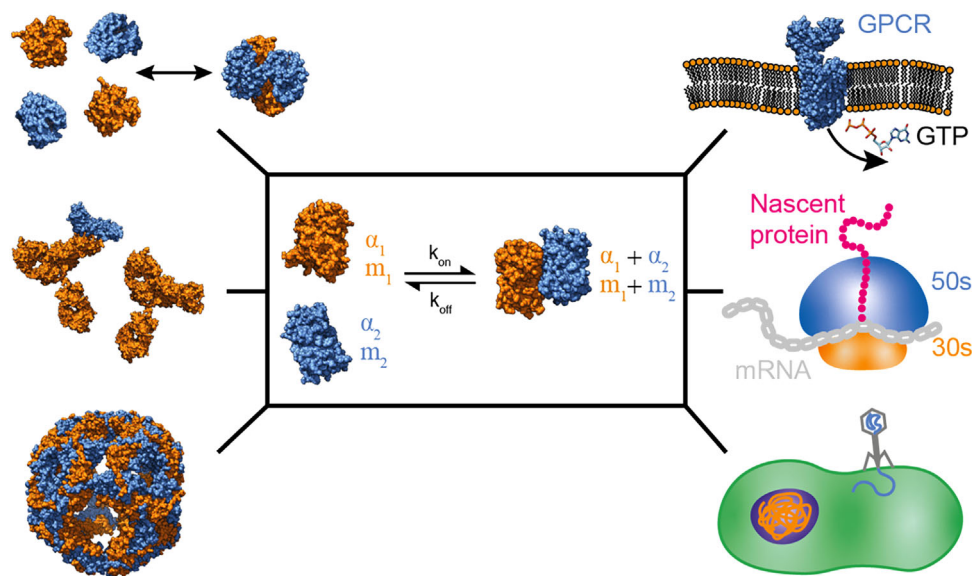


**Figure 13.** Importance of protein-protein interactions and their relationship to polarizability and mass. Counter-clockwise from top left: oligomerisation, antibody-antigen interactions, protein stability, viral infection, protein synthesis, G-protein coupled receptor signalling.

that actually manifest the mechanisms of interest, remain difficult if not impossible to observe directly.

Label-free detection of single biomolecules by light scattering is attractive for studying protein-protein interactions in a close-to-native environment because of its universality, but has struggled in both development and application due to the associated weak signals. To overcome this limitation, early studies exploited plasmonic amplification of the electromagnetic field,<sup>[291, 292]</sup> or inelastic scattering.<sup>[293]</sup> More recently, elastic scattering has been shown to enable single molecule sensitivity using both plasmonic structures,<sup>[221, 294, 295]</sup> and Rayleigh scattering.<sup>[296–298]</sup> For interferometric detection of elastically scattered light, the resulting signals are proportional to the polarizability  $\alpha_i$  of the scatterer, which has been shown to correlate exceptionally well with its molecular mass  $m_i$  (Figure 13).<sup>[299]</sup> As a result, interferometric scattering data add critical – and universal – information about molecular structure, composition and identity to a pure detection modality.

## 8.2. Current Challenges and Required Advances

The key challenge associated with detecting and quantifying single proteins and their complexes with elastically scattered light arises from their small size (2–20 nm) and consequently minuscule scattering cross sections, and from their refractive indices being similar to water. A typical 50 kDa protein will only scatter a small number of photons in one ms, even at high incident power densities of  $1 \text{ MW cm}^{-2}$ . The weak scattering imposes a hard limit on detection sensitivity and the precision achievable when relying on scattered photon detection. Even if the challenge of collecting sufficient scattered photons is met, however, specific detection always has to be achieved on top of any background signatures from spurious reflections, sample inhomogeneities or signals created by other scatterers. The required advances can

be coarsely summarised as a quest for more scattered light, extended detection time, improved statistics and additional information beyond scattering alone.

### 8.2.1. More Light

Particle contrast can be amplified by either boosting the total number of detected photons to reduce shot noise (Figure 14a) or by increasing the number of scattered photons relative to a reference field (Figure 14b). Both can be achieved by higher incident power densities, ultimately limited by the need to prevent sample damage. An alternative approach involves confining the incident light by means of total internal reflection (TIR),<sup>[300]</sup> wave guides,<sup>[298]</sup> or dielectric or plasmonic<sup>[221]</sup> nanostructures. The confinement can boost the local electric field amplitude from two-fold (TIR) to beyond 10-fold for plasmonic structures, although it may be that such increases in local field strength could damage the sample and are subject to ultimately the same limitations as far-field approaches as they increase the local intensity experienced by the analyte. At the same time, resonance enhancement could result in more significant energy deposition – causing damage at lower intensities.

### 8.2.2. More Time

Current approaches to detecting single proteins by light scattering rely largely on detecting individual proteins after binding to a surface. Since the change in contrast is too small to be directly detected, a ratiometric approach is employed: several frames before and after a landing event are separately averaged, and the two resulting images are divided. Consequently, every protein is only measured once. The precision of a contrast measurement of one single protein could be significantly improved if it could be

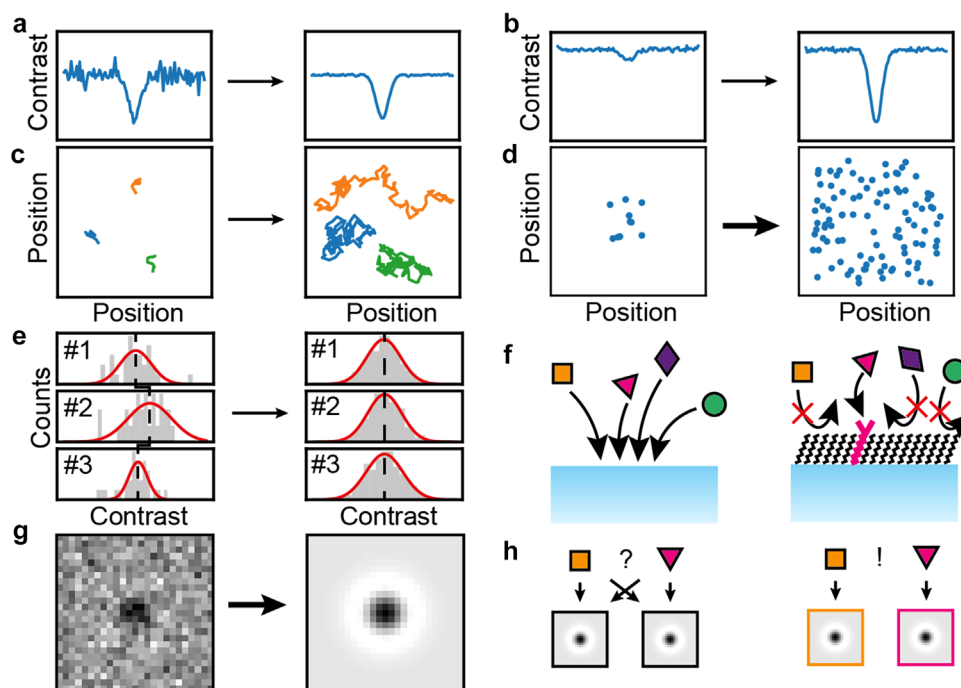


**Figure 14.** Future challenges of light scattering-based microscopy. a) Detector improvement for lowering shot noise. b) Amplification of light scattering. c) Prolonged, repeated observation. d) Larger field of view for improved statistics. e) Improving measurement precision of individual molecules (#1, #2, #3) by higher statistics per molecule. f) Passivated/activated surfaces for selective measurements. g) Image processing for improving image quality. h) Classification algorithms or additional experimental information (fluorescence, polarisation, etc.) to differentiate otherwise indistinguishable particles.

performed multiple times (Figure 14e), akin to efforts in charge detection mass spectrometry.<sup>[301]</sup> Making multiple interferometric scattering measurements requires that the molecule be mobile and distinguishable from the background multiple times. One route to achieve this is to adsorb proteins to a solid supported lipid bilayer on which they can diffuse in 2D (Figure 14c),<sup>[302, 303]</sup> or through the use of nanofluidics to achieve 3D trapping.<sup>[304]</sup>

### 8.2.3. More Particles

The lack of specificity and temporal resolution for light scattering-based detection limits the number of particles that can be detected per unit time. One approach is to devise optical setups with a larger field of view (Figure 14d). Both longer and increased sampling of individual molecules will improve the precision of the measurement, making it possible to distinguish between species of similar mass (Figure 14e). Alternatively, selective surfaces can help by allowing only one species in a complex mixture to bind while rejecting others (Figure 14f). Enhanced image processing algorithms, which have been successfully applied e.g. to transmission electron microscopy (TEM) data, could help by improving measurement precision through classification rather than relying on independent, individual measurements (Figure 14g).

### 8.2.4. More Information

The lack of specificity of elastically scattered light means that particles landing at an interface are only distinguishable by

their scattering contrast. Combining scattering with fluorescence could help distinguish species in a complex mixture or add a distance readout – through Förster resonance energy transfer. Polarisation-resolved measurements could also add orientational information while acquisition of scattering at multiple colors could add specificity to the experiment (Figure 14h).

## 8.3. Conclusions

Light scattering microscopy has recently demonstrated its major potential as a universally applicable approach for studying biomolecular structure and dynamics. To date, the most powerful implementations of this approach have been based on interferometric scattering detection on microscope cover glass. Given that there is now ample evidence that label-free detection and quantification of single biomolecules in solution is not only possible, but can deliver additional information about the species of interest with high measurement precision, alternative approaches to illumination, immobilization, and detection are likely to bring about significant improvements over the next decade. Central to this success will be a genuine broadening of the research base – away from a relatively small number of highly specialized approaches towards much broader efforts directed at the key components involved in the measurement including and combining: detection, illumination, data analysis, and very importantly – assays. Some of the most dramatic recent technological advances for the life sciences have required such interdisciplinary, and concerted efforts – and similar approaches will be required to realize the full potential of light scattering-



based studies of biomolecules. A natural question to ask: where do these improvements end, what are the ultimate limits and how will we get there? There are two simple answers: one is incremental in all relevant aspects (detectors, light sources, sample preparation, data analysis). How powerful such an approach can be, has been demonstrated by the dramatic improvements in cryoEM over the past decade. Alternatively, we could encounter a step change – although it appears that this would necessarily require some mechanism by which either the power density, or the cross section would need to be dramatically enhanced. In principle solutions to this problem exist, how applicable they are for dynamic investigations of biomolecules remains the question.

## 9. Coherent Brightfield Microscopy

(Yi-Teng Hsiao, Chia-Lung Hsieh\*)

### 9.1. Introduction

Transmission brightfield microscopy is the earliest and arguably the simplest configuration of optical microscopy. Because of its simplicity and robustness, the brightfield microscopy has been the workhorse for histopathology for over a century (e.g., Hematoxylin and Eosin (H&E) stained tissue samples).<sup>[305]</sup> Employing the transmission geometry, the phase contrast microscopy and Nomarski's differential interference contrast (DIC) microscopy have become the standard tool for visualization of biological cells.<sup>[306]</sup> The transmission geometry has also been widely adopted in digital holographic microscopy and quantitative phase imaging where the optical phase delay of the specimen is measured for reconstructing its organization.<sup>[247, 307, 308]</sup> Conventional transmission microscopy employs incoherent light sources (e.g., incandescent/mercury lamp and LEDs) for illumination to avoid the troubles of speckle. However, due to the low spatial coherence, it is difficult to deliver the incoherent light to the sample at a high intensity, which eventually restricts the detection sensitivity. White light illumination also experiences chromatic dispersion that often lowers the optical contrast of the image. Here, we introduce a brightfield microscopy that is equipped with a highly coherent laser for illumination, which is referred to as "coherent brightfield (COBRI) microscopy".<sup>[88]</sup>

### 9.2. COBRI Microscopy: Detecting Forward Scattering Light Through Interference

The simplest form of COBRI microscopy is depicted in **Figure 15a** where a condenser lens focuses a stationary laser light onto the sample, and a microscope objective together with a tube lens form a 4F system to record the transmitted image with a digital camera. In this configuration, the illumination area has a Gaussian profile whose size is determined by the numerical aperture (NA) of the condenser lens. More uniform illumination over a defined area can be achieved by rapid scanning of a focused beam where the NA of the condenser is increased by using an objective and the beam scanning is performed by a two-axis

acousto-optic deflector (AOD) (see **Figure 15b**).<sup>[88]</sup> Compared with the conventional brightfield microscopy with white light illumination, COBRI microscopy offers a higher image contrast of biological cells and nanoparticles mainly because the chromatic dispersion is avoided.<sup>[88]</sup> Moreover, the laser illumination of COBRI easily provides the local light intensity required for ultrahigh speed image recording (e.g., an intensity of  $10 \mu\text{W} \mu\text{m}^{-2}$  at the sample for the acquisition rate 100 000 fps).<sup>[88]</sup>

The detected intensity of COBRI image is the superposition of the forward scattered signal of the sample and the non-scattered transmitted reference beam.

$$I_{det} = |E_t + E_s|^2 = |E_t|^2 + |E_s|^2 + 2|E_t||E_s|\cos\theta \quad (16)$$

where  $I_{det}$  is the detected intensity;  $E_t$  and  $E_s$  are the optical complex fields of the transmitted reference light and the forward scattered light of the sample, respectively;  $\theta$  is the phase difference between  $E_t$  and  $E_s$ . When imaging a sub-diffractive object,  $\theta$  is a function of the axial position of the sample relative to the focus of microscope objective as the result of Gouy phase shift, where both constructive ( $\theta = 0$ ) and destructive ( $\theta = \pi$ ) interference could occur (**Figure 15c**).<sup>[88]</sup> For small nanoparticles,  $|E_s| \ll |E_t|$  and the interference term is much greater than the scattering intensity  $|E_s|^2$ . The interference also brings the detection into the shot-noise limited regime that is nearly immune from the detector noise.<sup>[309]</sup> More discussion on the comparisons between the interferometric and darkfield schemes can be found in other reviews.<sup>[310, 311]</sup> The COBRI contrast can be enhanced by back-pupil function engineering via inserting a dot-shaped attenuator at the Fourier plane of the sample that preferentially reduces the reference beam intensity (**Figure 15b**).<sup>[312]</sup> With contrast enhancement, single 10 nm AuNPs were successfully visualized and their diffusive motions are resolved with 10 nm spatial precision at a frame rate of 1000 Hz.<sup>[312]</sup>

As a common-path image-based interferometry, the COBRI microscopy shares many features with the interferometric scattering (iSCAT) microscopy, and COBRI can be considered as the transmission counterpart of iSCAT.<sup>[313]</sup> We point out that the relatively weak intensity of the reference beam in iSCAT microscopy (typically served by the reflection at the interface of supporting coverglass and the aqueous medium) readily enhances the optical contrast for detection. While the transmitted reference beam is inherently strong in COBRI, by corresponding back-pupil function engineering that attenuates the transmitted reference beam, it has been shown that COBRI microscopy offers the identical detection sensitivity as iSCAT under the same amount of illumination intensity.<sup>[312]</sup>

The key difference between COBRI and iSCAT microscopy relies on the choice of signal for detection: forward scattering in COBRI and backscattering/reflection in iSCAT. Although the detection geometry has little effect on single-particle imaging, it results in considerable differences when imaging biological cells. **Figure 15d** displays the COBRI and iSCAT images of a biological cell. Note that the detection sensitivity of COBRI and iSCAT are matched intentionally by adopting the suitable back-pupil function engineering in COBRI. Comparing these two images in **Figure 15d**, it is clear to see that the iSCAT image contains the interference rings that are absent in the

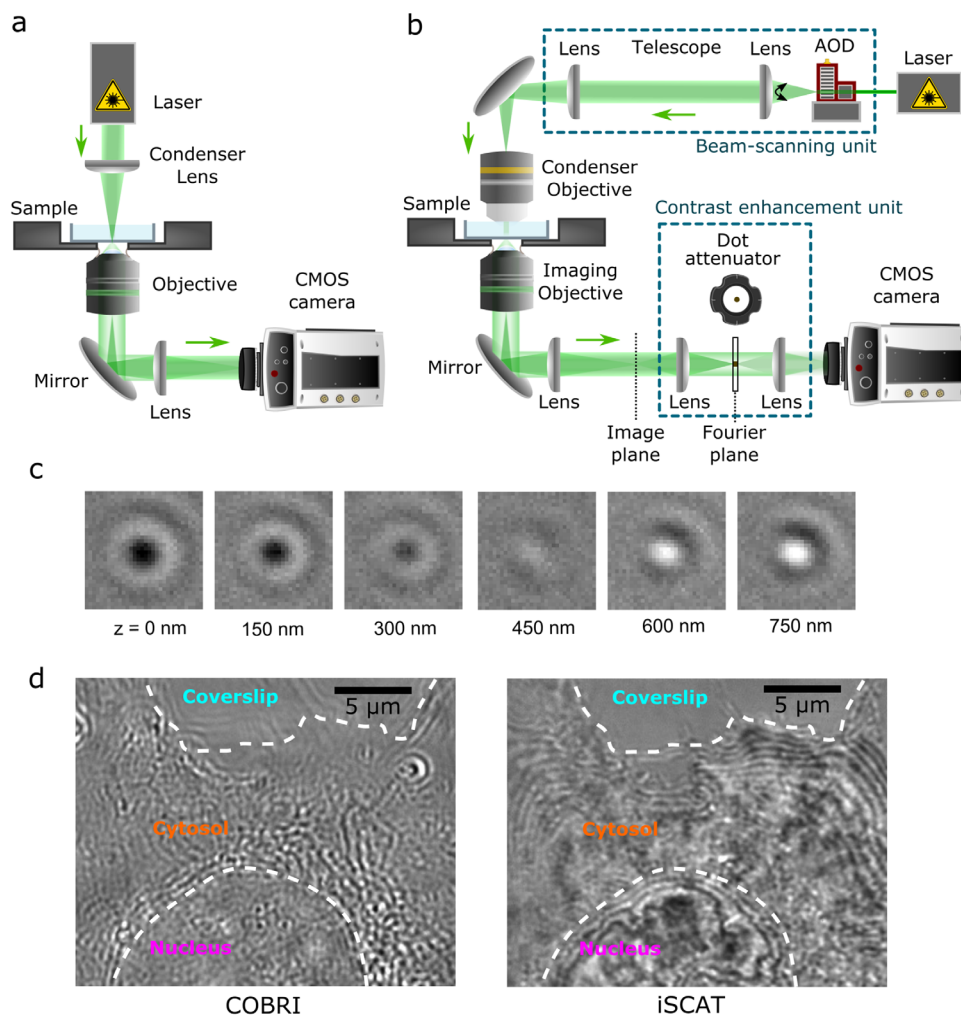


**Figure 15.** Coherent brightfield (COBRI) microscopy. a) Schematic of the simplest configuration of COBRI microscopy with a stationary widefield illumination. b) Schematic of COBRI microscopy with beam-scanning unit and contrast-enhancement unit. c) COBRI images of a virus particle at different axial positions, showing z-dependent COBRI contrast. Reproduced with permission.<sup>[88]</sup> Copyright 2017, American Chemical Society. d) Side-by-side comparison of the COBRI (left) and iSCAT (right) images of a HeLa cell cultured on coverslip. The dashed lines mark the boundaries of the nucleus and the cell body.

COBRI image. This is because the cell surface membrane is reflective and its height is spatially varying, giving an additional heterogeneous interference pattern.<sup>[314, 315]</sup> This membrane reflection has also been observed in the early works of interference reflection microscopy (IRM) and reflection contrast microscopy (RCM),<sup>[316–318]</sup> which can be considered as the iSCAT microscopy with low-coherence light illuminations. The iSCAT signal of the live cell plasma membrane can be highly dynamic due to the spatial fluctuation of the membrane. The strong and dynamic signal of the cell membrane may complicate the imaging of other objects in the cellular environment, e.g., tracking artificial and biological nanoparticles. In contrast, the cell membrane is transparent in transmission and has negligible effect on the COBRI imaging of biological cells. Therefore, the live cell imaging is expected to be easier by COBRI microscopy in transmission (except for measuring the membrane morphology where the iSCAT microscopy in reflection is clearly more suitable).

### 9.3. Imaging and Tracking Single Nanoparticles by Ultrahigh-Speed COBRI Microscopy

The COBRI microscopy without contrast enhancement readily enables direct visualization of biological nanoparticles with a diameter > 150 nm in diameter.<sup>[88]</sup> Under COBRI, single vaccinia virus particles ( $\approx 250$  nm) and native intracellular vesicles can be clearly visualized (Figure 16a). The biological nanoparticles constantly move in the live cells, which undergoes the diffusive motion driven by thermal fluctuation and the directional active transportation. By using a high-speed CMOS camera as the detector, the movement of single particles can be captured with microsecond time resolution ( $10^3$ – $10^6$  frames per second). The position of the nanoparticle can be determined via single-particle localization by fitting its image with a point-spread function (PSF) function.<sup>[319, 320]</sup> Besides the scattering signal of the bionanoparticles of interest, COBRI also records the scattering from other cell structures that appears as a

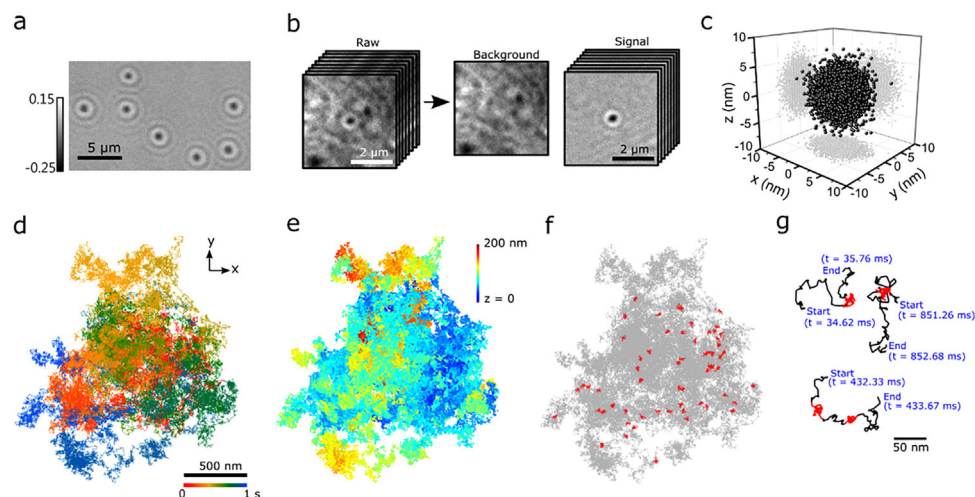


**Figure 16.** Ultra-high-speed 3D tracking of a single vaccinia virus particle on the surface of a live cell by COBRI microscopy. a) COBRI image of single vaccinia virus particles. b) Estimation and removal of cell background enables background-free imaging of the virus particle. c) Localization precision of a single virus particle is better than 3 nm in 3D. d) Lateral diffusion trajectory of a virus particle on the live cell plasma membrane, recorded at 100 000 fps. e) Reconstructed 3D trajectory of the virus particle. f) Highly transient (sub-millisecond) nano-confinements of the virus particle detected in the trajectory (highlighted in red). g) Representative trajectory segments of transient confinements of the virus particle. Adapted with permission.<sup>[88]</sup> Copyright 2017, American Chemical Society.

spatially heterogeneous background. This nonspecific scattering background complicates the direct visualization of the particle and lowers the precision of particle localization, posing a general challenge in detection and localization of particles by scattering-based microscopy.<sup>[319, 321]</sup> An effective remedy for the nonspecific background is to measure the background separately and remove it from the raw image by image post-processing. In the case of tracking nanoparticles in biological cells, the particle is often much more dynamic than the large biological cell structures, so the moving particle signal can be distinguished from the relatively static cell background based on their different temporal characteristics. A common strategy for background estimation is to calculate a temporal averaged image of a video that is recorded at a high speed (Figure 16b).<sup>[321, 88]</sup> More effective background estimation can be achieved by exploiting the a priori knowledge of the PSF.<sup>[319]</sup> With proper background removal and signal calibration, single virus particles and cell vesicles can be tracked with a spatial precision of a few nanometers in 3D (Figure 16c).<sup>[322, 88]</sup> The strategies of fast interference image recording and processing are generally applicable to iSCAT imaging in reflection. The high-speed and accurate single-particle tracking by iSCAT has been demonstrated in live cell environments.<sup>[320]</sup>

Figure 16d displays the trajectory of a single vaccinia virus particle on the plasma membrane of a live cell, recorded at 100 000 fps with 3 nm spatial precision. The data show that the virus particle diffuses rapidly on the surface of the cell. The 3D reconstruction of the diffusion trajectory represents the morphology of the cell surface (Figure 16e). Interestingly, the ultrahigh spatiotemporal resolution captures the highly transient (sub-millisecond) confinements of the virus particle at the nano-sized zones, presumably as the result of interactions between the virus and the membrane receptors (Figure 16f,g). The detection of these short-lived events occurring at the nanoscale requires exquisite sensitivity, stable signal, and high spatial and temporal resolutions simultaneously, which are supported simultaneously by the inter-

ference scattering imaging of COBRI microscopy. Using similar methods, the native intracellular vesicles can be visualized and their bidirectional motions are resolved with microsecond time resolution and nanometer spatial precision.<sup>[322]</sup>

#### 9.4. Future Perspectives

The common-path image-based interferometry, e.g., iSCAT/COBRI microscopy, exhibits excellent stability that enables sensitive detection, visualization, and tracking of very small, nano-sized particles. The reliable scattering signal facilitates ultrahigh-speed measurements that has been challenging for the fluorescence-based techniques due to the photobleaching effect.<sup>[323, 324]</sup> One of the applications is to study single-molecule dynamics by using gold nanoparticles as the scattering nanoprobe of the molecules.<sup>[311, 325, 326]</sup> It has been shown that with proper labeling, the nanoparticle introduces no artifacts to the membrane molecule, and thus the single-molecule diffusion can be resolved at the unprecedented spatiotemporal regimes.<sup>[320, 325]</sup> Using metallic nanoparticles as imaging probes has the advantages of plasmon-enhanced optical cross sections, which facilitates simultaneous scattering- and absorption-based photothermal imaging that is useful for discriminating the particle signal from the biological background.<sup>[327, 328]</sup>

The high sensitivity of iSCAT/COBRI microscopy readily supports immense applications of bioimaging beyond tracking single nanoparticles. Indeed, the recent label-free phase imaging have resolved various cell organelles with high resolutions.<sup>[329]</sup> In principle, with a higher sensitivity, iSCAT/COBRI microscopy could detect more nanoscopic objects in the cell. The critical issue is the signal-to-background ratio because the complex biological environment is expected to create considerable nonspecific background. It is recently shown that the signal-to-background ratio can be improved by exploiting the rich temporal information

encoded in a dynamic measurement.<sup>[330]</sup> Machine learning has been used to establish the complex relationships between the interference images of a biological sample and the distributions of specific molecules of interest.<sup>[181, 182, 331]</sup> The combination of iSCAT/COBRI imaging and machine learning-assisted data processing would provide the opportunity for label-free, high-speed, long-term, multiplex bioimaging.

We foresee that iSCAT/COBRI microscopy will enable exciting label-free imaging of biological cells. Because the cells have small structures compared to the optical wavelength, there is a need to improve the spatial resolution of scattering-based interference microscopy. There have been a few demonstrations of resolution enhancement by phase-sensitive interference microscopy.<sup>[332, 333]</sup> The general concept is to record the high spatial frequency signal by sequential oblique illuminations. Similar strategies can be exploited to improve the spatial resolution of iSCAT/COBRI microscopes. In addition, the spatial resolution can be improved by digital deconvolution.<sup>[95]</sup> We anticipate that the quantitative amplitude and phase retrieval by iSCAT/COBRI will soon become routine, making them the highly sensitive quantitative phase imaging (QPI) modalities. With the QPI by iSCAT/COBRI microscopy, the deconvolution can be exploited to enhance the spatial resolution, potentially reaching the super-resolution regime.

## 10. Plasmon-Enhanced Optical Ptychography and Phase Imaging

(Brian Abbey\*)

### 10.1. Introduction

The recovery of phase information from measurements of the diffracted intensity or flux of a wavefield is the basis for many types of phase contrast imaging. These techniques generally do not necessitate any staining or labeling of the sample and involve the computational reconstruction of quantitative phase information.<sup>[334, 335]</sup> Of the numerous types of label-free coherent imaging methods that have emerged, ptychography has proved to be one of the most successful. Originally developed in the context of Scanning Transmission Electron Microscopy (STEM), ptychography has already had a significant impact for X-ray,<sup>[336]</sup> electron,<sup>[337]</sup> as well as optical microscopy.<sup>[338–340]</sup>

The original concept for the ptychographic method is generally credited to Walter Hoppe, who published a series of papers on the topic in the late 1960's and early 70's.<sup>[341]</sup> Hoppe's idea was to collect a dataset comprising multiple diffraction patterns, formed by laterally translating the sample with respect to a finite illumination in discreet overlapping steps. The diffraction data then constitutes a convolution of the sample with itself, and the localized illumination function which is common to all datasets. This convolution or 'folding' of the diffraction data gave rise to the name ptychography, first used by Hegerl and Hoppe in 1972, where 'ptycho' comes from the Greek word 'to fold' ( $\pi\tau\upsilon\chi\acute{\omicron}\varsigma$ ).<sup>[342]</sup> The lateral shifting of the position of the illumination with respect to the real-space position of the sample, has the rather profound effect of creating a phase ramp in reciprocal-space. Provided the relative location of each of the measurement points can be determined, the phase relationship between the diffraction patterns can be uniquely determined.

Unlike most optical microscopy techniques, the spatial resolution of ptychography is not limited by the properties of any image forming lenses that may be used. Instead, the spatial resolution of ptychography is determined by the Numerical Aperture (NA) subtended by the square of the modulus of the wavefield (intensity) measured at the detector plane. This means a high-resolution image can be reconstructed using low NA lenses<sup>[96]</sup> or even using no optics at all.

It has also been reported that by exploiting the high degree of data 'redundancy' in ptychography or via combination with aperture scanning it is possible to obtain a 'super-resolution' image beyond the diffraction limit.<sup>[86]</sup> There are three mechanisms applicable to ptychography which contribute to improving the spatial resolution beyond the numerical aperture of the detected diffraction signal. First the "synthetic aperture" effect in which data is collected from the specimen using a plane wave incident at different angles.<sup>[343]</sup> Data from this different range of scattering angles can be combined to form a larger "synthetic" diffraction pattern on the detector which can be inverted to form a super-resolved image. Second, "analytic continuation" in which the measured diffraction signal is treated as the convolution of the spatial frequency spectrum of the specimen convolved with the Fourier Transform of the exit pupil of the optical system apertured by the detector.<sup>[344]</sup> Convolution ensures that the recorded diffraction data contains information from the specimen's entire frequency spectrum enabling extrapolation of the diffraction patterns beyond the measured data. Finally, 'dithering': sub-pixel lateral shifting of the specimen by a non-integer number of pixels can also contribute to an enhanced resolution (although this may be more accurately described as de-aliasing as opposed to super-resolution).<sup>[345]</sup> Achieving super-resolution in ptychography depends on successfully exploiting one or more of these effects. Another advantage afforded by optical ptychography is contrast. The ability to generate label-free, high-contrast, quantitative amplitude and phase information is attractive for bioimaging. A key feature differentiating ptychography from other phase contrast techniques is that the complex probe function is typically computationally recovered in a simultaneous operation along with the sample refractive index.<sup>[346]</sup> This avoids errors which can be introduced via an imperfect knowledge or measurement of the incident illumination and provides a reference against which the quantitative optical properties of the sample can be retrieved.

Recently there has been significant interest in further improving the sensitivity of optical phase microscopy by exploiting plasmonic nanostructures.<sup>[347]</sup> The combination of phase imaging and plasmon-enhanced sensing has the potential to deliver exceptional sensitivity for weakly interacting specimens. Phase imaging setups incorporating plasmon-enhancement include interferometry (Figure 17A-E),<sup>[348]</sup> holography,<sup>[349]</sup> Differential Interference Contrast (DIC),<sup>[350]</sup> and ptychography (Figure 17F-G).<sup>[87]</sup> Analysis of coherent scattering has also been used as a means of visualising the complex optical plasmon fields generated by metallic nanostructures using near-field scanning microscopy. For example, Hillenbrand et al. were able to directly image the phase and amplitude associated with resonantly induced plasmon oscillation to a spatial resolution of 30 nm using a carbon nanotube as the optical probe.<sup>[334]</sup> In the case of Plasmon-Enhanced ptychography (PE-ptychography) enhancement of both the amplitude and phase for histological



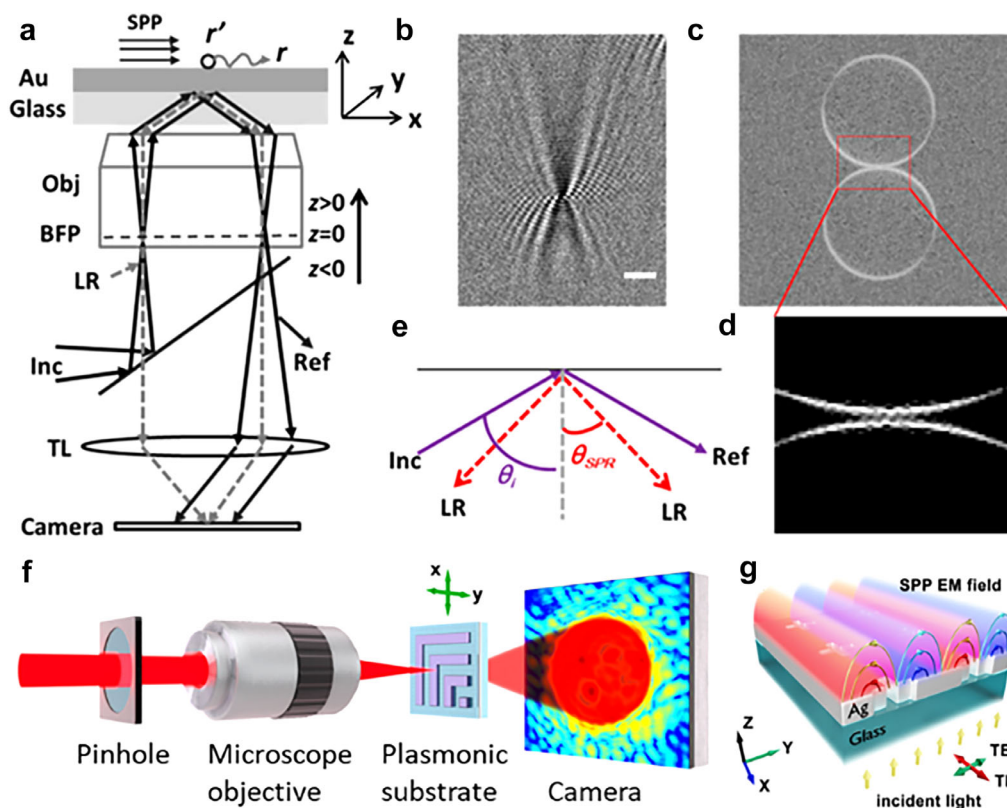


**Figure 17.** Experimental setups and mechanism for interferometric plasmonic microscopy (a–e) and plasmon-enhanced ptychography (f–g). a) Schematic showing the interferometric plasmonic microscopy (iPM) setup. b) iPM real-space image showing a 40 nm Ag nanoparticle and c) in reciprocal space. e) Diagram showing incident angle ( $\theta_i$ ) and resonance angle ( $\theta_{SPP}$ ). Inc (incident beam); Obj (objective); BFP (back-focal-plane); LR (leakage radiation); Ref (reflective beam); TL (tube lenses). Reproduced with permission.<sup>[350]</sup> Copyright 2019 American Chemical Society. f) Experimental set-up for PE-ptychography. g) Schematic of the evanescent electromagnetic field generated by SPPs. EM, electromagnetic; TM, transverse magnetic; TE, transverse electric. Reproduced with permission.<sup>[87]</sup> Copyright 2021 Springer Nature.

tissue sections was demonstrated (Figure 18a–b). Typically, the variation of amplitude and phase for biological samples is quite linear over the visible range. However, the introduction of plasmon-mediated near-field interactions induces significant and often contrasting variations in the complex Refractive Index (RI) as a function of wavelength (Figure 18c–f).

## 10.2. Current Status and Future Prospects

The incorporation of nanostructures into phase imaging has already been shown to deliver superior performance in terms of contrast. However, for most plasmon-enhanced phase imaging, sub-diffraction limited super-resolution has yet to be clearly demonstrated. In the case of polarization-controlled holographic imaging of nanoantennas<sup>[349]</sup> the authors resolve the amplitude signal arising from individual nanoantenna's to a peak width of approximately 0.3  $\mu\text{m}$ . This was using a source comprising a tungsten-halogen lamp filtered to produce a central wavelength of 600 nm with a full-width-at-half-maximum (FWHM) of 50 nm. Other proposals for achieving super-resolution, plasmon-enhanced phase imaging include the recovery of the high frequency components of the scattered signal beyond the NA of the imaging system, which are modulated by sur-

face plasmons.<sup>[350]</sup> This is possible using a variety of different image reconstruction techniques including synthetic aperture microscopy<sup>[348]</sup> and ptychography.<sup>[86]</sup>

To date, super-resolution using PE-ptychography has yet to be experimentally demonstrated whilst other the label-free approaches have thus far only achieved relatively modest (up to 25%) improvement in spatial resolution beyond the diffraction limit.<sup>[349, 350]</sup> However, these ideas are still relatively new and have not yet had time to fully realize their potential for label-free, super-resolution bioimaging. Other more practical issues to consider are ease of use and cost of fabrication. For instance, some of the methods proposed for plasmon-enhanced phase imaging involve complex aperiodic patterning or expertise in image reconstruction and analysis. These issues, in the long term, may prove challenging for the wide adoption of these techniques by the optical microscopy community.

## 10.3. Next Steps in Development

The advantages of using plasmonics in terms of sensitivity are further augmented by access to quantitative phase information. Critically, this information can help to improve specificity to different types of analytes or cells which is a key feature

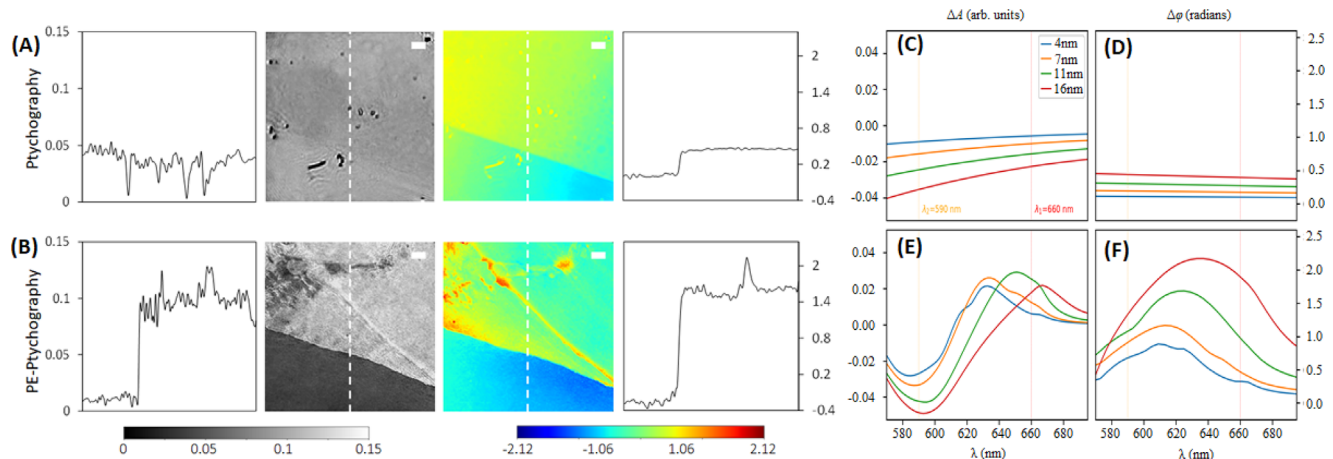


**Figure 18.** Plasmon-enhanced images of ocular nerve tissue and simulated amplitude and phase contrast predicted for different thicknesses of carbon. a) Ptychography without plasmon enhancement and b) PE-ptychography. The graphs represent line outs through the same 70 nm thick edge feature on the histological tissue section, with significantly enhanced contrast observed in both the amplitude and phase when using PE-ptychography. Note that the spatial resolution for both ptychography and PE-ptychography, based on lineouts of the edge of the tissue, are equal to  $719 \text{ nm} \pm 5 \text{ nm}$  ( $\lambda = 660 \text{ nm}$ ). The two vertical lines indicate the two different wavelengths ( $\lambda$ ) at which ptychography data was collected during the experiment. c) Amplitude and d) phase variation as a function of wavelength without the plasmonic device, e) amplitude and f) phase variation as a function of wavelength with the plasmonic device in place for four different carbon thicknesses indicated in the top right-hand corner of c). Reproduced with permission.<sup>[87]</sup> Copyright 2021 Springer Nature.

required for diagnostic applications. Very few (if any) of these concepts, however, have progressed to the point at which they could be applied within a clinical setting although they have shown potential for significantly improving the sensitivity and resolution of conventional phase imaging. A key feature of these techniques is that the interaction between surface plasmons and biological specimens fundamentally alters the complex sample Exit Surface Wave (ESW). This creates challenges for quantitatively interpreting the reconstructed phase in terms of the local properties of biological samples (e.g. dry density and dry mass of cells). Whereas extracting useful biological information from conventional quantitative phase contrast measurements is comparatively straightforward, caution must be applied when making the same types of claims in relation to plasmon-enhanced phase imaging. The RI information measured using these approaches is the result of a modification of the plasmon-resonance structure generated by the active nanostructures and the local complex dielectric constant of the sample. The latter is often spatially varying on length scales which may be comparable to the spatial resolution of the measurement or even the to the size of the plasmonically active nanostructures themselves. Deconvolution of the sample properties from the near-field response of the plasmonic device will require significant work to understand and model the properties of both the device and sample. In the case of biological cells and tissues it is not yet clear whether it is even feasible to be able to replicate the complexity and local heterogeneity of such samples in simulation. Although, there have been attempts in the literature to construct such models which may potentially be used to represent the ‘average’ properties of the sample.<sup>[351]</sup> Hence, significant research is required to enable plasmon-enhanced phase imaging to achieve comparable levels of quantitative reliability in terms of bioimaging as conventional phase contrast microscopy techniques such as interferometry or holography.

Whilst label-free plasmon-enhanced phase imaging offer many opportunities in terms of flexibility, applicability, and ease-of-use, there is considerable scope to improve specificity still further. This is particularly true in applications where label-free bioimaging is being developed as a potential adjunct or even alternative to molecular labeling. An obvious next step to improving specificity is to combine plasmon-enhanced phase contrast microscopy with hyperspectral imaging techniques. Since the variation in the complex RI of plasmonic devices is typically highly non-linear with wavelength (Figure 18c-f), different sample components have vastly different optical contrast properties depending on the incident wavelength. Hence, merging these two approaches could deliver exceptional performance in differentiating (sub-)cellular components and distinguishing them from the surrounding host environment.

However, the generation of large spatially and spectrally resolved datasets creates new challenges in terms of analysis. Deep learning has already been demonstrated as a potential tool for optimizing the design and predicting the output of plasmonic nanostructures.<sup>[352]</sup> It has also been proposed as a technique for analyzing the plasmonic resonance output of these devices.<sup>[353]</sup> Deep-learning algorithms have already been applied successfully for a variety of biosensing and bioimaging applications. For example, a machine learning approach was recently used to optimize the design and fabrication of plasmonic nanostructures for mobile broadband RI sensing (Figure 19).<sup>[354]</sup> Given the complexity and volume of data that could be generated by plasmon-enhanced phase imaging of biological specimens the application of machine learning algorithms could revolutionize the analysis of label-free plasmon-resonance data. It may enable the extraction and generation of multiplexed images from a single dataset and could even be used to generate a ‘fingerprint’ or ‘barcode’ for certain classes of cell or disease state.<sup>[355]</sup> Whilst the implementation and integration of deep learning approaches

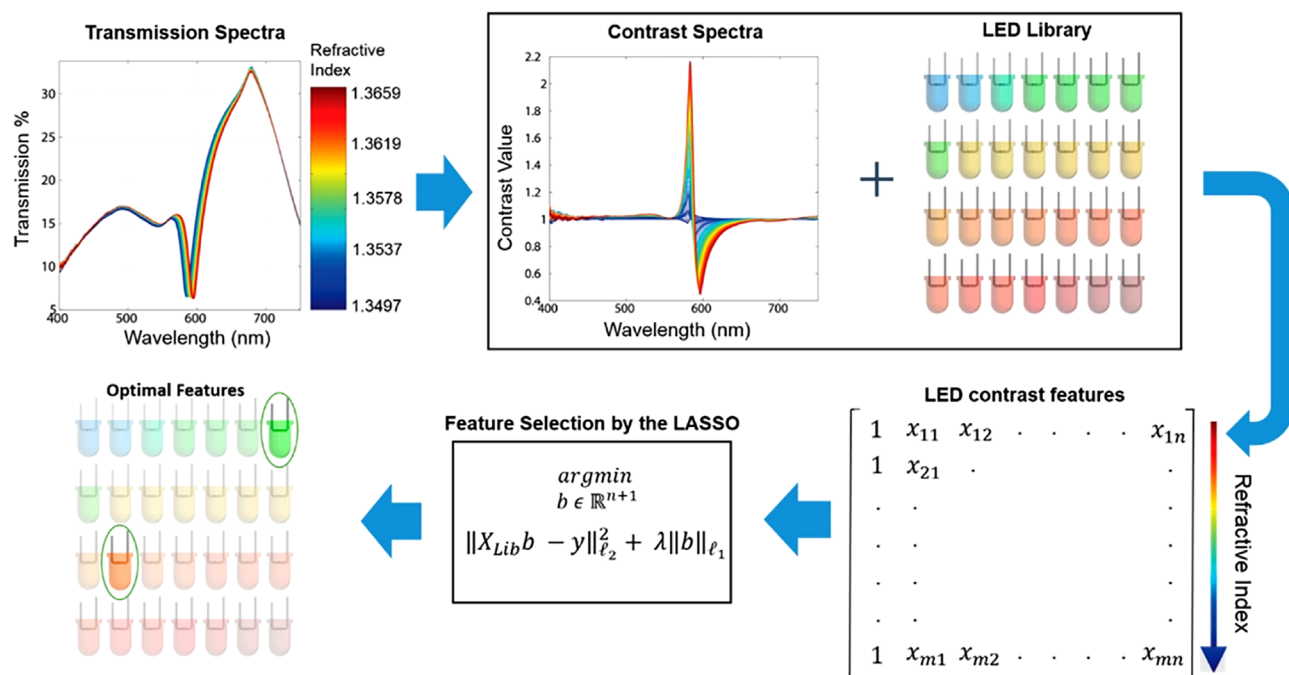


Figure 19. Schematic illustration of the machine learning framework. Reproduced with permission.<sup>[354]</sup> Copyright 2017 American Chemical Society.

into plasmon-enhanced bioimaging is currently technically feasible, caution must be applied based on the very limited (or in many cases non-existent) availability of high-quality training data. For example, although it appears feasible to train a neural network to quantitatively analyze PE-ptychography data using a combination of plasmon-resonance data plus high-quality simulations, at the time of writing, such ideas have yet to be explored.

#### 10.4. Conclusions

The addition of quantitative phase information to plasmonic microscopy opens up many new and exciting avenues of research for label-free bioimaging. In terms of ‘real-world’ biological samples, however, most of the published techniques are still in the early stages of development. As new approaches to large-scale, high-quality nanofabrication become increasingly accessible<sup>[356]</sup> plasmonic devices are expected to become increasingly common in bioimaging. Exploiting the specific interaction of the local sample dielectric constant with plasmonic nanostructures in combination with phase imaging could add a much higher degree of specificity, facilitating multiplexed imaging and enabling specific (sub-) cellular features to be highlighted. As larger, higher-quality datasets become available there are also opportunities to exploit deep learning approaches which offer the promise of maximizing the amount of information that can be extracted from plasmon-enhanced phase imaging data. In terms of achieving super-resolution, several of the techniques discussed have already achieved spatial resolutions just beyond the diffraction limit. In the case of plasmon-enhanced ptychography, there are several possible pathways to super-resolution although the reconstruction of higher order plasmon-mediated diffraction data, be-

yond the numerical aperture, is likely the most promising avenue for future development.

## 11. Circular Intensity Differential Scattering Microscopy

(Alberto Diaspro\*, Aymeric LeGratiet, Paolo Bianchini)  
(Dedicated to the memory of Ignacio Tinoco Jr. (1930-2016) and Gary C. Salzman (1942-2020)).

### 11.1. Introduction

The transition of optical microscopy to optical nanoscopy allows to super-resolve the position of objects and, more interestingly, of biological molecules to a spatial resolution better than the one imposed by the wavelength of light. It is not related to violating physical laws but of implementing the smart concepts analyzed by Toraldo di Francia and Luksosz,<sup>[357]</sup> namely: adding information to the light detection process and reducing the field of view.

The coupling with fluorescence labeling of the object to be visualized permits to spatially resolve details of intricate extended cellular substructures. Recently, technological advances in sensing photons allowed to extend the capabilities in the temporal domain adding spectroscopic fluorescence features, including lifetime and polarization.<sup>[358]</sup> However, fluorescence realized by specific labeling as a contrast mechanism has shown some limitations also when boosted by the nanoscale performances. Among them, single molecule imaging poses a problem related to possible effects on crowding in terms of re-organization of important biological macromolecules like chromatin in the cell<sup>[359]</sup> nucleus and their labeling, as also reported by means of a correlative approach.<sup>[360]</sup> In this scenario, methods that use a label-free

approach as a contrast mechanism go beyond the trend to become highly relevant for studying structure and function relationships in biological systems.<sup>[149]</sup> This fact also has a considerable impact on the development of new diagnostic instrumentation in medicine like those using polarization as mechanism of contrast.<sup>[361, 362]</sup> It is a fact that the variety of advanced Stokes-Mueller approaches and the growing aptitude for multimodal information gathering combined with artificial intelligence can be an additional strength for applications in biomedical and clinical research.<sup>[363]</sup>

Circular Intensity Differential Scattering (CIDS) is a label-free optical biophysical method originated as a differential measurement of the circular right and left polarized light scattered by a specimen outside the absorption bands instead of considering its differential absorption as in the case of circular dichroism. CIDS can be also seen as one of the 16 elements of the Mueller matrix used to generate multiparameter label-free optical images in microscopy. This approach was proven to be a gold standard label-free technique to study the molecular conformation of important biological macromolecules like chromatin and to enable rapid identification of a variety of viruses of clinical significance. In early works, it was demonstrated the potential of studying long-range chiral organization on a scale down to 1/10th–1/20th of the illumination wavelength. This hands the approach to label-free nanoscale optical microscopy. In this review, we discuss methods and technologies used for measuring this signal coming from complex macro-molecules ordering.

## 11.2. Circular Intensity Differential Scattering (CIDS)

CIDS microscopy has its foundation in the development of the theory of differential imaging as extension of the experiments carried out on the interaction of circularly polarized with structures whose size is arbitrary with respect to the wavelength of the illumination.<sup>[364]</sup>

More specifically, the circularly polarized light was used to study biological macromolecules, large oriented biological helices, in terms of circular dichroism, CD.<sup>[365]</sup> Circular dichroism is the difference in the extinction coefficient of matter impinged by left and right circularly polarized radiation. When investigating specimens containing large biomolecular motifs, CD signals produced an unexpected signature outside the absorption bands.<sup>[366]</sup> This signature was proven to be due to differential scattering cross section.<sup>[364]</sup> The spatial distribution of the angular scattered light which considers the preferential scattering of left and right circularly polarized illumination by the specimen at a given direction is defined as:

$$\text{CIDS}(\theta) = \frac{I_l(\theta) - I_r(\theta)}{I_l(\theta) + I_r(\theta)} \quad (17)$$

where  $I_{l,r}$  are the detected intensities for the left and right circular polarization states at a certain scattering angle ( $\theta$ ), respectively.<sup>[364]</sup> A paradigmatic example was early given by CIDS measurements of a suspension of the helical sperm head of the Mediterranean octopus *Eledone cirrhosa*.<sup>[367]</sup> Its left-handed helix approximately 43  $\mu\text{m}$  long, with a pitch and radius of 1  $\mu\text{m}$  and 0.65  $\mu\text{m}$ , respectively, demonstrated the availability of strong

signals in the wavelength regions above 300 nm outside the absorption bands of the nucleic acid acids and proteins components of the sperm head.<sup>[368]</sup> Theoretical analysis of the optical models have shown that CIDS signatures are most sensitive to the helical parameters.<sup>[364, 369, 370, 89]</sup> Both theory and experiments lead to the observation that the differential scattering cross section is a function of higher chiral order of important biopolymers like chromatin-DNA.

## 11.3. Discussion

The CIDS signature was initially measured on solutions demonstrating the ability of discriminating viral<sup>[371]</sup> and bacterial<sup>[372]</sup> species opening an interesting window of medical applications. Moreover, the results obtained on isolated chromatin in solution at different level of organization,<sup>[373]</sup> induced by modulating the salt concentration, pointed out to the charming possibility of monitoring chromatin compartmentalization in the cell nucleus.<sup>[374]</sup>

The development of a microscope was pushed by the availability of the photo elastic modulator, as device to control polarization states of the illumination and of the detected photons.<sup>[375]</sup> The CIDS signal is also part of a multiparameter analysis that can be done using the Mueller matrix approach. In this approach, modulating four states of polarization one can produce sixteen data set that can be transformed in label-free images when implemented in the optical pathway of an optical microscope.<sup>[375]</sup>

To take advantage of a beam scanning architecture, a fast generation of the polarization states to obtain a good signal-to-noise ratio at the pixel-dwell time rate, typically in the  $\mu\text{s}$  range, one can also exploit the simultaneous emission of orthogonal polarization states from a Zeeman effect laser providing alternate polarization states without the need for further active components.<sup>[376]</sup> At the very same time allowing compactness and simplicity of construction that are key elements for a more effective dissemination of label-free techniques and their use in biology and medicine. Another step to facilitate the interpretation of the multiple parameter data encoded in the polarization-based signals is given by the combination of Mueller matrix microscopy with the phasor approach.<sup>[377]</sup> The full matrix is converted into four Stokes vector<sup>[378]</sup> images and then a Fourier transform algorithm is applied to each of these images.<sup>[379]</sup>

Figure 20a shows an effective implementation of a multiparameter CIDS microscope also endowed of fluorescence capabilities. The illumination is implemented using a Ti-Sapphire microscope able to prime two-photon excitation fluorescence and at the very same time to generate a CIDS signal using a photoelastic modulator operating at the operating frequency  $\omega$  and a lock-in amplifier selecting the 1<sup>st</sup> and 2<sup>nd</sup> harmonic signals at  $\omega$  and  $2\omega$ . These signals plus the DC signal allow to extract Mueller matrix elements intensities including CIDS, the 4<sup>th</sup> element of the 1<sup>st</sup> row of the matrix.<sup>[374, 375]</sup> In case of a viral sample, for example the coronavirus sars-cov2 as sketched in Figure 20b, one can predict a potential in discriminating among spherical droplets containing spherical particles endowed of spikes.<sup>[378]</sup> This is in tune with the rapid microbial detection early demonstrated on flu viruses and other infections.<sup>[371]</sup> The phasor representation can be used to allow medical doctors and clinicians to visualize



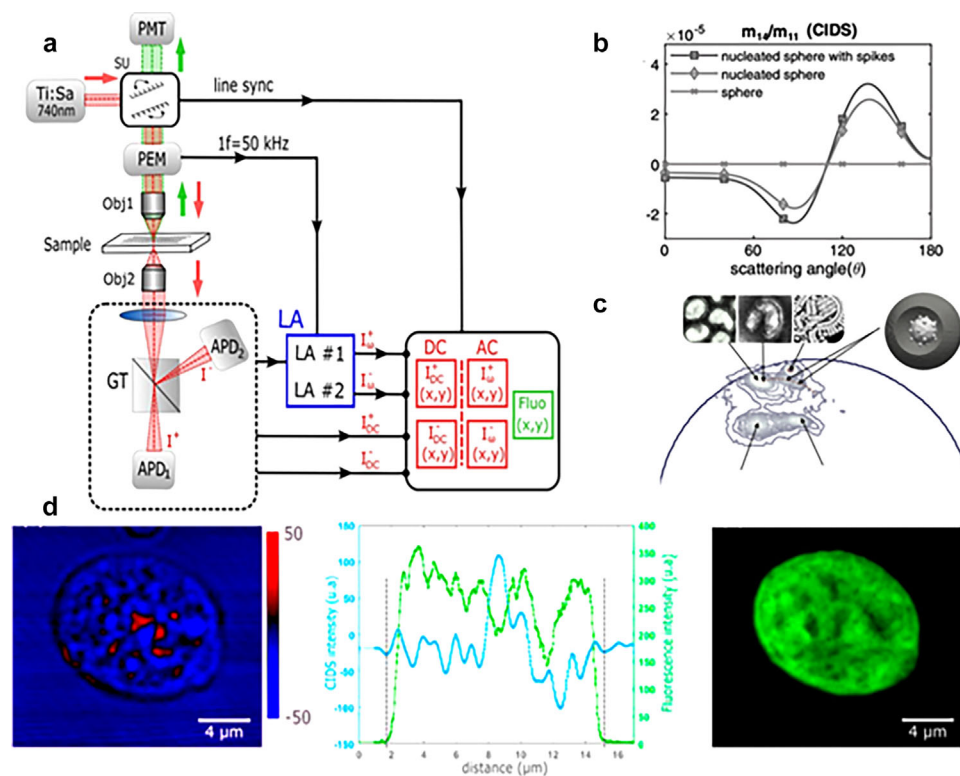


**Figure 20.** a) Block diagram of the CIDS scanning microscope. The red and green arrows correspond to the transmitted polarimetric and to the reflected fluorescence path, respectively.<sup>[374]</sup> b) An example of theoretical results about the presence of a spike-virus in a spherical droplet with size comparable to sars-cov2.<sup>[378]</sup> c) Use of the Phasor analysis to distinguish species on the basis of CIDS signature.<sup>[380]</sup> d) Normalized CIDS (blu) image of an isolated HEK nucleus after extraction compared with fluorescence intensity (green) signature based on DNA labeling.<sup>[374]</sup> Labels: Ti:Sa: Titanium-Sapphire coherent laser source tuned at 740 nm to prime both CIDS and two-photon excitation fluorescence. SU: Scanning Unit. PEM: Photoelastic Modulator at 50 kHz resonant frequency. Obj1: Microscope objective to image the sample. Obj2: Microscope objective used as a condenser to collect the transmitted light. GT: Glan-Taylor prism. APD1 and APD2: Avalanche Photodiode for +45° and -45° polarization detection after the GT. LA: Lock-in Amplifiers. LA#1 and LA#2: input channels of the LA, locked at 50 kHz from the reference signal of the PEM. The two APDs are both connected to each channel of the LA and also directly to the control unit. The terms “I +” and “I -” are the detected intensities +45° and -45° polarization projections after the GT, respectively. a,d) Adapted with permission.<sup>[374]</sup> Copyright 2018, The Authors, published by Optica Publishing Group. b) Adapted with permission.<sup>[378]</sup> Copyright 2021, The Optical Society.

the possible presence of a classified population in a friendly and effective way.<sup>[380]</sup> Figure 20c shows an example based on a population classification. Figure 20d shows the label-free ability of detecting a different compaction of chromatin in the cell nucleus using “classical” fluorescence DNA signature as benchmark.<sup>[374]</sup>

#### 11.4. Conclusion

Studies of nuclear architecture reveal that the dynamic properties of nucleic acids and proteins in the nucleus are critical for their function. In the case of labeling with fluorescent molecules of different sizes, despite the essential spectroscopic and morphological information that one can collect at an unprecedentedly available temporal and spatial resolution, one has two aspects that are worth to be considered, namely: 1) the crowded condition of high-density biopolymers increases producing an expected effect in terms of mobility and organization; 2) not always one can fluorescently label a sample, especially within a clinical perspective. CIDS can sense the conformation of biological macromolecules and identification of viruses of clinical signif-

icance at the nanoscale offering a map that is comparable to the one built using super resolved localization of fluorescent tags. The coupling with artificial intelligence algorithms and super-resolved fluorescence microscopy approaches offers the chance of performing an interesting training of supervised machine learning programs towards the transformation of label free images into super resolved ones, for example using a CNN (Convolutional Neural Network) operating on CIDS and fluorescence maps stemming from the very same sample.<sup>[182, 381]</sup> Since CIDS and other polarization related parameters demonstrated the ability to provide information related to the molecular level, one can predict that polarization-based contrast mechanisms will soon play an important role in cell and molecular biophysics. Moreover, CIDS applications range from those instruments using synchrotron radiation and ordinary sources<sup>[368]</sup> from virus identification to organizational motifs of chromatin in the cell nucleus allowing to access structural information from atoms to surfaces, from single cells to tissues and organs in a label-free way.<sup>[382]</sup> Other elements of the Mueller matrix offer the very same chance of CIDS pending a model establishing the relationship between label-free and fluorescence imaging.<sup>[370, 373, 374, 89]</sup>

## 12. Super-Resolved Off-Axis Holographic Multiplexing

(Natan T. Shaked\*)

### 12.1. Status

Super-resolved quantitative imaging of rapid dynamic biological processes with fine spatial details and without labeling is of interest for many medical, biological, and biophysical studies. Holographic imaging uses interference to acquire the complex wave front of a sample, containing both its amplitude and quantitative phase profiles, where the latter represents the structure of the sample. In transmission imaging mode, the quantitative phase is proportional to the optical path delay of the sample, which is equal to the product of the sample thickness and its refractive index, enabling visualization of mostly transparent biological samples, which have only small absorption, such as biological cells *in vitro*, in a meaningful contrast without using cell labeling. Holography is diffraction limited, as many other optical imaging techniques, and various techniques of super-resolution can be integrated with holographic imaging, thus gaining not only amplitude super-resolution, but also label-free quantitative-phase super-resolution. Generally, there are two main approaches to holographic wave-front acquisition. In on-axis holography,<sup>[383]</sup> the two beams interfere with no angle between them, which causes mixing of the sample and reference beam intensities with the complex wave front of the sample. Therefore, this approach requires acquisition of three or four phase-shifted holograms of the same sample instance in order to isolate the sample complex wave from the unwanted waves. If these holograms are acquired sequentially, at different times, fast dynamic processes cannot be recorded. If these holograms are acquired together, three or four camera planes are needed, requiring extended sensor sizes with slower frame rates, and causing registration problems between the different camera planes. Alternatively, parallel on-axis holography can be implemented by more complicated camera setups such as using pixel division.<sup>[384]</sup>

Off-axis holography<sup>[385]</sup> captures the complex wave front of the sample within a single camera exposure, which is highly relevant for quantitatively acquiring dynamic samples. This is done by inducing a small angle between the sample and reference beams creating the interference pattern of the hologram. This single-exposure mode is possible since in the spatial-frequency domain, there is a full separation between the auto-correlation (DC) terms, or the sample and reference beam intensities, and each of the cross-correlation (CC) terms, each of which contains the complex wave front of the sample. This spatial-frequency separation typically occurs across a single axis, which allows compressing additional information across the other axes as well. This can be done by optical multiplexing of several holograms with different interference fringe orientations into a single multiplexed hologram, acquired in a single camera exposure, and full reconstruction of the complex wave fronts encoded. Each of these complex wave fronts can contain additional information from the imaged sample, meaning that multiplexing allows recoding more information with the same number of camera pixels. This is highly beneficial for highly

dynamic samples that need to be recorded without multiple camera exposures. The multiple wave-front information multiplexed into the hologram can be used to obtain super-resolution by illuminating the sample from different angles and building a synthetic aperture that is larger than the one provided by the optical system. Thus, although the microscope objective can pass only limited spatial-frequency content of the sample due to a limited numerical aperture, passing simultaneously different angular perspectives of the sample through the microscope objective, each of them encodes different spatial-frequency content of the sample, can be used to reconstruct a larger synthetic aperture, eventually achieving a super-resolved reconstructed wave front. Holographic multiplexing is the mechanism that enables separation of the different spatial-frequency contents from the simultaneous angular channels, allowing the correct reconstruction of the super-resolved wave front of the sample.

Early implementations of simultaneous super-resolution by synthetic aperture by multiplexed holography used ultrasonic light diffractor to generate small diffraction angles, hence obtained a low synthetic aperture.<sup>[386]</sup> Later on, Leith et al.<sup>[387]</sup> used a spatially incoherent source and diffraction gratings to obtain simultaneous super-resolution holographic imaging across a single dimension. Mico et al.<sup>[388]</sup> used a vertical-cavity surface-emitting laser (VCSEL) array to constitute individually coherent sources that are mutually incoherent, so that each tilted beam provided a separate spatial-frequency content of the sample and interfered with the coinciding reference beam in one-dimensional holographic multiplexing geometry.

Figure 21 presents the off-axis holography process and how it can be used to obtain super-resolution by simultaneously capturing an increased synthetic aperture, which is larger than the one provided by the optical system. This is done by optical multiplexing of several complex wave-fronts together, while sharing the camera grayscale dynamic range, which brings to negligible errors for mostly transparent phase objects.<sup>[389]</sup> As shown in Figure 21a from left to right: in regular off-axis holography, the sample is illuminated by a single beam S1 and is magnified by a microscope objective MO; a mutually coherent clear reference beam R is superimposed with the sample magnified image on a digital camera at a small off-axis angle; where an off-axis hologram with straight parallel fringes is created; this hologram is digitally Fourier transformed, resulting in central DC terms and a pair of shifted complex-conjugate CC terms; one of the CC terms is cropped and centered; and inverse Fourier transformed, resulting in the complex wave front (amplitude and quantitative phase) of the sample, which is limited by the numerical aperture of the system. The quantitative phase enables visualizing biological samples in a label-free manner. In Figure 21b, to increase the resolution by simultaneous synthetic aperture, multiplexing two complex wave fronts into a single off-axis hologram is performed. From left to right: the sample is illuminated from two angles by S1 and S2, each collecting a different spatial-frequency content from the sample; the magnified sample images are superimposed with a reference wave R on the camera, and captured by the camera in a single exposure; where a multiplexed off-axis hologram is created; after a digital Fourier transform, we obtain the central DC terms, two pairs of shifted CC terms, and unwanted cross-terms CCx, none of which overlaps with the other terms; two cropped CC terms, CC1 and CC2, are positioned

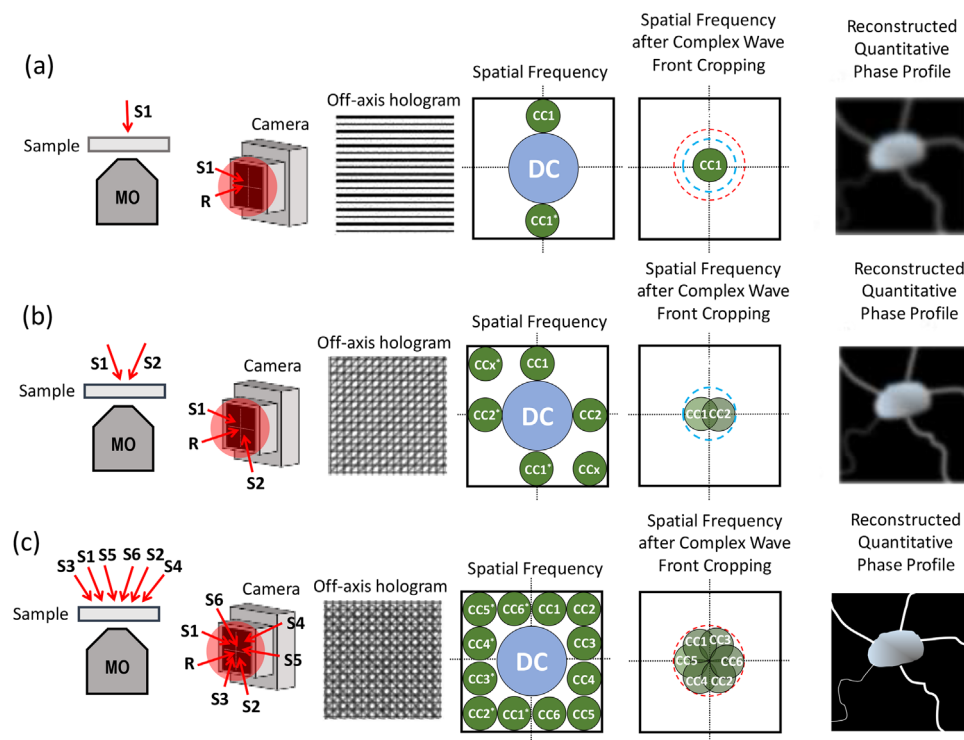


**Figure 21.** Principles of label-free quantitative imaging with super-resolution by off-axis holography. a) Regular off-axis holography. b) Multiplexing two wave fronts into a single hologram. c) Multiplexing six wave fronts into a single hologram.

in the spatial-frequency domain, so that the numerical aperture is synthetically increased.; after an inversed Fourier transform, we obtain the complex wave front of the sample with increased resolution. From this wave front, we can extract the quantitative phase profile of the sample, which requires two-dimensional phase unwrapping digital processing to avoid  $2\pi$  ambiguities, or experimentally acquiring the sample with several wavelengths and generating a larger synthetic wavelength.<sup>[390]</sup>

## 12.2. Current and Future Challenges

The size of the synthetic aperture directly affects the resolution of the reconstructed image. Constructing large synthetic apertures requires collecting many angular projections. Highly dynamic samples require simultaneous collection of all angular projections. Recent implementations provided off-axis holographic multiplexing of up to six simultaneous wave-front channels, each carries different spatial-frequency content from the sample, and all are acquired in a single camera exposure, which can then be reconstructed to an extended synthetic aperture and the super-resolved image.<sup>[90]</sup> As shown in Figure 21c from left to right, six beams S1–S6 illuminate the sample from different angles, each capturing a different spatial-frequency content of the sample; these beams are superimposed on the camera with a reference beam R, resulting in a six-pack multiplexed off-axis hologram; digitally Fourier transforming this hologram results in the central DC terms and six pairs of shifted CC terms, assuming that unwanted cross-terms are avoided, all of them efficiently occupying the entire spatial-frequency domain without

overlaps; CC1–CC6 are cropped and positioned in the spatial-frequency domain, isotopically for optimal resolution increase, so that an extended synthetic aperture is constructed; after an inverse Fourier transform, we obtain the super-resolved complex wave front of the sample. Six is the maximum number of wave fronts that can be multiplexed for optimal spatial-bandwidth consumption, without overlap of CC terms in the spatial frequency domain. Alternatively, when imaging sparse samples, more than six complex wave fronts can be multiplexed.<sup>[90]</sup> The resolution enhancement analysis and its limit in synthetic aperture setting have been discussed elsewhere.<sup>[95]</sup>

For multiplexing multiple wave fronts into a single hologram, we need to avoid unwanted cross-terms between nonmatching pairs of beams, which might overlap with the wanted terms and diminish the capability for full multiplexing. An example of a pair of unwanted cross-terms between the two sample beams themselves, created when multiplexing two wave fronts, is shown in Figure 21b, where the unwanted cross-terms appear across the diagonal direction on the spatial-frequency domain. This problem might become critical when more than two wave front channels are multiplexed, due to possible overlaps between the various terms.

Another issue is that even without overlaps of terms in the spatial-frequency domain, there is a risk of loss of information since multiple off-axis fringe patterns share the same dynamic range of the camera grayscale levels.

Finally, the current setups of off-axis holographic multiplexing are bulky, expensive, require optical expertise to align and use, and are sensitive to mechanical vibrations, making them less attractive for working in biological labs and medical clinics.

### 12.3. Advances in Science and Technology to Meet Challenges

Regarding the first problem, there are three possible solutions in order to avoid unwanted terms in holographic multiplexing: using different polarizations, using different light sources or wavelengths, and using coherence gating.

Beams of orthogonal polarizations do not interfere with each other. Therefore, it is possible to encode the wave fronts to different polarization states, and use polarizers after the sample to separate the channels to different interference fringe orientations on the camera. This solution, however, allows multiplexing up to four wave front channels, due to the lack of more than two orthogonal polarization states.

Using different illumination wavelengths for each sample and reference beam pair is a more valid solution for avoiding unwanted cross-terms. Color filters can be used after the sample to split each beam pair of a different wavelength to create another interference fringe orientation on the camera.

A different solution to the problem of unwanted cross-terms is based on utilizing the low-coherence properties of the light source. Here, we can avoid the unwanted cross-terms by making sure that the path difference between nonmatching pairs of beams is longer than the coherence length of the source, and therefore they do not interfere on the camera. This can be obtained by newly develop two-dimensional VCSEL arrays or other sets of coherent sources which are mutually incoherent. Another solution is using a super-continuum source with a tunable filter as a low-coherence source with delay lines in the optical paths (such as glass windows of various thicknesses), which create a different beam path for each pair of sample and reference beams. Here again, nonmatching sample and reference beams will not create interference, thus avoiding unwanted cross-terms between the imaging channels. More-elegant solutions might be developed with the introduction of new, controllable low-coherence sources, as well as specialized two-dimensional diffraction grating to split the beams in the optical system with inherited optical path delays.

Regarding the second problem of several imaging channels that share the same dynamic range of the camera, it is expected to be less critical for phase objects, such as biological cells in vitro and thin elements tested in optical metrology, which are mostly transparent, thus inducing minimal reconstruction-quality loss. When the amplitude of the sample becomes non-negligible, solving this problem requires cameras with larger bit depth. The signal-to-noise ratio (SNR) of the reconstruction when using 8-bit cameras versus 16-bit cameras for off-axis holographic multiplexing was quantified in Ref. [389] The introduction of rapid digital cameras with large bit depths is expected to significantly improve the ability to multiplex the maximum number of possible wave-front channels with minimal SNR decrease.

The third problem of bulkiness, meticulous alignment, and sensitivity to vibrations is expected to be solved by the introduction of nearly common-path modules, which are portable to existing imaging systems. Rather than splitting the reference and sample beams right after the light source,<sup>[385, 391]</sup> dictating bulky, complex and vibration-sensitive imaging setups, these modules create the reference beam from the sample beam itself, yielding more portable setups that are less sensitive to vibrations, inex-

pressive, and easier to align and use, even in clinical setting. Off-axis multiplexing of two and three wave-front fields of view of the samples has been implemented recently with these compact external interferometric modules,<sup>[392–395]</sup> but their application for super-resolution holographic imaging with synthetic aperture, as well as multiplexing of more than three wave-front channels inside these compact modules, are yet to be achieved.

One of the high-impact medical applications for off-axis holographic multiplexing is label-free super-resolved imaging flow cytometry that requires imaging several thousand of cells per second during rapid flow, due to its ability for high-resolution image analysis of a large number of cells during rapid flow, for liquid samples obtained from body fluids.

### 12.4. Conclusions

Simultaneous wave-front acquisition is a powerful tool for label-free super-resolution imaging of dynamic samples, creating quantitative contrast even for mostly-transparent samples, such as biological cells in vitro. Super-resolution in this setup can be obtained by multiplexing several wave fronts, each of which samples a different spatial-frequency content of the sample, into the same camera image. Each of these wavefronts is optically encoded into an off-axis interference pattern, with fringes oriented differently. Following the multiplexed off-axis hologram acquisition, a synthetic aperture of larger spatial-frequency content can be reconstructed, thus obtaining super-resolved imaging. By avoiding unwanted cross-terms of non-machining interference patterns and using cameras with large bit depths, up to six simultaneous wave-front channels can be reconstructed. By using external portable modules, these systems are expected to become more available and affordable, providing new rapid super-resolved label-free quantitative imaging capabilities for clinical diagnosis and biological assays.

## 13. Tomographic Diffractive Microscopy

(Bertrand Simon\*, Nicolas Verrier, Matthieu Debailleul, Olivier Haeberlé)

### 13.1. Introduction

Conventional optical microscopy is mostly used as a simple imaging tool, for detection of features, or morphological measurements. This is because the complex interaction of light with the observed sample usually translates into intensity-only images. Also, resolution is still limited in far-field optical microscopy (except for fluorescence microscopy). We here present tomographic microscopy, an extension of Digital Holographic Microscopy, emphasizing its true 3D imaging capabilities, its ability to retrieve the complex index of refraction distribution within the observed sample, also achieving this with an improved resolution compared to conventional intensity-only microscopies. Common configurations are described and future evolutions are presented, as well as challenges this technique still faces.



### 13.2. Early Developments

For unlabelled samples, things changed with the invention of Gabor holography.<sup>[250]</sup> Allowing for precise measurement of amplitude and phase of a diffracted field, holography paved way for quantitative measurements of optical constants at microscopic level. Seminal paper by Wolf<sup>[248]</sup> has established the relation linking the diffracted field to the index of refraction distribution creating this field. The classical treatment starts from the Helmholtz equation in an inhomogeneous medium, introducing  $n$  as the complex refractive index of refraction and  $\lambda$  as the wavelength in vacuum. For weakly diffractive specimens, considering that the first Born approximation is valid, the diffracted field amplitude  $e$  is small compared to the incident field of amplitude  $A_{inc}$ , which finally leads to write in Fourier space<sup>[91]</sup>:

$$e(\mathbf{k}, \mathbf{k}_{ill}) = 8\pi^3 A_{inc} k_0^2 \tilde{N}(\mathbf{k} - \mathbf{k}_{ill}) \quad (18)$$

Here  $k_0 = 2\pi/\lambda$ ,  $\mathbf{k}_{ill}$  is the wavevector of the illumination, and  $\mathbf{k}$  represents the diffracted wavevector. This equation provides direct correspondence between the diffracted far-field amplitude  $e(\mathbf{k}, \mathbf{k}_{ill})$  in direction  $\mathbf{k}$ , from  $\mathbf{k}_{ill}$  illumination, and the Fourier coefficient of the relative permittivity of the object  $\tilde{N}(\mathbf{k} - \mathbf{k}_{ill})$ : when Born approximation holds, the diffracted field depicts a subset of the 3-D Fourier transform of the sample permittivity distribution. In linear scattering and with momentum conservation, this subset of  $\mathbf{k}_{obj}$  is simply constructed using the fundamental equation:  $\mathbf{k}_{obj} = \mathbf{k}_{diff} - \mathbf{k}_{ill}$ , and implying energy conservation  $\|\mathbf{k}_{diff}\| = \|\mathbf{k}_{ill}\|$ .

However, despite some promising early results,<sup>[396, 397]</sup> the technique did not attract the interest of the community. This can be explained by the cost or non-availability of lasers, CCDs and computers at that time to acquire and process data.

### 13.3. Status

Situation has changed at the beginning of the new millennium, reviving the domain,<sup>[256, 398, 399, 95]</sup> which has experienced growing development in recent years. Implementations of the technique have been very diverse, emphasizing the advantages and drawbacks of its various configurations. **Figure 22** describes the construction of the Optical Transfer Function (OTF) support for transmission configurations in Digital Holographic Microscopy and several variants of Tomographic Diffractive Microscopy (TDM),<sup>[400]</sup> a technique also known as synthetic aperture microscopy, tomographic phase microscopy, holotomography, optical diffraction tomography, scanning holographic microscopy, optical microtomography, phase nanoscopy, holographic tomography...

*TDM with illumination rotation* (TDM-IR) is the most common. It has for main advantage that not having to rotate the sample makes it a more general approach, applicable to a large variety of samples. Conventional sample preparation between glass and cover glass, between cover glasses or in Petri dishes can be used. Furthermore, when high-resolution is targeted, use of high numerical objective-condenser configuration is mandatory. As a consequence, working distances are small, and inducing sample rotation in that case can be difficult. Rotating the illumination is on the contrary simple and can be performed in a variety

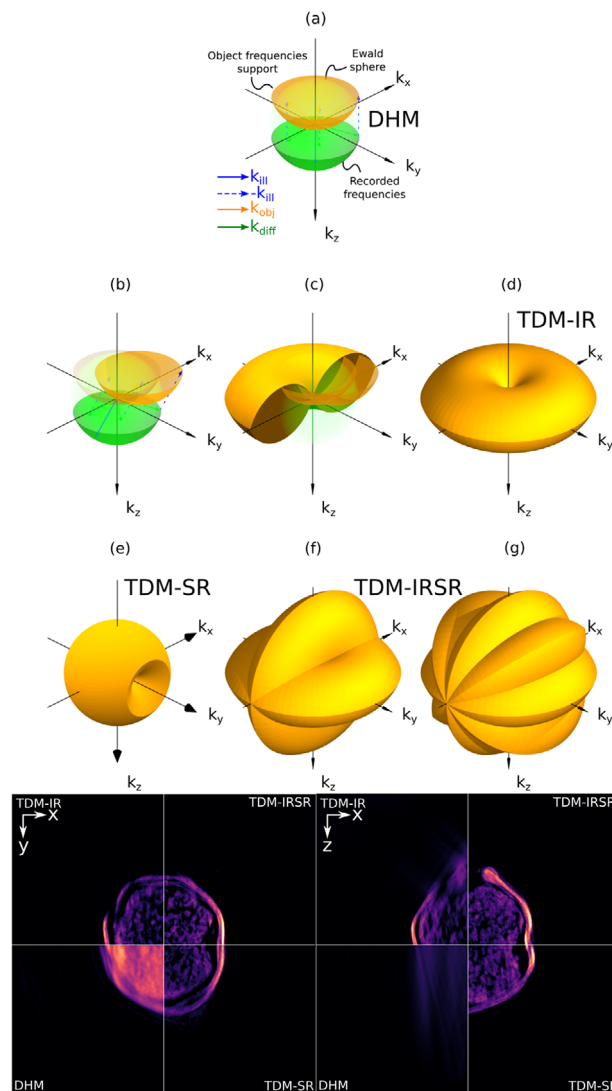


**Figure 22.** Optical Transfer Function (OTF) for various configurations in transmission TDM. a) Digital holographic microscopy: the OTF depicts a cap of sphere with large lateral, but limited longitudinal extension. b) With inclined illumination, same positions of  $\mathbf{k}_{diff}$  vectors provide new  $\mathbf{k}_{obj}$  vectors. c,d) With many illuminations, a filled, extended OTF is obtained. e) With sample-rotation, an almost completely filled sphere is obtained (but of lesser extension than in previous case). f,g) OTFs combining illumination and sample rotation with 2, and 4 evenly spaced specimen positions. Bottom row: *Betula pendula* pollen grain images in DHM and three TDM variants. Left composite image depicts x-y slice in the focal plane, showing improved resolution in TDM, but only twice that of DHM. Contrast is however better thanks to better optical sectioning. Right composite image highlights the large differences in imaging capabilities along the optical axis. Only TDM-IRSR can deliver true improved and isotropic resolution, while holography is not, strictly speaking, a true 3-D imaging method when considering transparent samples: only *optical thickness* can be measured.

of ways. Rotating mirrors,<sup>[398]</sup> rotating Pechan prisms,<sup>[396]</sup> galvanometric mirrors and fast tip-tilt mirrors<sup>[400]</sup> have been used. Alternately, pure optical means have also been successfully implemented, involving Spatial Light Modulators<sup>[401]</sup> or Digital Micromirror Devices.<sup>[402]</sup> A specific advantage of illumination rotation is that exact knowledge of the illumination direction is not

mandatory, as it can indeed be directly retrieved from the processing of the recorded holograms.<sup>[91][403]</sup> The main drawback of this approach is the peculiar form of its OTF, Figure 22c, which translates into strongly anisotropic resolution. While this approach indeed delivers the best lateral-resolution<sup>[403, 95]</sup> low sectioning capabilities result from the so-called missing-cone of unrecorded frequencies along the optical axis.

*TDM with sample rotation* (TDM-SR) on the contrary can deliver (almost) isotropic resolution as deduced from Figure 22e. The main difficulty in that case is to ensure accurate rotation of the sample. A simple and efficient approach can be to embed cells within a rotating capillary, but one has then to deal with curved optical surfaces, which may induce aberrations. In that case also, larger working distance are mandatory, leading to use of lower aperture objectives. Optical and acoustical tweezers have also been successfully used.<sup>[404]</sup> While more challenging, they allow using conventional sample preparation and use of high Numerical Aperture (NA), high magnification objectives. Cells being often polarized, electric oscillating field can also be used to induce rotation. In some cases, the sample itself can be directly rotated,<sup>[397]</sup> such as when characterizing optical fibres, to which samples can also be attached, or textile yarns, pulled-glass micropipettes, SNOM (Scanning Near Field Optical Microscopy) tips<sup>[400]</sup>... In some cases such as blood cells, one can even use their natural tendency to tumble when moving through microfluidic channels to perform microtomography.<sup>[262]</sup>

*Combining illumination with sample rotation* (TDM-IRSR) has also been proposed: an extended and fully filled OTF is obtained<sup>[400]</sup> (Figure 22f,g). This adds advantages of both above-mentioned TDM variants, however also combines their difficulties, which probably explains why it is not more popular.

The lateral and axial extensions of the OTFs for these configurations have been detailed in,<sup>[400]</sup> with  $\lambda$  the wavelength of observation,  $n$  the index of refraction of the immersion medium, and  $\theta$  the aperture collecting angle of the microscope (so that  $NA = n \sin\theta$ ):

$$\Delta v_{x,y}^{Holo} = \frac{2n \sin \theta}{\lambda} \quad \Delta v_z^{Holo} = \frac{n(1 - \cos \theta)}{\lambda} \quad (19)$$

For TDM with illumination rotation (IR) one obtains:

$$\Delta v_{x,y}^{TDM-IR} = \frac{4n \sin \theta}{\lambda} \quad \Delta v_z^{TDM-IR} = \frac{2n(1 - \cos \theta)}{\lambda} \quad (20)$$

With sample rotation (SR), one has:

$$\Delta v_{x,z}^{TDM-SR} = \frac{4n \sin(\theta/2)}{\lambda} \quad \Delta v_y^{TDM-SR} = \frac{2n \sin \theta}{\lambda} \quad (21)$$

and when combining both approaches, one gets:

$$\Delta v_{x,y,z}^{TDM-IRSR} = \frac{4n \sin \theta}{\lambda} \quad (22)$$

So, TDM provides two main advantages: firstly, it delivers quantitative images of the index and absorption within samples. Then, it allows for improved resolution compared to DHM, thanks to its extended support, and improved resolution compared to conventional microscopy, thanks to its (theoretically)

constant transmission OTF, while high frequencies are otherwise rapidly attenuated in intensity-only, conventional transmission microscopy.

*TDM with white light*<sup>[256]</sup> is another approach for tomography, consisting in using white light illumination and a SLIM (Spatial light interference microscopy) module.<sup>[405]</sup> When changing the k-vector norm in Figure 22a, the position of the detected cap of sphere is fixed, but its radius changes, so that the final OTF takes the shape of a bowl.<sup>[91][256]</sup> Similar results are obtained when varying the wavelength in a holographic microscope as in.<sup>[406]</sup> While the lateral resolution and axial sectioning capabilities are lower, the main advantage of this method is that it can be more easily implemented onto a conventional wide-field transmission microscope.

*TDM in reflexion mode* is also possible. While TDM in transmission is mainly used for studying transparent biological samples, TDM in reflexion has been developed for investigating surfaces and interfaces, e.g. for microelectronics device inspection. In that case, high index of refraction contrast and noticeable polarization effects have to be taken into account, but when appropriate inversion methods are implemented, those lead to the highest demonstrated resolution in label-free, far-field microscopy, with  $\lambda/10$  features successfully identified,<sup>[407]</sup> albeit requiring prior knowledge about the specimen's index of refraction to achieve such performances.

*Advanced image reconstructions:* in parallel with hardware development, very substantial efforts have been devoted to improving image reconstruction. The fastest approaches are based on direct Fourier transforms, under Born and Rytov approximations, but their application is limited to small samples exhibiting low index of refraction contrasts (see for example Refs<sup>[408, 409]</sup>). Iterative methods (re)computing both the reconstructed image and its spectrum, comparing it to the acquired data, such as the Gerchberg-Papoulis method allow for better reconstructions, but are more time consuming.

For thicker samples, samples with high index contrast, or sample inducing multiple scattering, one has to use more advanced methods, based on the propagation of the electromagnetic field through the sample.<sup>[410]</sup> This can be performed assuming samples properties to simplify computations. But in the most extreme cases, when considering thick samples with high index contrast, birefringence, or semi-conductor, or metallic samples, complete electromagnetic problem must be involved, using Finite Difference-Time Difference (FDTD) solver.<sup>[411]</sup> While these methods have proven being much more precise, and sometimes essential to get realistic results, it is at a strong cost in terms of computational power, memory and time. But with the continuous progress of computers in terms of processing power and memory, one can expect these advanced methods to be more widely used.

Then, in recent years, artificial intelligence and machine learning has also gained strong interest in the domain. A main advantage of these approaches is their efficiency at reducing missing-cone induced reconstruction artefacts.<sup>[412, 413]</sup> Convolutional Neural Networks (CNN) have been successfully used, as well as methods taking benefit from dictionary of structures. Skipping prior training is advantageous, but requires more computational effort. Conversely, large sets of properly labelled training images are difficult to constitute, and prior training is time consuming,

but then rapid reconstructions are possible when the network has been trained.

Finally, an interesting hardware-software joined development is the possibility to avoid interferometric measurements, by numerical reconstruction of the phase. This can be for example done from sets of intensity images, solving Transport of Intensity Equation,<sup>[414]</sup> or using wavefront analysers.<sup>[415]</sup> Doing so simplifies the microscope optical design, but transfers complexity towards numerical reconstruction of the amplitude/phase data from intensity only images.

### 13.4. Current and Future Challenges

In the last decade, TDM has turned from a promising technique into a well-established one to study microscopic specimens with a 3-D, label-free, and quantitative approach.

It has found applications in many fields, and is actively developed by several groups worldwide. Companies like TomoCube and NanoLive are now commercializing systems, for end-users not interested in instrumentation development.

But there are challenges not yet addressed to further improve the technique, and widen applications.

The importance of working with isotropic-resolution images is vastly overlooked. Even simple quantities as volumes are difficult to accurately measure at sub-micrometric scale in transmission-only TDM, because of the missing-cone problem.<sup>[400]</sup> Index of refraction or species concentrations are even more problematic. Demonstrated approaches to tackle this limitation require combining sample rotation with illumination rotation, and as a consequence are limited to freestanding specimens, while 4Pi<sup>[398]</sup> and mirror-assisted TDM<sup>[416, 417]</sup> are promising for all kind of samples, but have not yet been fully demonstrated.

The index of refraction in itself provides some selectivity, but the technique could be much more specific, if a full multimodal implementation of TDM would be available. Hyperspectral,<sup>[418, 419]</sup> polarized<sup>[398, 420]</sup> TDM could in principle add some chemical selectivity to imaging.

To study dynamic samples, or for high-throughput screening, possible in holographic, fluorescence and conventional staining microscopy, a real-time acquisition, reconstruction, and 3D display of the observed sample image would be very helpful (see Refs.<sup>[421, 422, 423, 424, 425, 247]</sup> and references therein). This will require important development to fasten acquisitions and numerical image computation.

Another direction of evolution of the technique will be the observation of large samples, in a similar way the development of SPIM (Selective Plane Illumination Microscopy) fluorescence microscopy has allowed going from cellular level to small organisms, organoids, embryos, or even small animals organs.

Finally, TDM is in fact still diffraction limited. The thriving development of fluorescence nanoscopy relies on nonlinearities such as saturation, or molecular switching, which are the keys to break the Abbe limit. But switching molecules have no equivalent in terms of index of refraction. Resolution under 100 nm in unlabelled optical microscopy relies on capturing the evanescent field by SNOM or with microsphere-assisted microscopy. But such techniques are by definition limited to surface imag-

ing. Obtaining true superresolution in TDM now represents the grand challenge in the domain.

### 13.5. Conclusions

Tomographic microscopy is gaining attention in biology, thanks to its capacity of imaging unlabelled samples at high resolution, with some specificity provided by quantification of the sample index of refraction (see recent reviews<sup>[247, 422–425]</sup> and references therein). Future developments could increase its domains of application towards material sciences, or metrology of micro-nanofabrication.

## 14. Scanning Near-Field Optical Microscope for Quantitative Nano-Imaging and Nano-Spectroscopy

(Sheng Wang\*, Mengkun Liu\*)

### 14.1. History and Status

Optical microscope and spectroscopy have been versatile and powerful characterization tools to study light-matter interactions in condensed matter and biological systems. Conventional optical techniques are constrained by the well-known Abbe diffraction limit, which restricts the spatial resolution to be approximately half the wavelength of the illumination light. Driven by vibrant research into quantum materials and molecular interactions at the nanoscale, researchers have been actively developing label-free and super-resolution nanoscopy with wide spectral energies spanning from below 0.1 meV to above 1000 meV. The idea of utilizing high-momentum components of evanescent waves to achieve subdiffractional imaging dated back to as early as late 1920s.<sup>[426, 427]</sup> Edward H. Syngé, starting in 1928, proposed a series of experimental schemes to collect the surface-bound electromagnetic field from a nanoscale orifice in a planar metallic film (Figure 23a) or from metallic particles (Figure 23b) placed within nanometers from the sample. The former concept formed the basis for the aperture-type scanning near-field optical microscope (a-SNOM, Figure 23c) and the latter one brought about the scattering-type scanning near-field optical microscope (s-SNOM, Figure 23d). However, the implementation of these ingenious proposals were hampered by various technical difficulties, notably the controllable placement of the nanoscale aperture in close vicinity of the sample and extraction of the weak nanoscale light from the overwhelming background. These technical hurdles had been later overcome with the invention of various scanning probe microscopes (SPM) including scanning tunneling microscope (STM) and atomic force microscope (AFM).

Prototypical aperture/waveguide based scanning probes achieving super-resolution imaging at visible and microwave wavelengths was demonstrated in the 1980s.<sup>[426, 427]</sup> Since then, steady improvement and perfection in SNOM techniques have been made. a-SNOM features great operation flexibilities with aperture/fiber/waveguide coupled near-field tips that can yield various types of experimental schemes and clean near-field signal extraction.<sup>[428]</sup> Notably, aperture waveguide method in terms

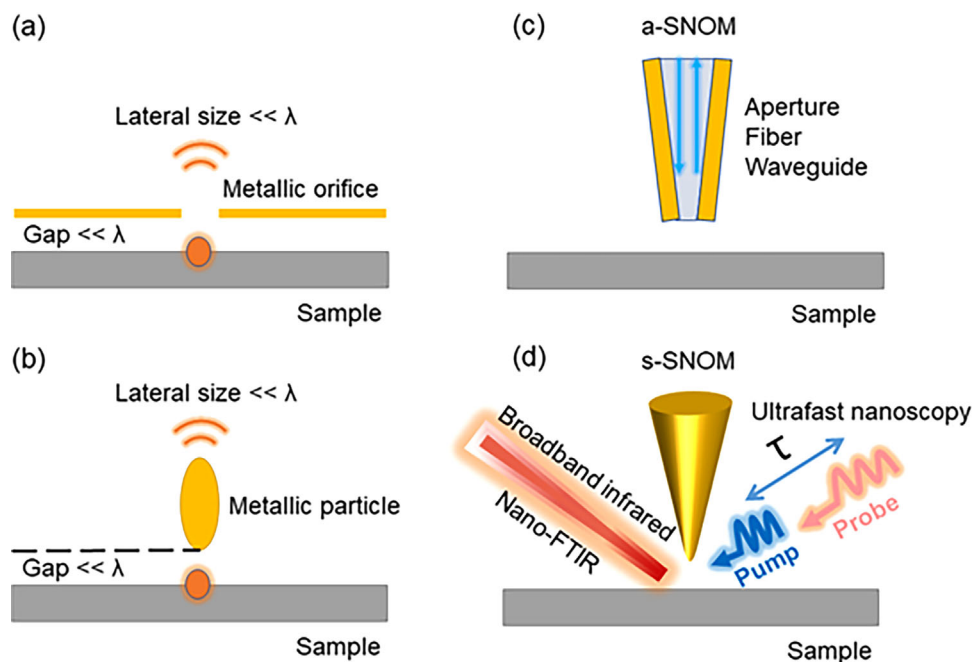


**Figure 23.** Schematic illustrations of scanning near-field optical microscope (SNOM). a) The original proposal of aperture-type SNOM (a-SNOM) by Edward H. Syngé. The nanoscale orifice can convert localized near field into propagating far-field wave. b) The original proposal of scattering-type SNOM (s-SNOM) by Edward H. Syngé. The metallic nanoparticle can scatter localized near field into propagating far-field wave. c) Modern a-SNOM based on a scanning probe microscope with an aperture/fiber/waveguide coupled near-field tip. d) Modern s-SNOM based on a tapping-mode atomic force microscope. The integration of Fourier-transform infrared spectroscopy (FTIR) with s-SNOM gives rise to Nano-FTIR. The integration of pump-probe spectroscopy with s-SNOM ends up as ultrafast nanoscopy, which combines nanometer spatial resolution with femtosecond temporal resolution.

of impedance-matched coaxial cables has been leveraged to efficiently guide microwave radiation to the tip apex for near-field interaction with the sample. This configuration at microwave regime is commonly referred to as scanning microwave impedance microscope (sMIM) and can routinely image sample conductivity and permittivity at a spatial resolution of  $\approx 20\text{--}100\text{ nm}$ .<sup>[429]</sup> s-SNOM at infrared frequencies started to gain momentum in the 1990s with the development of broadband light sources and the need for their integration.<sup>[38, 426, 427]</sup> The active modulation of tip-sample distance and subsequent high-harmonics demodulation of the scattering optical signal substantially suppress the background scattering and can achieve a spatial resolution of  $\approx 10\text{--}20\text{ nm}$  in routine operation. Due to the scattering nature, s-SNOM working in visible, infrared (IR), and terahertz (THz) wavelength regimes have been developed and employed to characterize a wealth of optical phenomena.<sup>[38, 430–433]</sup> Importantly, the pseudo-heterodyne detection scheme has been developed for background-free near-field spectroscopy. This scheme simultaneously retrieves near-field optical signal amplitude and phase by interferometric detection of scattered light utilizing a phase-modulated reference wave.<sup>[434]</sup> When the tip-sample convolution effects are considered with sufficient modeling, complex dielectric functions of the sample can be obtained in a quantitative fashion.<sup>[38, 435]</sup>

Diffraction-limited optical spectroscopy methods can be naturally extended to deep subwavelength resolution when integrated with SNOM.<sup>[38, 431]</sup> The integration of Fourier-transform infrared spectroscopy (FTIR) with s-SNOM gives rise to Nano-FTIR (Figure 23d), which allows broadband infrared nano-

spectroscopy with nanometer spatial resolution ( $< 20\text{ nm}$ ).<sup>[431, 436]</sup> Nano-FTIR has proven to be a powerful analytical tool to probe low-energy excitations and correlations in complex heterogeneous solid matter and molecular vibrational fingerprints in biological specimens. The integration of s-SNOM with ultrafast time-resolved techniques such as pump-probe spectroscopy is of utmost interest because it enables the interrogation of non-equilibrium dynamics of quantum materials at the nanoscale (Figure 23d).<sup>[431, 432]</sup> This ultrafast nanoscopy has been successfully developed for some spectral ranges and has provided unique insight into the dynamics of polaritonic modes of van der Waals semiconductors.<sup>[430–432, 437]</sup> While SNOM is facile to operate in ambient conditions, a cryogenic environment has also been realized to study temperature-sensitive effects such as phase transitions and electron–phonon coupling in quantum materials.<sup>[38, 438, 439]</sup>

## 14.2. Current and Future Challenges

There have been multiple ongoing forefronts of extending the capabilities of SNOM. One is the realization of multimodal SNOMs, which interface optical nano-imaging with nanomechanical and nanoelectrical mapping to better unravel the structure-property relationship of nanomaterials. The correlative nano-imaging serves to examine the intriguing interplay between photo-excitations, electronic properties, and mechanical responses in heterogeneous materials, such as photoinduced electrical and mechanical effects in organic-inorganic perovskites



and two-dimensional materials.<sup>[440, 441]</sup> The differing SPM operation modes for different types of characterizations make it challenging to achieve a multifunctional SNOM. s-SNOM is based on a tapping-mode AFM with moderate modulation of the tip-sample distance. On the contrary, nanomechanical and nanoelectrical methods usually require intimate contact between the tip and the sample. Consequently, complex tip manipulation or multipath scanning methods are usually required.

Another forefront is the integration of various conventional far-field optical spectroscopy techniques with SNOM. Broadband spectroscopy spanning from visible to THz requires optimal tip geometries and sizes for different wavelengths. The commercially available metallic AFM tips (e.g., PtIr-coated tips) usually have the best performances in the infrared range because the tip configuration offers optimal field enhancement with mid-IR illuminations (e.g., CO<sub>2</sub> laser at 10.6 μm).<sup>[433, 436, 439]</sup> Specially designed tips are therefore largely mandatory at visible and THz frequency ranges for achieving higher detection sensitivity and signal-to-noise ratio (SNR). In ultrafast pump-probe SNOM, low SNR is also a major concern due to the nominally weak pump-induced change in the near-field probe signal.

In-liquid and in-situ infrared vibrational nano-spectroscopy can provide intrinsic, label-free nanoscale chemical information on biological, chemical and electrochemical processes in aqueous environment. However, strong broadband IR absorption from vibrational and rotational modes of liquid water and aqueous solutions presents a large undesirable background.

Magneto-optical spectroscopy is instrumental in investigating topological photonics and magnetoplasmonics. SNOM operating in high magnetic fields for magneto-optical nano-spectroscopy has so far remained elusive. A significant barrier to the practical realization of a magnetic SNOM is the efficient optical open access to a cryogenic sample-scan AFM in ultrahigh vacuum (UHV) chambers.

Lastly, the quantitative analysis and interpretation of SNOM data have been nontrivial because detailed fitting and stringent modeling are usually required to include the intricate convoluted tip-sample effects.<sup>[38, 428, 429, 435]</sup>

### 14.3. Advances in Science and Technology to Meet Challenges

The development and perfection of diverse SPM configurations pave the way for a multimodal SNOM. A frequency-modulation Kelvin force probe microscope based on a tapping-mode AFM can be seamlessly combined with s-SNOM, providing simultaneous surface potential and optical responses at nanoscale resolution.<sup>[440]</sup> AFM operating in peak force tapping mode offers delicate control of the interaction force between tip and sample, enabling robust tip-sample intimate contact and large modulation in one cycle. Careful interfacing SNOM with peak force mode promises a multimodal SPM capable of correlative nanoscale optical, electrical, and mechanical mapping for cross-domain research.<sup>[441]</sup> In the quest for a magnetic SNOM, tremendous efforts are underway to customize a sample-scan cryogenic AFM in a high magnetic field in order for easy access to optical excitation and detection. An alternative approach is guiding light via a tapered conical fiber tip in a tip-scan a-SNOM or s-SNOM in a cryogenic UHV chamber with a high magnetic

field, hence obviating the need for external optical open accesses. To circumvent the unavoidable water IR absorption background for in-liquid SNOM, graphene-encapsulated liquid cells have been developed as a thin IR-transparent membrane to separate AFM operating in air and the liquid phase. IR s-SNOM with in-liquid AFM operation and optimized total internal reflection excitation has been demonstrated as a universal approach to infrared nano-spectroscopy in native aqueous environment due to enhanced signal emission and minimized water IR absorption and far-field background.<sup>[442]</sup>

Advances in electromagnetic modeling and nanofabrication have enabled on-demand tip engineering for specific purposes. Quantum and nonlocal effects have been included in nanophotonic modeling to provide more accurate predictions on local field enhancement and tip-sample near-field interaction.<sup>[443]</sup> The improved simulation results offer crucial guidance for controllable and cost-effective nanofabrication of desired near-field tips. For visible illuminations, tip apex nanostructure can be properly designed to leverage plasmonic resonance effect to enhance near field and elevate detection sensitivity. The tip length at THz range needs to be critically engineered for the tip to function as an efficient optical antenna for s-SNOM operation.<sup>[430]</sup> For a-SNOM, an advanced campanile probe composed of a metal-dielectric-metal waveguide to efficiently guide light to the apex has been shown in both simulation and experiment to be reasonably broadband and highly efficient for spectroscopic nano-imaging.<sup>[444]</sup> Tip engineering is also conducive to ultrafast pump-probe SNOM. A smart tip design can offer optimal near-field enhancement for both the pump and probe lights. In addition, proper tip engineering can boost lateral sensitivity for measurements of the in-plane photoresponse. The on-demand tip design and fabrication are markedly powerful yet far from easy. Further improvement and perfection are needed to achieve reliable and reproducible tip engineering for versatile applications.

Beyond rigorous analytical models,<sup>[38, 435]</sup> recent progress on data-driven machine learning (ML) methods can partially tackle the complex tip-sample convolution problems in s-SNOM.<sup>[445]</sup> An artificial neural network can be trained to learn the correlation between the sample's dielectric function and the experimentally measured near-field signal using a limited set of nano-spectroscopy data. The ML method enables fast and robust extraction of quantitative material properties from tip-specific raw data without sophisticated finite-element numerical simulations.

Part of the challenges and prospects are summarized in **Figure 24**. Note that due to the limited scope of this section and the limitations of the authors, Figure 24 is by no means an exhaustive roadmap and serves merely as a guiding resource.

### 14.4. Conclusions

SNOM technique has been progressively perfected as a regular and robust nano-imaging and nano-spectroscopy instrument, which serves to reveal quantitative structure-property relationship at the nanoscale. While challenges remain in the interfacing with other SPM modalities and in the integration with various far-field optical techniques, researchers have paved plausible pathways en route to a broadband and multimodal nanoscale

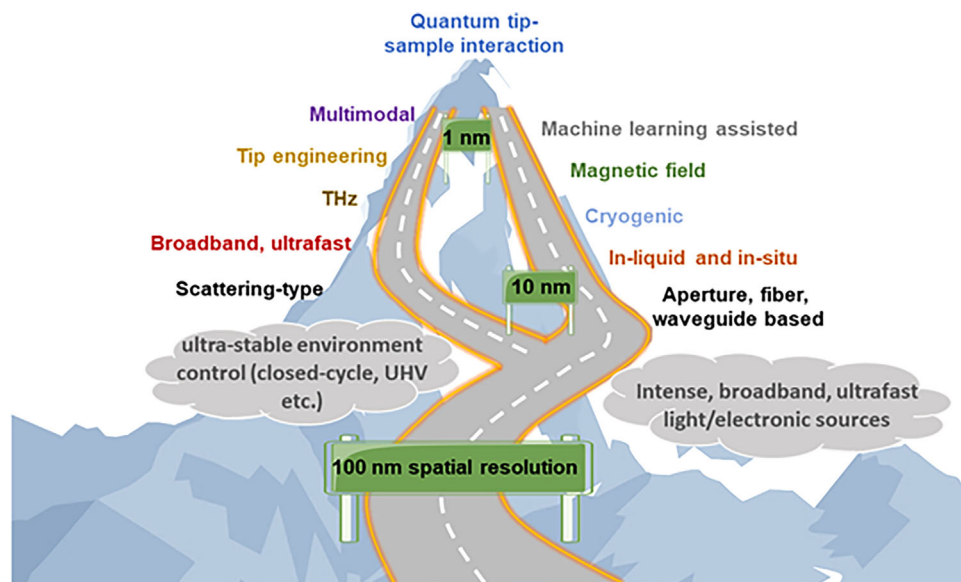


**Figure 24.** Pathways en route to broadband and multimodal SNOM for quantitative nano-imaging and nano-spectroscopy.

characterization platform. With the exciting new technological and theoretical advances, SNOM technique is poised to become an essential label-free and quantitative nanoscopy method with exceptional spatial, temporal, and spectral resolution.

### Theme III: Nonlinear Optics Approaches

#### 15. Absorption-Based Super-Resolution Imaging

(Yeran Bai, Ji-Xin Cheng\*)

##### 15.1. Status

Super-resolution microscopy enables the visualization of previously unseen details in conventional imaging where the illumination light cannot be focused smaller than the diffraction limit. Due to the widespread application of fluorescence imaging in biomedical research, the majority of efforts in super-resolution imaging have been pursued along the direction of fluorescence nanoscopy.<sup>[9]</sup> However, fluorescence imaging suffers from issues including photobleaching, phototoxicity, and perturbation to intracellular functions. On the contrary, the absorption happens universally in light-matter interactions, hence allowing label-free detection. Based on electronic transition and vibrational transition, UV-Vis and infrared (IR) absorption spectroscopy have found broad applications in chemistry, biomedical and material science.<sup>[446, 447]</sup> Despite its rising popularity, the spatial resolution in absorption-based imaging remains to be diffraction-limited. To address the unmet need to improve the spatial resolution of absorption-based imaging, many methods have been proposed. The first category is near-field IR absorption spectroscopy. By utilizing a nanometer-sized aperture or an atomic force microscopy (AFM) tip, near-field IR spectroscopy has been demonstrated with nanometer resolution and high sensitivity down to single-molecule level.<sup>[448, 449]</sup> In AFM-IR nanoscopy, a AFM tip is used to

sense the absorption-induced thermal expansion. The IR spectra with nanometer spatial resolution are obtained by sweeping the IR light to different wavelengths and record the tip oscillations. The second category is termed optical photothermal detection (Figure 25), where the pump beam is selected at the absorption peaks of the analyte, and the probe beam is selected outside the absorption range.<sup>[450–452, 65]</sup> For molecules with high absorption coefficient but low quantum yield, the absorbed energy is converted into heat, which causes a localized temperature increase. Since the physical property including volume and refractive index are dependent on temperature, the local environment experiences a transient change due to the photothermal process. The probe beam passing through the sample carries the modulation by the environment, which can be detected through lock-in or optical phase measurement. For the electronic state photothermal detection, a nearly threefold increase of spatial resolution compared to diffraction limit has been demonstrated for nanoparticles with non-linear absorption when the pump beam exceeds the linear absorption fluence threshold.<sup>[450]</sup> For vibrational state photothermal detection, various efforts have been demonstrated to break the diffraction limit of the IR pump beams. Since the spatial resolution is determined by the probe beam in the photothermal imaging, one order of magnitude increase over the diffraction-limited resolution has been demonstrated with a visible or near-IR probe beam.<sup>[451, 452, 65]</sup> The development of IR photothermal imaging also enables unprecedented performance in label-free chemical imaging for live cells in the aqueous environment at the sub-micrometer resolution.<sup>[453, 454, 65]</sup> The third category is based on ground-state depletion in transient absorption processes. The pump beam is split into two arms with one arm temporally modulated but spatially unmodified; while the other arm is sent to a spatial light modulator to create a doughnut-shape beam shape. When these two pump beams combine with the modulated probe beam and sent to a sample, super-resolution imaging is achieved at the very center of the focal spot.<sup>[66]</sup>

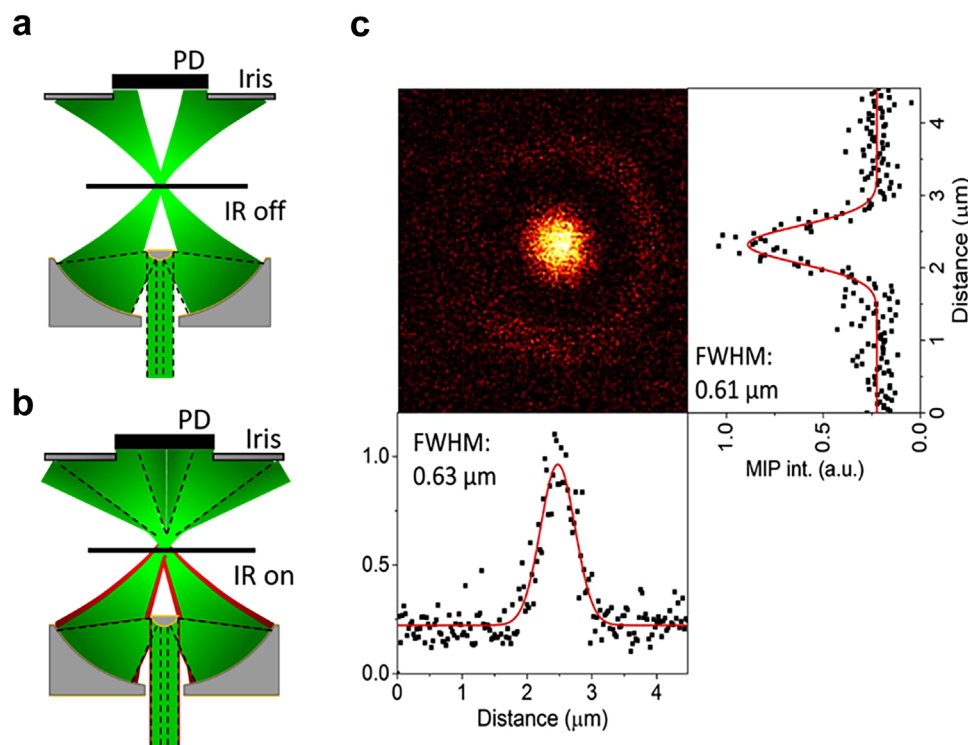


**Figure 25.** Concept and spatial resolution characterization of IR photothermal imaging. a) Visible beam propagation geometry when the IR beam is off. b) When the IR light is on, the photothermal effect leads to deflection of the visible beam. c) IR photothermal imaging of a 500-nm polymer bead. The horizontal and vertical line profile cross the center of the bead indicating a sub-micrometer spatial resolution. Adapted with permission.<sup>[65]</sup> Copyright 2016, The Authors, some rights reserved; exclusive licensee AAAS. Distributed under a Creative Commons Attribution NonCommercial License 4.0 (CC BY-NC).

## 15.2. Current and Future Challenges

Although the near-field methods have provided the highest spatial resolution so far, the low imaging throughput restrains broader applications of these methods. On the contrary, far-field methods greatly improve the speed and the field of view. A typical acquisition time get a single-cell image is about tens of seconds with the pixel dwell time of 1 to 30 ms for a scanning geometry.<sup>[451, 65]</sup> However, to observe highly dynamic samples, higher imaging speed is expected. Additionally, the pump-probe signal is only generated at the overlapped area of the two beams. For IR photothermal imaging, the focal spot between the IR pump and visible probe has one order of magnitude difference and thus only about 1% IR photons contribute to the signal generation.

In addition to the need for further increasing photon budget and push imaging speed, depth-resolved imaging is also required for most biological-related research. The near-field methods are restricted to characterize the surface of the samples. For nonlinear absorption, since it requires overlap of two tightly focused beams to produce a signal, depth-resolved imaging can be realized in scanning the foci in 3D.<sup>[450, 66]</sup> The depth-resolved IR photothermal imaging has also been demonstrated in the same manner.<sup>[65]</sup> On the other hand, it is harder to achieve depth-resolved imaging in widefield modalities since the beams are not tightly focused.

To facilitate the adoption of super-resolution methods to biologists, multimodal imaging capacities are needed. Although IR spectroscopy provides fingerprints of the analyte, the specificity for certain intracellular organelles or certain proteins still needs further exploration. Combining the abovementioned methods with other analytical tools could maximize the content acquired. Adding fluorescence capability would be a very appealing option since it is the most widely used tool for biologists. However, conventional IR imaging does not compatible with fluorescence imaging. The spatial resolution between fluorescence imaging and IR imaging makes it hard to register the point of interest.

The detection sensitivity in current far-field super-resolution absorption-based methods is limited to sub-micrometer particles. Single bacterium sensitivity has been achieved both with the scanning system and the widefield system.<sup>[451, 455, 456]</sup> Using confocal configuration, a single virus has been imaged with the scanning far-field IR photothermal microscope.<sup>[457]</sup> Since the photothermal process is transient, with a typical thermal decay time at hundreds of nanoseconds to several microseconds, the system needs to be optimized for improving detection efficiency. Simulation of the photothermal processes suggests that a high peak intensity heating beam should be selected to maximize the temperature increase for nanosized objects.<sup>[452]</sup> In the meantime, heating power should be considered to avoid thermal damage when observing live cell samples.

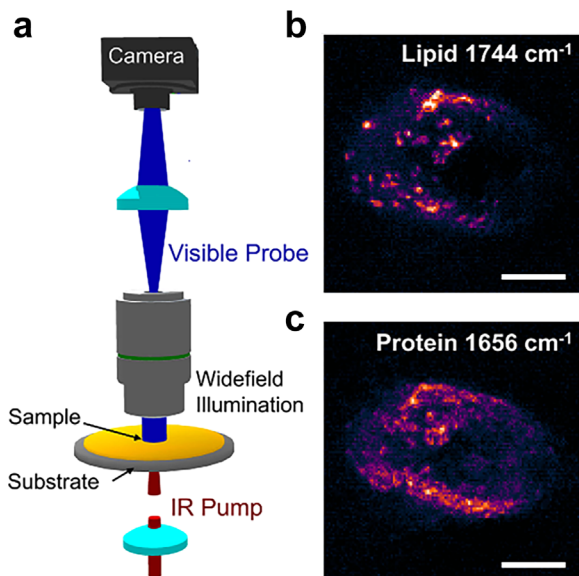


**Figure 26.** Widefield IR photothermal imaging setup and live-cell chemical maps. a) Mid-IR pump and visible probe are loosely focused to the sample and thus enables the widefield detection of the photothermal responses. b,c) Label-free live ovarian cancer cell imaging targeted at the lipid C=O bond vibration and the protein amide I band. Scale bars: 10  $\mu\text{m}$ . Adapted with permission.<sup>[454]</sup> Copyright 2019, The Authors, some rights reserved; exclusive licensee AAAS. Distributed under a Creative Commons Attribution NonCommercial License 4.0 (CC BY-NC).

### 15.3. Advances in Science and Technology to Meet Challenges

To boost the imaging speed, widefield photothermal imaging has been proposed.<sup>[454, 458]</sup> In the widefield imaging modality (Figure 26), the illumination area of the IR and visible beams are matched. Therefore, all pump photons can be fully utilized to generate signal. Synchronization between lasers, cameras, and modulation electronics enabled ultrafast chemical imaging speed over a large field of view.

To improve the depth imaging resolvability in widefield-detected photothermal imaging, methods such as optical diffraction tomography<sup>[459]</sup> have been proposed. Multiple angle illumination of the visible beams expanded the bandwidth in the frequency spectrum, and thus improved the resolution. Other 3D imaging modalities such as optical coherence tomography can also be coupled into current photothermal systems to achieve volumetric imaging capability.

The multimodal imaging is easy to implement in the far-field super-resolution techniques due to the two-beam configuration in pump-probe experiments. The probe beam is spectrally in the visible or near-IR range, which falls in most fluorescence excitation spectra. Work has been done using the fluorescence dye as a thermal sensor to probe the photothermal processes, where the fluorescence emission efficiency is a function of temperature.<sup>[460]</sup> In this work, fluorescence is used as a detector as well as an indicator of certain organelles. Integrating the specificity of fluorescence labeling and IR photothermal imaging would make fingerprinting different organelles under certain microenvironments possible. In addition to fluorescence imaging, other analytical methods such as Raman spectral measurements are also com-

patible with IR photothermal imaging. Li et al. demonstrated the combination of IR and Raman on the same setup, where a 532-nm probe laser in IR photothermal detection also functions as the Raman excitation laser.<sup>[455, 456]</sup>

The detection sensitivity in IR photothermal imaging can be further improved. For the current scanning system, most of the demodulation methods are based on lock-in amplifiers. However, the lock-in amplifier might not be the ideal selection to demodulate the signal. Since the pulsed heating beam is typically with a low duty cycle (<10%), the corresponding photothermal signal produces many harmonics. While the lock-in amplifier only picks up fundamental frequencies, the higher harmonics signal is neglected which leads to lower detection sensitivity. A recently developed photothermal dynamic imaging system successfully addresses this limitation by digitizing the whole photothermal process.<sup>[461]</sup> After performing the Fourier transform, all the harmonics is added to enhance the signal-to-noise ratio. In the meantime, all recorded data adds another benefit of time-resolved imaging. By performing the digitization, a four-fold signal-to-noise ratio is demonstrated. In addition to the data streaming optimization, the careful design of sample substrate would also improve the detection sensitivity. Substrate engineering such as interferometric scattering or plasmonic scattering is an effective way to boost imaging sensitivity.<sup>[221, 462]</sup>

### 15.4. Conclusions

Absorption-based super-resolution imaging is evolving exponentially over the past few years. Providing label-free, nanometer to sub-micrometer resolution capability, chemical selectivity, absorption-based super-resolution imaging offers unprecedented performance in investigating nanomaterials and biomedical samples. Looking into the future, it is anticipated that this rising field will continue to expand and will deepen the understanding about molecular machinery inside a cell and a functional material.

## 16. Pump-Probe Super-Resolution Microscopy

(Paolo Bianchini\*, Behjat S. Kariman, Alberto Diaspro)

### 16.1. Introduction

Optical microscopy uniquely provides non-invasive imaging of biological specimens and is an essential tool in life sciences. In particular, fluorescence microscopy is probably the most widely used technique to image living specimens, and much effort has been dedicated to improving it over one of its intrinsic limits, i.e., resolution. However, it requires the introduction of exotic fluorescence stains, which could become the major obstacle to studying a living specimen in its physiological conditions. Label-free methods result in the solution to such a limit without missing consolidated characteristics, i.e., specificity and resolution. Therefore, label-free chemical imaging is becoming one of the best choices to answer this challenge.

In this context, non-linear optical processes—i.e., when observable signal non-linearly depends on the illumination intensity—have captured the attention of life scientists for the development of label-free and super-resolved



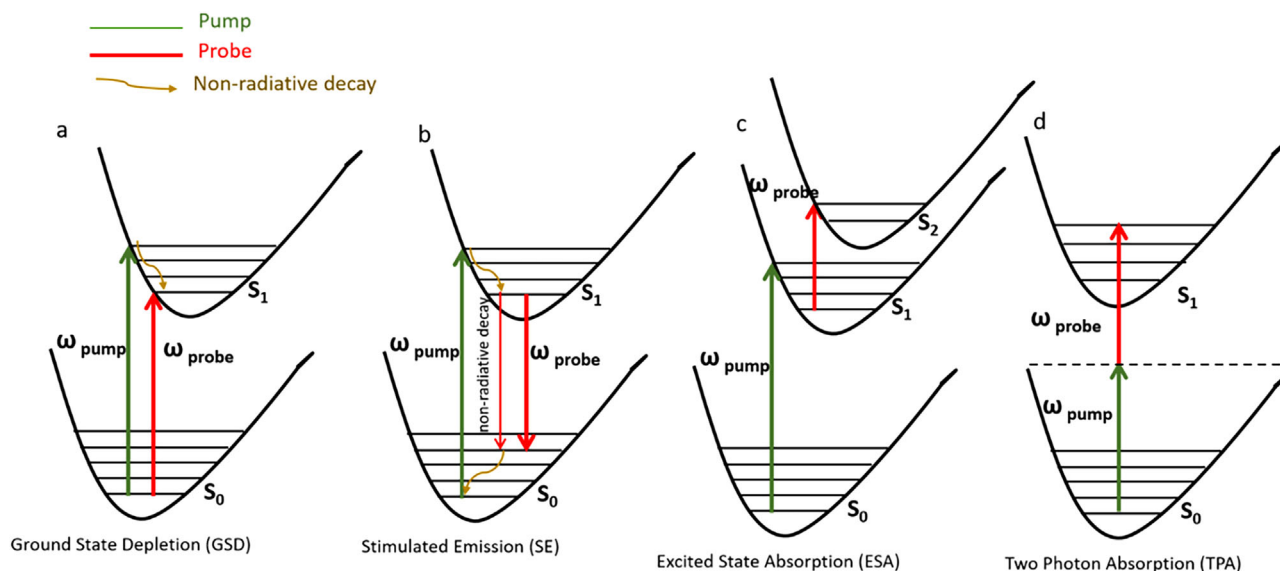


**Figure 27.** Energy level diagrams of pump-probe microscopy based on contrast mechanisms of a) ground state depletion, b) stimulated emission, c) excited state absorption, and d) two-photon absorption.

approaches.<sup>[14, 15, 463–465]</sup> In particular, pump-probe microscopy can image a wide range of specimens at high speed and resolution using different modalities: transient absorption, stimulated Raman scattering (SRS), coherent anti-stokes Raman scattering (CARS), second harmonic generation (SHG), two-photon excitation fluorescence (2PEF), etc. The saturation of some light-driven processes can be exploited in fluorescence microscopy to shrink the point spread function beyond the diffraction limit. Among those methods, it is worth noting stimulated emission depletion (STED) nanoscopy<sup>[15]</sup> and saturated excitation (SAX)<sup>[466]</sup> microscopy, which are based on far-field focused laser scanning systems. Point scanning remains one of the most flexible approaches since it enables a vast assortment of spectroscopical experiments while imaging. It can also explore the advantages of using proper wavelengths in a broad range of the spectrum from ultraviolet (UV) through visible (vis) up to the near-infrared (NIR) energies. For instance, many innovations exploiting NIR allow imaging at increased depth, improving resolution, contrast, molecular specificity, and, most importantly, label-free capabilities.<sup>[467]</sup> Illumination with NIR laser light very often deals with non-linear frequency conversion and non-linear absorption processes. Such light–matter interactions provide molecular contrast without needing exogenous labels and preserve the local biochemical environment of the target molecules.<sup>[468]</sup> In general, they involve the second  $\chi^2$  and third  $\chi^3$  order of susceptibilities.<sup>[469]</sup> Transient absorption is related to third-order non-linearity susceptibility but rarely implicates fluorescence emission. Its recent application in microscopy has broadened the range of suitable targets while providing high contrast in weak or non-fluorescent samples.<sup>[66, 67]</sup> The contrast mechanism comes from the observation of processes such as ground-state depletion (Figure 27a), stimulated emission (Figure 27b), excited-state absorption (Figure 27c) and two-photon absorption (Figure 27d).

When such processes are saturable with the irradiation intensity, they can be exploited for super-resolution microscopy.<sup>[30]</sup>

Transient absorption can be exploited by a pump-probe approach, which is a well-known spectroscopic method used to study the time-dependent ultrafast phenomena in matter. When applied for microscopy imaging, it brings the following advantages: while keeping specificity, it is label free<sup>[470]</sup>; it is not invasive nor destructive, thus suitable for living cell and tissue imaging<sup>[471]</sup>; it has three-dimensional (3D) sectioning capability and a high penetration depth.<sup>[472]</sup> Dong et al., in the 1990s, realized the first pump-probe microscope to measure the fluorescence lifetime through SE detection.<sup>[473]</sup> But only in 2007, thanks to the introduction of a high-frequency modulation scheme to detect melanins in cells,<sup>[474]</sup> transient absorption microscopy has started to be strongly developed and applied in many different research fields, from material to biological sciences. Pump-probe microscopy possesses non-fluorescent-based contrast, single-particle sensitivity, and high temporal resolution. Therefore, not only it allows characterizing the carrier dynamics of metallic and semiconducting nanostructures for studying their optoelectronic properties, but it also became relevant in mapping weakly or non-fluorescent nanostructures (like single-walled carbon nanotubes, nanodiamonds, gold nanoparticles ...) in biomedical applications inside living cells and tissues.<sup>[475]</sup> For instance, the Cheng group investigated the properties of single-walled carbon nanotubes (SWNTs), distinguishing semiconducting from metallic SWNTs by means of the phase of the pump-probe signal.<sup>[476]</sup> Among carbon-based materials, graphene is one of the most intensively studied.<sup>[477]</sup> Due to its linear electronic band structure, graphene shows a wavelength-independent, broadband optical absorption in the NIR part of the spectrum,<sup>[478]</sup> and a large third-order susceptibility  $\chi^{(3)}$ .<sup>[479]</sup> These properties make graphene very well suited to be studied by pump-probe super-resolution microscopy using NIR wavelengths. The pump-probe signal of graphene is linear with respect to the applied pump and probe powers and the number of graphene layers.<sup>[480]</sup> While at low powers, the linear behavior is satisfied, at higher powers, the signal saturates, as predicted by the state-filling effect of the higher electronic states.<sup>[481]</sup>

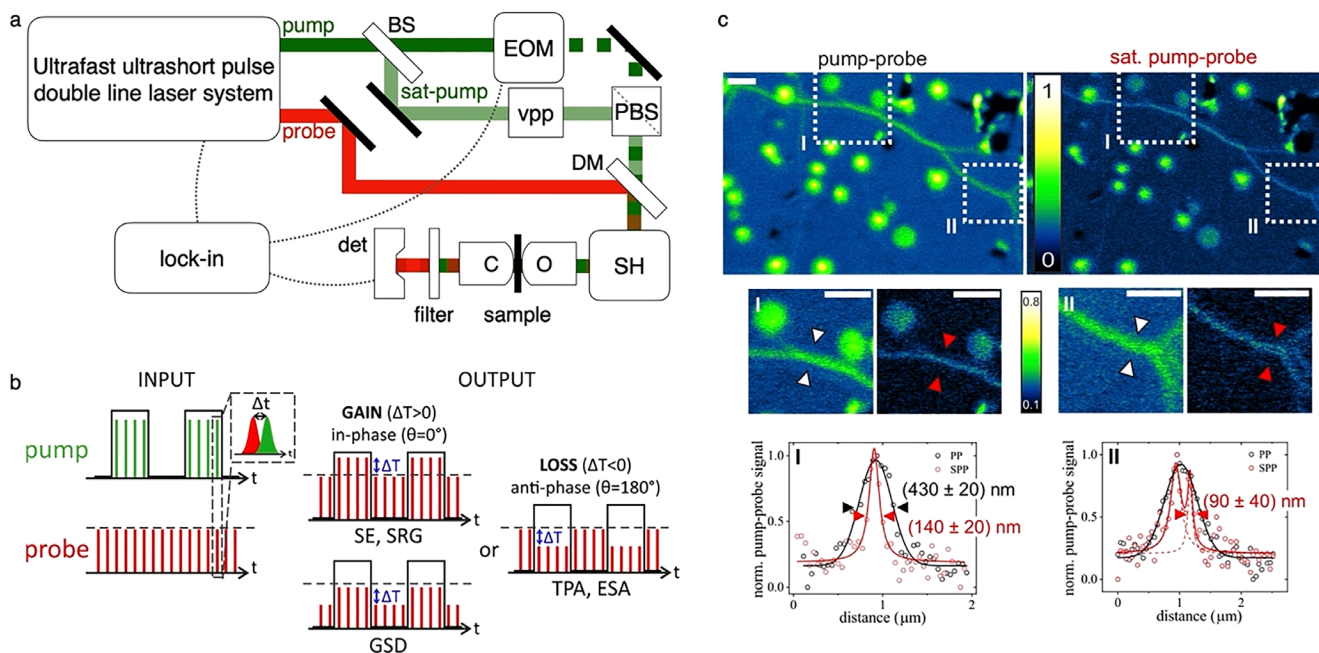


**Figure 28.** a) Example of a two-beam laser-scanning pump-probe nanoscope setup. BS: beam splitter, EOM: an electro-optical modulator for intensity modulation, vpp: vortex phase plate, DM: dichroic mirror, PBS: polarizing beam splitter, SH: scanning head unit, O: objective, C: condenser, det: detector. The pump beam is shown in green while the probe beam in red. b) Temporal modulation behavior of input and output pulse trains before and after interacting with the sample. Depending on the light–molecule interaction, the probe beam can undergo either a relative gain (SE, SRG, GSD) or a loss (TPA, ESA) in its output intensity ( $\Delta T$ ), exhibiting in-phase ( $\theta = 0^\circ$ ) or anti-phase ( $\theta = 180^\circ$ ) modulation, respectively. The pump temporal modulation is shown as a black square wave. The input probe intensity is marked by a dashed grey line. The tunable temporal delay ( $\Delta t$ ) of input pulses is shown in the inset graph. c) Normalized pump–probe and saturated pump–probe images of SLG folding and defects. Scale bar 2  $\mu\text{m}$ . Zoomed regions I and II are also presented, and line profiles across the arrows are shown as black dots (non-saturated case, PP) and red dots (saturated case, SPP). Gaussian fits of the non-saturated data are shown as solid black lines, while Lorentzian single-peak (I) and double-peak (II) fits of the saturated data are shown as solid red lines. The dashed red lines in graph II highlight the single Lorentzian peaks retrieved from the analysis. The obtained resolution is marked in the graphs as full-width-half-maximum of the fitted curves. Adapted with permission.<sup>[67]</sup> Copyright 2019, American Chemical Society.

Such a particular property enables far-field nanoscopy as defined by the Nobel laureate Stefan Hell in 2003.<sup>[482, 483]</sup> Therefore pump-probe microscopy become nanoscopy, a valuable, fast, sensitive, and non-destructive tool to map the local excited state dynamics and characterize the nano-defects.<sup>[484, 67]</sup>

## 16.2. The Pump-Probe Setup Enabling Super-Resolution

In a typical pump-probe microscope (Figure 28a), a pump pulse excites the molecule, and a probe pulse interrogates the transient excited states. Optical pump and probe can provide images by detecting changes in probe light intensity induced by the pump on the sample carrier population in either transmission or reflection modality. The pump-probe process at the molecular level can be defined by the absorption coefficient, an electronic transition between different levels.

Depending on the kind of transition that the material undergoes, the probe intensity can exhibit either a loss or a gain. The reason includes the following possible effects: excited-state absorption (loss), and two-photon absorption (2PE) (loss), stimulated emission (SE) (gain), and ground-state depletion (GSD) (gain) shown in (Figure 28b). The latter was used in microscopy to overcome diffraction barrier light in 2007,<sup>[485]</sup> following the

most general concept of RESOLFT (reversible saturable optical fluorescence transition).<sup>[486]</sup> The number of molecules in the ground state is decreased upon photoexcitation due to an intense pump beam, leading to increased transmission of probe pulse and absorption reduction at probe frequency. When GSD can be saturated, e.g., carbon materials like graphite and graphene, a STED-like scheme is applicable, and super-resolution is realized by detecting the remaining probe absorption in the neighborhood of the zero-intensity feature of the depletion beam.<sup>[67]</sup>

Such light-matter interaction is recorded as an intensity variation of the probe beam, which is detected by a non-descanned photodiode, a notch filter removes the pump signal, and the modulation is isolated from the background by electronic filtering with a lock-in amplifier locked at the frequency imposed to the electro-optical modulator, which controls the pump intensity. Subdiffraction spatial resolution is then realized by applying an unmodulated doughnut-shaped pump (Figure 28a). The pulses of such a beam need to be temporally aligned with the pump and probe ones, and this is generally realized with optical delay lines. To avoid molecular selection rules and to realize a good doughnut beam featuring a real zero-intensity level at the center, circular polarization at the sample plane is required.<sup>[487]</sup> This condition can be easily realized by means of two retarder plates, i.e., a half- and a quarter-wave plate.

### 16.3. Far-Field Nanoscopy Imaging of Single Layer Graphene

Pump-probe nanoscopy has been successfully demonstrated to image graphite nanoplatelets,<sup>[66]</sup> and single layer graphene (SLG).<sup>[67]</sup> The depletion of their ground state exponentially decays with the increase of the pump power. It has the same behavior as the excited fluorescence state in the case of STED. So that the final resolution will be limited only by the maximum saturation-pump power can be applied to the sample.

From the published results setting the saturation power to  $2.0 \text{ MW cm}^{-2}$  it is already enough to achieve a resolution of about  $225 \text{ nm}$  ( $\approx \lambda/3.0$ ) on graphite,<sup>[66]</sup> while on graphene with about  $7.0 \text{ MW cm}^{-2}$  is possible to achieve a resolution of the order of  $\approx \lambda/10$  (Figure 28c).<sup>[67]</sup>

In Figure 28c, we show an example of comparison between conventional pump-probe (PP) and saturated pump-probe (SPP) images of SLG with its multilayer islets. The spatial resolution improvement thanks to saturation beam is remarkable.

### 16.4. Conclusions and Perspectives

The pump-probe approach allows resolving and monitoring chemical and atomic ultrafast processes without the need for fluorescence emission. The latter is a standard in microscopy, allowing specificity and super resolution requesting a dedicated probe.<sup>[358]</sup> Therefore, a label-free method is of particular interest. It can avoid invasive procedures and allow long imaging sessions without loss in signal, i.e., photobleaching. However, since pump-probe microscopy is realized by employing ultrafast and ultrashort-pulse laser sources, such a method allows for multimodal imaging in which fluorescence, harmonic generation, and coherent Raman scattering, when needed, can be easily combined, and correlated. In some cases, like for carbon nanomaterials, the transient absorption process is saturable at the time scale of the laser pulses, thus, super-resolution can also be achieved following the general RESOLFT concept. In particular, graphene, which recently becomes one of the most studied materials because of its implication in many sciences and society fields, shows a linear electronic band structure, and a wavelength-independent, broadband optical saturable absorption in the NIR, together with a large third-order susceptibility  $\chi^{(3)}$ . This characteristic makes pump-probe nanoscopy ideal for mapping the carrier dynamics in all its different graphene forms. Nevertheless, since transient saturable absorption is not a unique property of graphene, we may envision novel pump-probe nanoscopy implementations on many other molecules, able to probe the molecular organization and dynamics of a cell with a spatiotemporal resolution that can assist in deciphering the most puzzling mechanisms of life.

## 17. Super-Resolution Raman Microscopy

(Katsumasa Fujita\*)

### 17.1. Status

Raman microscopy has emerged as one of the key modalities of imaging methods for biological and medical research. Vibrational spectroscopy of endogenous molecules in a sample can

provide information about biological samples that is not available using conventional imaging techniques. While the small cross-sectional area of Raman scattering has hindered powerful analytical capabilities in the life sciences, recent developments in optics and laser technology have resulted in techniques that improve image acquisition speed for both spontaneous and coherent Raman scattering microscopy. Surface-enhanced Raman scattering (SERS) is also used to reduce image acquisition time and increase the sensitivity of Raman detection. As with other optical imaging techniques, the spatial resolution of Raman microscopy is limited by the wave nature of light. Therefore, many attempts have been made to overcome this limitation using super-resolution fluorescence imaging strategies such as stimulated emission depletion (STED), single molecule localization microscopy (SLM), and structured illumination microscopy (SIM).<sup>[488]</sup>

### 17.2. Current and Future Challenges

Although Raman scattering and fluorescence emission are different physical phenomena, they can share the same techniques to overcome the resolution limit. In particular, spontaneous Raman scattering has the same imaging properties as fluorescence microscopy, which uses incoherent light to generate sample images. The techniques used for super-resolution fluorescence imaging are essentially valid for spontaneous Raman imaging. Coherent Raman microscopy (e.g., coherent anti-Stokes Raman scattering microscopy (CARS), stimulated Raman scattering microscopy (SRS)) uses coherent light to generate images and has different imaging properties from fluorescence microscopy. However, since they are based on laser scanning, the methods used in STED microscopy<sup>[15]</sup> and saturation excitation (SAX) microscopy<sup>[466]</sup> are effective in overcoming the resolution limitation.

The STED-based technique is used for both spontaneous and coherent Raman microscopy using laser scanning. By superimposing a donut-shaped beam on the Gaussian spot for Raman excitation, the signal at the peripheral region of the Gaussian spot is suppressed, limiting the volume of signal generation within the excitation spot. Several methods have been proposed to suppress signal generation such as prepopulation of vibrational state, ground state depletion, pump photon depletion, and phonon suppression. In any case, in order to obtain spatial resolution beyond the limit, it is important to introduce a nonlinear relationship between signal suppression/generation and excitation intensity, otherwise the enhancement will be limited to the contrast enhancement of high spatial frequencies.

The use of STED microscopy in Raman imaging is more difficult than in fluorescence imaging because of the short lifetime of the vibrational excitation state. The typical fluorescence lifetime of dyes with high quantum yields is a few nanoseconds, whereas the lifetime of vibrationally excited states is as short as  $\approx \text{ps}$ . Therefore, higher laser intensities are needed to suppress the Raman signal, and it is difficult to suppress the signal deeply enough to obtain high spatial resolution as in STED microscopy of fluorescence. Fluorescence microscopy can even offer more time to manipulate the signal through transition to triplet and dark state, photoisomerization, which are used in ground state



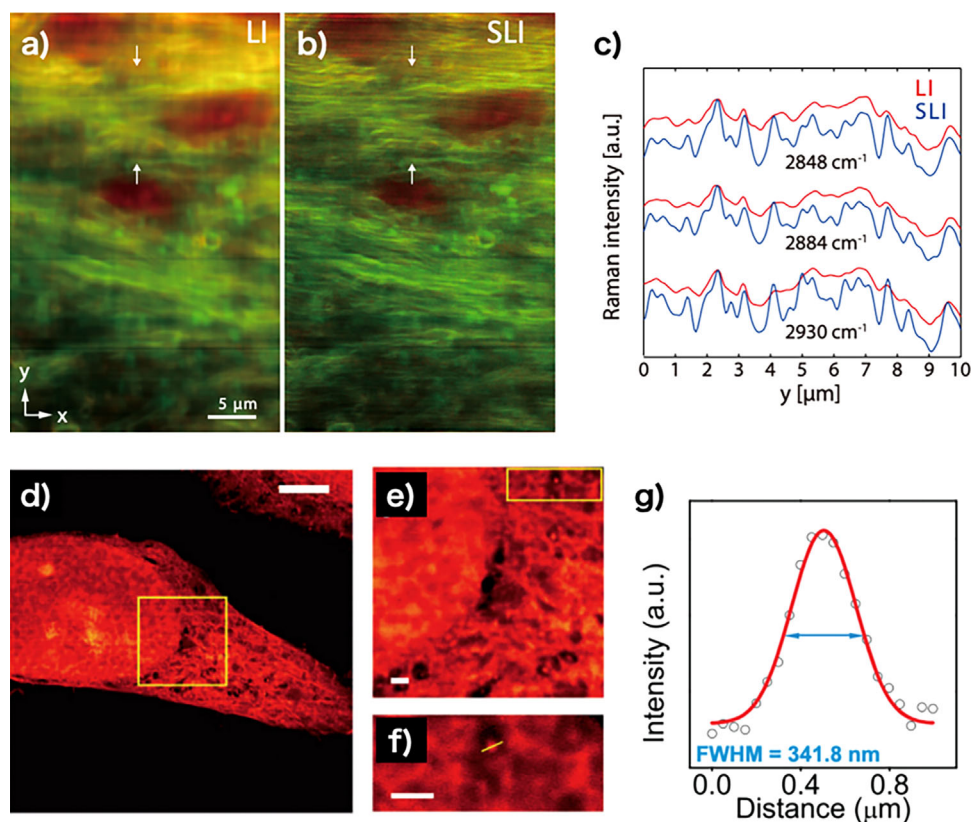


**Figure 29.** Examples of label-free super-resolution Raman imaging. A mouse brain tissue observed by a) conventional line illumination and b) structured line illumination Raman microscopy using 532 nm excitation. Raman peaks at  $1682\text{ cm}^{-1}$  (amide-I, red) and  $2848\text{ cm}^{-1}$  ( $\text{CH}_2$  stretching, green) were used for image reconstruction. c) the intensity profiles of Raman band observed between the arrows in a) and b). d)-f) SRS images of an expanded HeLa cell. A vibrational mode of  $\text{CH}_3$  at  $2940\text{ cm}^{-1}$  was detected by using 1031.1 nm Stokes and 791.2 nm pump beams. e) and f) are zoomed images of the yellow box region in d) and e), respectively. g) the line profile on the yellow line in f). Scale bars:  $30\text{ }\mu\text{m}$  in d) and  $2\text{ }\mu\text{m}$  in e) and f). a-c) Reproduced under the terms of the CC BY 4.0 License.<sup>[493]</sup> Copyright 2015, The Authors, published by Springer Nature. d-g) Reproduced under the terms of the CC BY 4.0 License.<sup>[496]</sup> Copyright 2021, The Authors, published by Springer Nature.

depletion (GSD) microscopy and RESOLFT microscopy. It is difficult to realize these techniques in Raman microscopy as effectively as in fluorescence microscopy.

Another approach to achieve super-resolution imaging in laser scanning Raman microscopy is to introduce a higher-order nonlinear response in the Raman effect. By saturating the Raman effect, a higher-order nonlinear relationship is induced between the signal and the incident light, and the signal generation is localized within the focal volume. So far, the use of saturation in CARS and SRS has been demonstrated<sup>[489, 68]</sup> for high-resolution coherent Raman imaging based on SAX microscopy. It has also been demonstrated to induce higher-order CARS in a sample and to achieve super-resolution vibrational imaging of biological samples.<sup>[490]</sup> The use of photothermal nonlinearity in Raman scattering has also been exploited to realize super-resolution imaging in confocal Raman microscopy.<sup>[491]</sup>

SIM can be used for spontaneous Raman and SERS imaging because its imaging properties are the same as those of fluorescence microscopy. Since a typical SIM involves wide-field detection, applying SIM to filter-based Raman microscopy is straightforward.<sup>[492]</sup> However, it sacrifices the spectral resolution and require a long measurement time for hyperspectral imaging. The SIM-based technique has also been applied to line illumi-

nation Raman microscopy, where the sample is irradiated with a line-shaped focus and the image is formed by conventional imaging for the direction of the irradiated line (Figure 29a-c).<sup>[493]</sup> Similarly, image scanning microscopy (ISM) is also effective to improve the spatial resolution of Raman microscopy.<sup>[494]</sup> The use of  $4\pi$  optics was also demonstrated, which realized the detection of the detection volume for the axial direction effectively.<sup>[495]</sup>

As mentioned above, manipulation of Raman signals is not as easy as fluorescence signals, so there are few applications of SLM in Raman imaging. It is well known that SERS signal show blinking by reflecting the condition of molecules on a metal surface. This blinking effect was exploited to perform SLM in SERS imaging.<sup>[497]</sup> However, there are still challenges in applying this technique because it requires manipulation of SERS hotspots on the sample.

### 17.3. Advances in Science and Technology to Meet Challenges

Although the super-resolution techniques used for fluorescence imaging have been explored, the spatial resolution achieved for Raman imaging is still limited. This is because of the difficulty of manipulating the Raman effect in target molecules. To push



the current limit, innovative ways to control the Raman effect, such as the capability of switching Raman effect and induction of highly nonlinear relations between incident light and Raman effect, need to emerge. Another difficulty in the high-resolution Raman imaging is its weak signal. The reduced detection volume in high-resolution imaging can provide only small detection signals, which requires a much longer exposure time. The reduction of signal-to-noise ratio (SNR), making the practical resolution lower. Therefore, increasing the Raman signal or reducing noise is inevitable to improve the spatial resolution further. Recently, a technique to improve the SNR by using the squeezed light has been demonstrated in SRS microscopy,<sup>[498]</sup> which is expected to contribute to the improvement of spatial resolution in SRS imaging.

The use of non-optical methods is another direction. Recently, expansion microscopy has been applied to super-resolution SRS imaging. In expansion microscopy, the volume of the sample is expanded by swellable polyelectrolyte hydrogels, of which volume can be highly increased by being immersed in a solvent, before observation.<sup>[499]</sup> The size of the sample can be increased by a factor of 4.5 to 20 in the linear dimensions, and a more detailed spatial distribution of the target can be observed than with conventional techniques, even using diffraction-limited optical microscopy. The expansion microscopy technique has been applied to observe tissue samples by SERS and SRS microscopy (Figure 29d-g).<sup>[496, 500]</sup> Although this technique cannot be used on live samples, it extends the usefulness of vibration microscopy for investigating microstructures in cells.

Switching the capabilities of Raman scattering has recently been demonstrated using chemical compounds.<sup>[501]</sup> It has been shown that isomerization of the molecular structure can change the Raman spectrum. This switching capability can be used for both STED and SLM-type super-resolution techniques. At this time, it may be difficult to apply this strategy to molecules intrinsic to the samples, but as our understanding of the photophysical properties of molecules improves, it will eventually show us how to manipulate the Raman scattering cross-section of molecules.

#### 17.4. Conclusions

The development of super-resolution Raman imaging has proceeded mainly by using methods developed for fluorescence microscopy. Although these methods are effective in principle, it is practically difficult to achieve a spatial resolution of 100 nm or higher. Furthermore, it would be necessary to develop a method suitable for Raman imaging, where pre-preparation of samples is not expected, unlike fluorescence imaging. In other words, we need to develop a fully optical super-resolution technique that does not rely on the manipulation of sample properties.

Currently, the main applications of Raman spectroscopy are in material science and industry, such as nanomaterials, semiconductors, batteries, polymers, and pharmaceuticals. Although super-resolution techniques have been intensively developed for the observation of biological samples so far, exploring application in materials science is important for super-resolution Raman imaging. In fact, these applications typically involve samples that are more resistant to photodamage and produce more signal than biological samples, which can be advantages in realizing super-resolution imaging. Since such material analysis is

performed without labeling, label-free super-resolution Raman imaging is inevitable. Also, while SEM and AFM are the primary choices for high-resolution imaging, the ability to provide high-resolution 3D imaging, a major advantage of optical microscopy, is attractive to this field.

## 18. Silicon Non-Linearity Based Super-Resolved Pump-Probe Imaging

(Moshe Sinvani, Zeev Zalevsky)

### 18.1. Introduction

In optical microscopy the property of diffraction limits the resolution and yields that one cannot image spatial details being smaller than half of the wavelength of the illuminating light because such small spatial features cause light to propagate as evanescent rather than a harmonic wave. Various concepts were proposed in the attempt of bypassing this physical limitation.<sup>[502–505]</sup>

One important breakthrough that initiated the field of nanoscopy and which was applied for fluorescence imaging proposed a new type of scanning fluorescence microscope.<sup>[14, 287]</sup> This imaging concept could reach a resolution of 35nm and it was named stimulated emission depletion (STED).<sup>[506]</sup> Further improvement of that concept was generated in years to follow<sup>[507–509]</sup> leading eventually to imaging capabilities of  $\approx 5$ nm for fluorescent color centers in diamond crystal.<sup>[510]</sup> STED concept exploited the typical characteristics of the fluorescent molecules. Two beams were used to obtain the super-resolved imaging. The first is a pulsed laser beam acting as a pump beam having optimal Gaussian point spread function (PSF) and being focused on the examined sample while acting as the fluorescence excitation source. A second pulsed laser beam which has a donut shape, is stimulating depleting fluorescence laterally around the center of the excitation beam spot while leaving the center region of the focal spot active to continue and emit fluorescence. Due to this process the imaging PSF is laterally sharpened since the lateral regions of the PSF coinciding with the donut shape beam are significantly attenuated and only the central part of the PSF of the excitation beam produce emission from the sample, which leads to enhanced imaging resolution.

Besides STED additional approaches were also introduced aiming to produce a nanometric imaging resolution while all using various physical aspects of the fluorescence effect such as the stochastically sparse subsets of fluorophores, namely the photoactivated localization microscopy (PALM) approach<sup>[244, 511–514]</sup> or as stochastic optical reconstruction microscopy (STORM) approach.<sup>[515]</sup> PALM exploits the spontaneously occurring phenomenon of photobleaching while STORM exploits the reversible switching between a fluorescent on-state and a dark off-state of a fluorescence dye.

Example of other methods developed in the field of nanoscopy and which also involve interaction of probe-pump beams include for instance adding to the surface that is to be imaged a photochromic absorption modulated layer<sup>[516]</sup> or using the concept of saturated transient absorption microscopy where usage of materials with very small absorption saturation level<sup>[66]</sup> is applied to

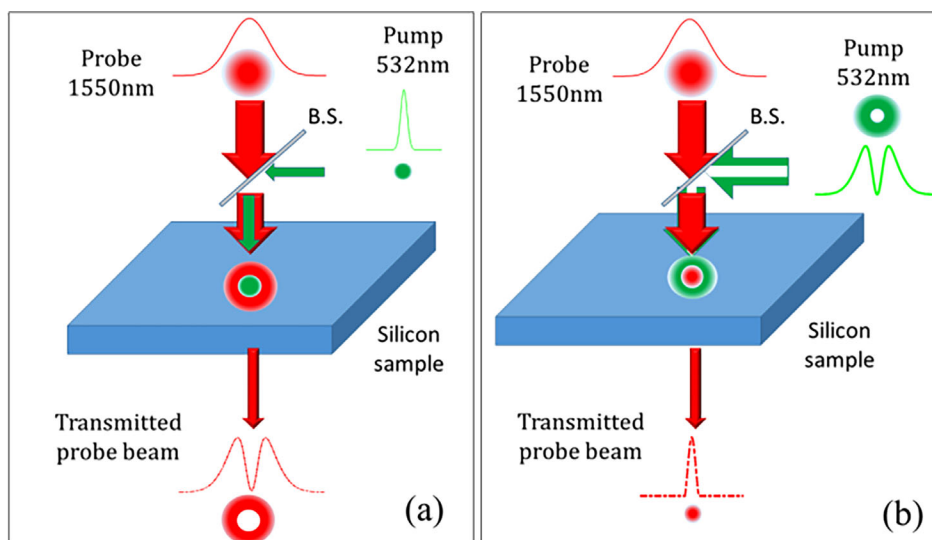


**Figure 30.** Illustration of the operation principle for the two possible directions: a) A narrow pump Gaussian beam at 532 nm, creates a hole in the middle of a wider IR probe beam. b) Donut shape 532 nm pump beam blocks the periphery of the Gaussian IR probe beam and transmits only a narrow beam in its center. Reproduced with permission.<sup>[69]</sup> Copyright 2018, Optical Society of America under the terms of the OSA Open Access Publishing Agreement.

obtain sub-diffraction resolution in far field. Additional methods use various types of silicon-coated gold nanoparticles that allow to generate a time multiplexing super-resolved imaging by modifying the PSF into a donut-like shape while utilizing the plasma dispersion effect (PDE)<sup>[517]</sup> or by using coherent anti-Stokes Raman scattering (CARS) approach.<sup>[518–520]</sup>

In our research, we use the plasma dispersion nonlinearity occurring in silicon in order to realize a super-resolved nanoscope capable of providing significant advantage to the micro-electronic industry in the field of failure analysis. Our concept involved a pump-probe scanning architecture that maps the silicon wafer with nano-metric resolution that could be extracted not only from the surface of the integrated circuit but also from its deeper layers. The photons of the pump are absorbed in the silicon chip and generate free electrons that shape the PSF of the probe that is near infra-red (IR) wavelength of 1550nm. The reshaping of the probe PSF is done through the plasma dispersion non-linearity causing either narrowing of the PSF or to the generation of a narrow dip in its center i.e. in both cases the PSF of the probe has high spatial frequencies being higher than the limits sets by the laws of diffraction. When such sharpened PSF scans the inspected sample (i.e. the PSF is multiplied by the spatial content of the target), the high spatial frequencies of the sample are down-converted and become low spatial frequencies that can propagate from the sample to the imaging sensor as harmonic rather than evanescent waves and thus be sensed and decoded.

## 18.2. The Concept

As mentioned above our method is based upon PDE in silicon in which near infra-red (IR) laser probe beam (at wavelength that regularly is not absorbed in silicon) can be spatially shaped by the silicon's locally changed refractive index (its real as well as its imaginary part) that is modified via another pump laser beam

that its photons are being absorbed in the silicon and by that create change in the free electrons density. The spatial shaping of the probe beam generates in its PSF higher spatial frequencies and after scanning the inspected object may produce a super-resolved image. Note that the proposed super resolving mechanism is a non-linear effect because the absorption coefficient for the probe is proportional to the power of the pump and therefore following the Beer-Lambert law, the total absorption of the probe is exponentially related to the absorption coefficient.

Unlike in the STED method, the proposed approach has flexibility in the manner of how the PSF of IR probe beam is done. One direction is to induce a hole or a dip in the center of the probe's PSF by applying a narrower Gaussian pump beam coinciding with the center of the probe's PSF<sup>[518]</sup> (Figure 30a). However, in this case, the PSF has a shape requiring post-processing decoding to reconstruct the super-resolved image. Another direction is to apply a donut shape pump beam. In this case, the central part of the IR beam passes through while its lateral surrounding is significantly attenuated (Figure 30b). Then the scanning of the narrowed probe PSF produces the super-resolved result without the need for any further post-processing. In both cases, high spatial frequencies are induced and reflected in the nano scales via the same free charge carrier-induced absorption mechanism.

To further demonstrate the proposed operation principle we show some experimental results presenting the breaking of the diffraction limit by generating a narrow dip in the center of the probe's beam PSF that can lead also to sub-wavelength super-resolved imaging capabilities when performing scanning with the experimentally shaped PSF beam.<sup>[69]</sup>

In Figure 31, we presented how that shaping of the probe PSF is obtained. In order to obtain a super-resolved image the pump and the probe beam need to synchronously scan the inspected sample. They need to do the scanning together because in order to obtain superresolution, the probe PSF needs to be shaped. This shaping is obtained only due to the pump beam. The process of

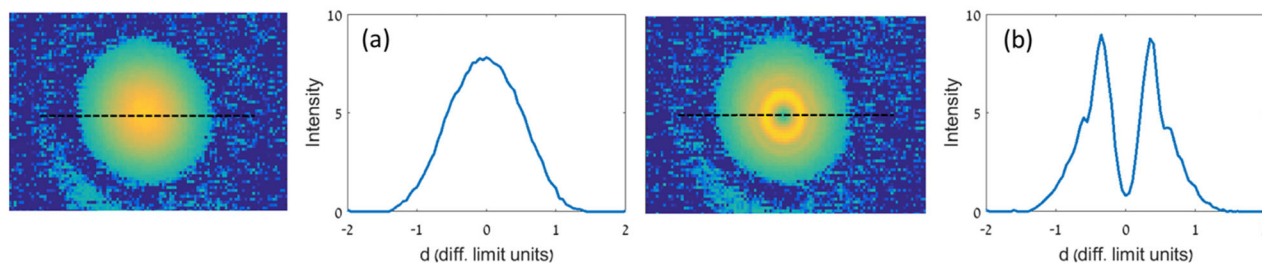


**Figure 31.** The dip generated in the Gaussian IR probe beam was induced by the green pump beam. One diffraction limit unit is 600  $\mu\text{m}$ . a). The image of the transmitted Gaussian probe beam and its profile. b). The shaped probe beam and its profile. The probe beam is having a dip that is superimposed on its center by the pump beam. Reproduced with permission.<sup>[69]</sup> Copyright 2018, Optical Society of America under the terms of the OSA Open Access Publishing Agreement.

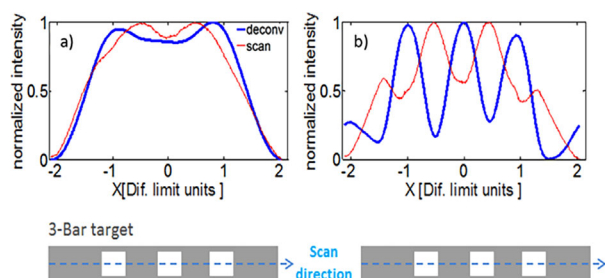


**Figure 32.** Gaussian probe IR laser beam at the diffraction limit scan across a resolution target containing 3-bars having a period of 500  $\mu\text{m}$ : a) Without applying the pump beam. No resolution improvement is obtained. b) A scan of the target with the pump beam creating a dip in the probe's beam PSF. Super-resolution is obtained and the target is reconstructed. The red lines are the direct scan results. The blue lines are the direct scan results deconvoluted with the shape of the probe beam having the central dip. Reproduced with permission.<sup>[69]</sup> Copyright 2018, Optical Society of America under the terms of the OSA Open Access Publishing Agreement.

super-resolved reconstruction obtained following the scanning of the inspected sample is presented in **Figure 32**. The super-resolving experiment of **Figure 32** includes imaging a resolution target that is composed of 3-bars having spatial period of 500  $\mu\text{m}$ .

The IR beam was focused on the silicon surface with a very low NA lens (one diffraction limit unit is 600  $\mu\text{m}$ ) and the camera was without a lens. When scanning the resolution target only with the probe beam and without illuminating with the pump beam, the probe's PSF is not narrowed, and no superresolution is obtained (**Figure 32a**). However, when the scanning is performed both with the probe as well as with the pump beam, the probe's PSF is narrowed and the superresolving result is extracted (**Figure 32b**). In both cases, the raw scan is colored in red. Knowing the beam PSF we used MATLAB software to perform a standard Wiener filter algorithm to de-convolute the raw scan, and the results are colored in blue. Superresolved results are clearly seen in the images of **Figure 32b**.

Further development of our approach while using time-tunable pulses for the pump and the probe allowed us to play with the position of the focus of the probe beam and control its focusing and defocusing processes in deeper layers of the silicon chip<sup>[521–526]</sup> and not only on the wafer's surface. We used probe near IR (at  $\lambda = 1.55 \mu\text{m}$ ) beam and a pump beam at  $\lambda = 775\text{nm}$  with 30 ps pulse width, with a donut shape (generated via beam

shaping vortex phase plate). Both the probe and the pump beams were lunched collinearly and simultaneously (with some time delay between the pump and the probe pulses). Thus, the proposed PSF shaping method is not only suitable for overcoming the diffraction resolution limit in silicon microscopy, but it may also allow doing this deep under the silicon surface dependent on the pump wavelength and the pump/probe lasers pulse widths.

### 18.3. Conclusions

The proposed super resolution concept that is based upon silicon non-linearity called plasma dispersion, to generate failure analysis super-resolved image with nano metric resolution after scanning the integrated circuit with a pump–probe collinearly aligned beams. Our super-resolving approach allows improving the imaging resolution beyond the diffraction limit and towards the nanometric scale but obtaining it not only on the surface of the silicon wafer but also deeper inside, which is being a significant advantage in the field of failure analysis of integrated circuits.

## 19. The Rise of Mie-Tronics-Based Nonlinear Scattering Imaging

(Xiangping Li\*, Guan-Jie Huang, Shi-Wei Chu\*)

### 19.1. Status

Traditional super-resolution imaging mostly relies on manipulating nonlinear behaviors of fluorescence emission, including on/off switching of the molecules deterministically or stochastically, saturation of excitation/emission, and high-order multiphoton excitation.<sup>[488]</sup> Despite the great success of super-resolution fluorescence techniques in cell biology and biomedical sciences, one major challenge is the limited photon yield due to photobleaching and low photostability. Therefore, developing a fluorescence-free contrast agent is highly desirable for super-resolution techniques.

Light scattering by nanoparticles is ubiquitous in many subjects of optics. The associated Mie theory and optical properties may lay the foundation for a new type of imaging probes. The excitation and interaction between radiating multipoles of different orders expand the emerging field of “Mie-tronics” to further

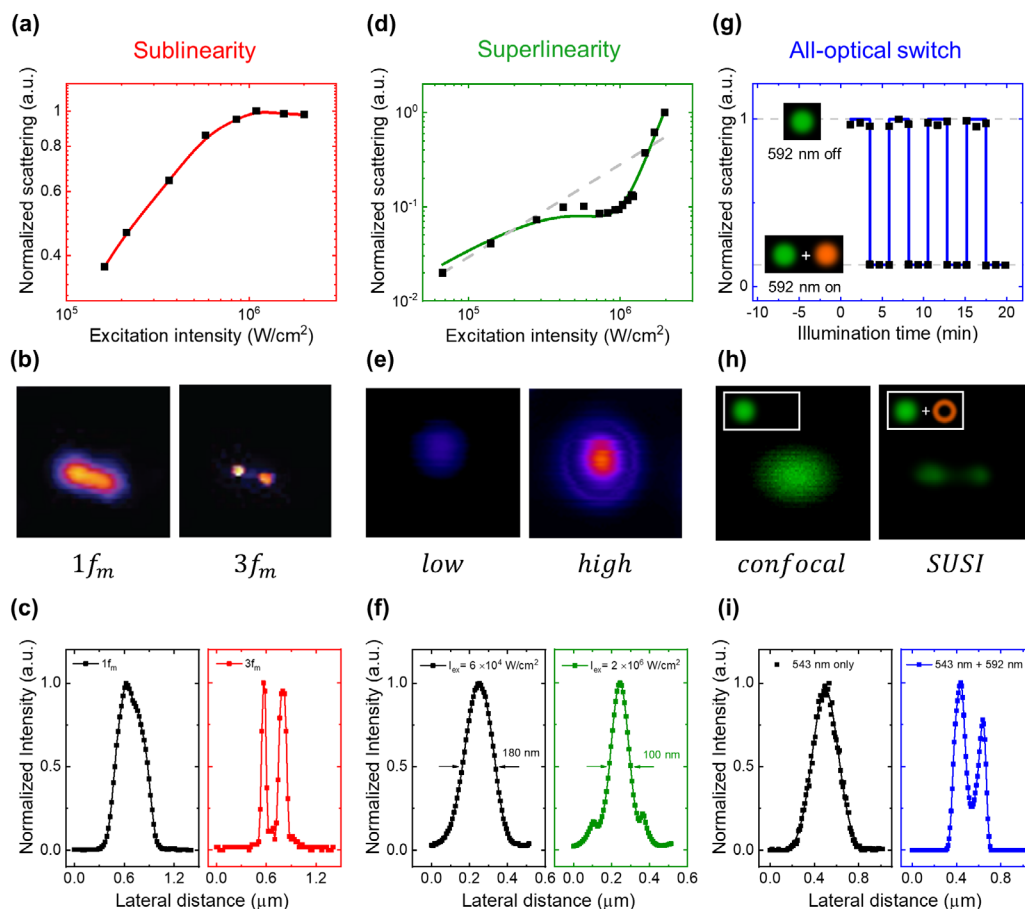


**Figure 33.** Optical nonlinearity and super-resolution imaging in plasmonic NS. Panels (a), (d), and (g) are various types of nonlinearities, including sublinearity (a), super-linearity (d), and all-optical switch (g), from a single gold nanosphere (80- or 100-nm diameter). b,e,h Super-resolution scattering images are obtained by SAX microscopy (b), where images are reconstructed by signal demodulated at  $f_m$  and  $3f_m$ , where  $f_m$  is the temporal modulation frequency; by super-linear microscopy (e), where images are formed under low and high illumination; and by SUSI microscopy (h), where a  $\lambda = 592$ -nm donut suppression beam is applied. Panels (c), (f), and (i) are corresponding line profiles, quantifying the resolution enhancement. a–c) Reproduced with permission.<sup>[532]</sup> Copyright 2014, American Physical Society. d–f) Reproduced with permission.<sup>[534]</sup> Copyright 2014, American Chemical Society. g–i) Reproduced under the terms of the CC-BY license.<sup>[529]</sup> Copyright 2016, Springer Nature.

manipulate Mie resonances from imaging to nanophotonic applications. Interested readers may refer to this recent review to explore advances in Mie-tronics.<sup>[527]</sup> We have proposed to adopt scattering from Mie-resonators, especially in plasmonic and dielectric nanostructures (NS) as a novel super-resolution contrast. The reasons include 1) scattering intensity from Mie-resonators is particularly strong due to resonance enhancement; 2) scattering does not suffer from photobleaching; 3) NS scattering offers high photostability. However, typically intrinsic nonlinearities of metal and dielectric materials are weak.

Recently, our groups unraveled giant nonlinearities in both plasmonic and dielectric Mie-resonators,<sup>[528, 529, 70]</sup> whose behaviors can be manipulated by excitation wavelength and NS morphology. The underlying nonlinear mechanism is based on photothermal and thermo-optical effects, which interact with Mie-resonance and modulate NS scattering intensity. In brief, as laser excitation wavelength is located near the Mie resonance peak of NS, absorption and the consequent photothermal heating becomes more efficient.<sup>[70]</sup> Subsequently, temperature rise modifies the NS refractive index via thermo-optical effect, and

the index alteration is amplified by Mie resonance, leading to significant scattering variation, that corresponds to nonlinear behaviors.

In the theoretical aspect, a self-consistent model based on Maxwell and heat equations has been developed to quantitatively deduce the Mie enhanced photo-thermo-optic nonlinearity.<sup>[530]</sup> In experiment, we develop an x-scan method based on a laser scanning microscope to characterize the optical nonlinearities of a single NS.<sup>[531]</sup> The idea of x-scan is to scan a focused Gaussian beam laterally across a NS, whose diameter is much smaller than the Gaussian beam width, and collect its emission. If the NS exhibits a nonlinear response, the resulting images deviate from the Gaussian profile (linearity) and the nonlinear coefficient is derived directly from the deviation. Through the x-scan method, various nonlinearities are observed, including sub-linearity, super-linearity, and all-optical switch (Figures 33 and 34).

These nonlinearities are all applicable to super-resolution imaging in both plasmonic and dielectric NSs. As a NS is illuminated by a focused Gaussian beam, whose intensity gradually increases, the nonlinear behaviors should first appear in the



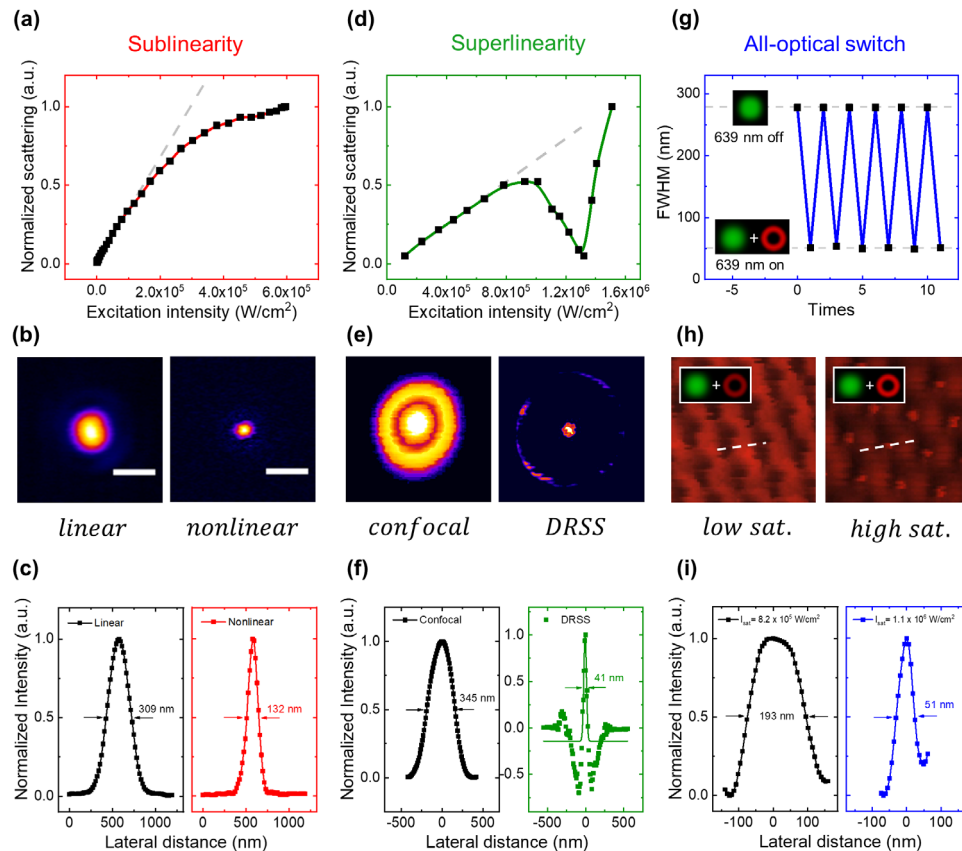


**Figure 34.** Optical nonlinearity and super-resolution imaging in dielectric NSs. Panels (a), (d), and (g) are various types of nonlinearities, including sub-linearity (a), super-linearity (d), and all-optical switch (g), from a single silicon NS or silicon NS array. b,e,h Super-resolution scattering images are obtained by SAX microscopy (b); by differential signal processing in super-linear microscopy denoted as differential reverse saturation scattering (DRSS) (e); and by STED-like microscopy (h), where a  $\lambda = 693$ -nm donut suppression beam is applied under low and high illumination to present different scattering saturated levels. Panels (c), (f), and (i) are corresponding line profiles, quantifying the resolution enhancement. a–c) Reproduced under the terms of the CC-BY license.<sup>[70]</sup> Copyright 2020, The Authors, published by Springer Nature. d–f) Reproduced under the terms of the CC-BY license.<sup>[528]</sup> Copyright 2020, The Authors, published by Springer Nature. g–i) Reproduced with permission.<sup>[536]</sup> Copyright 2021, OSA publishing.

centermost region of the focus. Therefore, the extraction of nonlinear signals results in effective reduction of the point spread function, and thereby super-resolution imaging.

In the case of sub-linearity, saturation excitation (SAX) microscopy achieves super-resolution via extracting nonlinear scattering by temporal modulation of excitation plus harmonic demodulation of emission (Figure 33a–c for plasmonic and Figure 34a–c for dielectric NSs).<sup>[532, 70]</sup> A more straightforward super-resolution approach is through super-linearity,<sup>[533]</sup> which enables direct observation of the resolution enhancement (Figure 33d–f).<sup>[534]</sup> Combining sub-linear and super-linear effects, along with differential signal processing, the single-NS image width can be further reduced to below 50 nm (Figure 34d–f).<sup>[528]</sup>

It is well known that all-optical switch of emission enables resolution enhancement. The most famous example is stimulated emission depletion (STED),<sup>[488]</sup> which relies on switch on/off fluorescence. We pioneered in demonstrating all-optical switch with scattering from both plasmonic and dielectric NSs.<sup>[529, 70]</sup> That is, scattering intensity decreases as increasing the illumination intensity. Borrowing the setup from STED microscopy, where peripheral scattering is suppressed by a donut beam, we succeed

in resolving two adjacent plasmonic scatterers by suppression of scattering images (SUSI) (Figure 33g–i).<sup>[529]</sup> Ouyang et al. extended this concept, introducing saturation scattering competition (SCC), where excitation and the depletion beams are at the same wavelength and the depletion beams are at the same wavelength to prevent the chromatic aberration.<sup>[535]</sup> Very recently, the concept of SUSI is demonstrated in dielectric NSs via manipulating the polarization state of illumination, as shown in Figure 34g–i.<sup>[536]</sup>

## 19.2. Current and Future Challenges

We have shown that scattering, from plasmonic or dielectric nanoparticles, exhibits a significant nonlinear response due to the interplay of Mie resonance and photo-thermo-optic effects. The nonlinear Mie scattering provides a novel contrast for super-resolution imaging, via the technical approaches of SAX, super-linear microscopy, SUSI, etc. However, the general purpose of super-resolution microscopy should be the investigation of “unknown” structures, but in current status, most experiments adopt plasmonic and dielectric NSs with well-defined morphologies (size, shape, etc.). Typically, only one or two exci-

tation wavelengths are selected to meet the NS resonance peaks, and to optimize the nonlinear efficiency. Therefore, one major challenge is to develop a new scattering-based nonlinear super-resolution technique that is able to examine unidentified NSs.

A common goal of optical super-resolution techniques is to push toward the resolution of electron microscopy. The state-of-the-art fluorescence nanoscopy has now enabled  $\approx 1$ -nm spatial resolution in 3D<sup>[537]</sup>! It is critical to borrow experiences from fluorescence imaging to boost the spatial resolution of scattering-based microscopy. In principle, the resolution of nonlinear imaging techniques such as SAX and SUSI is unlimited, depending on how strong is the nonlinear response. Thus, one major challenge is to substantially improve the nonlinear light-matter interactions in Mie resonators.

From Figures 33 and 34, the best resolution of nonlinear scattering imaging is about 40-nm, which is much smaller than the NS diameter itself. An interesting question is to understand the underlying mechanism of the coherent scattering super-resolution image formation. For instance, the ultrafast temporal dynamics of the nonlinear Mie-scattering has not yet been thoroughly scrutinized.<sup>[538]</sup>

### 19.3. Advances in Science and Technology to Meet Challenges

In order to generate nonlinear scattering in NSs with various morphologies and resonance wavelengths, one plausible strategy is to adopt a broadband light source such as a super-continuum laser. Please note that most of the results in Figures 33 and 34 are carried out with continuous-wave lasers, while commercially available fiber-based super-continuum laser in general has a nanosecond pulse width, and custom-made super-continuum may have pulse width as short as a few femtoseconds. Therefore, on the one hand, combining super-continuum with a wavelength-selection tool and x-scan confocal microscopy may provide the desirable capability of generating nonlinear scattering in many different NSs, thus enabling the observation of “unknown” structures. On the other hand, the nanosecond/femtosecond pulse nature of the super-continuum laser offers a playground to explore the nonlinear scattering effect in diverse time scales. In particular, the nanosecond pulse may be the most efficient in transient heating of the NS, while the femtosecond pulse shall be preferred to study the carrier dynamics by pump-probe spectroscopy.

The second challenge is to enhance spatial resolution of scattering images, via the approach of enhancing optical nonlinearity. It is well known that nonlinear light-matter interactions are significantly amplified in a high-Q cavity. In most results of Figures 33 and 34, the Q-factor of Mie resonance is merely on the order of 10. Manipulating the interaction between multipoles of different orders can lead to exotic optical phenomena such as nonradiating anapole,<sup>[539]</sup> supercavity mode, and quasi-bound states in the continuum,<sup>[540]</sup> pushing Q-factor of single-particle Mie resonance toward  $10^3$ , and that of a metasurfaces as high as  $10^6$ ! The unprecedented high-Q resonance may lead to significant enhancement in the image precision. Under a tightly focused scenario of microscopy, an emerging trend is to explore spatially dependent mode excitation,<sup>[541]</sup> and multipole interference to enhance local field as well as nonlinearity.

### 19.4. Concluding Remarks

Through the investigations over the past decade, giant photothermal nonlinearities on scattering has been unraveled, in both plasmonic and dielectric nanoparticles. Various nonlinear responses are discovered, and applied to resolution enhancement on the nanoparticles. Looking back to the title of this roadmap article “Label-free Super-resolution Imaging”, the readers may feel confused that these nanoparticles shall serve as extrinsic “labels” when applying to biological specimens. However, optical microscopy is useful not only for biology, but also for material sciences. We would like to advocate the development of nonlinear Rayleigh scattering microscopy as a novel contrast mechanism to inspect metal and semiconductor nanostructures. In addition, the nonlinear light-matter interaction may readily extend from Rayleigh scattering, into absorption or other forms of emission, to form an array of super-resolution imaging contrast tools.

## 20. Label-Free Super-Resolution Microscopy by Non-Linear Photomodulated Reflectivity

(Omer Tzang, Dror Hershkovitz, Ori Cheshnovsky\*)

### 20.1. Status

The urge to explore the properties, structure, dynamics, and functionality at the nanoscale has inspired the onset of ultrahigh-resolution imaging techniques. In particular, super resolution (SR) fluorescence-based microscopy, with resolution down to few nanometers is very useful in biological research where functional groups can be selectively labeled. However, in many cases, in material inspection or imaging of unprocessed biological tissues, far-field, label-free, imaging modality is desirable. Near field Scanning Optical microscopy does provide label-free SR by coupling light to proximate nanostructures, however it is confined to a range of few tens of nanometers off the surface. Recently, far-field label-free SR methods, based on ground state depletion<sup>[66]</sup> and Photo-acoustics<sup>[542]</sup> were introduced. Our methodology, Non-linear Photo-Modulated Reflectivity (NPMR) is based on the nonlinear changes in the reflectance of materials,  $\Delta R$ , caused by an ultra-short pump pulse.<sup>[543]</sup>

In NPMR, a modulated train of ultra-fast pump pulses focused on the sample, photo-induces temperature and/or charge-carriers density changes, within the diffraction limited spot. The material undergoes fast exchange dynamics of between various degrees of freedom. Electronic excitation (10–500 fs) is followed by carrier–carrier and carrier–phonon scattering/thermalization processes (500 fs–10 ps),<sup>[544]</sup> leading to changes in the dielectric function. A spatially overlapping, delayed, constant-intensity train of probe pulses monitors the induced nonlinear  $\Delta R$  by the detection of the high harmonics changes in the probe reflectance. The idea is illustrated in **Figure 35**. A comprehensive account on NPMR is found in a review chapter.<sup>[545]</sup>

The nonlinear components of reflection due to photomodulation (at  $\omega_m$ ) are demodulated at the corresponding harmonic frequencies ( $\omega_m, 2\omega_m, 3\omega_m, \dots$ ) in a lock-in amplifier. The  $n$ th harmonics components of the reflectivity scale with the

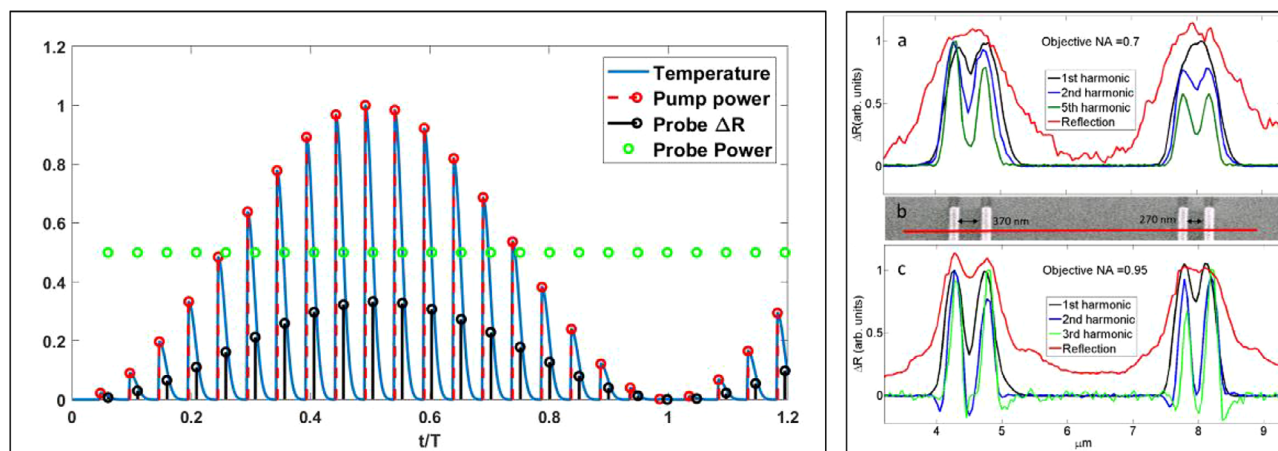


**Figure 35.** (Left) The essentials of NPMR. A train of intensity modulated pump pulses (red) is focused on a sample. Focused and position overlapping train of probe pulses (green), with constant intensity, are delayed by a few ps. The increase of the sample temperature, induced by the pump pulses give rise to changes in the probe reflectivity (blue line). The black dots represent the changes in the probe-reflectivity. The harmonics analysis of changes in reflectivity with a lock-in amplifier, provide the nonlinearity of the response. (Right) the improvement in resolution of at test sample increasing with the harmonics order. Reproduced with permission.<sup>[466]</sup> Copyright 2015 American Chemical Society.

nth power of the excitation. As a result, the effective PSF<sub>pp</sub> comprises of the product of PSF<sub>probe</sub> and that of the pump laser to the power of the nonlinearity order  $n$ ,  $PSF_{pump}^n$ . In all dimensions, the PSF<sub>pp</sub> scales down by  $\sqrt[n]{n}$  for Gaussian focused beams. By recording the NPMR while scanning the sample, super-spatial resolution is achieved. A pure sinusoidal modulation of the pump beam is needed to warrant that the weak nonlinear response originates solely from the physical response of the system. This purity is achieved by driving an Acousto-Optic Modulator (or other modulators) by an Arbitrary Waveform Generator, tuned to generate a pure sinusoidal light intensity modulation.<sup>[546]</sup> The short ( $\approx 100$ s) optimization process, reduces the harmonic distortion down to  $10^{-4}$ .

How about the optimal time scales? A short  $\approx 1$  ps pump pulse, is desirable to prevent the photo-excited spatial distribution of induced properties from diffusing and blurring the initial excitation profile. The time delay between pulses of the pump and the probe (P&P) should be optimized to match the relevant physical property (0–2 ps). The repetition rate of the P&P should allow

for a thorough electronic and thermal relaxation between subsequent pairs of laser pulses. A schematic view of the experimental system is presented in **Figure 36**.

SR using NPMR was first demonstrated on Si nanostructures,<sup>[543]</sup> and showed the reduction the PSF down to 85 nm (Figure 35 left). It was further applied to plasmonic structures of gold and  $V_2O_3$ . By its nature, NPMR excels in characterizing semiconductors and metals in vacuum, ambient and liquid, semi-transparent, and opaque systems. An equivalent, fluorescence-dependent SR technique, is SAX.<sup>[466]</sup> There, harmonics of the fluorescence, caused by saturating the modulated excitation, are detected.

## 20.2. Current and Future Challenges

One significant difficulty in a routine use of P&P technique is the need to spatially co-focus and fine-tune the delays of the P&P pulses, and eliminates the need for these adjustments.<sup>[547]</sup> In Single laser NPMR, the train of laser pulses is intensity modulated,

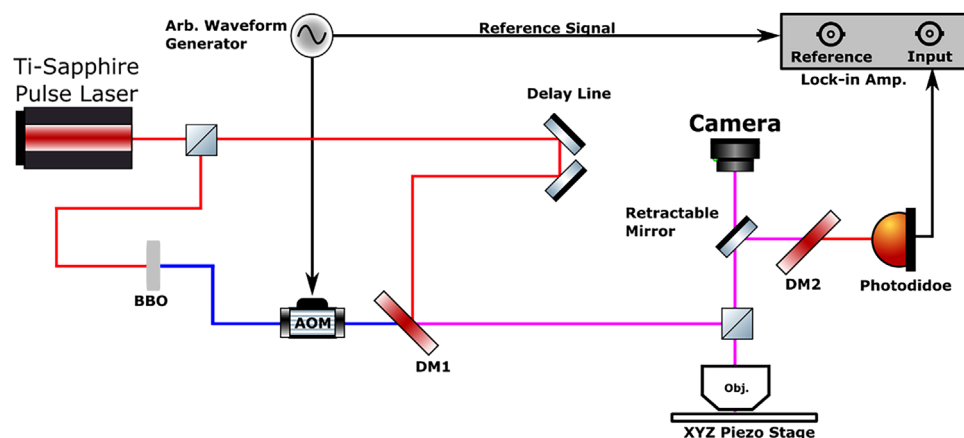


**Figure 36.** A schematic view of the experimental system. The role of the galvo mirror is to enable the combination of SPOM and NPMR.

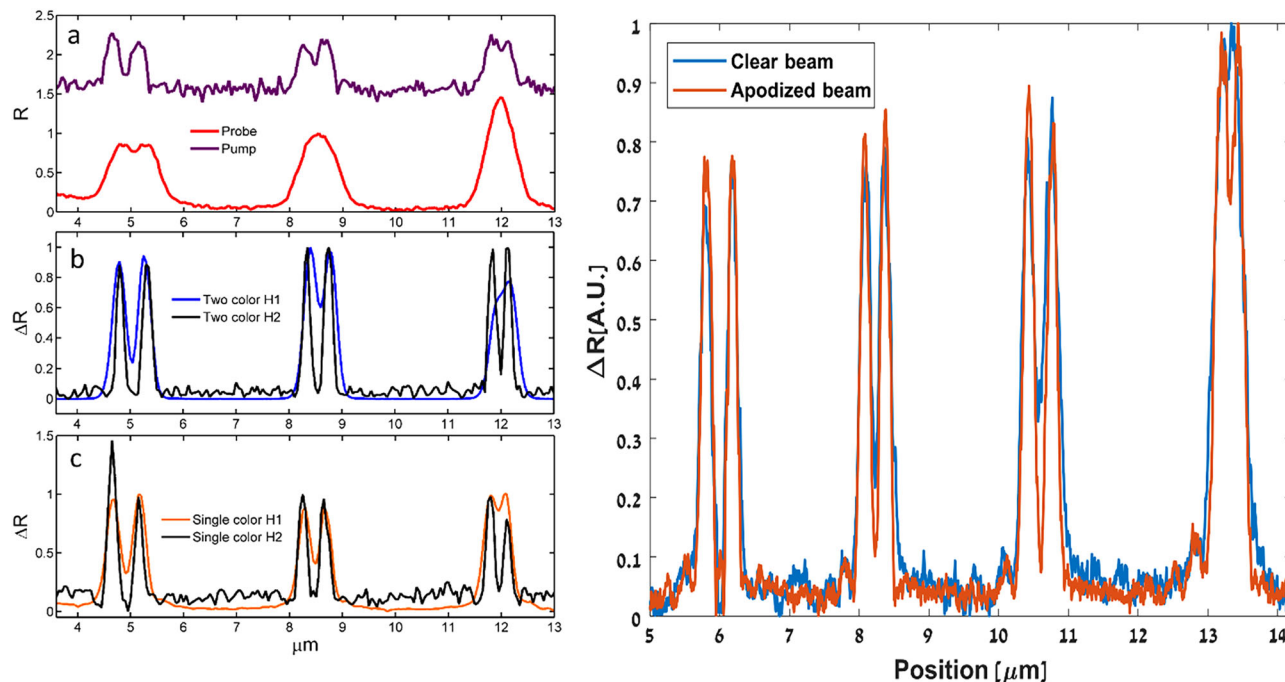


**Figure 37.** (Left) Super resolution Photo-modulated reflectivity using single color or two colors. The sample consists of Au double lines, 125 nm wide, with gaps of 370, 270, and 180 nm, respectively. a) Line imaging of probe reflection (red) and pump reflection (purple). b) Two-color photo-modulated reflectivity line imaging using first (blue), and second (black) harmonics. c) Single color photo-modulated reflectivity using first (orange), and second (black) harmonics. Note the resolution enhancement ( $95 \pm 5$  nm) at  $2\omega_1$  in both two and single-color modalities. Reproduced with permission.,<sup>[548]</sup> Copyright 2012, OSA Publishing. (Right) The effect of apodization: Line scan of SR target using clear beam (blue) and apodized beam (brown).

and its reflectance is measured at higher harmonics. The pump pulse excites the sample and the changes in its reflectivity are measured simultaneously. The measured  $\Delta R$  is a weighted average, of changed in reflectivity induced in early stages of the same pulse. This approach is lacking optimized P&P delay or optimized probe wavelength, and thus reduces the signal substantially. It is also highly dependent on the timescales of photo-excited dynamics in the examined samples. However, due to its simplicity, this modality may be beneficial to many applications, as depicted in **Figure 37** (left). A set of 100 nm thick, 125 nm wide pairs of gold stripes fabricated on Sapphire substrate, shows an equal resolution of  $95 \pm 5$  nm for the second harmonics of both single laser and P&P. We inferred that the reflectivity changes due to electron excitation in Au are fast enough (approximately 100 fs) to be detected by a single 2 ps pulse. In Silicon sample,  $\Delta R$  evolves slower ( $\approx 700$  fs) and is not probed efficiently by NMPR with a single 2 ps pulse.

In NPMR, the signal of high orders,  $n$ , degrades exponentially, while SR evolves as the  $\sqrt{n}$ . Therefore, we combined NPMR with other, efficient resolution enhancement modalities:

### 20.2.1. Spatial overlap modulation Nonlinear optical Microscopy (SPOM-NOM))

The enhancement of resolution in SPOM nonlinear optical microscopy (SPOM-NOM), is achieved by modulating the spatial overlap between two color pulses, and monitoring the nonlinear optical processes excited by a combination of two-color pulses.

SPOM-NOM was used for resolution enhancement in sum frequency imaging<sup>[548]</sup> or stimulated Raman scattering.<sup>[549]</sup> However, the point spread function of SPOM,  $PSF_{SPOM}$ , representing the second derivative of the diffraction limited PSF, suffers from artifacts resulting from its negative lobes.

The combination of NPMR with SPOM, while benefiting from improved resolution, dramatically reduces the negative lobes.<sup>[547]</sup> The combined PSF consists of the product of  $PSF_{pump}^n$  and  $PSF_{SPOM}$ . The negative lobes of  $PSF_{SPOM}$  overlap with low intensities in  $PSF_{pump}^n$ . In our studies, the probe was spatially modulated at  $\omega_{SPAT}$  using a mirrored galvanometer, while the intensity of the pump was modulated at  $\omega_m$  using the AOM. The co-demodulated signal at  $\omega_{ref} = n\omega_m + 2\omega_{SPAT}$  combines the integrated response of SPOM (second order) and NPMR. The incorporation of SPOM improved the resolution by  $\approx 15\%$ , down to  $85 \pm 5$  nm, in accordance with our simulation. It replaced additional 1–2 higher harmonics in NPMR, yet provided about tenfold higher signal. As simulated, the intrinsic negative lobes of the PSF of SPOM are significantly reduced due to the slimmer PSF of NPMR.

### 20.2.2. Resolution Improvement via Beam Shaping

So far, we based resolution enhancement on Gaussian diffraction-limited spots. However, by employing a phase and/or amplitude filter in the beam path, we can engineer a smaller central spot at the focal plane. The annular tails in the PSF, generated by such filters, are less pronounced in high orders of the  $PSF_{pump}^n$ , and are practically nulled in NPMR due



to lack of spatial overlap with a probe Gaussian beam. Spatial filters have demonstrated substantial improvement in resolution in confocal setups.<sup>[550]</sup> To prove the principle in NPMR, we used an annular gold amplitude mask.<sup>[551]</sup> to obtain a symmetric donut-shaped beam. Figure 37 (right) shows the effect of the beam apodization. In two scans we tested SR by measuring the second order NPMR, using a single color, linearly polarized, 400nm laser and a 0.95NA air objective. The resulting resolution was 155nm and 130 nm for the clear and the apodised beams respectively. This  $\approx 16\%$  reduction in the PSF width, matches the theoretical prediction. We emphasize that sophisticated beam shaping such as Bessel beams or super oscillation beams should further improve the resolution.

### 20.3. Advances in Science and Technology to Meet Challenges

Raman microscopy, with its material-specific spectral features, is a label-free counterpart to fluorescence microscopy. While Raman tip enhancement methods,<sup>[552]</sup> interleaved with scanning probe microscopy, provide rich information with nanometric resolution, they are confined to surface studies. Fujita and coworkers introduced a far-field combination of structured illumination and micro-Raman microscopy to achieve SR. We used photo-modulated nonlinear Raman scattering to achieve SR.<sup>[491]</sup> However, this approach proved impractical, due to its very low signals. The progress in resonance-enhanced time-gated Raman spectroscopy, with cross sections orders of magnitude higher, may resolve the problem and enable label-free SR with chemical recognition. In this modality only the interfering fluorescence is suppressed by time-gating the Raman signal to overlap with a subnanosecond excitation pulse.<sup>[553]</sup>

### 20.4. Conclusions

We have presented the essentials of NPMR for far-field, label-free, SR microscopy. Unlike some other modalities, in NPMR sample treatment or preparation is not required. NPMR is suitable to characterize variety of materials: at any wavelength that materials absorb, semiconductors, and metals, in vacuum or ambient, in liquids or solids.

While the signal of high orders,  $n$ , degrades exponentially, the incremental improvement in SR evolves as the  $\sqrt{n}$ . In order to enhance resolution it is practical to combine NPMR with other resolution enhancement modalities, as discussed. In any SR technique the sensitivity strongly declines with the size of the examined objects. One way to partially cope with this problem is to exploit resonance enhancement in NPMR. E.G. tuning the Probe wavelengths near to a plasmonic resonant wavelength, can enhance the sensitivity of measurements for specific sizes and materials.

## 21. Structured Illumination-Based Nonlinear Label-Free Super-Resolution Microscopy

(Mikko J. Huttunen\*, Stefan G. Stanciu)

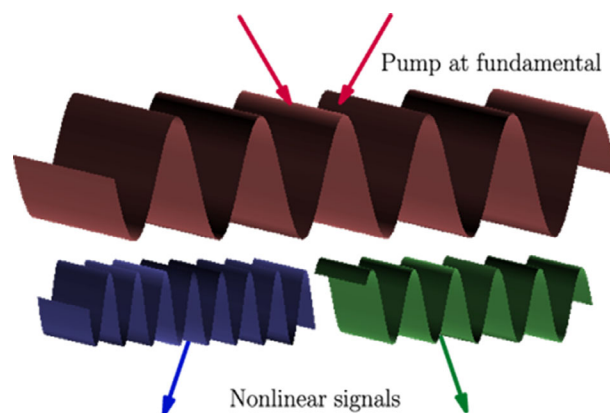


**Figure 38.** Schematic for nonlinear structured illumination-based super-resolution microscopy. By spatially modulating the incident/excitation fields, one can detect higher spatial frequencies associated with the sample. After reconstruction, an image with improved resolution can be formed.

### 21.1. Status

When objects are imaged using ultra-fast light sources with high peak-power, the occurring light-matter interaction may become nonlinear giving rise to novel contrast mechanisms that enable the imaging of various samples based on their intrinsic properties (Figure 38).<sup>[554]</sup> The main advantages of nonlinear optical microscopy, also known as multiphoton microscopy (MPM) are that **I**) the nonlinear processes provide novel, label-free contrast mechanisms, and **II**) it becomes easier to improve penetration depth by using longer wavelength excitation. Over the past years, an important focus of attention has been placed on the development of nonlinear super-resolution techniques, which are likely to lead to many interesting bioimaging applications for label-free nonlinear optics (NLO).<sup>[472]</sup>

Among the most widely used nonlinear microscopy techniques are those based on second-harmonic generation (SHG), third-harmonic generation (THG),<sup>[555]</sup> and coherent anti-Stokes Raman scattering (CARS).<sup>[556]</sup> The main advantage of these nonlinear optical processes is that they occur intrinsically in samples providing means to perform label-free imaging. The SHG signals originate from non-centrosymmetric molecules, with collagen, the most abundant protein in the human body, and the main constituent of the extracellular matrix, being one of them.<sup>[557]</sup> THG signals mainly originate from interfaces where sharp spatial variations of the refractive indices occur, enabling the imaging of lipid droplets and cellular membranes, among others.<sup>[558]</sup> The most flexible processes in terms of achievable contrast in NLO microscopy are coherent Raman scattering processes, such as CARS or stimulated Raman scattering (SRS), that provide true chemical contrast by allowing specific imaging of molecules whose chemical bond vibrational frequencies match with the difference of a pair of pump and probe beams.<sup>[559]</sup>

In addition to above, two-photon excitation fluorescence (2PEF) and three-photon excitation fluorescence (3PEF) processes, also largely popular in the context of NLO microscopy, can intrinsically take place in samples, provided that the

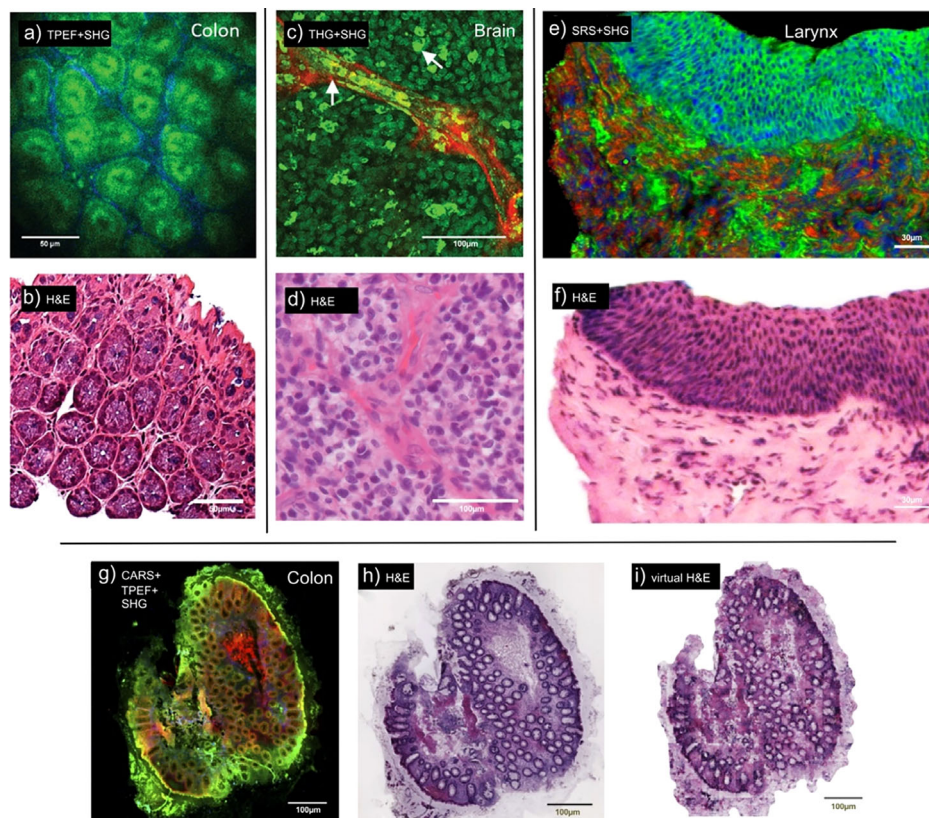


**Figure 39.** Label-free tissue imaging with non-linear optical microscopy modalities. a) TPEF+SHG and b) H&E images of murine colon. The TPEF+SHG image (green:TPEF, red:SHG) was collected ex vivo through an endomicroscopy objective. Adapted under the terms of the CC-BY license.<sup>[575]</sup> Copyright 2019, The Authors, published by Wiley-VCH GmbH. c) THG+SHG (green:THG, red:SHG) and d) H&E images of human brain affected by glioblastoma, showing hypercellularity, vascular proliferative changes, and aggregation of macrophages (arrows). Adapted under the terms of the CC-BY license.<sup>[555]</sup> Copyright 2019, The Authors, published by Wiley-VCH GmbH. e) SRS+SHG (green: lipids SRS@2845cm<sup>-1</sup>, blue: proteins SRS@2930cm<sup>-1</sup>, red: collagen SHG) and f) H&E images of laryngeal squamous cell carcinoma tissues. Adapted with permission.<sup>[559]</sup> Copyright 2019, Ivyspring International Publisher. g) CARS+TPEF+SHG (green:TPEF, red:CARS, blue:SHG), h) H&E and i) virtual H&E images of human colon. The virtual H&E image was computed from the NLO image using Deep Learning. Adapted with permission.<sup>[570]</sup> Copyright 2021, The Authors, published by Optica Publishing Group.

respective multiple of the pump wavelength coincides with some electronic transition present in the sample.<sup>[472]</sup> Most commonly, nonlinear autofluorescence is utilized to image reduced nicotinamide adenine dinucleotide phosphates[NAD(P)H]] and flavin adenine dinucleotides (FAD).<sup>[560]</sup> Particularly the ratio of these signals, known as the redox ratio, is commonly utilized to investigate metabolic cell activity, that can be linked to severe diseases/disorders such as to carcinogenesis.

The above-discussed nonlinear processes have already enabled many applications (Figure 39).<sup>[472]</sup> SHG microscopy is now commonly utilized to characterize collagen morphology of tissues, e.g. providing valuable information of fibrosis, wound healing and carcinogenesis.<sup>[561, 562]</sup> Incoherent multiphoton processes (2/3PEF) excel in calcium imaging, due to which combined 2/3PEF and THG microscopy are often used for in-vivo imaging of the brain.<sup>[563]</sup> In addition to the above applications, coherent Raman scattering techniques, particularly CARS microscopy, have been found to be useful e.g. in time-resolved analysis of lipid droplet growth, assembly and composition.<sup>[556]</sup> As shown in several landmark works, coherent Raman modalities are highly complementary to NLO techniques based on autofluorescence and harmonic generation (Figure 39).

## 21.2. Current and Future Challenges

The most obvious challenges to address in label-free nonlinear imaging are *imaging speed*, *penetration depth*, and achievable *resolution*. The latter challenge can be alleviated to a degree by utilizing structured-illumination-based super-resolution techniques,<sup>[72, 564–566]</sup> such as image scanning microscopy (ISM) or rescan microscopy.<sup>[73, 567, 568]</sup> The achievable resolution improvement depends on the order of the nonlinear process and of the technique used, but in essence  $\approx 100$  nm resolution is already achievable for some NLO modalities.<sup>[569]</sup> A major challenge is to develop techniques that could further improve the achievable lateral resolution to the range of values (<20 nm) now already available in super-resolved fluorescence microscopies based on contrast-agents. However, in terms of current and future challenges, lateral resolution is only a single figure of merit that limits the emergence of novel applications. Many of the nonlinear structured-illumination microscopy techniques are based on widefield configuration resulting in somewhat poor axial resolution.

In addition to axial resolution, in some imaging applications, e.g. intravital imaging, the penetration depth is as well an

important parameter. Nonlinear microscopy modalities in general are advantageous in this respect because absorption and scattering of incident light can be considerably decreased when moving to longer pump wavelengths.<sup>[571]</sup> However, it has turned out to be very challenging to combine high ( $\approx 100$  nm) spatial resolution with long ( $> 100$   $\mu\text{m}$ ) penetration depths.<sup>[569]</sup> Furthermore, even when compromises in resolution can be accommodated, imaging deep tissues (e.g.,  $< 1$  mm) is still a major problem. Improvements in deep tissue imaging with high resolution can be expected to take place by advances in machine learning and artificial intelligence-based methods.

The demands of imaging are also shifting towards large-area and volumetric imaging.<sup>[572, 573]</sup> For example in histopathologic applications, whole slide imaging using more conventional imaging modalities, that have been combined with automated image processing approaches based on artificial intelligence are quickly becoming commonplace.<sup>[574]</sup> It can be expected that similarly also MPM modalities will be developed to stages, where large-area imaging becomes a default option. In addition to whole slide imaging, an upcoming trend in histopathology seems to be the shift to volumetric imaging, which has many advantages over traditional approaches that rely on imaging microns thick sample sections. In short, never-ending need for speed exists.

A final challenge that many of the nonlinear super-resolution microscopy techniques face is that the achievable contrast mechanisms in label-free imaging are somewhat restricted subsequently limiting the potential imaging applications. Fortunately, MPM modalities have already found many niche applications. However, the limited contrast admittedly restricts to some extent the applicability of developed techniques.

### 21.3. Advances in Science and Technology to Meet Challenges

With current knowledge, it seems likely that the lateral resolution cannot be improved much below the  $\approx 100$  nm limit, unless new ideas to circumvent the diffraction limit emerge. However, many of the current imaging applications might not benefit dramatically from improved *lateral* resolution. Instead, improvements in the *axial* resolution are highly desirable. This challenge could be remedied for example by combining structured-illumination microscopy with the temporal focusing scheme,<sup>[569]</sup> or by using laser-scanning structured illumination microscopy (SIM) or nonlinear image scanning microscopy (ISM).<sup>[568]</sup>

The limitations in the achievable penetration depth are another major existing challenge in bioimaging applications. A straightforward, although technologically non-trivial solution is to continue nudging the excitation and emission wavelengths towards longer wavelengths inside the second near-infrared region (NIR-II, 1000–1700 nm),<sup>[571]</sup> where water absorption is however an important challenge to address, together with losses in resolution. Here, further development of commercially available and affordable ultrafast laser systems seems necessary, facilitating new research groups and imaging facilities to acquire/build NIR-II capable nonlinear imaging systems.

Enhancing the penetration depth is also extremely relevant to current NLO endomicroscopy efforts, which suggest that we

are not far from a next generation of NLO tomographs capable of imaging not only easily accessible body parts, such as skin, but also other parts of the human body that can benefit of NLO contrast and resolving power, such as the gastrointestinal tract (Figure 39a).<sup>[575]</sup> However, additional progress in miniaturization is obviously required in order to probe internal organs, such as the heart, kidney, lungs, liver, etc., that have been thoroughly discussed in the context of ex-vivo NLO imaging. Furthermore, in-vivo imaging is particularly dependent on imaging speed, to be discussed below. This is because internal organs have their inherent movement due to blood circulation, which yields motion artifacts. Avoiding these issues requires high-speed scanning, which poses additional complications compared to enhancing imaging speeds of bench-top systems.

Steady improvements in the imaging speeds will likely take place by further development of imaging systems. The most straightforward approach is to move away from single-point scanning modalities towards multi-point, line-scanning or even widefield modalities.<sup>[572, 573]</sup> Furthermore, widefield techniques could be made considerably faster by more widespread use of low/medium repetition rate amplified laser systems, that would allow reaching  $\approx 100$  GW  $\text{cm}^{-2}$  illumination peak intensities while still keeping mean powers compatible with live imaging.<sup>[573]</sup>

The final challenge mentioned above concerns the limited contrast mechanisms that arise in label-free imaging applications. Most of nonlinear imaging modalities (SHG, THG, 2PEF, and 3PEF) provide contrast only towards quite specific cell and tissue types. However, smart control of the polarization state of the excitation and/or emission beams might provide new possibilities, particularly when coherent SHG and THG modalities are used.<sup>[576]</sup> In the longer run, further development of coherent Raman scattering techniques, such as CARS and SRS, seems however a more probable remedy for the limited contrast.<sup>[556]</sup> In addition, the challenges associated with limited contrast and subsequent interpretation of the NLO images are already being alleviated by the emergence of artificial intelligence methods for digital staining, e.g., based on generative adversarial networks.<sup>[570]</sup> These allow the translation of raw NLO images, which can be cumbersome to interpret even by experts, into versions that closely resemble traditional histopathology images, and whose content is therefore highly accessible (Figure 39g–i). Furthermore, artificial intelligence has also been demonstrated as having interesting potential for NLO based automated histopathology.<sup>[559, 562]</sup>

### 21.4. Conclusions

The field of label-free non-linear optical microscopies has witnessed important progress over the past years, and a wide palette of applications has been reported to date. Advances will take place with further technology development. Particularly promising are the recent activities where artificial intelligence and computational imaging approaches are combined with state-of-the-art imaging techniques. One can envisage that soon non-linear label-free large-scale imaging techniques become standard techniques that e.g., facilitate human patient diagnosis both ex-vivo and in-vivo.



## Theme IV: Advanced Superlens Designs

### 22. Surface Electromagnetic Wave Lenses and Transformation Optics

(Vera N. Smolyaninova, Igor I. Smolyaninov\*)

#### 22.1. Introduction

Starting from early 2000s several novel and important research directions have developed in label-free super-resolution optical microscopy,<sup>[577]</sup> which are quickly demolishing the resolution limit of conventional optical microscopy due to diffraction. The first one is making use of nonlinear optics.<sup>[287]</sup> In general, the nonlinear optical microscopy techniques implement photo-switching of and saturation of fluorescence down to single molecule level, so that spatial resolution of the order of 20 nm is achieved. However, these techniques rely on spatial scanning of either samples or light sources, which is a relatively slow mechanical process. During approximately the same time considerable progress in transformation optics, plasmonics,<sup>[578]</sup> and metamaterials<sup>[122]</sup> enabled drastic improvement in spatial resolution of conventional linear far-field optical microscopy. First, John Pendry realized that negative refractive index metamaterials may be made into a flat “perfect lens,” so that high-resolution (almost perfect) optical images could be obtained due to negative refraction. Such a perfect image is formed by the amplified evanescent waves (or surface plasmons) which exist at the boundaries separating the positive and negative index materials. Recent examples of the experimental realization of this approach may be found in.<sup>[579]</sup> However, the magnification of a planar “perfect lens” is limited to 1. A major step to bypass this limitation was achieved by the development of surface plasmon-assisted microscopy,<sup>[124]</sup> in which image magnification in two spatial dimensions has been demonstrated in the geometric optics limit. Soon it was realized that the improved spatial resolution of 2D plasmonic microscopy relies on the “hyperbolic” dispersion law of surface plasmons, which may be expressed as

$$k_{xy}^2 - |k_z|^2 = \frac{\epsilon_d \omega^2}{c^2} \quad (23)$$

where  $\epsilon_d$  is the electric permittivity of the metal film substrate,  $k_{xy} = k_p$  is the component of the plasmon wave vector along the propagation direction, and  $k_z$  is the wave vector component (exponential decay constant) in the perpendicular direction. This approach was further developed in the “optical hyperlens” designs by Narimanov et al.<sup>[126]</sup> and Engheta et al.,<sup>[127]</sup> which make use of a concentric arrangement of multiple thin metal and dielectric cylinders, which form a hyperbolic optical metamaterial. Such a metamaterial arrangement results in a strongly anisotropic tensor of dielectric permittivity, in which the radial  $\epsilon_r$ , and the tangential  $\epsilon_\theta$  tensor components have opposite signs. The dispersion relation of such a metamaterial

$$\frac{k_r^2}{\epsilon_\theta} - \frac{k_\theta^2}{|\epsilon_r|} = \frac{\omega^2}{c^2} \quad (24)$$

does not exhibit any diffraction limit. Light propagates through such a hyperbolic metamaterial in the form of well-defined radial

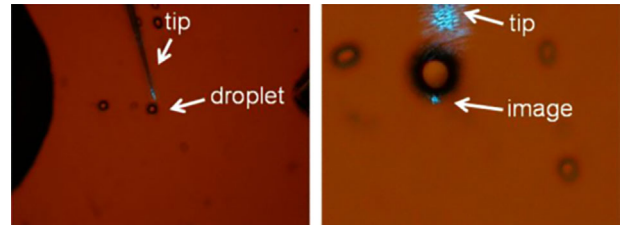


**Figure 40.** When a glycerin microdroplet is illuminated near its edge with a tapered fiber tip, an image of the tip may be seen at the opposite edge of the microdroplet. Adapted with permission.<sup>[131]</sup> Copyright 2010, The Optical Society.

rays. If a radiating sample is placed near the inner rim of such a hyperlens structure, the lateral separation of rays radiated by the sample increases towards the outer rim, thus providing image magnification. Such magnifying hyperlenses were realized in both 2D and 3D configurations.<sup>[212, 580, 581]</sup> Far-field optical resolution of at least 70 nm has been achieved using a 2D plasmonic hyperlens. The goal of this paper is to outline further promising directions in 2D microscopy, which would potentially move the resolution scale of linear far-field optical microscopy toward the 10 nm scale and beyond. We anticipate that this may be accomplished by using the newly discovered class of surface electromagnetic waves which propagate along gradual interfaces of lossy optical media.<sup>[582, 583]</sup>

#### 22.2. Two-Dimensional Transformation Optics

As mentioned above, a plasmonic microscope used in the 2D geometric optics mode may exhibit considerably increased spatial resolution compared to the conventional three-dimensional microscopes. This is an expected result, since operation of plasmonic microscopes relies on the hyperbolic dispersion law—see Equation (23). In an additional recent development, we also showed that such transformation optics (TO) devices as various invisibility cloaks, which require quite sophisticated spatial profiles of anisotropic electric permittivity and magnetic permeability, may be emulated by microfabricated tapered waveguides and micro-droplets.<sup>[131]</sup> This interesting fabrication shortcut results in broadband low-loss performance of the TO devices in the visible frequency range, which is very difficult to achieve by conventional means. Moreover, the same approach was successfully applied to fabrication of the inverted Eaton and Maxwell fisheye microlenses,<sup>[131]</sup> which were recently introduced as superb imaging devices, which do not require negative refraction.<sup>[130]</sup> For example, a refractive index distribution which needs to be emulated in a microdroplet or a microlens so that a resulting 2D device would act as an inverted Eaton lens is described by the following equation:

$$n = 1 \text{ for } r < R, \text{ and } n = \sqrt{\frac{2R}{r} - 1} \quad (25)$$

This refractive index distribution may be emulated by varying the microdroplet thickness, as described in.<sup>[131]</sup> An example of such a microdroplet-based Eaton lens is shown in **Figure 40**.

As illustrated in **Figure 41**, two segments of the Eaton lens which have different magnitudes of parameter  $R$  can be



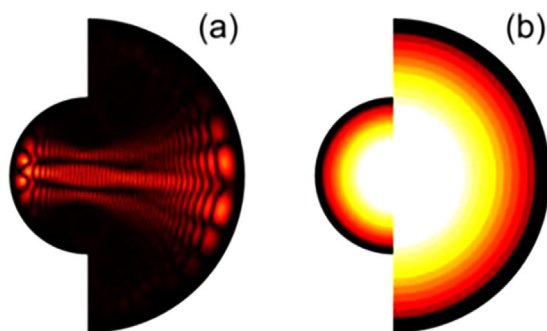


**Figure 41.** Numerical simulations of image magnification ( $M = R_1/R_2 = 2$ ) using a compound inverted Eaton lens. Adapted with permission.<sup>[131]</sup> Copyright 2010, The Optical Society.

combined in order to achieve image magnification. In such a configuration the image magnification equals  $M = R_1/R_2$ , while the image resolution is defined by the wavelength of the optical mode (regular light or surface plasmon) which is used in the imaging device. We should also note that near-field image magnification has been proposed in recent experiments with high-index liquid-immersed microspheres.<sup>[584]</sup>

### 22.3. Towards Nanometer-Scale Resolution using Novel Surface Wave Modes

The familiar examples of surface electromagnetic waves include surface plasmons, which may exist at sharp interfaces between metals and dielectrics,<sup>[578]</sup> and Zenneck waves, which may exist at surfaces separating highly lossy conductive media and lossless dielectrics. However, consideration of a “more physical” situation in which the electric permittivity (or conductivity) of a material changes continuously across some gradual interface, leads to appearance of a new class of deeply subwavelength surface waves.<sup>[582, 583]</sup> It appears that low-loss surface electromagnetic waves may exist at planar gradual interfaces between lossy media, even if the dielectric losses are very high on both sides of the interface. This very recent and highly unexpected result seems to be applicable to most any electromagnetic frequency range from the very low frequencies (VLF) of radio waves all the way up to the UV light. The TM wave equation in such cases takes the form of a one-dimensional Schrodinger equation

$$-\frac{\partial^2 \Psi}{\partial z^2} + \left( -\frac{\epsilon(z)\omega^2}{c^2} - \frac{1}{2} \frac{\partial^2 \epsilon}{\epsilon \partial z^2} + \frac{3(\partial \epsilon / \partial z)^2}{\epsilon^2} \right) \Psi = -\frac{\partial^2 \Psi}{\partial z^2} + V\Psi = -k^2 \Psi \quad (26)$$

where the wave function is introduced as  $E_z = \psi / \epsilon^{1/2}$ . Note that for the TM wave the effective potential energy  $V(z)$  near the interface between highly lossy media may become almost purely real even if “ $\epsilon''(z) \gg \epsilon'(z)$ ”. This is happening if the gradient terms dominate in Equation (26). It appears that such materials as graphite and silicon (which have almost purely imaginary  $\epsilon$  in the UV range) appear to be highly suitable for UV nanophotonics applications. As illustrated in **Figure 42**, the typical wavelengths of these newly discovered surface waves appear to fall into a few nanometers range, while propagation length of these waves

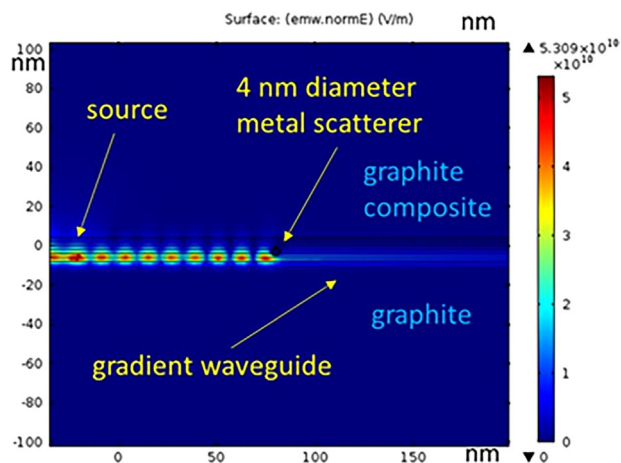


**Figure 42.** Numerical modeling of excitation and scattering of surface electromagnetic waves in a gradient waveguide made of doped graphite at  $\lambda_0 = 275$  nm. The guided UV field propagating through the waveguide is scattered by a 4 nm diameter metal nanowire which is located near the waveguide.

may be much larger than the skin depth in a homogeneous lossy medium.<sup>[212]</sup> As a result, these novel surface waves and the 2D microscopy arrangements described above appear to be ideal to further push resolution of the far-field linear optical microscopy techniques down to nanometer scale.

### 22.4. Conclusions

We have described several examples of two-dimensional super-resolution microscopy devices, which may be nanofabricated and studied using currently available modern fabrication techniques. These devices achieve 70 nm spatial resolution with conventional surface plasmons, which far exceeds resolution of conventional optical microscopy. Utilization of the newly discovered class of surface electromagnetic waves which propagate along gradual interfaces of lossy optical media should further bring the spatial resolution of 2D microscopes down to 10 nm scale and beyond. While the material base of nanophotonic devices using surface plasmons is limited to a few low-loss materials such as good metals and some oxides, the novel class of surface waves is supported by a much larger number of highly lossy media. In particular, such lossy materials as graphite and silicon may be ideal materials to use in UV nanophotonics applications.

## 23. Perfect Imaging

(Ulf Leonhardt\*, Sahar Sahebdivan\*)

Richard Feynman<sup>[585]</sup> questioned the diffraction limit of imaging, for a simple physics reason: the propagation of light is reversible. The equations that govern the light propagation, Maxwell’s equations, are time-reversible. Changing the sign of the magnetic-field components in an electromagnetic wave would send the wave back to where it came from. If it was emitted from a point source it would, upon time reversal, focus with point-like precision. One may object that sending light back to its

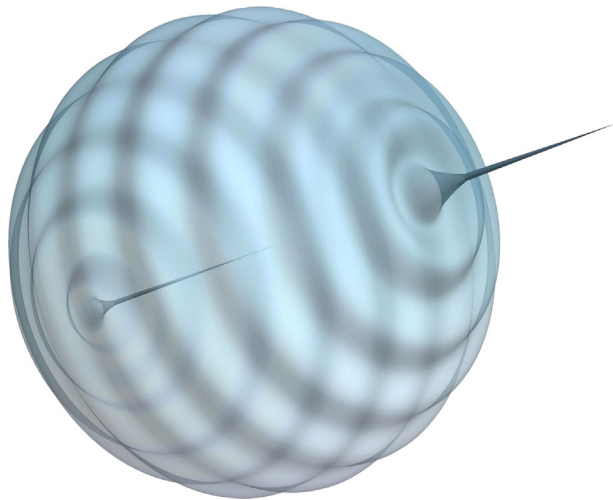


**Figure 43.** Wave propagation on the surface of a sphere. The wave is emitted from a point source at some point on the surface. While propagating, the wave initially expands but then focuses on the point antipodal to the source. If the wave gets absorbed at the image the focus has point-like precision as the peaks show.

source does not qualify as imaging, as the source and the image are the same. But, manipulating both the electric and the magnetic field, we may deflect the light and let it reverse to a different point, forming a distinct, perfect image there.

The diffraction limit is not a fundamental law of nature, but rather a feature of conventional lenses – that is Feynman's argument.<sup>[585]</sup> Yet there is a counter-argument: for time reversal, it is not enough to reverse the field, the source must be reversed, too. Suppose we only reverse the field and then let it focus in empty space. An incoming spherical wave  $(4\pi r)^{-1}e^{-ikr}$  with wavenumber  $k$  produces the outgoing wave  $-(4\pi r)^{-1}e^{ikr}$  where the sign describes the reflection of light. The interference between the incoming and the outgoing wave gives a focal spot proportional to  $\text{sinc}(kr)$ , which agrees with the diffraction limit! However, if we also reverse the source, no outgoing wave is there and the light is perfectly focused, as has been experimentally demonstrated.<sup>[586]</sup> Reversing the source is easy: instead of an emitter, we just need an absorber. The absorber takes out the incident wave and records the image. Even if only a small part of the incident light is absorbed, that part is perfectly focused. Perfect imaging is possible in principle.

Whether perfect imaging is possible in practice depends on the practicalities of time-reversing the field. For microwaves<sup>[128]</sup> one can use an array of receivers, electronics to conjugate the field, and emitters to send it back. However, there is a way to do all this passively, with gradually varying index media. It makes use of the connection between dielectric media and geometries.<sup>[587]</sup> Imagine that light is confined to the surface of a sphere (**Figure 43**). Suppose a light wave is emitted from one point on the sphere, say the South Pole. The outgoing wave expands until it contracts and focuses on the North Pole, as if it got time-reversed while crossing the Equator. Obviously, this is also true for all other source points: any point on the sphere is perfectly imaged at its antipodal point (**Figure 43**). The curved space of the sphere performs the time-reversal required for perfect imaging.

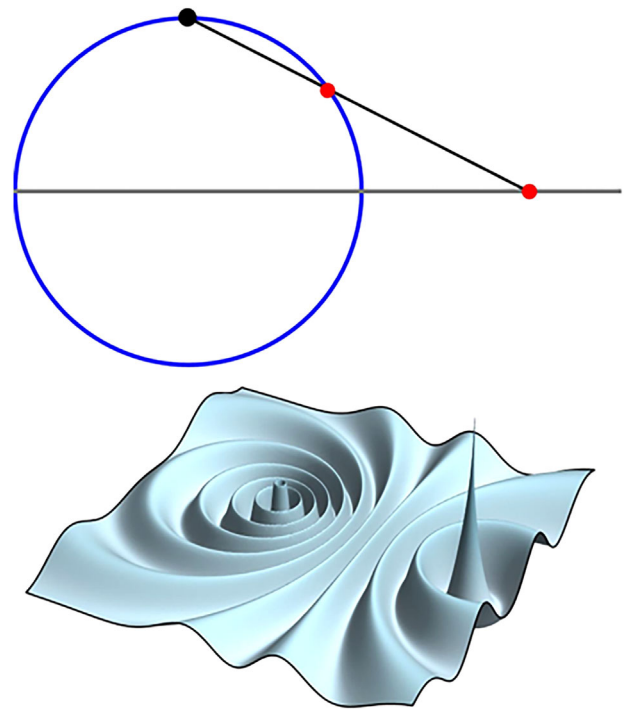


**Figure 44.** Stereographic projection. In the stereographic projection, a line is drawn from the North Pole of the sphere to the point to be projected. Where this line intersects the plane through the Equator lies the projected point. The top picture shows the stereographic projection in a cut through the sphere. The lower picture shows the wave on the sphere (**Figure 1**) projected accordingly. The stereographic projection is a conformal map that preserves angles and just distorts distances. An isotropic material does the same. In particular, Maxwell's fish eye<sup>[9]</sup> acts like a sphere in stereographic projection.<sup>[8]</sup> As light can be perfectly focused on a sphere (**Figure 43**) it can be perfectly focused in Maxwell's fish eye,<sup>[130]</sup> too, provided the image gets absorbed and does not interact with the source.<sup>[601, 603]</sup>

Curved geometries like the surface of the sphere affect the diffraction limit in another way as well: they modify the uncertainty relation between position and momentum.<sup>[588, 589]</sup> In the absence of sources and drains – and without curvature – the diffraction limit follows from the uncertainty relation.<sup>[590]</sup> So curved spaces will modify the resolution of imaging. However, this effect goes away in the limit of a large radius of curvature, whereas the sphere, how large it may be, would, in the presence of source and drain, time-reverse and perfectly focus light.

Now, curved spaces like the sphere can be implemented with dielectric media.<sup>[587]</sup> In the stereographic projection<sup>[587, 591]</sup> (**Figure 44**) the surface of the sphere is projected onto the plane. Here a variable measure of length plays the role of the curved two-dimensional surface in three-dimensional space. The measure of length is the refractive index. For implementing a sphere in the  $(x, y)$  plane in appropriate units we need the index profile<sup>[591]</sup>  $n = 2n_0/(1 + x^2 + y^2)$ . Maxwell himself wrote down<sup>[592]</sup> such a profile and noticed that light rays go in circles in it and are perfectly focused. Much later it was shown<sup>[130, 593]</sup> that not only rays but waves are perfectly focused, too. Maxwell's profile<sup>[592]</sup> is known as Maxwell's fish eye, because such gradually varying index media reminded Maxwell on the eyes of fish. It is the archetype of

absolute optical instruments<sup>[594]</sup> where from any given point in the source region all rays focus at one or several points in the imaging region.

Absolute optical instruments come with restrictions: they cannot really magnify or, to be more precise, their magnification is given by the ratio of refractive indices around the image and the source. Furthermore, both the object and the image lie inside the device like the focal points in an elliptical mirror, except that for an absolute optical instrument all source and image points are foci.

Absolute optical instruments capable of perfect imaging require a considerable index range. In the case of Maxwell's fish eye, the device is infinitely extended and the index goes to zero at infinity. Luckily, one can modify the fish eye<sup>[130]</sup> by surrounding it with a mirror at the unit circle (in device units) without compromising its functionality,<sup>[130]</sup> which makes the device finite and confines the index range to  $\{n_0, 2n_0\}$ . Achieving a factor of two in index modulation is still difficult to implement by doping a material, but it can be done with planar waveguides in silicon photonics.<sup>[595]</sup> Here the thickness of a silicon layer on silica plays the role of the refractive index; with variable thickness one can implement refractive-index profiles like Maxwell's fish eye.<sup>[595]</sup>

Does perfect imaging work? The community reacted with considerable skepticism<sup>[596]</sup> after the idea was proposed.<sup>[596]</sup> The lively discussion in the literature has been very helpful in refining and clarifying the ideas, but the ultimate test of any physics idea is the experiment. Two types of experiments<sup>[597–599]</sup> were performed, both with microwave radiation. In the first,<sup>[597]</sup> the spherical geometry (Figure 43) was implemented for microwaves. The waves were confined between two closely spaced spherical mirrors such that they effectively propagated on the surface of a sphere. Radiation was injected at one point by a cable and extracted by another cable movable around the image position. At well-defined resonances, radiation was only transmitted when the source and the detector were aligned with  $1/105$  wavelength precision. This proves that perfect imaging works, but apparently only at resonance frequencies.<sup>[600, 601]</sup>

In the second set of experiments,<sup>[598, 599]</sup> modified fish eyes were made using microwave metamaterials. Two coaxial cables inserted at the image points served as sources, and an array of cables as detectors in the imaging area. The detectors appeared to have resolved the two sources, despite them being considerably closer to each other than half a wavelength. However, the results were not reproducible in computer simulations. Furthermore, the figure of the main experimental results showed a subtle inconsistency. The plotted intensities of the image points were perfectly symmetric, although the sources were not. As was later confirmed,<sup>[602]</sup> only half of the image data were plotted and the other half were “not measured”. According to Ref. [602] the image values were “assumed to be symmetrical” while, at the same time, the two sources were given different phases, making the field naturally asymmetrical.

Why did the experiments in Refs<sup>[598, 599]</sup> not work? The problem was that the detectors were acting back onto the sources.<sup>[601]</sup> Both the sources and the detectors were cables connected to a microwave synthesizer. The sources were not just transmitting a fixed amount of radiation, but they were also receiving radiation reflected at the sources and they were reacting to it. In Feynman's objection to the diffraction limit, there is a clear causal distinc-

tion between source and image. The source emits first, then the radiation is focused by effective time reversal, and the image is taken last. In the experiments in Refs<sup>[598, 599]</sup> the image acts back onto the source as if the future would act back onto the past, messing up the causal order between source and image. Only at well-defined sharp resonances, like in the experiment on the sphere,<sup>[597]</sup> no radiation is reflected and all radiation goes through from the sources to the detectors with perfect resolution.<sup>[601]</sup>

Despite a few caveats,<sup>[601]</sup> one may still agree with Feynman<sup>[585]</sup> that here is no fundamental reason why perfect imaging should not work. The experiments<sup>[597–599, 602]</sup> and their analysis<sup>[600, 601, 603]</sup> have highlighted a crucial requirement for achieving subwavelength resolution with absolute optical instruments: the field reflected at the detectors must not interact with the sources. If this is guaranteed then perfect resolution is perfectly possible.

## 24. Microsphere Superlens and Metamaterial Solid Immersion Lens

(Zengbo Wang\*, Boris Luk'yanchuk, Limin Wu)

### 24.1. Status

In 2011, super-resolution imaging by microsphere superlens emerged as a simple yet effective method to overcome the diffraction limit that limits the resolution of conventional lenses.<sup>[136]</sup> Significant progress has since been made. Here, key advances including the development of scanning superlens system, metamaterial solid immersion lens (mSIL), super-resolution physics, and bio-superlens are discussed along with the challenges in this field. For more detailed review on the technique and other superlens applications in interferometry, endoscopy, and others, please refer to refs. [604, 605].

### 24.2. Microsphere Nanoscopy

#### 24.2.1. Overview

The field of microsphere superlens research dates back to 2000 when it was discovered that a microsphere could generate subwavelength focus.<sup>[606]</sup> This effect became known as ‘photonic nanojet (PNJ)’ since 2004 and was widely used in laser cleaning, laser direct nano-writing and signal enhancement,<sup>[605]</sup> among other applications. The achievement of 80 nm resolution in laser patterning by microsphere<sup>[607]</sup> motivated the research on microsphere nanoscopy, first published in 2011.<sup>[136]</sup> As shown in Figure 45a, the technique uses microsphere as superlens to image the contacting nanoscale objects. The superlens collects and transforms the near-field evanescent waves, which carry the high-spatial-frequency information about the object, into the propagating waves reaching the far-field and leading to a formation of a magnified virtual image. The evanescent-to-propagating-conversion (ETPC) efficiency determines the final imaging resolution.<sup>[608]</sup> Further improvement of the resolution can be accomplished by enhancing the ETPC efficiency. These ideas motivated the development of the mSIL superlens



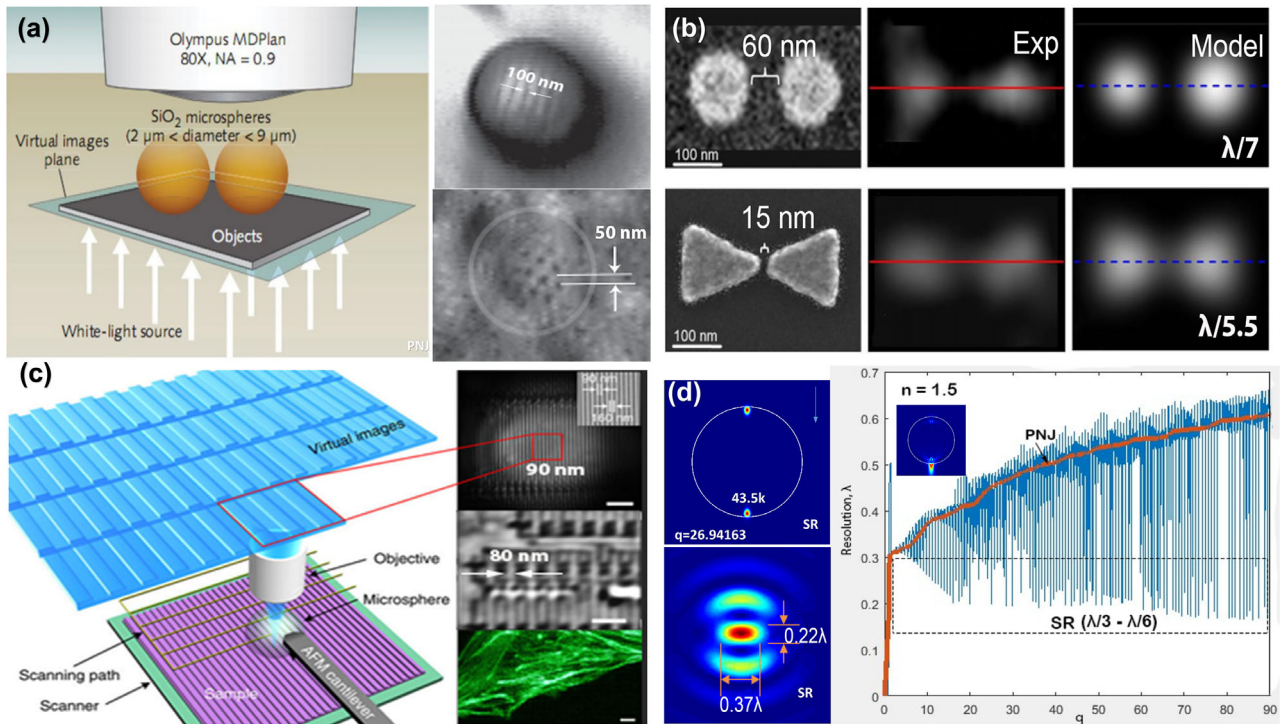


**Figure 45.** Microsphere nanoscopy. a) Contact mode setup and imaging examples (50–100 nm samples). Reproduced with permission.<sup>[136]</sup> Copyright 2011, Springer Nature. b) Resolution analysis by the PSF convolution method ( $\lambda = 405$ , confocal mode). Reproduced with permission.<sup>[138]</sup> Copyright 2015, Wiley-VCH. c) Non-contact scanning superlens imaging setup and examples (microsphere attached to AFM tip, sample: 80–90 nm nanodevices, and fluorescent-labeled actin filament). Reproduced with permission.<sup>[612]</sup> Copyright 2016, Springer Nature. d) SR mode demo at size parameter  $q = 26.94164$  with peak value  $\approx 43.5k$  and theoretical resolution  $\approx \lambda/3 - \lambda/6$  for  $n = 1.5$ ,  $q = 0-90$  microspheres.

discussed below, which provides improved ETPC efficiency with enhanced optical super-resolution and imaging quality.<sup>[144]</sup>

In contact mode, the microsphere superlens can resolve 50–100 nm scale objects (e.g., nanostructures and devices (Figure 45), subcellular structures and adenovirus<sup>[609]</sup>) using a wide-field microscope. Smaller features, i.e., 15–25 nm nanogaps, can be resolved with superlens under a confocal microscope.<sup>[138, 610]</sup> Since resolution of an imaging system is often characterized by the point spread function (PSF) instead of by the minimal resolvable feature sizes, Allen et. al. developed a convolution-based resolution analysis method and derived the best resolution for microsphere nanoscopy is  $\approx \lambda/6 - \lambda/7$  (Figure 45b).<sup>[138]</sup> A higher estimation for resolution of  $\lambda/8$  could be obtained if the final image's contrast is adjusted for clarity before convolution, giving calibrated resolution of  $\approx \lambda/6 - \lambda/8$  for the technique. Such method is now widely used to calculate the PSF resolution for the superlens, which avoids exaggerated resolution claim beyond  $\lambda/10$  based on the minimal resolvable feature sizes.

In non-contact mode, resolution of the superlens drops rapidly when particle-sample distance ( $\Delta z$ ) increases, from  $\lambda/7$  at  $\Delta z = 0$  (contacting) to  $\lambda/3.8$  at  $\Delta z \approx \lambda/2$  (half wavelength). Super-resolution typically degrades if the distance exceeds one wavelength. Extending the working distance (WD) of a superlens is a major challenge for this technique which is discussed later.

A variety of microspheres have been used as superlenses for imaging, including BaTiO<sub>3</sub> (BTG), Polystyrene (PS) and SiO<sub>2</sub> microspheres with typical size between 3 and 80 μm. For an optimum imaging, the optical contrast (OC, i.e., refractive index ratio

between microsphere and surrounding media) is recommended within 1.4–1.75.<sup>[136, 611]</sup> Therefore, for high-index microspheres such as BTG ( $n = 1.9-2.1$ ) and others, an immersion media (e.g., water or transparent resin) is often used to optimize the OC to maximize the performance.

#### 24.2.2. Scanning Superlens

The ability to position microsphere superlens at desired location and scanning over an area are essential for practical applications. Single microsphere has a narrow field-of-view (FOV), scanning is utilized to expand FOV for imaging larger-area and for dynamic imaging. Several scanning schemes have been demonstrated, such as integration with AFM system<sup>[612]</sup> and encapsulation of microsphere in solid film.<sup>[138]</sup> Figure 45c shows the AFM-based scanning superlens system built by attaching a microsphere to an AFM tip and use precision motion system of AFM to control particle-sample distance and scanning across the sample surface. The system can work in both contact and non-contact scanning modes. A  $96 \times 96 \mu\text{m}^2$  sized sample image was obtained in 3 mins with super-resolution at  $\lambda/6.3$  level for 80–90 nm objects, which is about 200 times faster compared to the ordinary AFM. Another scanning approach is to bond the microsphere directly with the objective lens to form a unibody design,<sup>[613]</sup> which was used in commercial microsphere nanoscope developments.<sup>[614]</sup> The resolution of commercial systems is limited to  $\approx 137-150$  nm



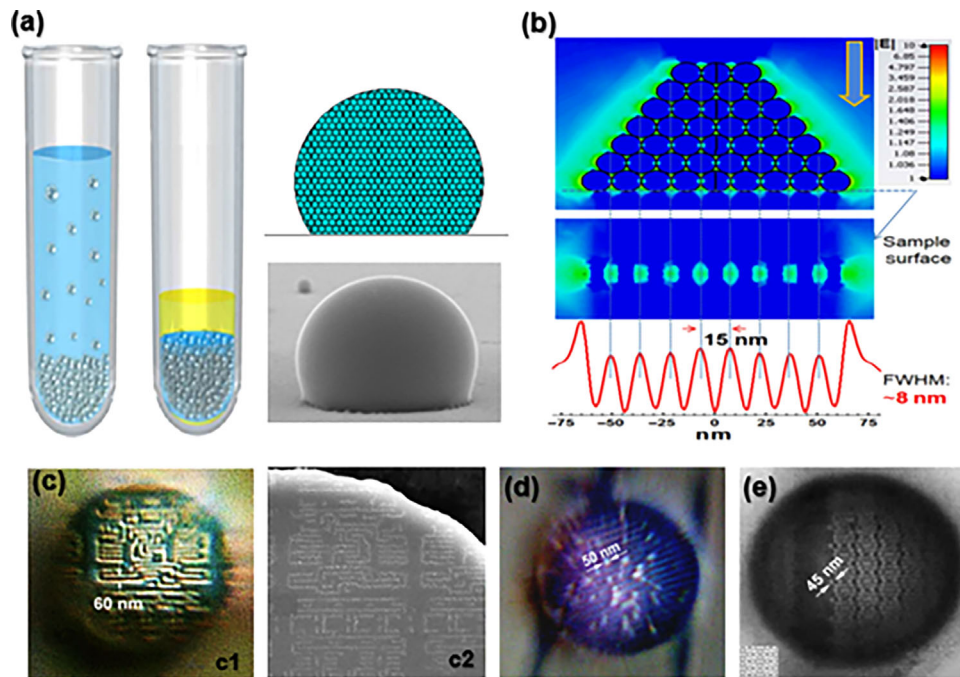


**Figure 46.** Metamaterial solid immersion lens (mSIL). a) Concept of mSIL and synthesis approach. b) Near-field coupling between nanoparticles in mSIL transforms incident propagating wave into large-area structured evanescent wave illumination of substrate at FWHM resolution  $\approx 8$  nm. c1) Super-resolution imaging of 60 nm feature on IC chip by mSIL. c2) Bottom surface of mSIL detached from c1 sample. d) 50 nm Polystyrene particle imaged by mSIL. e) 45 nm IC chip imaged by mSIL. Reproduced with permission.<sup>[144]</sup> Copyright 2016, The Authors, published by AAAS.

(measured by PSF) due to difficulties of attaining contact scanning mode.

### 24.2.3. Super-Resolution Physics

A complete theory for microsphere nanoscopy is still under development and one of the latest results is the wave theory of virtual imaging by microsphere.<sup>[615]</sup> The mechanism behind microsphere nanoscopy has been under debate since its birth. The PNJ effect was first considered as the main mechanism. However, calculations show that super-resolution strength by PNJ is weak, typically  $\approx \lambda/2 - \lambda/3$  for  $n = 1.5 - 1.6$  particles. To explain the strong super-resolution  $\approx \lambda/6 - \lambda/8$  observed in experiments, other mechanisms were studied. Excitation of whispering-gallery mode (WGM) in microsphere allows to explain resolution up to  $\approx \lambda/4$ . Very recently, new super-resonance (SR) modes in microsphere were discovered.<sup>[616]</sup> A typical SR mode field distribution is shown in Figure 45d. It has a pair of highly localized hotspots ( $|E|^2 > 10^4 - 10^5$ , three orders higher than PNJ of  $10 - 10^2$ ) near the bottom and top apex of the microsphere. A strong resolution of  $\approx \lambda/3 - \lambda/6$  is observed in Figure 45d. Deeper resolution and stronger field enhancement ( $10^9 - 10^{11}$ )<sup>[617]</sup> by SR effect is possible for other particles, which requires further investigations. Moreover, some other mechanisms also contribute to resolution enhancement, such as plasmonic substrate effect and non-traditional illumination method (e.g., partial and inclined illumination<sup>[278, 612]</sup> and near-field evanescent-wave illumination using fluorescent nanowire<sup>[618]</sup> and localized plasmonic structured illumination<sup>[619]</sup>).

### 24.2.4. Bio-Superlens

Another trend in the field is the development of biological superlenses using biomaterials such as spider silks,<sup>[620]</sup> cyanobacteria, live yeast cells,<sup>[621]</sup> and lipid droplets,<sup>[622]</sup> where typically 100 nm features can be resolved (not PSF). These bio-superlenses may open the intriguing route for developing multifunctional biocompatible bioimaging tools for sensing and single-cell diagnosis, which will be further advanced in the future.

### 24.3. Metamaterial Solid Immersion Lens (mSIL)

A notable achievement in the field is the development of mSIL in 2016. mSIL is an artificially engineered three-dimensional all-dielectric superlens assembled by high-index nanoparticles (Figure 46) that supports enhanced ETPC efficiency. Exploiting 15 nm high-index ( $n = 2.55$ )  $\text{TiO}_2$  nanoparticles as building blocks, we fabricated  $\text{TiO}_2$  mSIL with widths of 10–20  $\mu\text{m}$  (Figure 46a) and demonstrated excellent super-resolution performance. It generates a sharp image with a resolution of at least 45 nm ( $\approx \lambda/8.5$  PSF resolution, Figure 46c), which exceeds the resolution of all previous superlenses. A new super-resolution mechanism was discovered in mSIL. The near-field coupling between neighboring nanoparticles in closely stacked media can effectively guide and transform the propagating wave into a large-area array of structured evanescent wave illumination field (Figure 46b). Inversely, the composite media supports highly efficient ETPC that lead to enhanced super-resolution. Similar works have been reported using other materials like  $\text{ZrO}_2$

to replace  $\text{TiO}_2$ .<sup>[623]</sup> Recently, Dhama et al. designed and fabricated full-sphere  $\text{TiO}_2$  mSIL and compared the imaging performance with BTG microsphere. The results confirmed that mSIL superlens performs consistently better than BTG superlens in terms of imaging contrast, sharpness, clarity, field of view, and resolution.<sup>[624]</sup> Besides mSIL, gradient solid immersion lenses (Maxwell fisheye) may provide another route toward near-perfect super-resolution imaging.<sup>[625, 626]</sup>

#### 24.4. Current and Future Challenges

The imaging contrast by microsphere nanoscopy is often low due to the relatively weak ETPC efficiency. The low-contrast problem can be partially solved by mSIL with enhanced ETPC. While mSIL has shown greater imaging resolution and quality over other superlenses, its structure-integrity, lifetime in air/liquid and suitability for scanning imaging remains unknown which demands more investigations.

Increasing WD in dielectric superlens nanoscopy while retaining super-resolution is a key challenge in the field. Using partial and inclined illumination have shown the possibility to extend the working distance from sub-wavelength scale to more than one wavelength scale.<sup>[612]</sup> Other proposals are needed to extend WD to at least  $5 \mu\text{m}$  scale to enable a truly 3D super-resolution imaging of biological details and processes. Developing a higher speed nanoscopy system remains another challenge for the technique. Deeper tissue imaging, and combination of superlens with other super-resolution techniques (e.g., fluorescent nanoscopy) to achieve multi-modal super-resolution imaging systems will also be the future challenge for the technique.

#### 24.5. Advances in Science and Technology to Meet Challenges

Recent advances in photonics, nanomaterials, metamaterials, and artificial intelligence (AI) could be utilized to address the discussed challenges. Introducing superlenses like microsphere/mSIL into a conventional optical microscope system leads to unwanted aberrations that reduce imaging contrast and quality, despite the resolution is improved locally at a region under the microsphere. This contradiction could be solved by using adaptive optics technology to correct the aberrations so that high-contrast super-resolution image can be obtained.<sup>[627]</sup> Another possible solution is to use metasurface, which can be designed and placed in front of the dielectric superlenses to realize similar function to the adaptive optics. Highly tuneable Metamaterials and metasurfaces will also be the promising solution to enable the development of long-WD superlens due to its flexibility in phase, amplitude, polarization, and wavefront engineering.<sup>[628]</sup> Combining superlenses with multiphoton microscopy may offer another solution to develop a long-WD superlens imaging system, e.g., using nonlinear effect to enhance resolution at the far-field zones. Due to significant amount of data generated during scanning superlens over a large-area, AI and machine learning technologies are particularly useful to process the big data to generate desired output image or extract features from a large-image. The latter property is especially useful for developing systems capable of tracking dynamics in biological samples.

#### 24.6. Conclusions

Dielectric superlenses made from microsphere and nanoparticles and other materials have proven to be the effective tools to overcome the diffraction limit. Optical super-resolution of  $\approx \lambda/6 - \lambda/8$  (measured by PSF) has been demonstrated in real-time, label-free imaging of a variety of samples and processes in fields such as biology, material, and medicine research. The superlens technology has the potential to revolutionize the field of optical microscopy when the discussed challenges are resolved.

### 25. Microspherical Superlens Imaging: Fundamental Origins of Super-Resolution

(Alexey V. Maslov\*, Vasily N. Astratov)

#### 25.1. Status

The use of dielectric microspheres in contact with label-free or fluorescent objects, the technique to which we will refer here as microspherical superlens imaging (MSI),<sup>[136, 138, 584, 611, 629]</sup> see **Figure 47**, revolutionized the biomedical and nanoplasmonic imaging a decade ago because of its significantly better resolution compared to the standard microscopy and its relative simplicity compared to the advanced fluorescence (FL) microscopy represented by localization<sup>[630]</sup> or stimulated emission depletion (STED)<sup>[631]</sup> techniques. The experimentally observed MSI resolution exceeds the solid immersion lens (SIL) limit,  $\delta = \lambda/(2n_s \sin\theta)$ , where  $\lambda$  is the vacuum wavelength,  $\theta$  is the half angle of the light collection cone, and  $n_s$  is the refractive index of the microsphere. An intriguing situation in this area is that after a decade of intense experimental and theoretical studies, the origin of this super-resolution remains largely obscure.

The main properties of MSI can be summarized as the following three experimental findings: a) the resolution is systematically higher for smaller microspheres ( $2 \mu\text{m} < D < 10 \mu\text{m}$ , where  $D$  is the diameter) and can reach  $\lambda/6 - \lambda/7$  exceeding the SIL limit<sup>[138, 611]</sup>; b) higher index ( $n_s \approx 2$ ) microspheres inside liquid or plastic coverslips provide higher resolution<sup>[584]</sup> that can be qualitatively explained by the SIL effect; c) best resolution results are usually obtained for nanoplasmonic objects<sup>[629]</sup> or for FL objects coupled to short-period nanoplasmonic arrays.<sup>[632]</sup> The most rigorous approach to the explanation of resolution so far was based on exact numerical solutions of the Maxwell equations. The computational results for the point spread function (PSF), which is the classical estimate of resolution, show significantly larger width than the experimental resolution, as illustrated in **Figure 47c**.

#### 25.2. Current and Future Challenges

A few approaches to explain the MSI super-resolution have been considered.

##### 25.2.1. Photonic Nanojets

It was suggested originally that the observed super-resolution is linked to the ability of microspheres to form nanojets.<sup>[136]</sup> This

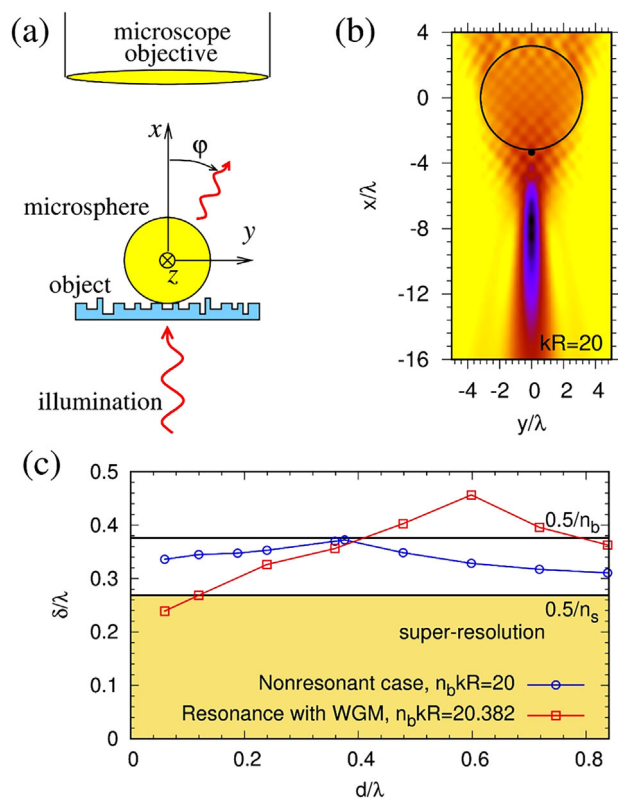


**Figure 47.** a) Schematic of MSI in the transmission geometry. b) Virtual image of a dipole marked by the dot near the microsphere. The image intensity is plotted as a function of the transverse coordinate  $y$  and position  $x$  of the focal plane of the objective. The refractive index of the microsphere is  $n_s = 1.4$  and of the background is  $n_b = 1$ . c) Resolution  $\delta$  for imaging in water  $n_b = 1.33$  background for the index contrast  $n_s/n_b = 1.4$ . The horizontal lines define two diffraction limits ( $0.5\lambda/n_b$  for water and  $0.5\lambda/n_s$  for SIL) and the colored area defines the super-resolution regime. The data points for frames (b) and (c) were taken from Ref. [140]; for frame (c) they were rescaled for the immersion case.

stimulated several studies in which the modeling of nanojet formation was performed<sup>[633, 634]</sup> assuming its reciprocal relation to resolution. However, the reciprocity of focusing and imaging may work with propagating waves, but if evanescent waves are involved it is likely to be invalid.<sup>[140]</sup> Besides that, the width of photonic nanojets can be only slightly smaller than the diffraction limit of  $\lambda/2$  in air and only for microspheres with diameters much smaller than used in the experiments.<sup>[604, 635, 636]</sup> Thus, the existence of a direct relation between the super-resolution and the nanojet formation was subjected to serious doubt.

### 25.2.2. Incoherent Imaging and PSF modeling

In the incoherent imaging regime, the image is obtained as a convolution of the PSF and the object shape (field intensity). One way to explain the super-resolution in MSI is to demonstrate the narrowness of the PSF. This direction was followed in several studies which applied various computational techniques to point-source (dipole) emission near microspheres.<sup>[139, 140, 637, 638]</sup> Due to the complexity of the problem most of the PSF simulations are two-dimensional (2D)<sup>[139, 140, 637]</sup> except some cases where the Mie

theory is used in 3D.<sup>[638]</sup> In 2D geometry, see Figure 47a, one can put a point current source at distance  $d$  from the microsphere

$$J(x, y, t) = \hat{y} j_0 \delta(y) \delta(x + R + d) e^{-i\omega t} \quad (27)$$

and calculate its emission which is collected by the objective forming an image.<sup>[140]</sup> The solution of the Maxwell equations describes the outcoupling of not only the propagating but also the evanescent components of the point source. The prominence of WGMs in microspheres calls for separate analysis in resonant and nonresonant cases.

Figure 47b shows a typical image in the non-resonant case for continuously moving focal plane of the objective. The virtual image is formed below the microsphere. Figure 47c summarizes the resolution (the FWHM of the PSF corrected for magnification) in the case of liquid immersion. In the nonresonant case, the resolution is  $\approx \lambda/3$ , which is slightly better than the diffraction limit of  $\lambda/(2n_b)$  of imaging in water, and depends very weakly on the gap  $d$ . This means that the evanescent fields do not affect the PSF width. In the resonant case, the resolution can reach  $\lambda/4$ , which is still noticeably below the experimental observations, and the images typically have sidelobes. The resolution increases with decreasing gap which correlates with the excitation of WGMs. The role of polarization on the PSF was also studied by considering dipoles oriented tangentially and radially relative to the microsphere surface.<sup>[637, 639]</sup> The narrowest PSF, about  $0.28\lambda$  in air, is achieved for radial polarization. While the PSF analysis provides some insight into MSI properties, it fails to explain the experimentally observed super-resolution.

## 25.3. Advances in Science and Technology to Meet Challenges

Many modalities of experimental MSI and variety of objects with different properties used in these studies suggest that it is unlikely that a single factor would reveal the origin of super-resolution.

### 25.3.1. Coherent Imaging Regime

In the Abbe coherent imaging theory,<sup>[640]</sup> the imaged object is represented as a sum of periodic components defined by their spatial frequencies. The incident wave is diffracted by each component. The diffracted waves are collected by the objective and directed to an image plane, where interference between the diffracted waves produces an image. The incoherent imaging regime is realized only as a limiting case of coherent imaging under special arrangements, for example, if the object is illuminated by a very broad angular spectrum of plane waves that are mutually incoherent. This condition can, however, break down, for example, due to the presence of a microsphere.

In coherent imaging the resolution is defined as the smallest period  $L = \lambda/2$  of the object's spatial component which can create a propagating diffracted wave. A microsphere near an object can scatter even evanescent diffracted components, similar to plane waves in the Mie theory. A key question is whether these waves can be used to form an image. To demonstrate the possibility of image formation from an evanescent wave with an in-plane



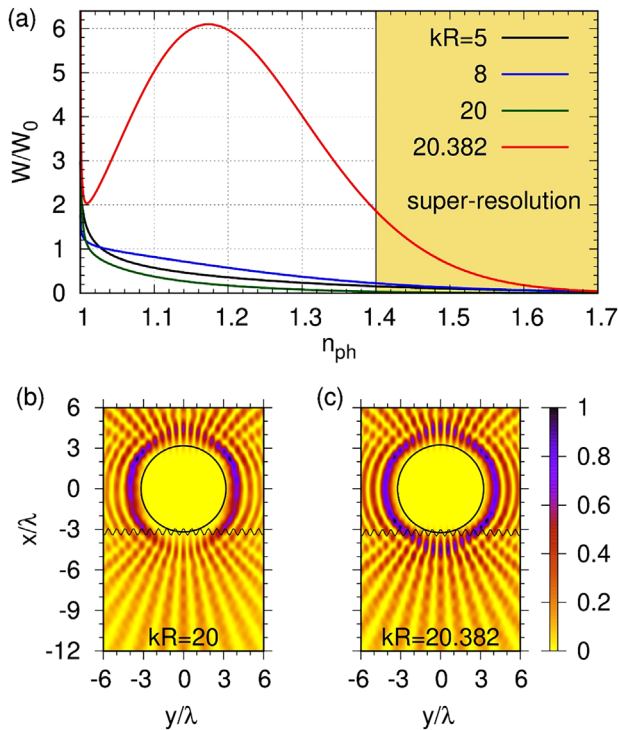


**Figure 48.** Imaging of subwavelength current distribution (Equation (28)). a) Scattered energy  $W$  (normalized to some  $W_0$ ) toward the objective ( $-\pi/2 < \varphi < \pi/2$ ) as a function of the phase index of the current for several values of the particle size. The nonresonant case is exemplified by  $kR = 5, 8, 20$ , the resonant case by  $kR = 20.382$  (WGM with azimuthal number  $m = 24$ , see Figure 4 in Ref. [643]). The colored area defines the region  $n_{ph} > n_s$  in which the resolution above the SIL limit can be achieved. b,c) Images produced by the current with  $n_{ph} = 1.6$  for various focal plane locations for  $kR = 20$  and  $kR = 20.382$ . The images are normalized to their maximum values, which in (c) is 46 times higher than in (b). The oscillating curves near the microspheres in (b,c) illustrate current (Equation (28)).

wavenumber  $h_0$ , let us consider a current source placed parallel to the horizontal  $y$ -axis near the bottom of a microsphere with  $n_s = 1.4$  in a background medium with  $n_0 = 1$ , as schematically illustrated in Figure 48b,c:

$$J_y(x, y) = 2j_0 \cos(h_0 y) \delta(x + R) e^{-i\omega t} \quad (28)$$

A gap between the current and the microsphere will only change the intensities of the emission and of the resulting image. For the results in Figure 48, the scattering problem was solved rigorously using the cylindrical functions. The phase velocity of the current wave is  $v_{ph} = \omega/h_0 = c/n_{ph}$ , where  $n_{ph}$  is the phase index. The evanescence of the field created by current (Equation (28)) in the absence of the microsphere is provided by  $h_0 > n_0 \omega/c$ . This is equivalent to the condition that the spatial current period  $L = 2\pi/h_0 = \lambda/n_{ph}$  is smaller than the wavelength in the background material  $\lambda/n_0$ , that is  $L < \lambda/n_0$  or  $n_{ph} > n_0$ . The physical meaning of the standard SIL limit is that for  $n_{ph} > n_s$  (or  $L < \lambda/n_s$ ), the current would not emit in a uniform medium even with index  $n_s$  and, therefore, no image should be formed.

### 25.3.2. Fundamental Role of the Curvature of the Microsphere

The situation is dramatically changed in the presence of a microsphere since it scatters the evanescent field creating waves which go towards the objective, see Figure 48a. The key property is that while the emission decreases monotonically with increasing  $n_{ph}$ , it persists even for  $n_{ph} > n_s$ . There is no any qualitative change near the value  $n_{ph} = n_s$ . It was pointed out in Refs.[641, 642] that an evanescent wave can be converted to propagating by the curvature of the microsphere through a modified Snell's law. The condition for such conversion, as defined by Eq. (13) in Ref. [642], implies that if the spatial period  $L$  of an evanescent wave incident on the sphere satisfies  $L > \lambda/n_s$ , its conversion to a propagating wave is possible. However, this condition is equivalent to the SIL limit. In contrast, Figure 48a demonstrates the possibility of outcoupling of very high spatial frequency components, which exceed the SIL limit of the microsphere. The scattering of evanescent waves by spheres is often used to excite WGMs but is also related to imaging.<sup>[643, 644]</sup> In the non-resonant case, the higher extraction efficiency for higher spatial frequencies ( $n_{ph} > n_s$ ) is evident for the intermediate value of  $kR = 8$  compared to the smaller  $kR = 5$  or larger  $kR = 20$ . This qualitatively supports the experimentally observed higher resolution for mesoscale microspheres with diameters of about several wavelengths. The emission efficiency affects the visibility of fine features on the images. While the microsphere can outcouple high spatial frequency components, can they form an image by the objective? The image from the evanescent field generated by the subwavelength current, see Figure 48b, supports the possibility of imaging with a resolution better than in the SIL method, that is for  $n_{ph} > n_s$ .

In the calculation of the PSF, the microsphere also outcouples the evanescent component of the point current so why would the coherent regime provide a better resolution than incoherent? It is likely that in the infinitely broad spectrum of the point source, the contribution of the evanescent components is simply too weak to be noticeable. Indeed, the emission efficiency decreases with increasing spatial frequency of the evanescent field, see Figure 48a. In contrast, in the coherent imaging the evanescent components can play a dominant role since the diffraction on a high spatial period component of the object shape will not produce any propagating waves, except perhaps the zeros order. This, therefore, greatly limits the spatial bandwidth allowing the evanescent field contributions to be revealed.

### 25.3.3. Resonant Imaging

Figure 48a shows that the WGM resonance provides a much stronger current emission for all  $n_{ph}$  with a maximum when the phase velocities of the current and of the WGM are close. As a result, the image at the WGM resonance has much higher intensity than off-resonance, compare Figures 48b and 48c. In the resonant case, the image can be defined more by the properties of the WGM itself rather than by the current. Using this property, however, one can also envision a new imaging regime. Under a broadband frequency illumination, different spatial components of the diffracted evanescent fields can potentially excite different resonant modes. This may give a mapping between the spatial component of the evanescent field and the spatial distribution of the exited WGM, which then can potentially be transformed into



an image. Despite being more efficient, the resonant imaging can lead to many artifacts since the observed image can be dominated by the properties of the WGMs rather than by the object. Yet it offers exceptional opportunities for combining imaging and detection.

#### 25.3.4. Coherent Imaging of Resonant Structures and Nanoplasmonics

Many objects used for MSI resolution benchmarking have resonances, for example, localized surface plasmon resonances (LSPR), and the so-called plasmonic hot spots. Examples of such objects are bow-ties, dimers, plasmonic molecules, nanowires, nanoclusters, and arrays. In this case, the field that creates the image is not the diffracted incident field, but rather the reradiated modal field, which can be greatly enhanced.<sup>[645]</sup> This resonantly enhanced coherent field, in which high spatial frequency components are dominant, can be outcoupled by the microsphere enabling the image formation. Some modes may allow seeing extraordinarily small features but usually with distortion. The microsphere can potentially play a role in the excitation of the resonant modes. Alternatively, they can also be excited by fluorescent molecules. By contrast, if mutually incoherent waves are incident from all angles on a small resonator, the excitation of resonances is unlikely since it requires some coherence of the driving field at the resonator location.

#### 25.3.5. Integration with Other Super-Resolution Techniques

Due to widefield imaging and flexible illumination conditions MSI is suitable for integration with other super-resolution approaches and methods considered in this Roadmap. One example is interferometric techniques<sup>[145–147]</sup> discussed in Topic 28. Another example is the integration of micro-spheres or millimeter-scale ball lenses<sup>[646, 647]</sup> with cellphone imaging that permits building pocket-size microscopes as discussed in Topic 26.

### 25.4. Conclusions

The theoretical explanation of super-resolution values beyond the classical SIL limit represents an intriguing question laying at the intersection of fundamental physics of imaging and advanced numerical modeling methods. It is shown that the approach based on coherent imaging is likely to be relevant to many experimental situations and is promising for explaining the observation of extremely small features. The illumination (which includes multiple object-microsphere scattering) can create coherent fields in the region between the microsphere and the object. These fields can be enhanced by plasmonic resonances. The subwavelength scale of these fields in the object plane results in their evanescence in the normal direction in the absence of the microsphere. Due to the curvature of the microspherical surface these fields can be outcoupled and then create a magnified super-resolved image observable by the microscope objective. The narrow spatial bandwidth of the evanescent components may allow seeing even rather weak evanescent signals. However, coherent imaging

is prone to artifacts and image distortion effects. The WGM resonances of microspheres can significantly boost the outcoupling of the evanescent fields, but they can also lead to the presence of artifacts in the optical images. Our vision for future developments in this area is based on combination of several factors: a) coherent imaging regime, b) curvature of microsphere, c) WGM resonant enhancement as well as d) nanoplasmonic enhancement due to LSPRs and hot spots as main physical causes of super-resolution. The validity of this consideration for the explanation of super-resolution imaging and the specific roles played by these factors in different imaging scenarios require further confirmation, which can include specially designed experiments, theoretical and computational studies.

## 26. Smartphone Ball Lens Microscopy

(Vasily N. Astratov\*, Boya Jin)

### 26.1. Status

Since introducing megapixel CCD and CMOS sensor arrays in digital cameras in the 1990s and 2000s, the motivation to develop portable and lightweight microscope systems never faded away. Such pocket-size microscopes can be taken to the world's most remote locations. They can also help to answer some fundamental questions in astrobiology, such as to provide evidence of bacterial life on different planets or meteorites. Most importantly, they would allow certain medical procedures such as biopsy-free diagnostics of the skin cancers that can be performed at the point-of-care without using complicated facilities such as reflectance confocal microscopy, optical coherence tomography, multiphoton microscopy (MPM), and Raman spectroscopy.<sup>[648]</sup>

All these applications require label-free imaging with resolution sufficiently close to the classical diffraction limit, but not necessarily require optical super-resolution imaging. As an example, such diffraction-limited resolution is desirable for studying the spatial distribution of the lymphocytes and tumor cells to achieve a prognostic significance for melanoma diagnostics.<sup>[649, 650]</sup> The resolution of ordinary smartphones, however, is limited at the 20–30  $\mu\text{m}$  level due to the finite sizes of the pixels in the sensor array and insufficient magnification ( $M$ ) of the smartphone optics. This resolution is well below the classical diffraction limit,  $\lambda/(2NA)$ , where  $\lambda$  is the illumination wavelength (or emission wavelength in the case of fluorescence (FL)),  $NA = n\sin\theta$  is the numerical aperture,  $n$  is the index of refraction of the media surrounding the radiating point, and  $\theta$  is the half angle of the collection cone that enters the objective. Resolution of standard cell phones can be enhanced down to  $\approx 1.5 \mu\text{m}$  using microoptics solutions for FL samples,<sup>[651–655]</sup> however further increase of the resolution is made difficult by the limited magnification and significant spherical aberrations of such systems.

In this Topic, we briefly review main design approaches to development of smartphone microscopes and discuss the prospect of application of microspherical superlens imaging (MSI) for enhancing the resolution of cellphone microscopy. Previously, applications of MSI to nanoplasmonic structures

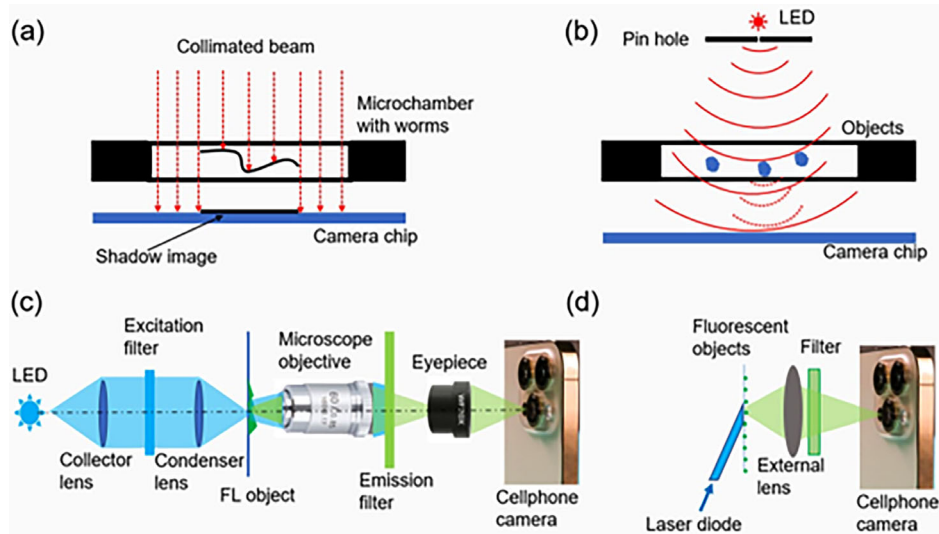


**Figure 49.** Designs of cellphone microscopy based on: a) Lensless shadow imaging on top of the sensor array, adapted with permission.<sup>[660]</sup> Copyright 2005, Elsevier. b) Digital in-line holographic imaging.<sup>[662–664]</sup> c) Combination with the microscope objective, adapted under terms of the CC-BY license.<sup>[651]</sup> Copyright 2009, The Authors, published by the Public Library of Science (PLOS). d) Microoptics solutions.<sup>[652–655]</sup>

allowed to achieve resolution  $\approx \lambda/6 - \lambda/7$  which exceeds the solid immersion lens (SIL) limit ( $\approx \lambda/(2n)$ ).<sup>[136, 584, 632, 656, 657]</sup> However, the smartphone optics doesn't have the quality of microscope objectives used in the previous MSI studies. Recently, it was shown that significantly larger millimeter-scale ball lenses with refractive index close to two provide large image magnifications ( $M > 30$ ) in contact conditions with the samples that allows to overcome the resolution limitations coming from the pixilation of the cellphone sensor array and achieve truly diffraction-limited resolution  $\approx 0.7 \mu\text{m}$  for visible light.<sup>[646, 647, 658, 659]</sup> It allows developing pocket-size handheld microscopes with the diffraction-limited resolution for a variety of applications.

## 26.2. Current and Future Challenges

Smartphone-based microscopy is attractive for developing diagnostics in low-resource settings, but its practical designs faced significant limitations.

### 26.2.1. Shadow Imaging

One of the first lensless designs includes a microfluidic channel on top of the CCD sensor array illuminated with a uniform light field, as illustrated in **Figure 49a**. The shadows of floating worms or other biomedical objects can be detected with the resolution determined by the sensor's pitch size, typically in 5–10  $\mu\text{m}$  range.<sup>[660]</sup> The resolution can be increased by using additional nanoaperture arrays in combination with the microscope imaging.<sup>[661]</sup> The latter technique has been termed optofluidic microscopy (OFM). The improved resolution of OFM methods, however, comes at the expense of increasing the size and complexity of the imaging system, so that it cannot be viewed as a pocket-size imaging solution.

### 26.2.2. Digital In-line Holographic Microscopy (DIHM)

Another lensless imaging solution is offered by the DIHM method where a spherical wave emanating from an aperture illuminates an object, and the interference of the light waves that passed through the objects (such as cells or microparticles) with the unscattered light creates the hologram of each object, which is detected using cellphone detector array, as schematically illustrated in **Figure 49b**. The lensfree hologram of each object permits rapid reconstruction of its microscopic image through digital processing.<sup>[662–664]</sup> The lens-free holographic approach provides a large field-of-view (FoV), but with a limited, micron-scale resolution combined with a significant computational load. In addition, this approach cannot be used to image samples prepared on standard glass slides due to the requirement that the sample be positioned in close proximity to the sensor.

### 26.2.3. Smartphone Combined with the Microscope Objective

As an example, a combination with 0.85 NA 60 $\times$  achromat objective and a 20 $\times$  wide field microscope eyepiece resulted in a system with FoV  $\approx 180 \mu\text{m}$ , an effective magnification onto the camera face of 28 $\times$ , and a measured spatial resolution  $d = 1.2 \mu\text{m}$ .<sup>[651]</sup> This resolution value is three times larger than the classical diffraction limit. Such a system reminds classical microscope design and, as a result, it is rather bulky and heavy.

### 26.2.4. Microoptics Solutions

To reduce the size and weight of imaging system, the long attachment with microscope objective was replaced with microlenses, as illustrated in **Figure 49d**. The use of ball lenses leads to significant aberrations that reduce image quality towards the edges of FoV.<sup>[653]</sup> There is also a tradeoff between the magnification

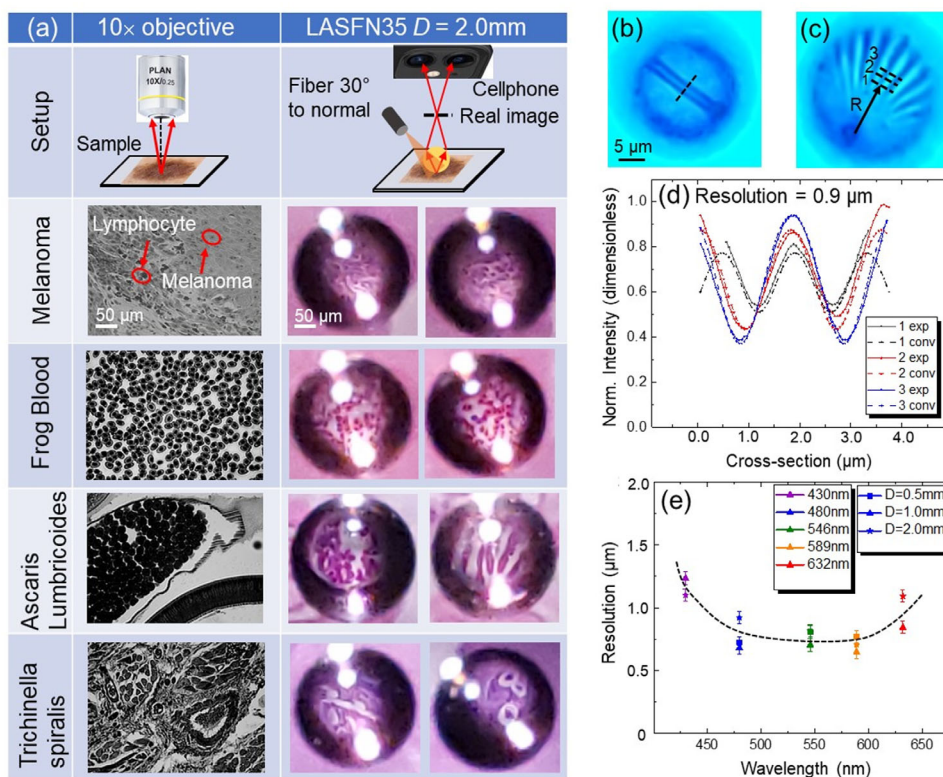


**Figure 50.** a) Comparison of images of various biomedical samples taken by a standard microscope with  $10\times$  ( $NA = 0.25$ ) objective (left column) and by proposed cellphone microscopy (right column) through LASFN35 ball lens with  $D = 2.0$  mm. Pairs of cellphone images are obtained at different positions of the ball lens. b) Image of double-stripe nanoplasmonic object resolved through the ball lens by cellphone microscopy at  $\lambda = 480$  nm. c) Image of “Siemens star” nanoplasmonic object resolved through the ball lens by cellphone microscopy at  $\lambda = 480$  nm. d) Intensity cross-sections measured using Siemens star target at different radial distances (indicated 1–3) in (c) and corresponding intensity profiles calculated by convolution with 2-D Gaussian PSF with FWHM =  $0.9\ \mu\text{m}$ . Good agreement with theory indicates that the resolution is  $0.9\ \mu\text{m}$ . e) Summary of resolution quantification for double-stripe objects performed using ball lenses with  $D = 0.5$  mm,  $1.0$  mm, and  $2.0$  mm at  $\lambda = 430$ ,  $480$ ,  $546$ ,  $589$ , and  $632$  nm. a, b, e) Adapted under terms of the CC-BY license.<sup>[659]</sup> Copyright 2023, The Authors, published by Wiley-VCH. c, d) Reproduced under terms of the CC-BY license.<sup>[658]</sup> Copyright 2023, The Authors, published by Springer Nature.

and FoV. Such systems were mainly used for imaging FL objects with a rather limited magnification and the best resolution about  $1.5\ \mu\text{m}$ .<sup>[652–655]</sup>

### 26.3. Advances in Science and Technology to Meet Challenges

A combination of smartphone microscopy with MSI methods allowed to suggest a radical way<sup>[646, 647, 658, 659]</sup> to dramatically increase the magnification and to exceed the resolution limitation determined by the pixilation of the cellphone sensor array. In the limit of geometrical optics, the lateral image magnification ( $M$ ) of ball lens is determined by the following equation<sup>[656]</sup>:

$$M(n', D, g) = \frac{-n'}{2(n' - 1)\left(\frac{2g}{D} + 1\right) - n'} \quad (29)$$

where  $D$  is the diameter of the ball lens,  $n' = n_{sp}/n_0$  is the refractive index contrast between the spherical ball lens and object space, and  $g$  is the gap between the object and ball lens. This equation shows that for zero gaps ( $g = 0$ ) magnification increases

asymptotically as  $n'$  approaches two. The ball lens creates a virtual image below the object for  $n' < 2$  and real image above the object for  $n' > 2$ . Experimentally the latter situation was realized by using the ball lens made by LASFN35 glass with refractive index  $n = 2.02$  at  $\lambda = 600\text{nm}$  and diameter of  $2.0$  mm separated from various biomedical structures with a sufficiently small distances ( $g = 0.17\ \mu\text{m}$ ), as it is illustrated in Figure 50a.

Comparisons of images of various biomedical samples in Figure 50a obtained by the conventional microscopy with  $10\times$  ( $NA = 0.25$ ) objective and by the smartphone microscopy illustrate their comparable quality of imaging. In the case of imaging through individual ball lens, FoV is limited by  $\approx D/10$ . In practice, the ball lens can be manipulated to extend FoV, as illustrated by the pairs of cellphone images obtained at different position of the ball lens. The quality of imaging by the cellphone microscopy is sufficient for studying the distribution pattern and density of tumor-infiltrating lymphocytes (TILs), which makes possible the study of infiltration and disruption of TILs into tumor nests or direct contact between TILs and tumor cells required for melanoma diagnostics.<sup>[649, 650]</sup> It should be noted, however, that the cases illustrated in Figure 50a were suboptimal for achieving the maximal resolution because of the glass coverslip with the



thickness of  $g = 0.17$  mm separating the ball lens from the biomedical samples. Under these conditions, the magnification of cellphone microscopy was limited at  $M = 7$  level.

To study the maximal magnification and resolution of the proposed method, the LASFN35 ball lenses with different diameters were placed directly on top ( $g = 0$ ) of the nanoplasmonic structures, as illustrated for a double-stripe object<sup>[647, 659]</sup> and ‘Siemens star’ target<sup>[658]</sup> in Figure 50b,c, respectively. We showed that because of the strong chromatic dispersion of the LASFN35 glass, magnification increases with the wavelength reaching extraordinarily large values  $M > 50$  for the red wavelengths.<sup>[647, 659]</sup> The methodology of resolution quantification<sup>[656]</sup> was based on comparing intensity cross-sections indicated by dashed lines in Figure 50b,c with the calculated intensity profiles. This procedure is illustrated in Figure 50d for three cross-sections (1–3) taken at different radial distances from the center of the Siemens star object, as shown in Figure 50c by dashed lines. The experimental intensity profiles in Figure 50d (solid lines) were obtained after subtracting a uniform scattering background intensity. Calculated profiles (dashed lines) were obtained by convolution of the “perfect” drawn object with the 2-D Gaussian point-spread function (PSF). The full width at the half maximum (FWHM) of PSF providing the best fit to the experimental data was accepted as a resolution of the system based on the Houston resolution criterion. The results of a similar resolution quantification performed with the double-stripe object are summarized in Figure 50e for various visible wavelengths. It is seen that for  $\lambda > 600$  nm the resolution capability of the ball lens reduces with  $\lambda$  that represents a typical diffraction-limited behavior. However, for  $\lambda < 500$  nm an opposite behavior was observed that indicates that at these wavelengths the resolution is still determined by the pixelation of the sensor array. Generally, a better resolution of  $\approx 0.67$   $\mu\text{m}$  was found for Au double-stripe object<sup>[659]</sup> compared to that for Cr Siemens star target.

## 26.4. Conclusions

With the advent of megapixel CCD and CMOS sensor arrays, the smartphone-based microscopy became attractive for developing medical diagnostics in low-resource settings, but its practical designs faced significant limitations. Several methods and optical designs have been proposed including shadow imaging, OFM, DIHM, combination with the microscope objectives, and microoptics solutions. However, the resolution of compact designs was limited at 1.5  $\mu\text{m}$  level. An integration of millimeter-scale ball lenses with index close to two with a smartphone allows the developing pocket-size microscopes that can be used for biopsy-free diagnostics of skin diseases. In contrast to previous studies, the compound ball lens/cellphone camera objective has the best resolution  $\approx 0.67$   $\mu\text{m}$  at  $\lambda = 589$  nm<sup>[646, 647, 658, 659]</sup> that corresponds to diffraction-limited imaging with  $\text{NA} \approx 0.4$ . Further increase of the resolution might become possible under two conditions: a) use of microspheres with diameters from several microns up to several tenths microns instead of millimeter-scale ball lenses, b) use of short-period nanoplasmonic arrays creating a “hot spot” plasmonic illumination for nanoscale objects.<sup>[632]</sup> It can help to demonstrate optical super-resolution imaging using the smartphones in future studies.

## 27. Imaging Beams for Subwavelength Resolution

(Constantin R. Simovski\*)

The diffraction limit of resolution of two mutually non-coherent point sources equals  $1/2$  only for objects in free space when the objective lens has f-number larger than unity. When the imaged object is inside a mirrored glass microparticle, when the objective diaphragm has low f-number and in some other cases, the superresolution is achieved without involving evanescent waves.<sup>[60, 665]</sup> In the theory of a hyperlens,<sup>[126, 127, 666]</sup> the sub-wavelength information of the object is carried out to the far zone by imaging beams which do not contain evanescent spatial harmonics. If the object is subsurface the evanescent waves are absent in the model of the hyperlens imaging.<sup>[667, 668]</sup> Despite the common belief, the absence of evanescent waves does not prohibit the subwavelength accuracy of the point-wise source location in the image.

This also refers to a glass microsphere that grants the subwavelength far-field image similarly to a hyperlens. The non-resonant superresolution results from the feature of the wave beam created by a point dipole source normally polarized to the surface of a glass microsphere. This unique feature is zero field on the axis of the wave beam transmitted through the microsphere. This zero exactly determines the line connecting the real point dipole and the virtual dipole created in accordance with the geometrical optics (GO). This fine location of the real source is possible for a wide range of the sphere sizes and refractive indices. For a normally oriented dipole and only for it the role of the diffraction by a microsphere for the transmitted beam is not important beyond the Mie resonances. This transmission can be thought as a problem of the GO. This solution is presented in Figure 1 for two values of the refractive index of the sphere. Meanwhile, our numerical studies have shown that a tangentially polarized dipole such the solution makes no sense—in the phase distribution of the transmitted beam—the information of the exact location of the dipole source is lost. As to a normally polarized dipole the GO predicts the novel regime of subwavelength imaging which corresponds to specific refractive indices  $n$  and radiuses  $R$  of the microsphere.

In the case  $n = 1.44$  GO predicts that all transmitted rays are parallel to the beam axis, and the ultimate angle of total internal reflection for the rays confined inside the sphere is  $\theta_{\text{TIR}} \approx \pi/4$  as shown in Figure 51a, whereas for  $n < 1.40$  the rays form a spherically divergent beam with the virtual center located at the axis  $y$ , as it is shown in Figure 51b. In Figure 51a, the intensity distribution is the function of the transverse coordinate  $x$ , and in Figure 51b, it is the function of the ray tilt angle. The situation illustrated by Figure 51b is known—all experimental studies of the superresolution granted by a microsphere refer to the case when the transmitted beam is conical. It is important that Figure 51 is applicable only to a normally polarized dipole. Consider the case  $n = 1.44$  depicted in Figure 51a. The beam intensity is effectively concentrated in a ring of inner radius  $R/2$  and outer radius  $R$ . The rays passing through this ring have nearly identical optical paths from the source to the plane  $y > 0$ . For  $R = 10\lambda$  the difference of their phases does not exceed  $\pi/4$ . Meanwhile, for a tangential dipole the beam intensity is nearly uniform in the whole cross-section of radius  $R$ . For the same  $R = 10\lambda$  the phase of the central



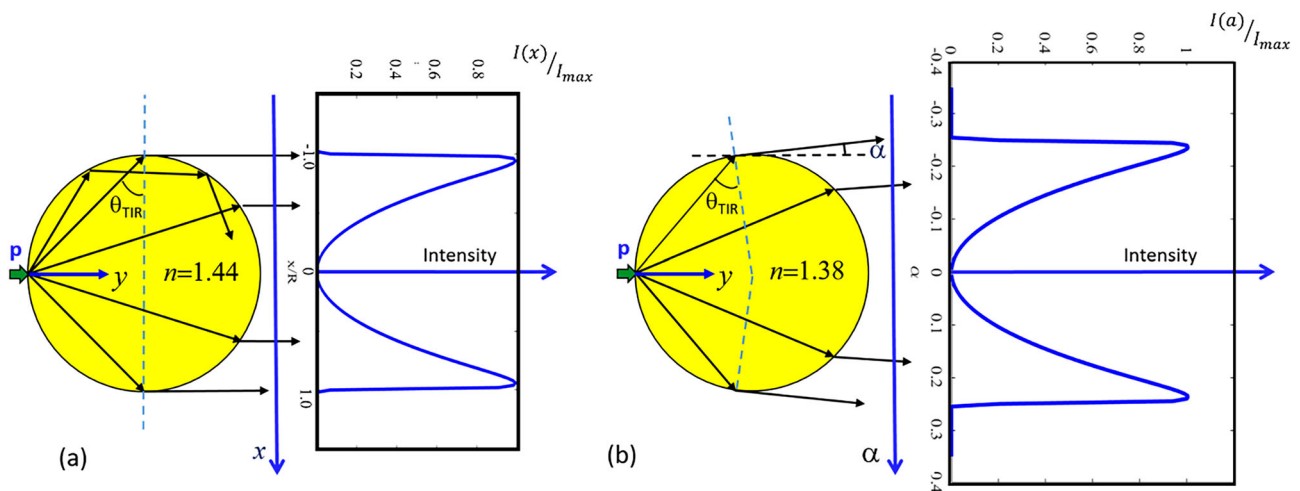


**Figure 51.** Normally polarized dipole  $\mathbf{p}$  creates an axially symmetric wave beam qualitatively described by the laws of geometrical optics. a) Non-divergent beam and its normalized intensity distribution over the transverse coordinate  $x$  normalized to the sphere radius  $R$ . b) Divergent beam and its intensity distribution over the angle  $\alpha$  of rays whose continuations cross at the same point—that of the virtual dipole located at the left of the sphere. Reproduced with permission.<sup>[639]</sup> Copyright 2021, Elsevier.

ray ( $x = 0$ ) taken in the same plane  $y > 0$  differs from that of the peripheral ray by  $\pi/2$ . The difference in the phases of rays cannot be neglected. So, the GO model for the tangential dipole is inconsistent.

Of course, the GO model does not allow us to estimate the superresolution. However, it offers an insight of its physics. Exact numerical simulations were done and confirmed this insight. In previous studies,<sup>[141, 669]</sup> we simulated the imaging beam formation and evolution for  $R/\lambda = 1\text{--}40$  and  $n = 1.3\text{--}1.7$ . In these 2D simulations, the dipoles were replaced by the dipole lines and the spheres—by the cylinders. The range of parameters  $R/\lambda = 4\text{--}20$ ,  $n = 1.5\text{--}1.7$  offers (beyond the Mie resonances) the transmitted beam with the flat phase front and intensity distribution which are close to those predicted by the GO model for  $n = 1.44$ . For  $R/\lambda = 20\text{--}30$ ,  $n = 1.6\text{--}1.7$ , and for  $R/\lambda = 4\text{--}25$ ,  $n = 1.3\text{--}1.5$  the imaging beam is conical as shown in Figure 51b. Next, we have simulated the evolution of both types of imaging beam up to the Rayleigh range  $D_R = 2R^2/\lambda$ <sup>[141]</sup> and up to  $D \gg D_R$ .<sup>[669]</sup> At the Rayleigh distance, both types of imaging beam are split due to oscillating angular dependence of the intensity but keep the same phase center, whereas the parallel beam sharply diverges becoming conical. Its phase center is pronounced enough – its size is smaller than  $R$ . This allows the superresolution in the scenario illustrated by Figure 52a. The divergent wave beam, for which the imaging scenario is illustrated by Figure 52b, also has a pronounced phase center. In both scenarios, a short-focus lens is needed to collect the imaging beam into a spot. If the focusing is not tight the point source is imaged as a ring because the imaging beam is hollow. Estimates of the resolution for both imaging scenarios presented in Figure 52 were done in a previous study.<sup>[669]</sup> This resolution can be further improved using the frequency-domain diagonal sampling of the CCD matrix.<sup>[670]</sup>

Since the point-spread function method does not work for hollow beams, we have done an additional study whose aim was to show that the information of the point source location is kept in the imaging beam with the subwavelength accuracy.

In these 2D simulations,<sup>[141]</sup> a macroscopic objective lens was replaced by microlens located at the distance  $D$  chosen so that  $R \ll D < D_R$ . The proper choice of the microlens allowed us to focus the parallel imaging beams into narrow spots. This microlens is a microcylinder of the same radius  $R$  as the imaging one but different refractive index. Since in our simulations the fields were time-harmonic we could not make two dipole sources really non-coherent. Instead, we made them non-interfering in the paraxial domain introducing the phase shift  $\pi/2$  for their dipole moments. The tight focusing by the 2D “microsphere” offers to a single point dipole the focal spot with minimal size  $w = 0.2\lambda$ , but due to the interference the superresolution was not achieved until we have introduced the substrate emulated by a substantial silicon block. The presence of the substrate flattens the phase front of the parallel imaging beams and enables superresolution. The best-simulated result is presented in Figure 53. The gap  $\delta$  between two Hertzian dipoles that we varied in the limits  $0.2\lambda\text{--}0.5\lambda$  was proportionally magnified in the image. The proportionality  $\Delta \sim \delta$  is illustrated by two values of  $\delta$  in Figure 53b. Asymmetric lateral maxima are due to the interference which is only partially suppressed beyond the beam axis  $y$ . Though in this structure the resolution is modest ( $\delta = 0.24 \lambda$ ) it shows that the subwavelength information on the mutual location of two-point dipoles is kept in the imaging beam.

Let us now discuss the imaging properties of a simple glass microsphere in comparison with a hyperlens. In a hyperlens, the subwavelength location of the object is granted by a tiny width of the imaging beam near its point source. This width is nonzero due to plasmonic losses and metamaterial granularity. A glass microsphere offering superresolution has neither high losses nor granularity. Its resolution may be restricted by the parasitic image created by the tangential polarization. However, simulations of ref. [671] show that this veiling effect is weak. Near-field interaction between the sphere and the object makes the normal polarization of the last one dominant even in the case when the structure is illuminated by the normally incident light.

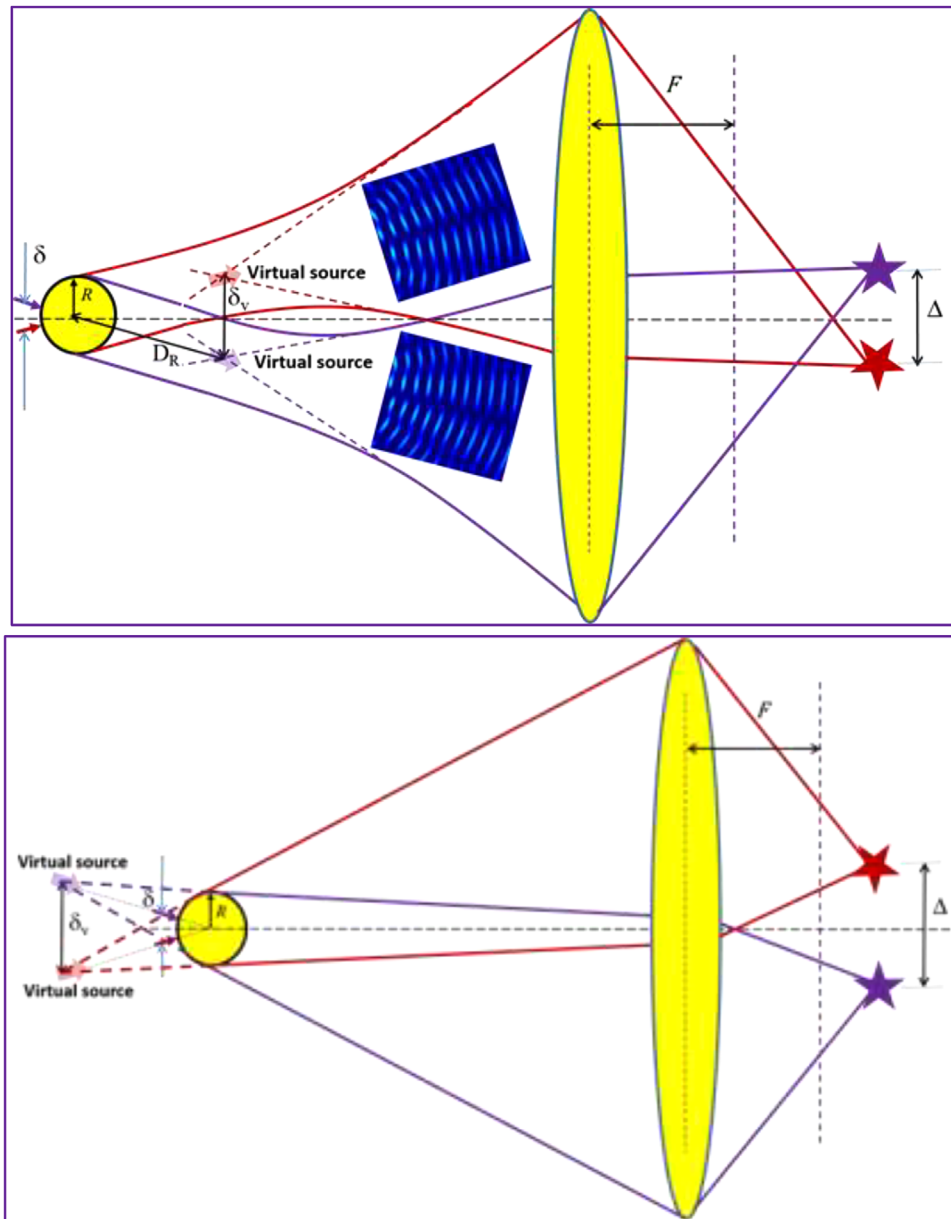


**Figure 52.** Two normally oriented dipoles are resolved despite the subwavelength gap  $\delta$ . The resolution occurs because the gap between two virtual sources is magnified so that  $\delta_v > \lambda/2$ . The lens grants an additional magnification ( $\Delta > \delta_v$ ). a) A beam of parallel rays transforms at the Rayleigh length  $D_R$  into a conical beam with a pronounced phase center (virtual source). In the inset, the simulated picture of this beam behind the Rayleigh range is presented. b) In the conventional scenario, the spherical fronts are created immediately behind the sphere. Reproduced with permission.<sup>[639]</sup> Copyright 2021, Elsevier.

## 28. Microsphere-Assisted Interference Microscopy

(Stephane Perrin\*, Paul Montgomery, Sylvain Lecler\*)

### 28.1. Status

Over the past century, the performance in optical microscopy has been improved with the development of numerous imaging techniques. These super-resolution or stochastic-functional techniques have indeed made it possible to overcome the well-

known diffraction limit. For this purpose, they require fluorescent markers, high-intensity illumination or scanning systems. Recently, sub-diffraction-limit imaging has been demonstrated experimentally by introducing glass microspheres in a classical optical microscope.<sup>[136]</sup> With their small size (within the Mie scattering regime), the microspheres behave as non-classical lenses. Microsphere-assisted microscopy is able to achieve a lateral resolution of up to  $\lambda/5$  in air and  $\lambda/7$  in immersion while being label-free and wide field. A transparent microsphere is usually placed in contact with or close to the object surface to be observed.<sup>[672]</sup>

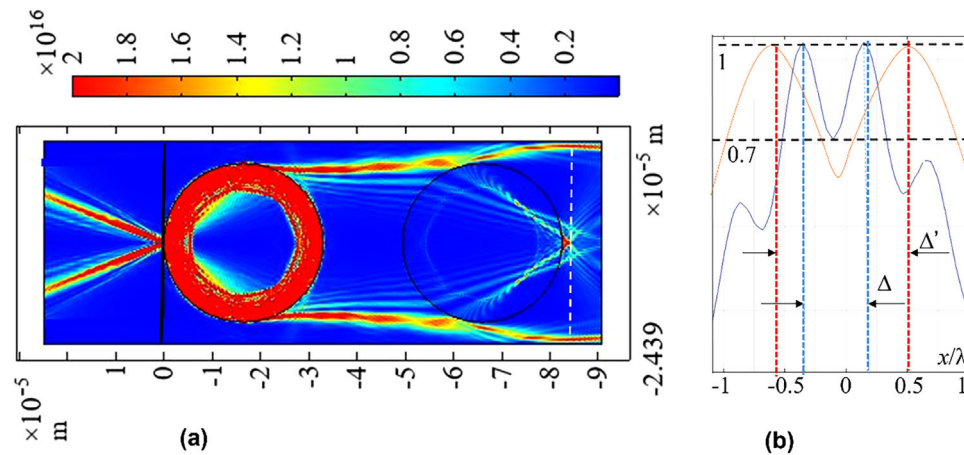


**Figure 53.** a) Intensity color map for two horizontal dipoles symmetrically sandwiched between a large silicon block and a 2D «microsphere» of glass and separated by the subwavelength gap  $\delta$ . The second «microsphere» operates as a lens. In its focal plane (dashed line) the image is formed. b) The intensity distribution in the image plane for two gaps:  $\delta = 0.24\lambda$  (blue curve) and  $\delta' = 0.5\lambda$  (pink curve). The image is magnified:  $\Delta = 0.49\lambda \approx 2\delta$  and  $\Delta' = 1.04\lambda \approx 2\delta'$ .

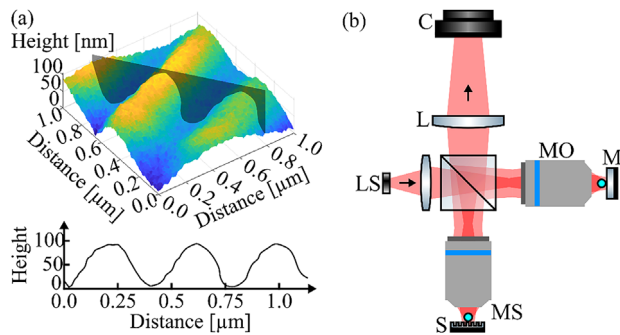


**Figure 54.** a) Surface topography reconstructions of a 200-nm-groove standard and b) layout of compensated microsphere-assisted interference microscope. LS, light source. MO, microscope objective. MS, microsphere. S, sample. M, reference mirror (with a microsphere). L, relay lens. C, camera.

The axial position of the microsphere with respect to the object also influences the formation and the nature (real or virtual) of the image.<sup>[673]</sup> The combination with interferometry, using low coherence light, enables the surface topography reconstruction of sub-wavelength objects with a high axial sensitivity (**Figure 54**). Linnik,<sup>[145]</sup> Mirau,<sup>[147]</sup> and Mach-Zehnder<sup>[148]</sup> configurations have been demonstrated. Furthermore, the use of techniques for compensating both the optical dispersion and optical aberrations, such as adding a similar microsphere in the reference arm (Figure 54b), can lead to an improvement in the accuracy of the height-map.<sup>[674]</sup> Coherent light can also be used in the microsphere-assisted digital holographic configuration, particularly useful with Mirau objectives due to the microsphere phase delay. This has been demonstrated with an  $\approx 500\ \mu\text{m}$  diameter microsphere.<sup>[146]</sup> Structured illumination<sup>[284]</sup> or oblique illumination<sup>[278]</sup> can be coupled to this configuration to further improve the resolution.

If most of the current interferometric microsphere-assisted microscopes have been implemented in the reflection mode, a digital holographic configuration microsphere-assisted micro-

scope has also been demonstrated in the transmission mode for cell imaging.<sup>[675]</sup>

## 28.2. Current and Future Challenges

Glass microspheres allow a significant increase in the lateral resolution in interference microscopy. Nevertheless, the possibility of performing contact-less measurement over a large field of view as well as the quantification of the resolving power remain real challenges.

The lateral field of view is typically a fifth of the size of the microsphere. The smaller the microsphere, the smaller the observation area. However, it is the use of the smaller microspheres that leads to a better sub-diffraction-limit ability. Thus, a compromise between the field of view and the resolution has usually to be made. Moreover, at this scale (diameter ranging from a few micrometers to  $\approx 50\ \mu\text{m}$ ), the manipulation of the microspheres is not easy and the control of the sphere-sample distance is not always accurate enough. In addition, the need to avoid polluting or damaging the object surface is essential. The imaging depth through the microspheres in the tomographic configuration also remains an open question.

Microsphere-assisted microscopy is able to resolve features having a period of 100 nm in air using white-light illumination.<sup>[136]</sup> However, up to now, the lateral resolution limit in direct imaging and interference imaging as a function of the optical (wavelength or refractive index) and geometrical (diameter or axial distance) parameters cannot be predicted due to the lack of a full explanation.

The super-resolution may come from three possible hypotheses. First, a plane wave illuminating a microsphere can generate a sub-diffraction-focused beam known as a photonic nanojet.<sup>[673]</sup> This may be considered as the sphere point spread function; however, its size ( $\approx \lambda/3$ ) is larger than the observed resolutions, meaning that the photonic nanojet alone cannot explain the resolution.<sup>[140]</sup> The second hypothesis concerns a potential interference effect. Due to the small optical path differences

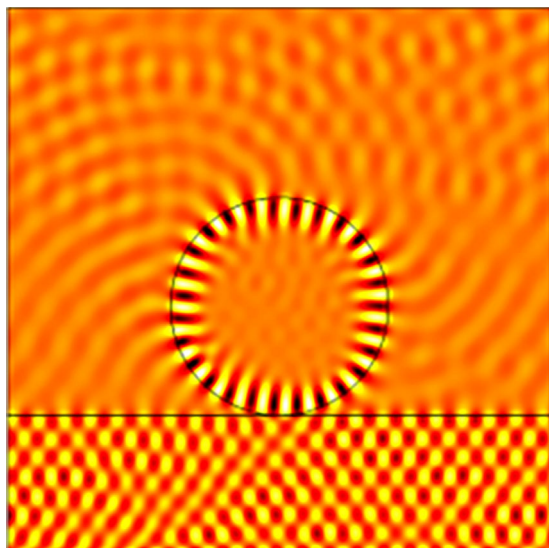


**Figure 55.** Real part of the electric field showing the evanescent wave coupling by a 4- $\mu\text{m}$ -diameter microsphere ( $n_{\text{sph}} = 1.5$ ). The evanescent wave was generated by total internal reflexion using a substrate/air interface and a plane wave with an incident angle of  $55^\circ$ .  $n_{\text{sub}} = 1.5$  and  $\lambda = 600 \text{ nm}$ .

involved, interferences can occur. Therefore, the phase difference between two close objects may create destructive interferences contributing to the ability to distinguish between their images.<sup>[147, 645]</sup> The last explanation considers the ability of the microsphere to collect evanescent waves. Its ability to convert near-field evanescent waves into far-field propagative waves has been demonstrated.<sup>[644]</sup> The evanescent waves contain the high spatial frequencies from a sample or from a point source.<sup>[676]</sup> Close to the microsphere, these waves are naturally coupled to whispering gallery modes inside the sphere. The whispering gallery modes are then coupled to the far field, due to the sample proximity, which breaks the spherical symmetry (**Figure 55**).

While this phenomenon is enhanced if resonances occur,<sup>[676, 677]</sup> the resonances are narrow. However, many resonances can take place if a broad-band source is used. Both virtual and real image formation has been theoretically demonstrated with higher resolution when resonances occur with specific configurations.<sup>[676, 677]</sup> A more general and predictive model is still required. Therefore, there is still a need to better understand and to try to take advantage of the influence of

the source coherence and whispering gallery mode resonances inside the microsphere on the resolution.

Another issue is that the lateral resolution in topography imaging is not the same as in direct imaging. The phase contrast must not only be detected but also quantified. However, when the lateral sizes of structures decrease, their profile measurements can be inaccurate. For this reason, in profilometry the lateral resolution is not limited to a half wavelength but more generally to one or several wavelengths. In white light microsphere-assisted profilometry the 3D topography of Blu-Ray<sup>®</sup> disc with a period of 320 nm can typically be reconstructed. Up to now, the best accuracy (an object with a period of around 200–300 nm) has been obtained in the configuration having a microsphere in the reference arm to compensate the aberration.<sup>[674]</sup>

### 28.3. Advances in Science and Technology to Meet Challenges

In order to resolve the challenges of the field of view, one solution would be to attach an array of microspheres or sup-hemispheres (**Figure 56**) to the microscope head, to scan laterally and to perform stitching of the acquired images in order to examine the high-spatial frequency details over the enlarged sample view.

Contact-less measurements over a wide field also require a mechanical or micro-mechanical system for displacing the microsphere matrix or the object to be tested. Then the gap between the spheres and the object surface needs to be measured in real time in order to maintain a distance smaller than a wavelength and also to avoid collisions. In addition, the choice of the matrix size has to be optimized for a given surface relief in order to decrease the transverse tilt of the matrix substrate which could lead to impacts with the highest parts of the sample.

An algorithm to define the image formation of point object sources only emitting high-spatial-frequency components could be usefully implemented. Based on previous work,<sup>[673]</sup> the phenomenon of sub-diffraction-limit imaging might then be retrieved as well as the relationship with the optical and geometrical parameters. This would enable the performance of microsphere-assisted microscopy to be clarified and even to define the transfer function.

### 28.4. Conclusions

Microsphere-assisted microscopy is a label-free imaging technique that has made it possible to considerably improve the resolving power in interference microscopy. Several technological

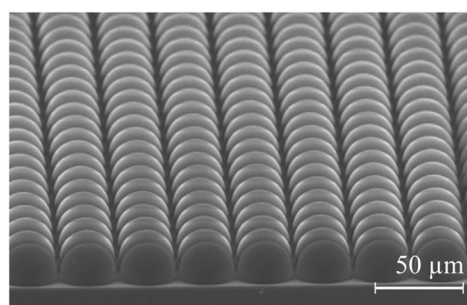
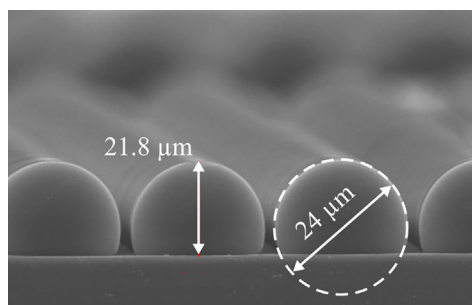


**Figure 56.** Arrays of sup-hemispheres. CSEM, Switzerland.<sup>[678]</sup>



challenges however remain before this innovative combination can be practically applied in the research and industrial environments. The main one consists in enlarging the observation area while maintaining the sub-diffraction-limit phenomenon and being contact-less. Other aims remain such as the theoretical quantification of the maximum possible gain in resolution.

## Acknowledgements

**Section 1:** Special thanks go to all groups who participated in this Roadmap and expressed their visions of the past, present, and future of this field. The author acknowledges the support of Center for Metamaterials, an NSF I/U CRC, Award No. 1068050. **Section 4:** The authors acknowledge the support of the Singapore Ministry of Education (Grant No. MOE2016-T3-1-006), the Engineering and Physical Sciences Research Council UK (Grant Nos. EP/N00762X/1 and EP/M009122/1). **Section 5:** This work was supported by the Gordon and Betty Moore Foundation. **Section 6:** The author acknowledges helpful interactions with C.-At. Motti and funding from Gordon and Betty Moore Foundation. Parts of Section 6 are based on the previous publication in *Advanced Photonics* [60], and are reproduced under the terms of the Creative Commons CC-BY license. **Section 7:** The authors acknowledge the following: National Institutes of Health (R01GM129709, R01CA238191) and National Science Foundation (0939511, 1450962, 1353368). In the memory of Prof. Gabriel Popescu. **Section 8:** P.K. is supported by an ERC Consolidator grant (PHOTOMASS 819593) and an EPSRC Leadership Fellowship (EP/T03419X/1). E.P. acknowledges funding from the German research foundation (PF991/1-1, Deutsche Forschungsgemeinschaft, DFG). The authors thank Catherine Lichten for valuable discussions. **Section 9:** This work was supported by Career Development Award, Academia Sinica, Taiwan (AS-CDA-107-M06); Ministry of Science and Technology (MOST), Taiwan (MOST 108-2112-M-001-038-MY3; MOST 110-2321-B-002-012). **Section 10:** The author acknowledges the support of the Australian Research Council through the Centre of Excellence in Advanced Molecular Imaging (CE140100011). This work was performed in part at the Melbourne Centre for Nanofabrication (MCN) in the Victorian Node of the Australian National Fabrication Facility (ANFF). Support from the La Trobe Biomedical and Environmental Sensor Technology (BEST) Research Centre is acknowledged. **Section 11:** The authors thank Colin J. R. Sheppard, M. Castello, and R. G. Johnson for useful discussions, and M. W. Ashraf, F. Callegari, A. Mohebi, A. Bendandi, N. Mazumder, R. Rajan, R. Marongiu, S. Piazza, I. Nepita, M. Oneto, M. Scotto for the experimental and theoretical activity on the CIDS architecture at DiasproLab. **Section 15:** This work was supported by the grants from Nation Institute of Health (R35GM136223, R01AI141439). **Section 16:** The authors thank Giulia Zanini for her valuable comments and discussion. **Section 19:** S.W.C. and G.J.H. acknowledge the support by the Ministry of Science and Technology (MOST), Taiwan, under grant MOST-112-2321-B-002-025, MOST-112-2112-M-002-032-MY3, MOST-112-2119-M-002-022-MBK, as well as support from the Center for Advanced Computing and Imaging in Biomedicine of NTU (NTU-112L900703) the Brain Research Center of NTHU under the Higher Education Sprout Project funded by the Ministry of Education in Taiwan. X.L. is supported by the National Key R&D Program of China (2018YFB1107200); the Guangdong Provincial Innovation and Entrepreneurship Project (Grant 2016ZT06D081). **Section 20:** The authors wish to thank Prof. Y. Rozenwax and Prof. H. Suchowski for their support. This research was partially supported by ISF grant 1294/18. **Section 21:** SGS acknowledges the financial support of UEFISCDI grant RO-NO-2019-0601 (MEDYCONAI) (NO Grants 2014–2021, Project contract no. 25 / 2021). M.J.H. acknowledges support from the Flagship of Photonics Research and Innovation (PREIN) funded by the Academy of Finland (Grant No. 320165). **Section 23:** U.L. was supported by ERC, ISF and the Murray B. Koffler Professorial Chair. **Section 24:** Funding support is acknowledged. Z.W.: UK Royal Society (IECR2\202178), Leverhulme Trust (RF-2022-659) and Bangor University BU-IAA Award (S49610); B.L.: Russian Science Foundation (Project #20-12-00389) and a Special Program of "BASIS" Foundation (Grant #21-2-10-39-1) for the development of theoretical physics at the Lomonosov Moscow State University.; L.W.: NKPs

(2017YFA0204600, China) and NSFC (51721002 and 52033003). **Section 25:** The work of AVM was supported by the Ministry of Science and Higher Education of the Russian Federation (Grant No. 075-15-2022-293). V.N.A. acknowledges a support by Center for Metamaterials, an NSF I/U CRC, Award No. 1068050. **Section 26:** This material was based upon work supported in whole or part by the North Carolina Biotechnology Center. This work was also supported by Center for Metamaterials, an NSF I/U CRC, Award No. 1068050. **Section 28:** Funding: Nano3D and SIBIC projects (SATT Conectus). The authors thank all the partners for their scientific contributions and discussions.

## Conflict of Interest

The authors declare no conflict of interest.

## Keywords

biomedical imaging, diffraction limit, label-free imaging, near-field imaging, optical microscopy, super-resolution, structured illumination

Received: January 17, 2022

Revised: March 30, 2023

Published online: October 30, 2023

- [1] E. Abbe, *Archiv. für Mikroskopische. Anatomie*. **1873**, 9, 413.
- [2] H. von Helmholtz, *Poggendorff Ann. Jubelbd* **1874**, 557.
- [3] L. Rayleigh, *Philos. Mag.* **1874**, 47, 81.
- [4] S. W. Hell, S. J. Sahl, M. Bates, X. Zhuang, R. Heintzmann, M. J. Booth, J. Bewersdorf, G. Shtengel, H. Hess, P. Tinnefeld, A. Honigmann, S. Jakobs, I. Testa, L. Cognet, B. Lounis, H. Ewers, S. J. Davis, C. Eggeling, D. Klenerman, K. I. Willig, G. Vicidomini, M. Castello, A. Diaspro, T. Cordes, *J. Phys. D: Appl. Phys.* **2015**, 48, 443001.
- [5] B. Huang, M. Bates, X. Zhuang, *Annu. Rev. Biochem.* **2009**, 78, 993.
- [6] C. Coltharp, J. Xiao, *Cell. Microbiol.* **2012**, 14, 1808.
- [7] C. Cremer, B. R. Masters, *Eur. Phys. J. H.* **2013**, 38, 281.
- [8] D. Baddeley, J. Bewersdorf, *Annu. Rev. Biochem.* **2018**, 87, 965.
- [9] L. Schermelleh, A. Ferrand, T. Huser, C. Eggeling, M. Sauer, O. Biehlermaier, G. P. C. Drummen, *Nat. Cel Biol.* **2019**, 21, 72.
- [10] Y. Jing, C. Zhang, B. Yu, D. Lin, J. Qu, *Frontiers in chemistry* **2021**, 9, 746900.
- [11] *Super-Resolution Microscopy: Methods and Protocols* (Ed: H. Erfle), 1st ed. Humana New York, NY, **2017**, ISBN: 1-4939-7265-0.
- [12] *Super-Resolution Imaging in Biomedicine* (Eds: A. Diaspro, A. M. J. Mark), van Zandvoort, 1st ed. CRC Press, Boca Raton, **2017**, ISBN 9780367782740.
- [13] B. R. Masters, *Superresolution Optical Microscopy*, 1st ed. Springer, Cham, **2020**, ISBN 978-3-030-21690-0.
- [14] S. W. Hell, J. Wichmann, *Opt. Lett.* **1994**, 19, 780.
- [15] G. Vicidomini, P. Bianchini, A. Diaspro, *Nat. Methods* **2018**, 15, 173.
- [16] S. W. Hell, M. Kroug, *Appl. Phys. B: Lasers Opt.* **1995**, 60, 495.
- [17] S. Bretschneider, C. Eggeling, S. W. Hell, *Phys. Rev. Lett.* **2007**, 98, 21803.
- [18] S. W. Hell, S. Jakobs, L. Kastrop, *Appl. Phys. A* **2003**, 77, 859.
- [19] T. Grotjohann, I. Testa, M. Leutenegger, H. Bock, N. T. Urban, F. Lavoie-Cardinal, K. I. Willig, C. Eggeling, S. Jakobs, S. W. Hell, *Nature* **2011**, 478, 204.
- [20] E. Betzig, G. H. Patterson, R. Sougrat, O. W. Lindwasser, S. Olenych, J. S. Bonifacio, M. W. Davidson, J. Lippincott-Schwartz, H. F. Hess, *Science* **2006**, 313, 1642.
- [21] R. Henriques, C. Griffiths, E. H. Rego, M. M. Mhlanga, *Biopolymers* **2011**, 95, 322.

- [22] M. J. Rust, M. Bates, X. Zhuang, *Nat. Methods* **2006**, *3*, 793.
- [23] M. Bates, S. A. Jones, X. Zhuang, *Cold Spring Harb Protoc* **2013**, *2013*, 498.
- [24] T. Dertinger, R. Colyer, G. Iyer, S. Weiss, J. Enderlein, *Proc. Natl. Acad. Sci. USA* **2009**, *106*, 22287.
- [25] T. Dertinger, R. Colyer, R. Vogel, J. Enderlein, S. Weiss, *Opt. Express* **2010**, *18*, 18875.
- [26] M. G. Gustafsson, *J. Microsc.* **2000**, *198*, 82.
- [27] R. Heintzmann, M. G. Gustafsson, *Nat. Photonics* **2009**, *3*, 362.
- [28] D. Li, L. Shao, B.-C. Chen, X. Zhang, M. Zhang, B. Moses, D. E. Milkie, J. R. Beach, J. A. Hammer, M. Pasham, T. Kirchhausen, M. A. Baird, M. W. Davidson, P. Xu, E. Betzig, *Science* **2015**, *349*, aab3500.
- [29] R. Turcotte, Y. Liang, M. Tanimoto, Q. Zhang, Z. Li, M. Koyama, E. Betzig, N. Ji, *Proc. Natl. Acad. Sci. USA* **2019**, *116*, 9586.
- [30] R. Heintzmann, T. M. Jovin, C. Cremer, *J. Opt. Soc. Am.* **2002**, *A19*, 1599.
- [31] S. W. Hell, *European patent EP* **1992**, 0491289.
- [32] S. W. Hell, E. H. K. Stelzer, S. Lindek, C. Cremer, *Opt. Lett.* **1994**, *19*, 222.
- [33] A. Egner, S. Jakobs, S. W. Hell, *Proc. Natl. Acad. Sci. USA* **2002**, *99*, 3370.
- [34] E. H. Syngé, *Phil. Mag.* **1928**, *6*, 356.
- [35] D. W. Pohl, W. Denk, M. Lanz, *Appl. Phys. Lett.* **1984**, *44*, 651.
- [36] A. Lewis, M. Isaacson, A. Harootunian, A. Murray, *Ultramicroscopy* **1984**, *13*, 227.
- [37] F. Zenhausern, M. O'boyle, H. Wickramasinghe, *Appl. Phys. Lett.* **1994**, *65*, 1623.
- [38] X. Chen, D. Hu, R. Mescall, G. You, D. N. Basov, Q. Dai, M. Liu, *Adv. Mater.* **2019**, *31*, 1804774.
- [39] M. Rang, A. C. Jones, F. Zhou, Z.-Y. Li, B. J. Wiley, Y. Xia, M. B. Raschke, *Nano Lett.* **2008**, *8*, 3357.
- [40] T. Neuman, P. Alonso-González, A. Garcia-Etxarri, M. Schnell, R. Hillenbrand, J. Aizpurua, *Laser Phot. Rev.* **2015**, *9*, 637.
- [41] J. Kohoutek, D. Dey, A. Bonakdar, R. Gelfand, A. Sklar, O. G. Memis, H. Mohseni, *Nano Lett.* **2011**, *11*, 3378.
- [42] D. Nowak, W. Morrison, H. K. Wickramasinghe, J. Jahng, E. Potma, L. Wan, R. Ruiz, T. R. Albrecht, K. Schmidt, J. Frommer, D. P. Sanders, S. Park, *Sci. Adv.* **2016**, *2*, e1501571.
- [43] C. E. Shannon, *Bell Syst. Tech. J.* **1948**, *27*, 379.
- [44] G. Toraldo di Francia, *Nuovo Cimento Suppl.* **1952**, *31X*, 426.
- [45] P. B. Fellgett, E. H. Linfoot, *Proc. R. Soc. London Ser.* **1955**, *A247*, 369.
- [46] W. Lukosz, *J. Opt. Soc. Am.* **1966**, *56*, 1463.
- [47] W. Lukosz, *J. Opt. Soc. Am.* **1967**, *57*, 932.
- [48] J. Cox, C. J. R. Sheppard, *J. Opt. Soc. Am.* **1986**, *A* *3*, 1152.
- [49] D. Rumelhart, G. Hinton, R. Williams, *Nature* **1986**, *323*, 533.
- [50] E. J. Candès, J. K. Romberg, T. Tao, *Commun. Pure Appl. Anal.* **2006**, *59*, 1207.
- [51] D. L. Donoho, *IEEE Trans. Inf. Theory* **2006**, *52*, 1289.
- [52] S. Gazit, A. Szameit, Y. C. Eldar, M. Segev, *Opt. Express* **2009**, *17*, 23920.
- [53] A. Szameit, Y. Shechtman, E. Osherovich, E. Bullich, P. Sidorenko, H. Dana, S. Steiner, E. B. Kley, S. Gazit, T. Cohen-Hyams, S. Shoham, M. Zibulevsky, I. Yavneh, Y. C. Eldar, O. Cohen, M. Segev, *Nat. Mater.* **2012**, *11*, 455.
- [54] G. Dardikman-Yoffe, Y. C. Eldar, *Opt. Express* **2020**, *28*, 27736.
- [55] Y. Rivenson, Z. Göröcs, H. Günaydin, Y. Zhang, H. Wang, A. Ozcan, *Optica* **2017**, *4*, 1437.
- [56] G. Barbastathis, A. Ozcan, G. Situ, *Optica* **2019**, *6*, 921.
- [57] Y. Rivenson, T. Liu, Z. Wei, Y. Zhang, K. de Haan, A. Ozcan, *Light Sci. & Appl.* **2019**, *8*, 23.
- [58] T. Pu, J.-Y. Ou, V. Savinov, G. Yuan, N. Papisimakis, N. I. Zheludev, *Adv. Sci.* **2021**, *8*, 2002886.
- [59] C. Rendon-Barraza, E. A. Chan, G. Yuan, G. Adamo, T. Pu, N. I. Zheludev, *APL Photon* **2021**, *6*, 066107.
- [60] E. Narimanov, *Adv. Photonics* **2019**, *1*, 056003.
- [61] R. P. Feynman, R. B. Leighton, M. Sands, *The Feynman lectures on physics*, Vol. 1. Pasadena: California Institute of Technology; **2013**, Chapter 30. Diffraction.
- [62] M. Tsang, *Contemp. Phys.* **2019**, *60*, 279.
- [63] R. Tenne, U. Rossman, B. Rephael, Y. Israel, A. Krupinski-Ptaszek, R. Lapkiewicz, Y. Silberberg, D. Oron, *Nat. Photonics* **2019**, *13*, 116.
- [64] A. A. Pushkina, G. Maltese, J. I. Costa-Filho, P. Patel, A. I. Lvovsky, *Phys. Rev. Lett.* **2021**, *127*, 253602.
- [65] D. Zhang, C. Li, C. Zhang, M. N. Slipchenko, G. Eakins, J.-X. Cheng, *Sci. Adv.* **2016**, *2*, e1600521.
- [66] P. Wang, M. N. Slipchenko, J. Mitchell, C. Yang, E. O. Potma, X. Xu, J.-X. Cheng, *Nat. Photonics* **2013**, *7*, 449.
- [67] G. Zanini, K. Korobchevskaya, T. Deguchi, A. Diaspro, P. Bianchini, *ACS Nano* **2019**, *13*, 9673.
- [68] Y. Yonemaru, A. F. Palonpon, S. Kawano, N. I. Smith, S. Kawata, K. Fujita, *Phys. Rev. Applied* **2015**, *4*, 014010.
- [69] H. Pinhas, O. Wagner, Y. Danan, M. Danino, Z. Zalevsky, M. Sinvani, *Opt. Exp.* **2018**, *26*, 25370.
- [70] Y.-S. Duh, Y. Nagasaki, Y.-L. Tang, P.-H. Wu, H.-Y. Cheng, T.-H. Yen, H.-X. Ding, K. Nishida, I. Hotta, J.-H. Yang, Y.-P. Lo, K.-P. Chen, K. Fujita, C.-W. Chang, K.-H. Lin, J. Takahara, S.-W. Chu, *Nat. Comm.* **2020**, *11*, 4101.
- [71] O. Tzang, A. Pevzner, R. E. Marvel, R. F. Haglund, O. Cheshnovsky, *Nano Lett.* **2015**, *15*, 1362.
- [72] M. J. Huttunen, A. Abbas, J. Upham, R. W. Boyd, *J. Opt.* **2017**, *19*, 085504.
- [73] C. J. R. Sheppard, S. B. Mehta, R. Heintzmann, *Opt. Lett.* **2013**, *38*, 2889.
- [74] H. Siedentopf, R. Zsigmondy, *Ann. Phys.* **1902**, *315*, 1.
- [75] F. Zernike, *Physica* **1942**, *9*, 686.
- [76] G. Nomarski, Interferential polarizing device for study of phase objects. US patent 2924142, priority on May 14 (1952).
- [77] A. Curtis, *J. Cell Biol.* **1964**, *20*, 199.
- [78] G. S. Kino, S. S. C. Chim, *Appl. Opt.* **1990**, *29*, 3775.
- [79] E. Cucho, F. Bevilacqua, C. Depeursinge, *Opt. Lett.* **1999**, *24*, 291.
- [80] P. Ferraro, S. Grilli, D. Alfieri, S. De Nicola, A. Finizio, G. Pierattini, B. Javidi, G. Coppola, V. Striano, *Opt. Express* **2005**, *13*, 6738.
- [81] S.-H. Hong, J.-S. Jang, B. Javidi, *Opt. Express* **2004**, *12*, 483.
- [82] G. Popescu, T. Ikeda, R. R. Dasari, M. S. Feld, *Opt. Lett.* **2006**, *31*, 775.
- [83] J. Zhang, E. Moradi, M. G. Somekh, M. L. Mather, *Sci. Reports* **2018**, *8*, 697.
- [84] K. Lindfors, T. Kalkbrenner, P. Stoller, V. Sandoghdar, *Phys. Rev. Lett.* **2004**, *93*, 037401.
- [85] P. Kukura, H. Ewers, C. Müller, A. Renn, A. Helenius, V. Sandoghdar, *Nat. Methods* **2009**, *6*, 923.
- [86] A. M. Maiden, M. J. Humphry, F. Zhang, J. M. Rodenburg, *J. Opt. Soc. Am.* **2011**, *A* *28*, 604.
- [87] E. Balaur, G. A. Cadenazzi, N. Anthony, A. Spurling, E. Hanssen, J. Orian, K. A. Nugent, B. S. Parker, B. Abbey, *Nat. Photonics* **2021**, *15*, 222.
- [88] Y.-F. Huang, G.-Y. Zhuo, C.-Y. Chou, C.-H. Lin, W. Chang, C.-L. Hsieh, *ACS Nano* **2017**, *11*, 2575.
- [89] A. Diaspro, C. A. Nicolini, *Cell Biophys.* **1987**, *10*, 45.
- [90] S. K. Mirsky, N. T. Shaked, *Opt. Express* **2019**, *27*, 26708.
- [91] O. Haeberlé, K. Belkebir, H. Giovaninni, A. Sentenac, *J. Mod. Opt.* **2010**, *57*, 686.
- [92] R. Heintzmann, *Phil. Trans. R. Soc. A* **2021**, *379*, 20210105.
- [93] K. Wicker, R. Heintzmann, *Nat. Photonics* **2014**, *8*, 342.
- [94] F. Hu, M. G. Somekh, D. J. Albutt, K. Webb, E. Moradi, C. W. See, *Sci. Reports* **2015**, *5*, 8589.
- [95] Y. Cotte, F. Toy, P. Jourdain, N. Pavillon, D. Boss, P. Magistretti, P. Marquet, C. Depeursinge, *Nat. Photonics* **2013**, *7*, 113.

- [96] G. Zheng, R. Horstmeyer, C. Yang, *Nat. Photonics* **2013**, *7*, 739.
- [97] V. Olshausen, A. Rohrbach, *Opt. Lett.* **2013**, *38*, 4066.
- [98] D. Ruh, J. Mutschler, M. Michelbach, A. Rohrbach, *Optica* **2018**, *5*, 1371.
- [99] Ø. I. Helle, F. T. Dullo, M. Lahrberg, J.-C. Tinguely, S. Ahluwalia, *Nat. Photonics* **2020**, *14*, 431.
- [100] X. W. Liu, C. F. Kuang, X. Hao, C. L. Pang, P. F. Xu, H. F. Li, Y. Liu, C. Yu, Y. K. Xu, D. Nan, W. D. Shen, Y. Fang, L. N. He, X. Liu, Q. Yang, *Phys. Rev. Lett.* **2017**, *118*, 076101.
- [101] C. Pang, J. Li, M. Tang, J. Wang, I. Mela, F. Ströhl, L. Hecker, W. Shen, Q. Liu, X. Liu, Y. Wang, H. Zhang, M. Xu, X. Zhang, X. Liu, Q. Yang, C. F. Kaminski, *Adv. Funct. Mater.* **2019**, *29*, 1900126.
- [102] F. Ströhl, I. S. Opstad, J.-C. Tinguely, F. T. Dullo, I. Mela, J. W. M. Osterrieth, B. S. Ahluwalia, C. F. Kaminski, *Opt. Express* **2019**, *27*, 25280.
- [103] M. Tang, Y. Han, D. Ye, Q. Zhang, C. Pang, X. Liu, W. Shen, Y. Ma, C. F. Kaminski, X. Liu, Q. Yan, Scalable universal tunable virtual-wavevector spatial frequency shift (TVSFS) super-resolution imaging. arXiv:2103.09321.
- [104] F. Wei, D. Lu, H. Shen, J. L. Ponsetto, E. Huang, Z. Liu, *Nano Lett.* **2014**, *14*, 4634.
- [105] J. L. Ponsetto, A. Bezryadina, F. Wei, K. Onishi, H. Shen, E. Huang, L. Ferrari, Q. Ma, Y. Zou, Z. Liu, *ACS Nano* **2017**, *11*, 5344.
- [106] A. Bezryadina, J. Zhao, Y. Xia, X. Zhang, Z. Liu, *ACS Nano* **2018**, *12*, 8248.
- [107] E. Narimanov, *ACS Photonics* **2016**, *3*, 1090.
- [108] Q. Ma, H. Qian, S. Montoya, W. Bao, L. Ferrari, H. Hu, E. Khan, Y. Wang, E. E. Fullerton, E. E. Narimanov, X. Zhang, Z. Liu, *ACS Nano* **2018**, *12*, 11316.
- [109] Y. U. Lee, J. Zhao, Q. Ma, L. K. Khorashad, C. Posner, G. Li, G. B. M. Wisna, Z. Burns, J. Zhang, Z. Liu, *Nat. Commun.* **2021**, *12*, 1559.
- [110] J. Haug, M. Malei, J. D. Shrouf, E. Narimanov, P. W. Bohn, A. J. Hoffman, *Opt. Express* **2021**, *29*, 42331.
- [111] M. Berry, N. Zheludev, Y. Aharonov, F. Colombo, I. Sabadini, D. C. Struppa, K. Tollaksen, E. T. F. Rogers, F. Qin, M. Hong, X. Luo, R. Remez, A. Arie, J. B. Götte, M. R. Dennis, A. M. H. Wong, G. V. Eleftheriades, Y. Eliezer, A. Bahabad, G. Chen, Z. Wen, G. Liang, C. Hao, C.-W. Qiu, A. Kempf, E. Katzav, M. Schwartz, *J. Opt.* **2019**, *21*, 053002.
- [112] M. V. Berry, S. Popescu, *J. Phys. A: Math. Gen.* **2006**, *39*, 6965.
- [113] F. M. Huang, N. I. Zheludev, Y. Chen, F. Javier Garcia de Abajo, *Appl. Phys. Lett.* **2007**, *90*, 091119.
- [114] F. M. Huang, T. S. Kao, V. A. Fedotov, Y. Chen, N. I. Zheludev, *Nano Lett.* **2008**, *8*, 2469.
- [115] N. I. Zheludev, *Nat. Mater.* **2008**, *7*, 420.
- [116] K. Huang, H. Ye, J. Teng, S. P. Yeo, B. Luk'yanchuk, C.-W. Qiu, *Laser Photonics Rev.* **2014**, *8*, 152.
- [117] G. H. Yuan, E. T. F. Rogers, T. Roy, N. I. Zheludev, *Opt. Express* **2014**, *22*, 6428.
- [118] C. Hao, Z. Nie, H. Ye, H. Li, Y. Luo, R. Feng, X. Yu, F. Wen, Y. Zhang, C. Yu, J. Teng, B. Luk'yanchuk, C.-W. Qiu, *Sci. Adv.* **2017**, *3*, e1701398.
- [119] K. Huang, F. Qin, H. Liu, H. Ye, C.-W. Qiu, M. Hong, B. Luk'yanchuk, J. Teng, *Adv. Mater.* **2018**, *30*, 1704556.
- [120] J. Xue, Z.-K. Zhou, L. Lin, C. Guo, S. Sun, D. Lei, C.-W. Qiu, X.-H. Wang, *Light: Sci. Appl.* **2019**, *8*, 101.
- [121] H. Nassenstein, *Opt. Commun.* **1970**, *2*, 231.
- [122] J. B. Pendry, *Phys. Rev. Lett.* **2000**, *85*, 3966.
- [123] V. Veselago, *Sov. Phys. Usp.* **1968**, *10*, 509.
- [124] I. I. Smolyaninov, J. Elliott, A. Zayats, C. C. Davis, *Phys. Rev. Lett.* **2005**, *94*, 057401.
- [125] Z. Liu, S. Durant, H. Lee, Y. Pikus, N. Fang, Y. Xiong, C. Sun, X. Zhang, *Nano Lett.* **2007**, *7*, 403.
- [126] Z. Jacob, L. V. Alekseyev, E. Narimanov, *Opt. Express* **2006**, *14*, 8247.
- [127] A. Salandrino, N. Engheta, *Phys. Rev. B* **2006**, *74*, 075103.
- [128] G. Leroosey, J. de Rosny, A. Tourin, M. Fink, *Science* **2007**, *315*, 1120.
- [129] E. G. van Putten, D. Akbulut, J. Bertolotti, W. L. Vos, A. Lagendijk, A. P. Mosk, *Phys. Rev. Lett.* **2011**, *106*, 193905.
- [130] U. Leonhardt, *New J. Phys.* **2009**, *11*, 093040.
- [131] V. N. Smolyaninova, I. I. Smolyaninov, A. V. Kildishev, V. M. Shalaev, *Opt. Lett.* **2010**, *35*, 3396.
- [132] E. T. F. Rogers, J. Lindberg, T. Roy, S. Savo, J. E. Chad, M. R. Dennis, N. I. Zheludev, *Nature Mater* **2011**, *11*, 432.
- [133] H. Cang, A. Salandrino, Y. Wang, X. Zhang, *Nature Comm* **2015**, *6*, 7942.
- [134] J. Y. Lee, B. H. Hong, W. Y. Kim, S. K. Min, Y. Kim, M. V. Jouravlev, R. Bose, K. S. Kim, I. Hwang, L. J. Kaufman, C. W. Wong, P. Kim, K. S. Kim, *Nature* **2009**, *460*, 498.
- [135] D. R. Mason, M. V. Jouravlev, K. S. Kim, *Opt. Lett.* **2010**, *35*, 2007.
- [136] Z. Wang, W. Guo, L. Li, B. Luk'yanchuk, A. Khan, Z. Liu, Z. Chen, M. Hong, *Nat. Commun.* **2011**, *2*, 218.
- [137] A. Darafsheh, G. F. Walsh, L. Dal Negro, V. N. Astratov, *Appl. Phys. Lett.* **2012**, *101*, 141128.
- [138] K. W. Allen, N. Farahi, Y. Li, N. I. Limberopoulos, D. E. Walker, Jr., A. M. Urbas, V. Liberman, V. N. Astratov, *Ann. Phys. (Berlin)* **2015**, *527*, 513.
- [139] Y. Duan, G. Barbastathis, B. Zhang, *Opt. Lett.* **2013**, *38*, 2988.
- [140] A. V. Maslov, V. N. Astratov, *Phys. Rev. Applied* **2019**, *11*, 064004.
- [141] R. Heydari, C. Simovski, *Phot. Nanostr. Fund. Appl.* **2021**, *46*, 100950.
- [142] A. R. Bekirov, B. S. Luk'yanchuk, Z. Wang, A. A. Fedyanin, *Opt. Mater. Express* **2021**, *11*, 3646.
- [143] F. Wang, L. Liu, H. Yu, Y. Wen, P. Yu, Z. Liu, Y. Wang, W. J. Li, *Nat. Commun.* **2016**, *7*, 13748.
- [144] W. Fan, B. Yan, Z. Wang, L. Wu, *Sci. Adv.* **2016**, *2*, e1600901.
- [145] F. Wang, L. Liu, P. Yu, Z. Liu, H. Yu, Y. Wang, W. J. Li, *Sci. Reports* **2016**, *6*, 24703.
- [146] M. Aakhte, V. Abbasian, E. A. Akhlaghi, A.-R. Moradi, A. Anand, B. Javidi, *Appl. Opt.* **2017**, *56*, D8.
- [147] I. Kassamakov, S. Lecler, A. Nolvi, A. Leong-Hoi, P. Montgomery, E. Hæggestrom, *Sci. Reports* **2017**, *7*, 3683.
- [148] Y. Wang, S. Guo, D. Wang, Q. Lin, L. Rong, J. Zhao, *Opt. Commun.* **2016**, *366*, 81.
- [149] V. Astratov, (ed.), *Label-Free Super-Resolution Microscopy*, Springer, Cham, **2019**.
- [150] E. Betzig, *Opt. Lett.* **1995**, *20*, 237.
- [151] J. Min, C. Vonesch, H. Kirshner, L. Carlini, N. Olivier, S. Holden, S. Manley, J. C. Ye, M. Unser, *Sci. Rep.* **2014**, *4*, 4577.
- [152] L. Zhu, W. Zhang, D. Elnatan, B. Huang, *Nat. Methods* **2012**, *9*, 721.
- [153] O. Solomon, M. Mutzafi, M. Segev, Y. C. Eldar, *Opt. Express* **2018**, *26*, 18238.
- [154] O. Solomon, Y. C. Eldar, M. Mutzafi, M. Segev, *SIAM J. on Img. Sci.* **2019**, *12*, 392.
- [155] A. Beck, M. Teboulle, In Y. C. Eldar, D. P. Palomar, Eds., *Convex Optimization in Signal Processing and Communications*, pp. 42–88. Cambridge university press, Cambridge, UK **2009**.
- [156] K. Gregor, Y. LeCun, *Proc. Of 27th Int. Conf. on machine learning* **2010**, 399.
- [157] V. Monga, Y. Li, Y. C. Eldar, *IEEE Signal Processing Magazine* **2021**, *17*.
- [158] D. Sage, H. Kirshner, T. Pengo, N. Stuurman, J. Min, S. Manley, M. Unser, *Nat. Methods* **2015**, *12*, 717.
- [159] M. Ovesný, P. Křížek, J. Borkovec, Z. Svindrych, G. M. Hagen, *Bioinformatics* **2014**, *30*, 2389.
- [160] E. Nehme, L. E. Weiss, T. Michaeli, Y. Shechtman, *Optica* **2018**, *5*, 458.
- [161] Y. B. Sahel, J. P. Bryan, B. Cleary, S. L. Farhi, Y. C. Eldar, *IEEE Signal Processing Magazine* **2022**, *39*, 45.



- [162] L. Kang, K. Takeo, In International Conference on Information Processing in Medical Imaging. **2009**, 362–373.
- [163] Z. Yin, T. Kanade, M. Chen, *Medical Image Analysis* **2012**, *16*, 1047.
- [164] F. Sha, Y. Lin, L. K. Saul, D. D. Lee, *Neural Computation* **2007**, *19*, 2004.
- [165] X. Wang, K. Yu, S. Wu, J. Gu, Y. Liu, C. Dong, Y. Qiao, C. C. Loy, in: *Computer Vision – ECCV 2018 Workshops*, (Eds: L. Leal-Taixé, S. Roth), Springer International Publishing, Cham, **2019**, pp. 63–79.
- [166] Y. Chen, Y. Xie, Z. Zhou, F. Shi, A. G. Christodoulou, D. Li, in: *2018 IEEE 15th International Symposium on Biomedical Imaging (ISBI 2018)*, IEEE, Washington, DC, **2018**, pp. 739–742.
- [167] Y. M. Sigal, R. Zhou, X. Zhuang, *Science* **2018**, *361*, 880.
- [168] Y. Rivenson, Z. Gorocs, H. Günaydin, Y. Zhang, H. Wang, A. Ozcan, ArXiv: 1705.04709 [Cs], submitted: May 2017.
- [169] Y. Rivenson, H. Ceylan Koydemir, H. Wang, Z. Wei, Z. Ren, H. Günaydin, Y. Zhang, Z. Göröcs, K. Liang, D. Tseng, A. Ozcan, *ACS Photonics* **2018**, *5*, 2354.
- [170] H. Wang, Y. Rivenson, Y. Jin, Z. Wei, R. Gao, H. Günaydin, L. A. Bentolila, A. Ozcan, bioRxiv <https://doi.org/10.1101/309641>, submitted: April 2018.
- [171] M. Weigert, U. Schmidt, T. Boothe, A. Müller, A. Dibrov, A. Jain, B. Wilhelm, D. Schmidt, C. Broaddus, S. Culley, M. Rocha-Martins, F. Segovia-Miranda, C. Norden, R. Henriques, M. Zerial, M. Solimena, J. Rink, P. Tomancak, L. Royer, F. Jug, E. W. Myers, *Nat. Methods* **2018**, *15*, 1090.
- [172] H. Wang, Y. Rivenson, Y. Jin, Z. Wei, R. Gao, H. Günaydin, L. A. Bentolila, C. Kural, A. Ozcan, *Nat. Methods* **2019**, *16*, 103.
- [173] H. Zhou, R. Cai, T. Quan, S. Liu, S. Li, Q. Huang, A. Ertürk, S. Zeng, *Opt. Lett.* **2020**, *45*, 1695.
- [174] C. Qiao, D. Li, Y. Guo, C. Liu, T. Jiang, Q. Dai, D. Li, *Nat. Methods* **2021**, *18*, 194.
- [175] J. Chen, H. Sasaki, H. Lai, Y. Su, J. Liu, Y. Wu, A. Zhovmer, C. A. Combs, I. Rey-Suarez, H.-Y. Chang, C. C. Huang, X. Li, M. Guo, S. Nizambad, A. Upadhyaya, S.-J. Lee, L. A. G. Lucas, H. Shroff, *Nat. Methods* **2021**, *18*, 678.
- [176] Y. Wu, Y. Rivenson, H. Wang, Y. Luo, E. Ben-David, L. A. Bentolila, C. Pritz, A. Ozcan, *Nat. Methods* **2019**, *16*, 1323.
- [177] L. Huang, H. Chen, Y. Luo, Y. Rivenson, A. Ozcan, *Light Sci. Appl.* **2021**, *10*, 62.
- [178] Y. Rivenson, H. Wang, Z. Wei, K. de Haan, Y. Zhang, Y. Wu, H. Günaydin, J. E. Zuckerman, T. Chong, A. E. Sisk, L. M. Westbrook, W. D. Wallace, A. Ozcan, *Nat. Biomed. Eng.* **2019**, *3*, 466.
- [179] Y. Zhang, K. de Haan, Y. Rivenson, J. Li, A. Delis, A. Ozcan, *Light Sci. Appl.* **2020**, *9*, 78.
- [180] K. de Haan, Y. Zhang, J. E. Zuckerman, T. Liu, A. E. Sisk, M. F. P. Diaz, K.-Y. Jen, A. Nobori, S. Liou, S. Zhang, R. Riahi, Y. Rivenson, W. D. Wallace, A. Ozcan, *Nat. Commun.* **2021**, *12*, 4884.
- [181] E. M. Christiansen, S. J. Yang, D. M. Ando, A. Javaherian, G. Skibinski, S. Lipnick, E. Mount, A. O’Neil, K. Shah, A. K. Lee, P. Goyal, W. Fedus, R. Poplin, A. Esteva, M. Berndl, L. L. Rubin, P. Nelson, S. Finkbeiner, *Cell* **2018**, *173*, 792.
- [182] C. Ounkomol, S. Seshamani, M. M. Maleckar, F. Collman, G. R. Johnson, *Nat. Methods* **2018**, *15*, 917.
- [183] Y. Lecun, L. Bottou, Y. Bengio, P. Haffner, *Proc. IEEE* **1998**, *86*, 2278.
- [184] O. Ronneberger, P. Fischer, T. Brox, ArXiv:1505.04597 [Cs] **2015**.
- [185] G. Huang, Z. Liu, L. Van Der Maaten, K. Q. Weinberger, in: *2017 IEEE Conference on Computer Vision and Pattern Recognition (CVPR)*, IEEE, Honolulu, **2017**, p. 2261.
- [186] F. Zhao, L. Zhu, C. Fang, T. Yu, D. Zhu, P. Fei, *Biomed. Opt. Express* **2020**, *11*, 7273.
- [187] W. Ouyang, A. Aristov, M. Lelek, X. Hao, C. Zimmer, *Nat. Biotechnol.* **2018**, *36*, 460.
- [188] K. He, X. Zhang, S. Ren, J. Sun, in: *2016 IEEE Conference on Computer Vision and Pattern Recognition (CVPR)*, IEEE, Las Vegas, **2016**, 770.
- [189] N. Boyd, E. Jonas, H. Babcock, B. Recht, BioRxiv **2018**, <https://doi.org/10.1101/267096>
- [190] E. Nehme, D. Freedman, R. Gordon, B. Ferdman, L. E. Weiss, O. Alalouf, T. Naor, R. Orange, T. Michaeli, Y. Shechtman, *Nat. Methods* **2020**, *17*, 734.
- [191] C. Ling, C. Zhang, M. Wang, F. Meng, L. Du, X. Yuan, *Photon. Res.* **2020**, *8*, 1350.
- [192] T. Nguyen, Y. Xue, Y. Li, L. Tian, G. Nehmetallah, *Opt. Express* **2018**, *26*, 26470.
- [193] Y. Xue, S. Cheng, Y. Li, L. Tian, *Optica* **2019**, *6*, 618.
- [194] J. Zhang, T. Xu, X. Li, Y. Zhang, Y. Chen, X. Wang, S. Wang, C. Wang, *IEEE Photonics J.* **2020**, *12*, 6900914.
- [195] T. Liu, K. de Haan, Y. Rivenson, Z. Wei, X. Zeng, Y. Zhang, A. Ozcan, *Sci. Rep.* **2019**, *9*, 3926.
- [196] Y. Wu, Y. Luo, G. Chaudhari, Y. Rivenson, A. Calis, K. de Haan, A. Ozcan, *Light Sci. Appl.* **2019**, *8*, 25.
- [197] L. Zwald, S. Lambert-Lacroix, ArXiv:1207.6868 [Math, Stat] **2012**.
- [198] I. J. Goodfellow, J. Pouget-Abadie, M. Mirza, B. Xu, D. Warde-Farley, S. Ozair, A. Courville, Y. Bengio, ArXiv:1406.2661 [Cs, Stat] **2014**.
- [199] J. Johnson, A. Alahi, L. Fei-Fei, ArXiv:1603.08155 [Cs] **2016**.
- [200] X. Lin, Y. Rivenson, N. T. Yardimci, M. Veli, Y. Luo, M. Jarrahi, A. Ozcan, *Science* **2018**, *361*, 1004.
- [201] J. Li, D. Meng, N. T. Yardimci, Y. Luo, X. Li, M. Veli, Y. Rivenson, M. Jarrahi, A. Ozcan, *Sci. Adv.* **2021**, *7*, eabd7690.
- [202] N. I. Zheludev, G. H. Yuan, *Nat. Rev. Phys.* **2022**, *4*, 421,.
- [203] T. Liu, C.-H. Chi, J.-Y. Ou, J. Xu, E. A. Chan, K. F. MacDonald, N. I. Zheludev, *Nat. Mater.* **2023**, *22*, 844.
- [204] A. B. Samokhin, A. S. Samokhina, *Differ. Equ.* **2016**, *52*, 1178.
- [205] V. Vemuri, G. S. Jang, *Journal of the Franklin Institute-Engineering and Applied Mathematics* **1992**, *329*, 241.
- [206] T. Pu, J. Y. Ou, N. Papisimakis, N. I. Zheludev, *Appl. Phys. Lett.* **2020**, *116*, 131105.
- [207] T. O. Pu, Y. J. V. Savinov, G. H. Yuan, N. Papisimakis, N. I. Zheludev, *Adv. Sci.* **2020**, *2020*, 2002886.
- [208] E. A. Chan, et al. Optical counting of particles too small to see. *CLEO/Europe-EQEC 2021, Learning in Imaging and Metrology I JSIV-2.5* **2021**.
- [209] <https://en.wikipedia.org/wiki/Microscopy>.
- [210] G. H. Yuan, E. T. F. Rogers, N. I. Zheludev, *Light: Sci. Appl.* **2019**, *8*, 2.
- [211] G. H. Yuan, N. I. Zheludev, *Science* **2019**, *364*, 771,.
- [212] Z. Liu, H. Lee, Y. Xiong, C. Sun, X. Zhang, *Science* **2007**, *314*, 1686.
- [213] L. Ferrari, C. Wu, D. Lepage, X. Zhang, Z. Liu, *Prog. Quantum. Electron.* **2015**, *40*, 1.
- [214] K. A. Willets, A. J. Wilson, V. Sundaresan, P. B. Joshi, *Chem. Rev.* **2017**, *117*, 7538.
- [215] Q. Ma, Z. Liu, *Natl. Sci. Rev.* **2018**, *5*, 141.
- [216] B. Wood, J. B. Pendry, D. P. Tsai, *Phys. Rev. B* **2006**, *74*, 115116.
- [217] E. E. Narimanov, *ACS Photonics* **2016**, *3*, 1090.
- [218] Y. U. Lee, K. Yim, S. E. Bopp, J. Zhao, Z. Liu, *Adv. Mat.* **2020**, *32*, 2002387.
- [219] Y. U. Lee, C. Posner, Z. Nie, J. Zhao, S. Li, S. E. Bopp, G. B. M. Wisna, J. Ha, C. Song, J. Zhang, S. Yang, X. Zhang, Z. Liu, *Adv. Sci.* **2021**, *8*, 2102230.
- [220] Y. U. Lee, S. Li, S. E. Bopp, J. Zhao, Z. Nie, C. Posner, S. Yang, X. Zhang, J. Zhang, Z. Liu, *Adv. Mat.* **2021**, *33*, 2006496.
- [221] P. Zhang, G. Ma, W. Dong, Z. Wan, S. Wang, N. Tao, *Nat. Methods* **2020**, *17*, 1010.
- [222] E. Mudry, K. Belkebir, J. Girard, J. Savatier, E. Le Moal, C. Nicoletti, M. Allain, A. Sentenac, *Nat. Photonics* **2012**, *6*, 312.
- [223] Y. Choi, M. Kim, C. Park, J. Park, Y. Park, Y. H. Cho, *Nano Lett.* **2022**, *22*, 2194.



- [224] C. Park, J. H. Park, C. Rodriguez, H. Yu, M. Kim, K. Jin, S. Han, J. Shin, S. H. Ko, K. T. Nam, Y. H. Lee, Y. H. Cho, Y. Park, *Phys. Rev. Lett.* **2014**, *113*, 113901.
- [225] C. Belthangady, L. A. Royer, *Nat. Methods* **2019**, *16*, 1215.
- [226] F. Wang, Y. Bian, H. Wang, M. Lyu, G. Pedrini, W. Osten, G. Barbastathis, G. Situ, *Light: Science and Applications* **2020**, *9*, 77.
- [227] E. Bostan, R. Heckel, M. Chen, M. Kellman, L. Waller, *Optica* **2020**, *7*, 559.
- [228] K. Monakhova, V. Tran, G. Kuo, L. Waller, *Opt. Express* **2021**, *13*, 20913.
- [229] E. Sakat, V. Giliberti, M. Bollani, A. Notargiacomo, M. Pea, M. Finazzi, G. Pellegrini, J.-P. Hugonin, A. Weber-Bargioni, M. Melli, S. Sassolini, S. Cabrini, P. Biagioni, M. Ortolani, L. Baldassarre, *Phys. Rev. Applied* **2017**, *8*, 054042.
- [230] B. Herman, K. Jacobson, *Optical Microscopy for Biology*, 1st ed. Wiley, New York **1990**.
- [231] J. W. Goodman, *Introduction to Fourier Optics*, 3rd ed. Eaglewood, Roberts & Co., **2004**.
- [232] J.-L. Lagrange, Sur une Loi generale d'Optique (Memoires de l'Academie de Berlin, 1803).
- [233] H. von Helmholtz, *Proceedings of the Bristol Naturalists' Society* **1874**, *1*, 435.
- [234] E. K. Abbe, Beiträge zur Theorie des Mikroskops und der mikroskopischen Wahrnehmung. *Archiv für mikroskopische Anatomie* **1873**, *9*, 413; A contribution to the theory of the microscope, and the nature of microscopic vision, *Proceedings of the Bristol Naturalists' Society*, **1874**, *1*, 200.
- [235] F. M. Huang, N. I. Zheludev, *Nano. Lett.* **2009**, *9*, 1249.
- [236] G. H. Yuan, E. T. F. Rogers, N. I. Zheludev, *Light Sci. Appl.* **2017**, *6*, e17036.
- [237] P. Sidorenko, A. Fleischer, Y. Shechtman, Y. C. Eldar, M. Segev, O. Cohen, *Nat. Commun.* **2015**, *6*, 8209.
- [238] J. L. Harris, *J. Opt. Soc. Am.* **1964**, *54*, 931.
- [239] C. E. Shannon, *Bell Syst. Tech. J.* **1948**, *27*, 623.
- [240] M. C. André, *Ann. de l'École Norm Sup. 2e série* **1876**, *5*, 275.
- [241] L. Raleigh, *Phil. Mag. S.* **1879**, *8*, 261.
- [242] F. L. Clerc, L. Collet, M. Gross, *Opt. Lett.* **2000**, *25*, 716.
- [243] F. Balzarotti, Y. Eilers, K. Gwosch, A. H. Gynn, V. Westphal, F. D. Stefani, J. Elf, S. W. Hell, *Science* **2017**, *355*, 606.
- [244] E. Betzig, J. Trautman, T. Harris, J. Weiner, R. Kostelak, *Science* **1991**, *251*, 1468.
- [245] D. Evanko, A. Heinrichs, C. Rosenthal, *Nature Cell Biol* **2009**, *11*, 1165.
- [246] G. Popescu, *Quantitative phase imaging of cells and tissues*, McGraw-Hill, **2011**.
- [247] Y. Park, C. Depeursinge, G. Popescu, *Nat. Photonics* **2018**, *12*, 578.
- [248] E. Wolf, *Opt. Commun.* **1969**, *1*, 153.
- [249] F. Zernike, *Science* **1955**, *121*, 345.
- [250] D. Gabor, *Nature* **1948**, *161*, 777.
- [251] E. N. Leith, J. Upatnieks, *JOSA* **1962**, *52*, 1123.
- [252] D. Zicha, G. A. Dunn, *J. Microscopy* **1995**, *179*, 11.
- [253] R. Wang, Z. Wang, L. Millet, M. U. Gillette, A. J. Levine, G. Popescu, *Opt. Express* **2011**, *19*, 20571.
- [254] H. Majeed, C. Okoro, A. Kajdacsy-Balla, K. C. Toussaint, G. Popescu, *J. Biomed. Opt.* **2017**, *22*, 046004.
- [255] Y. Kim, H. Shim, K. Kim, H. Park, S. Jang, Y. Park, *Sci. Rep.* **2014**, *4*, 6659.
- [256] T. Kim, R. Zhou, M. Mir, S. D. Babacan, P. S. Carney, L. L. Goddard, G. Popescu, *Nat. Photonics* **2014**, *8*, 256.
- [257] H. Majeed, S. Sridharan, M. Mir, L. Ma, E. Min, W. Jung, G. Popescu, *J. Biophotonics* **2017**, *10*, 177.
- [258] S. Uttam, H. V. Pham, J. LaFace, B. Leibowitz, J. Yu, R. E. Brand, D. J. Hartman, Y. Liu, *Cancer Res.* **2015**, *1274*, 2015.
- [259] X. Chen, M. E. Kandel, C. Hu, Y. J. Lee, G. Popescu, *Light: Sci. Appl.* **2020**, *9*, 142.
- [260] W. Choi, C. Fang-Yen, K. Badizadegan, S. Oh, N. Lue, R. R. Dasari, M. S. Feld, *Nat. Methods* **2007**, *4*, 717.
- [261] F. Charriere, A. Marian, F. Montfort, J. Kuehn, T. Colomb, E. Cuche, P. Marquet, C. Depeursinge, *Opt. Lett.* **2006**, *31*, 178.
- [262] F. Merola, P. Memmolo, L. Miccio, R. Savoia, M. Mugnano, A. Fontana, G. D'Ippolito, A. Sardo, A. Iolascon, A. Gambale, P. Ferraro, *Light: Sci. Appl.* **2017**, *6*, e16241.
- [263] N. Goswami, Y. R. He, Y.-H. Deng, C. Oh, N. Sobh, E. Valera, R. Bashir, N. Ismail, H. Kong, T. H. Nguyen, C. Best-Popescu, G. Popescu, *Light: Sci. Appl.* **2021**, *10*, 176.
- [264] C. Yin, X. Xiao, V. Balaban, M. E. Kandel, Y. J. Lee, G. Popescu, P. Bogdan, *Sci. Rep.* **2020**, *10*, 15078.
- [265] Z. Yan, M. Han, Y. Shi, A. Badea, Y. Yang, A. Kulkarni, E. Hanson, M. E. Kandel, X. Wen, F. Zhang, Y. Luo, Q. Lin, H. Zhang, X. Guo, Y. Huang, K. Nan, S. Jia, A. W. Orham, M. B. Mevis, J. Lim, X. Guo, M. Gao, W. Ryu, K. J. Yu, B. G. Nicolau, A. Petronico, S. S. Rubakhin, J. Lou, P. M. Ajayan, K. Thornton, et al., *Proc. Natl. Acad. Sci. USA* **2017**, *114*, E9455.
- [266] M. E. Kandel, M. Rubessa, Y. R. He, S. Schreiber, S. Meyers, L. M. Naves, M. K. Sermersheim, G. S. Sell, M. J. Szweczyk, N. Sobh, M. B. Wheeler, G. Popescu, *Proc. Natl. Acad. Sci. USA* **2020**, *117*, 18302.
- [267] H. Majeed, A. Keikhosravi, M. E. Kandel, T. H. Nguyen, Y. Liu, A. Kajdacsy-Balla, K. Tangella, K. W. Eliceiri, G. Popescu, *Sci. Rep.* **2019**, *9*, 14679.
- [268] C. Hu, J. J. Field, V. Kelkar, B. Chiang, K. Wernsing, K. C. Toussaint, R. A. Bartels, G. Popescu, *Nat. Photonics* **2020**, *14*, 564.
- [269] D. Zhang, L. Lan, Y. Bai, H. Majeed, M. E. Kandel, G. Popescu, J.-X. Cheng, *Light: Sci. Appl.* **2019**, *8*, 116.
- [270] C. Cvetkovic, R. Raman, V. Chan, B. J. Williams, M. Tolish, P. Bajaj, M. S. Sagar, H. H. Asada, M. T. A. Saif, R. Bashir, *Proc. Natl. Acad. Sci. USA* **2014**, *111*, 10125.
- [271] T. H. Nguyen, M. E. Kandel, M. Rubessa, M. B. Wheeler, G. Popescu, *Nat. Commun.* **2017**, *8*, 210.
- [272] M. E. Kandel, Y. R. He, Y. J. Lee, T. H.-Yu Chen, K. M. Sullivan, O. Aydin, M. T. A. Saif, H. Kong, N. Sobh, G. Popescu, *Nat. Commun.* **2020**, *11*, 6256.
- [273] T. Liu, K. de Haan, Y. Rivenson, Z. Wei, X. Zeng, Y. Zhang, A. Ozcan, *Sci. Rep.* **2019**, *9*, 3926.
- [274] C. Hu, M. E. Kandel, Y. J. Lee, G. Popescu, *Appl. Phys. Lett.* **2021**, *119*, 233701.
- [275] V. Micó, J. Zheng, J. Garcia, Z. Zalevsky, P. Gao, *Adv. Opt. Photonics* **2019**, *11*, 135.
- [276] J. M. Soto, J. A. Rodrigo, T. Alieva, *Opt. Express* **2017**, *25*, 15699.
- [277] M. E. Kandel, C. Hu, G. N. Kouzehgarani, E. Min, K. M. Sullivan, H. Kong, J. M. Li, D. N. Robson, M. U. Gillette, C. Best-Popescu, G. Popescu, *Nat. Commun.* **2019**, *10*, 4691.
- [278] V. Abbasian, Y. Ganjkhani, E. A. Akhlaghi, A. Anand, B. Javidi, A.-R. Moradi, *Journal of Optics* **2018**, *20*, 065301.
- [279] Y. Baek, Y. Park, *Nat. Photonics* **2021**, *15*, 354.
- [280] M. Paturzo, F. Merola, S. Grilli, S. De Nicola, A. Finizio, P. Ferraro, *Opt. Express* **2008**, *16*, 17107.
- [281] R. Horstmeyer, J. Chung, X. Ou, G. Zheng, C. Yang, *Optica* **2016**, *3*, 827.
- [282] J. Li, A. C. Matlock, Y. Li, Q. Chen, C. Zuo, L. Tian, *Advanced Photonics* **2019**, *1*, 066004.
- [283] T. O'Connor, A. Doblas, B. Javidi, *Opt. Lett.* **2019**, *44*, 2326.
- [284] Y. Ganjkhani, M. A. Charsooghi, E. A. Akhlaghi, A.-R. Moradi, *Opt. Commun.* **2017**, *404*, 110.
- [285] M. H. Jenkins, T. K. Gaylord, *Appl. Opt.* **2015**, *54*, 9213.
- [286] H. Hugonnet, M. Lee, Y. Park, *Opt. Express* **2021**, *29*, 6293.
- [287] S. W. Hell, *Science* **2007**, *316*, 1153.

- [288] F. Cheng, J. Zhao, Y. Wang, W. Lu, Z. Liu, Y. Zhou, W. R. Martin, R. Wang, J. Huang, T. Hao, H. Yue, J. Ma, Y. Hou, J. A. Castrillon, J. Fang, J. D. Lathia, R. A. Keri, F. C. Lightstone, E. M. Antman, R. Rabadan, D. E. Hill, C. Eng, M. Vidal, J. Loscalzo, *Nat. Genet.* **2021**, *53*, 342.
- [289] T. R. Simmons, G. Berggren, M. Bacchi, M. Fontecave, V. Artero, *Coord. Chem. Rev.* **2014**, *270–271*, 127.
- [290] J. Jumper, R. Evans, A. Pritzel, T. Green, M. Figurnov, O. Ronneberger, K. Tunyasuvunakool, R. Bates, A. Židek, A. Potapenko, A. Bridgland, C. Meyer, S. A. A. Kohl, A. J. Ballard, A. Cowie, B. Romera-Paredes, S. Nikolov, R. Jain, J. Adler, T. Back, S. Petersen, D. Reiman, E. Clancy, M. Zielinski, M. Steinegger, M. Pacholska, T. Berghammer, S. Bodenstein, D. Silver, O. Vinyals, et al., *Nature* **2021**, *596*, 583.
- [291] I. Ament, J. Prasad, A. Henkel, S. Schmachtel, C. Sönnichsen, *Nano Lett.* **2012**, *12*, 1092.
- [292] P. Zijlstra, P. M. R. Paulo, M. Orrit, *Nat. Nanotechnol.* **2012**, *7*, 379.
- [293] K. Kneipp, Y. Wang, H. Kneipp, L. Perelman, I. Itzkan, R. Dasari, M. Feld, *Phys. Rev. Lett.* **1997**, *78*, 1667.
- [294] E. Kim, M. D. Baaske, F. Vollmer, *Adv. Mater.* **2016**, *28*, 9941.
- [295] Y. Pang, R. Gordon, *Nano Lett.* **2012**, *12*, 402.
- [296] J. Ortega Arroyo, J. Andrecka, K. M. Spillane, N. Billington, Y. Takagi, J. R. Sellers, P. Kukura, *Nano Lett.* **2014**, *14*, 2065.
- [297] M. Piliarik, V. Sandoghdar, *Nat. Commun.* **2014**, *5*, 4495.
- [298] N. Li, T. D. Canady, Q. Huang, X. Wang, G. A. Fried, B. T. Cunningham, *Nat. Commun.* **2021**, *12*, 1744.
- [299] G. Young, N. Hundt, D. Cole, A. Fineberg, J. Andrecka, A. Tyler, A. Olerinyova, A. Ansari, E. G. Marklund, M. P. Collier, S. A. Chandler, O. Tkachenko, J. Allen, M. Crispin, N. Billington, Y. Takagi, J. R. Sellers, C. Eichmann, P. Selenko, L. Frey, R. Riek, M. R. Galpin, W. B. Struwe, J. L. P. Benesch, P. Kukura, et al., *Science* **2018**, *360*, 423.
- [300] P. von Olshausen, A. Rohrbach, *Opt. Lett.* **2013**, *38*, 4066.
- [301] A. Makarov, *Anal. Chem.* **2000**, *72*, 1156.
- [302] E. D. B. Foley, M. S. Kushwah, G. Young, P. Kukura, Label-free tracking and mass measurement of single proteins on lipid bilayers. *bioRxiv* **2021**, 2021.04.08.438951-2021.04.08.438951.
- [303] T. Heermann, F. Steiert, B. Ramm, N. Hundt, P. Schwill, Mass-sensitive particle tracking (MSPT) to elucidate the membrane-associated MinDE reaction cycle. *bioRxiv* **2021**, 2021.04.08.438961-2021.04.08.438961.
- [304] B. Špačková, H. Klein Moberg, J. Fritzsche, J. Tengeham, G. Sjösten, H. Šipová-Jungová, D. Albinsson, Q. Lubart, D. van Leeuwen, F. Westerlund, D. Midtvedt, E. K. Esbjörner, M. Käll, G. Volpe, C. Langhammer, *Nat. Methods* **2022**, *19*, 751.
- [305] R. D. Lillie, *A.M.A. Archives of Dermatology and Syphilology* **1954**, *70*, 549.
- [306] R. D. Allen, *Annual Review of Biophysics and Biophysical Chemistry* **1985**, *14*, 265.
- [307] W. Xu, M. H. Jericho, I. A. Meinertzhagen, H. J. Kreuzer, *Proc. Natl. Acad. Sci. USA* **2001**, *98*, 11301.
- [308] P. Gabriel, *Quantitative Phase Imaging of Cells and Tissues*, McGraw-Hill Education, New York **2011**.
- [309] Y.-H. Lin, W.-L. Chang, C.-L. Hsieh, *Opt. Express* **2014**, *22*, 9159.
- [310] G. Young, P. Kukura, *Annu. Rev. Phys. Chem.* **2019**, *70*, 301.
- [311] R. W. Taylor, V. Sandoghdar, *Nano Lett.* **2019**, *19*, 4827.
- [312] C.-Y. Cheng, Y.-H. Liao, C.-L. Hsieh, *Nanoscale* **2019**, *11*, 568.
- [313] C.-L. Hsieh, *Opt. Commun.* **2018**, *422*, 69.
- [314] J.-S. Park, I.-B. Lee, H.-M. Moon, J.-H. Joo, K.-H. Kim, S.-C. Hong, M. Cho, *Chem. Sci.* **2018**, *9*, 2690.
- [315] J.-S. Park, I.-B. Lee, H.-M. Moon, J.-S. Ryu, S.-Y. Kong, S.-C. Hong, M. Cho, *J. Phys. Chem. Lett.* **2020**, *11*, 10233.
- [316] H. Verschueren, *J. Cell Sci.* **1985**, *75*, 279.
- [317] A. S. G. Curtis, *J. Cell Biol.* **1964**, *20*, 199.
- [318] J. Bereiter-Hahn, C. H. Fox, B. Thorell, *J. Cell Biol.* **1979**, *82*, 767.
- [319] C.-Y. Cheng, C.-L. Hsieh, *ACS Photonics* **2017**, *4*, 1730.
- [320] R. W. Taylor, R. G. Mahmoodabadi, V. Rauschenberger, A. Giessl, A. Schambony, V. Sandoghdar, *Nat. Photonics* **2019**, *13*, 480.
- [321] C.-Y. Cheng, Y.-H. Liao, C.-L. Hsieh, *J. Phys. D: Appl. Phys.* **2021**, *54*, 364001.
- [322] Y.-F. Huang, G.-Y. Zhuo, C.-Y. Chou, C.-H. Lin, C.-L. Hsieh, *Nanoscale* **2017**, *9*, 6567.
- [323] K. Welscher, H. Yang, *Nat. Nanotechnol.* **2014**, *9*, 198.
- [324] S. Hou, J. Exell, K. Welscher, *Nat. Commun.* **2020**, *11*, 3607.
- [325] Y.-H. Liao, C.-H. Lin, C.-Y. Cheng, W. C. Wong, J.-Y. Juo, C.-L. Hsieh, *ACS Nano* **2019**, *13*, 10918.
- [326] C.-L. Hsieh, S. Spindler, J. Ehrig, V. Sandoghdar, *J. Phys. Chem. B* **2014**, *118*, 1545.
- [327] D. Lasne, G. A. Blab, S. Berciaud, M. Heine, L. Groc, D. Choquet, L. Cognet, B. Lounis, *Biophys. J.* **2006**, *91*, 4598.
- [328] Y.-C. Huang, T.-H. Chen, J.-Y. Juo, S.-W. Chu, C.-L. Hsieh, *ACS Photonics* **2021**, *8*, 592.
- [329] P. A. Sandoz, C. Tremblay, F. G. Van Der Goot, M. Frechin, *PLoS Biol.* **2019**, *17*, e3000553.
- [330] Y.-T. Hsiao, C.-N. Tsai, T.-H. Chen, C.-L. Hsieh, *ACS Nano* **2022**, *16*, 2774.
- [331] S. Cheng, S. Fu, Y. M. Kim, W. Song, Y. Li, Y. Xue, J. Yi, L. Tian, *Sci. Adv.* **2021**, *7*, eabe0431.
- [332] C. Yurdakul, O. Avci, A. Matlock, A. J. Devaux, M. V. Quintero, E. Ozbay, R. A. Davey, J. H. Connor, W. C. Karl, L. Tian, M. S. Ünlü, *ACS Nano* **2020**, *14*, 2002.
- [333] F. Jünger, D. Ruh, D. Strobel, R. Michiels, D. Huber, A. Brandel, J. Madl, A. Gavrilov, M. Mihlan, C. C. Daller, E. A. Rog-Zielinska, W. Römer, T. Lämmermann, A. Rohrbach, *Nat. Commun.* **2022**, *13*, 1758.
- [334] R. Hillenbrand, F. Keilmann, P. Hanarp, D. S. Sutherland, J. Aizpurua, *Appl. Phys. Lett.* **2003**, *83*, 368.
- [335] C. T. Putkunz, M. A. Pfeifer, A. G. Peele, G. J. Williams, H. M. Quiney, B. Abbey, K. A. Nugent, I. McNulty, *Opt. Express* **2010**, *18*, 11746.
- [336] I. Peterson, B. Abbey, C. T. Putkunz, D. J. Vine, G. A. Van Riessen, G. A. Cadenazzi, E. Balaur, R. Ryan, H. M. Quiney, I. McNulty, A. G. Peele, K. A. Nugent, *Opt. Express* **2012**, *20*, 24678.
- [337] Z. Chen, Y. Jiang, Y.-T. Shao, M. E. Holtz, M. Odstrčil, M. Guizar-Sicairos, I. Hanke, S. Ganschow, D. G. Schlom, D. A. Muller, *Science* **2021**, *372*, 826.
- [338] N. Anthony, G. Cadenazzi, K. A. Nugent, B. Abbey, Optical ptychographic microscopy for quantitative anisotropic phase imaging. in *Proc. SPIE* **2016**.
- [339] N. Anthony, C. Darmanin, M. R. Bleackley, K. Parisi, G. Cadenazzi, S. Holmes, M. A. Anderson, K. A. Nugent, B. Abbey, *Biomed. Opt. Express* **2019**, *10*, 4964.
- [340] N. W. Phillips, C. T. Putkunz, G. V. Riessen, H. D. Coughlan, M. W. M. Jones, B. Abbey, *Int. J. Mater. Res.* **2014**, *105*, 655.
- [341] W. Hoppe, *Acta Crystallogr. A* **1969**, *25*, 495.
- [342] R. Hegerl, W. Hoppe, Phase evaluation in generalized diffraction (ptychography). *Proc. Fifth Eur. Cong. Electron Microscopy*, **1972**, 628–629.
- [343] V. Mico, Z. Zalevsky, P. García-Martínez, J. García, *J. Opt. Soc. Am. A* **2006**, *23*, 3162.
- [344] R. W. Gerchberg, *Optica Acta: International Journal of Optics* **1974**, *21*, 709.
- [345] H. Ur, D. Gross, *CVGIP: Graphical Models and Image Processing* **1992**, *54*, 181.
- [346] A. Maiden, D. Johnson, P. Li, *Optica* **2017**, *4*, 736.
- [347] E. Balaur, S. O' Toole, A. J. Spurling, G. B. Mann, B. Yeo, K. Harvey, C. Sadatnajafi, E. Hanssen, J. Orian, K. A. Nugent, B. S. Parker, B. Abbey, *Nature* **2021**, *598*, 65.
- [348] T. S. Ralston, D. L. Marks, P. S. Carney, S. A. Boppart, *Nat. Phys.* **2007**, *3*, 129.

- [349] P. Bouchal, P. Dvořák, J. Babocký, Z. Bouchal, F. Ligmajer, M. Hrtoň, V. Křápek, A. Fařbender, S. Linden, R. Chmelík, T. Šíkola, *Nano Lett.* **2019**, *19*, 1242.
- [350] Y. Yang, C. Zhai, Q. Zeng, A. L. Khan, H. Yu, *ACS Nano* **2019**, *13*, 13595.
- [351] H. H. Chen, G. W. Brodland, *Journal of Biomechanical Engineering* **2000**, *122*, 394.
- [352] I. Malkiel, M. Mrejen, A. Nagler, U. Arieli, L. Wolf, H. Suchowski, *Light: Sci. Appl.* **2018**, *7*, 60.
- [353] R. E. Armstrong, M. Horáček, P. Zijlstra, *Small* **2020**, *16*, 2003934.
- [354] Z. S. Ballard, D. Shir, A. Bhardwaj, S. Bazargan, S. Sathianathan, A. Ozcan, *ACS Nano* **2017**, *11*, 2266.
- [355] D. P. Langley, E. Balaur, Y. Hwang, C. Sadatnajafi, B. Abbey, *Adv. Funct. Mater.* **2018**, *28*, 1704842.
- [356] E. Balaur, C. Sadatnajafi, B. Abbey, *J. Phys.: Conf. Ser.* **2020**, *1455*, 012005.
- [357] C. J. R. Sheppard, *Microsc. Res. Tech.* **2017**, *80*, 590.
- [358] A. Diaspro, P. Bianchini, *La Rivista Del Nuovo Cimento* **2020**, *43*, 385.
- [359] T. Misteli, *Science* **2001**, *291*, 843.
- [360] S. Jadavi, P. Bianchini, O. Cavalleri, S. Dante, C. Canale, A. Diaspro, *Microsc Res Tech* **2021**, *84*, 2472.
- [361] J. Qi, D. J. Elson, *Journal of Biophotonics* **2017**, *10*, 950.
- [362] C. He, H. He, J. Chang, B. Chen, H. Ma, M. Booth, *J. Light Sci. Appl.* **2021**, *10*, 194.
- [363] T. T. Pham, H. P. Nguyen, T. N. Luu, N. B. Le, V. T. Vo, N. T. Huynh, T. H. Le, Q. H. Phan, *J. Biomed. Opt.* **2022**, *27*, 075002.
- [364] I. Tinoco Jr., M. F. M. C. Bustamante, *Ann. Rev. Biophys. Bioeng.* **1980**, *9*, 107.
- [365] I. Tinoco, Jr., M. P. Freeman, *J. Phys. Chem.* **1957**, *61*, 1196.
- [366] M. F. Maestre, D. M. Gray, R. B. Cook, *Biopolymers* **1971**, *10*, 2537.
- [367] M. F. Maestre, C. Bustamante, T. L. Hayes, J. A. Subirana, I. Tinoco, Jr., *Nature* **1982**, *298*, 773.
- [368] F. Allen, C. Bustamante, (eds.), *Applications of Circularly Polarized Radiation using Synchrotron and Ordinary Sources*, Plenum Press, New York and London, **1984**.
- [369] M. Kim, L. Ulibarri, C. Bustamante, *Biophys. J.* **1987**, *52*, 929.
- [370] M. W. Ashraf, A. L. Gratiet, A. Diaspro, *Polymers* **2021**, *13*, 3422.
- [371] G. Salzman, J. K. Griffith, C. T. Gregg, *Appl. Environ. Microbiol.* **1982**, *44*, 1081.
- [372] A. Diaspro, G. Radicchi, C. Nicolini, *IEEE. Trans. Biomed. Eng.* **1995**, *42*, 1038.
- [373] A. Diaspro, M. Bertolotto, C. N. L. Vergani, *IEEE. Trans. Biomed. Eng.* **38**, 670.
- [374] A. L. Gratiet, L. Pesce, M. Oneto, R. Marongiu, G. Zanini, P. Bianchini, A. Diaspro, *OSA Continuum* **2018**, *1*, 1068.
- [375] W. S. Bickel, W. M. Bailey, *Am. J. Phys.* **1985**, *53*, 468.
- [376] F. Callegari, A. L. Gratiet, A. Zunino, A. Mohebi, P. Bianchini, A. Diaspro, *Front. Phys.* **2021**.
- [377] M. A. Digman, V. R. Caiolfa, M. Zamai, E. Gratton, *Biophys. J.* **2008**, *94*, L14.
- [378] M. W. Ashraf, R. Ranjan, A. Diaspro, *J. Opt. Soc. Am. B* **2021**, *38*, 1702.
- [379] A. L. Gratiet, L. Lanzano, A. Bendandi, R. Marongiu, P. Bianchini, C. J. R. Sheppard, A. Diaspro, *Biophys. J.* **2021**, *120*, 3112.
- [380] A. Mohebi, A. Le Gratiet, R. Marongiu, F. Callegari, P. Bianchini, A. Diaspro, *Appl. Opt.* **2021**, *60*, 1558.
- [381] A. Diaspro, In: *Expedition into the Nanoworld*, Springer, Cham, **2022**.
- [382] A. L. Gratiet, A. Mohebi, F. Callegari, P. Bianchini, A. Diaspro, *Appl. Sci.* **2021**, *11*, 1632.
- [383] I. Yamaguchi, T. Zhang, *Opt. Lett.* **1997**, *22*, 1268.
- [384] T. Tahara, Y. Lee, Y. Ito, P. Xia, Y. Shimozaoto, Y. Takahashi, Y. Awatsuji, K. Nishio, S. Ura, T. Kubota, O. Matoba, *Opt. Lett.* **2014**, *39*, 1673.
- [385] P. Marquet, B. Rappaz, P. J. Magistretti, E. Cuche, Y. Emery, T. Colomb, C. Depeursinge, *Opt. Lett.* **2005**, *30*, 468.
- [386] T. Sato, M. Ueda, G. Yamagishi, *Appl. Opt.* **1974**, *13*, 406.
- [387] E. N. Leith, D. Angell, C. P. Kuei, *J. Opt. Soc. Am. A* **1987**, *4*, 1050.
- [388] V. Mico, Z. Zalevsky, P. Garcia-Martinez, J. Garcia, *Opt. Express* **2004**, *12*, 2589.
- [389] G. Dardikman, N. T. Shaked, *J. Opt. Soc. Am. A* **2019**, *36*, A1.
- [390] N. A. Turko, P. J. Eravuchira, I. Barnea, N. T. Shaked, *Opt. Lett.* **2018**, *43*, 1943.
- [391] P. Gao, C. Yuan, *Light: Advanced Manufacturing* **2022**, *3*, 6.
- [392] P. Girshovitz, N. T. Shaked, *Light: Science and Applications* **2014**, *3*, e151.
- [393] A. Nativ, N. T. Shaked, *Opt. Lett.* **2017**, *42*, 1492.
- [394] N. Rotman-Nativ, N. A. Turko, N. T. Shaked, *Opt. Lett.* **2018**, *43*, 5543.
- [395] I. Frenklach, P. Girshovitz, N. T. Shaked, *Opt. Lett.* **2014**, *39*, 1525.
- [396] T. Noda, S. Kawata, S. Minami, *Appl. Opt.* **1992**, *31*, 670.
- [397] T. C. Wedberg, W. C. Wedberg, *J. Microsc.* **1995**, *177*, 53.
- [398] V. Lauer, *J. Microsc.* **2002**, *205*, 165.
- [399] Y. Sung, W. Choi, C. Fang-Yen, K. Badizadegan, R. R. Dasari, M. S. Feld, *Opt. Express* **2009**, *17*, 266.
- [400] B. Simon, M. Debailleul, M. Houkal, C. Ecoffet, J. Bailleul, J. Lambert, A. Spangenberg, H. Liu, O. Soppera, O. Haeberlé, *Optica* **2017**, *4*, 460.
- [401] S. Chowdhury, W. J. Eldridge, A. Wax, J. Izatt, *Optica* **2017**, *4*, 537.
- [402] D. Jin, R. Zhou, Z. Yaqoob, P. T. C. So, *Opt. Express* **2018**, *26*, 428.
- [403] M. Debailleul, V. Georges, B. Simon, R. Morin, O. Haeberlé, *Opt. Lett.* **2009**, *34*, 79.
- [404] M. Habaza, B. Gilboa, Y. Roichman, N. T. Shaked, *Opt. Lett.* **2015**, *40*, 1881.
- [405] Z. Wang, L. Millet, M. Mir, H. Ding, S. Unarunotai, J. Rogers, M. U. Gillette, G. Popescu, *Opt. Express* **2011**, *19*, 1016.
- [406] P. Hosseini, Y. Sung, Y. Choi, N. Lue, Z. Yaqoob, P. T. C. So, *Opt. Express* **2015**, *23*, 19752.
- [407] T. Zhang, C. Godavarthi, P. C. Chaumet, G. Maire, H. Giovannini, A. Talneau, M. Allain, K. Belkebir, A. Sentenac, *Optica* **2016**, *3*, 609.
- [408] D. Jin, R. Zhou, Z. Yaqoob, P. T. C. So, *J. Opt. Soc. Am. B* **2017**, *34*, B64.
- [409] J. Lim, A. Wahab, G. Park, K. Lee, Y. Park, J. C. Ye, *Opt. Express* **2017**, *25*, 30445.
- [410] S. Chowdhury, M. Chen, R. Eckert, D. Ren, F. Wu, N. Repina, L. Waller, *Optica* **2019**, *6*, 1211.
- [411] S. Shin, J. Eun, S. S. Lee, C. Lee, H. Hugonnet, D. K. Yoon, S.-H. Kim, J. Jeong, Y. Park, *Nat. Mater.* **2022**, *21*, 317.
- [412] F. Yang, T. Pham, H. Gupta, M. Unser, J. Ma, *Opt. Express* **2020**, *28*, 3905.
- [413] H. Chung, J. Huh, G. Kim, Y. Park, J. C. Ye, *IEEE Trans. Computational Imaging* **2021**, *7*, 747.
- [414] C. Zuo, J. Li, J. Sun, Y. Fan, J. Zhang, L. Lu, R. Zhang, B. Wang, L. Huang, Q. Chen, *Optics and Lasers in Engineering* **2020**, *135*, 106187.
- [415] Y. Ruan, P. Bon, E. Mudry, G. Maire, P. C. Chaumet, H. Giovannini, K. Belkebir, A. Talneau, B. Wattellier, S. Monneret, A. Sentenac, *Opt. Lett.* **2012**, *37*, 1631.
- [416] E. Mudry, P. Chaumet, K. Belkebir, G. Maire, A. Sentenac, *Opt. Lett.* **2010**, *35*, 1857.
- [417] L. Foucault, N. Verrier, M. Debailleul, J.-B. Courbot, B. Colicchio, B. Simon, L. Vonna, O. Haeberlé, *J. Opt. Soc. Am. A* **2019**, *36*, C18.
- [418] J. Jung, K. Kim, J. Yoon, Y. Park, *Opt. Express* **2016**, *24*, 2006.
- [419] Y. Sung, *Phys. Rev. Appl.* **2018**, *10*, 054041.
- [420] J. van Rooij, J. Kalkman, *Biomed. Opt. Express* **2020**, *11*, 2109.
- [421] J. Bailleul, B. Simon, M. Debailleul, L. Foucault, N. Verrier, O. Haeberlé, *Opt. Commun.* **2018**, *422*, 28.
- [422] T. Zhang, K. Li, C. Godavarthi, Y. Ruan, *Appl. Sci.* **2019**, *9*, 3834.
- [423] A. Kuś, W. Krauze, P. L. Makowski, M. Kujawińska, *ETRI Journal* **2019**, *41*, 61.



- [424] V. Balasubramani, A. Kuš, H.-Y. Tu, C.-J. Cheng, M. Baczewska, W. Krauze, M. Kujawińska, *Appl. Opt.* **2021**, *60*, B65.
- [425] X. Chen, M. E. Kandel, G. Popescu, *Adv. Opt. Photon.* **2021**, *13*, 353.
- [426] L. Novotny, *Progress in optics* **2007**, *50*, 137.
- [427] D. Richards, A. Zayats, D. W. Pohl, *Philos. Trans. A. Math. Phys. Eng. Sci.* **2004**, *362*, 701.
- [428] B. Hecht, B. Sick, U. P. Wild, V. Deckert, R. Zenobi, O. J. F. Martin, D. W. Pohl, *J. Chem. Phys.* **2000**, *112*, 7761.
- [429] M. E. Barber, E. Y. Ma, Z.-X. Shen, *Nature Reviews Physics* **2022**, *4*, 61.
- [430] T. L. Cocker, V. Jelic, R. Hillenbrand, F. A. Hegmann, *Nat. Photonics* **2021**, *15*, 558.
- [431] J. M. Atkin, S. Berweger, A. C. Jones, M. B. Raschke, *Adv. Phys.* **2012**, *61*, 745.
- [432] M. Liu, A. J. Sternbach, D. N. Basov, *Rep. Prog. Phys.* **2016**, *80*, 014501.
- [433] S. Wang, S. Zhao, Z. Shi, F. Wu, Z. Zhao, L. Jiang, K. Watanabe, T. Taniguchi, A. Zettl, C. Zhou, F. Wang, *Nat. Mater.* **2020**, *19*, 986.
- [434] N. Ocelic, A. Huber, R. Hillenbrand, *Appl. Phys. Lett.* **2006**, *89*, 101124.
- [435] A. Cvitkovic, N. Ocelic, R. Hillenbrand, *Opt. Express* **2007**, *15*, 8550.
- [436] H. A. Bechtel, S. C. Johnson, O. Khatib, E. A. Muller, M. B. Raschke, *Surf. Sci. Rep.* **2020**, *75*, 100493.
- [437] A. J. Sternbach, S. H. Chae, S. Latini, A. A. Rikhter, Y. Shao, B. Li, D. Rhodes, B. Kim, P. J. Schuck, X. Xu, X.-Y. Zhu, R. D. Averitt, J. Hone, M. M. Fogler, A. Rubio, D. N. Basov, *Science* **2021**, *371*, 617.
- [438] D. Lang, J. Döring, T. Nörenberg, Á. Butykai, I. Kézsmárki, H. Schneider, S. Winnerl, M. Helm, S. C. Kehr, L. M. Eng, *Rev. Sci. Instrum.* **2018**, *89*, 033702.
- [439] G. X. Ni, A. S. McLeod, Z. Sun, L. Wang, L. Xiong, K. W. Post, S. S. Sunku, B. Y. Jiang, J. Hone, C. R. Dean, M. M. Fogler, D. N. Basov, *Nature* **2018**, *557*, 530.
- [440] D. S. Jakob, H. Wang, G. Zeng, D. E. Otzen, Y. Yan, X. G. Xu, *Angew. Chem., Int. Ed.* **2020**, *59*, 16083.
- [441] H. Wang, L. Wang, D. S. Jakob, X. G. Xu, *Nat. Commun.* **2018**, *9*, 2005.
- [442] B. T. O'Callahan, K.-D. Park, I. V. Novikova, T. Jian, C.-L. Chen, E. A. Muller, P. Z. El-Khoury, M. B. Raschke, A. S. Lea, *Nano Lett.* **2020**, *20*, 4497.
- [443] R. Esteban, A. G. Borisov, P. Nordlander, J. Aizpurua, *Nat. Commun.* **2012**, *3*, 825.
- [444] W. Bao, M. Melli, N. Caselli, F. Riboli, D. S. Wiersma, M. Staffaroni, H. Choo, D. F. Ogletree, S. Aloni, J. Bokor, S. Cabrini, F. Intonti, M. B. Salmeron, E. Yablonovitch, P. J. Schuck, A. Weber-Bargioni, *Science* **2012**, *338*, 1317.
- [445] X. Chen, R. Ren, M. Liu, *Phys. Rev. Appl.* **2021**, *15*, 014001.
- [446] H.-H. Perkampus, *UV-VIS Spectroscopy and its Applications*. Springer Science & Business Media: 2013.
- [447] R. Wiesendanger, W. Roland, *Scanning probe microscopy and spectroscopy: methods and applications*, Cambridge university press, **1994**.
- [448] A. Dazzi, C. B. Prater, *Chem. Rev.* **2017**, *117*, 5146.
- [449] F. S. Ruggeri, B. Mannini, R. Schmid, M. Vendruscolo, T. P. Knowles, *Nat. Commun.* **2020**, *11*, 2945.
- [450] D. A. Nedosekin, E. I. Galanzha, E. Dervishi, A. S. Biris, V. P. Zharov, *Small* **2014**, *10*, 135.
- [451] Z. Li, K. Aleshire, M. Kuno, G. V. Hartland, *J. Phys. Chem. B* **2017**, *121*, 8838.
- [452] Y. Bai, J. Yin, J.-X. Cheng, *Sci. Adv.* **2021**, *7*, eabg1559.
- [453] J. M. Lim, C. Park, J.-S. Park, C. Kim, B. Chon, M. Cho, *J. Phys. Chem. Lett.* **2019**, *10*, 2857.
- [454] Y. Bai, D. Zhang, L. Lan, Y. Huang, K. Maize, A. Shakouri, J.-X. Cheng, *Sci. Adv.* **2019**, *5*, eaav7127.
- [455] X. Li, D. Zhang, Y. Bai, W. Wang, J. Liang, J.-X. Cheng, *Anal. Chem.* **2019**, *91*, 10750.
- [456] J. Xu, X. Li, Z. Guo, W. E. Huang, J.-X. Cheng, *Anal. Chem.* **2020**, *92*, 14459.
- [457] Y. Zhang, C. Yurdakul, A. J. Devaux, L. Wang, X. G. Xu, J. H. Connor, M. S. Ünlü, J.-X. Cheng, *Anal. Chem.* **2021**, *93*, 4100.
- [458] M. Tamamitsu, K. Toda, R. Horisaki, R. Horisaki, T. Ideguchi, T. Ideguchi, *Opt. Lett.* **2019**, *44*, 3729.
- [459] M. Tamamitsu, K. Toda, H. Shimada, T. Honda, M. Takarada, K. Okabe, Y. Nagashima, R. Horisaki, T. Ideguchi, *Optica* **2020**, *7*, 359.
- [460] Y. Zhang, H. Zong, C. Zong, Y. Tan, M. Zhang, Y. Zhan, J.-X. Cheng, *J. Am. Chem. Soc.* **2021**, *143*, 11490.
- [461] J. Yin, L. Lan, Y. Zhang, H. Ni, Y. Tan, M. Zhang, Y. Bai, J.-X. Cheng, (Preprint) **2021**.
- [462] O. Avcı, N. L. Ünlü, A. Y. Özkumur, M. S. Ünlü, *Sensors* **2015**, *15*, 17649.
- [463] W. Denk, J. H. Strickler, W. W. Webb, *Science* **1990**, *248*, 73.
- [464] C. J. R. Sheppard, R. Kompfner, *Appl. Opt.* **1978**, *17*, 2879.
- [465] A. Diaspro, P. Bianchini, G. Vicidomini, M. Faretta, P. Ramoino, C. Usai, *Biomed. Eng. Online* **2006**, *5*, 36.
- [466] K. Fujita, M. Kobayashi, S. Kawano, M. Yamanaka, S. Kawata, *Phys. Rev. Lett.* **2007**, *99*, 228105.
- [467] V. Astratov, Ed., *Label-Free Super-Resolution Microscopy*, Springer International Publishing, Cham **2019**.
- [468] J. Jiang, D. Grass, Y. Zhou, W. S. Warren, M. C. Fischer, *Opt. Lett.* **2021**, *46*, 1474.
- [469] P. A. Franken, A. E. Hill, C. W. Peters, G. Weinreich, *Phys. Rev. Lett.* **1961**, *7*, 118.
- [470] T. E. Matthews, I. R. Piletic, M. A. Selim, M. J. Simpson, W. S. Warren, *Sci. Transl. Med.* **2011**, *3*, 71ra15.
- [471] K.-Y. Ju, S. Degan, M. C. Fischer, K. C. Zhou, X. Jia, J. Yu, W. S. Warren, *J. Biomed. Opt.* **2019**, *24*, 051414.
- [472] A. Diaspro, G. Chirico, M. Collini, *Quarterly Reviews of Biophysics* **2005**, *38*, 97.
- [473] C. Y. Dong, P. T. So, T. French, E. Gratton, *Biophys. J.* **1995**, *69*, 2234.
- [474] D. Fu, T. Ye, T. E. Matthews, G. Yurtsever, W. S. Warren, *J. Biomed. Opt.* **2007**, *12*, 054004.
- [475] L. Tong, Y. Liu, B. D. Dolash, Y. Jung, M. N. Slipchenko, D. E. Bergstrom, J.-X. Cheng, *Nat. Nanotechnol.* **2011**, *7*, 56.
- [476] Y. Jung, M. N. Slipchenko, C. H. Liu, A. E. Ribbe, Z. Zhong, C. Yang, J.-X. Cheng, *Phys. Rev. Lett.* **2010**, *105*, 217401.
- [477] M. Ermin, K. Andreas, *Graphene and Carbon Nanotubes: Ultrafast Relaxation Dynamics and Optics*, Wiley-VCH Verlag GmbH & Co. KGaA, Weinheim **2013**.
- [478] R. N. Nair, P. Blake, A. N. Grigorenko, K. S. Novoselov, T. J. Booth, T. Stauber, N. M. R. Peres, A. K. Geim, *Science* **2008**, *320*, 1308.
- [479] E. Hendry, P. J. Hale, J. Moger, A. K. Savchenko, S. A. Mikhailov, *Phys. Rev. Lett.* **2010**, *105*, 097401.
- [480] L. Huang, G. V. Hartland, L.-Q. Chu, R. M. F. Luxmi, C. Lian, K. Tahy, H. Xing, *Nano Lett.* **2010**, *10*, 1308.
- [481] Q. Bao, H. Zhang, Z. Ni, Y. Wang, L. Polavarapu, Z. Shen, Q.-H. Xu, D. Tang, K. P. Loh, *Nano Res.* **2011**, *4*, 297.
- [482] S. W. Hell, *Nat. Biotechnol.* **2003**, *21*, 1347.
- [483] S. W. Hell, *Rev. Mod. Phys.* **2015**, *87*, 1169.
- [484] B. Gao, G. Hartland, T. Fang, M. Kelly, D. Jena, H. (Grace) Xing, L. Huang, *Nano Lett.* **2011**, *11*, 3184.
- [485] S. Bretschneider, C. Eggeling, S. W. Hell, *Phys. Rev. Lett.* **2007**, *98*, 413.
- [486] S. W. Hell, *Nanobiotechnology* **2005**, *1*, 296.
- [487] S. Galiani, B. Harke, G. Vicidomini, G. Lignani, F. Benfenati, A. Diaspro, P. Bianchini, *Opt. Express* **2012**, *20*, 7362.
- [488] S. J. Sahl, S. W. Hell, S. Jakobs, *Nat. Rev. Mol. Cell Biol.* **2017**, *18*, 685.
- [489] L. Gong, W. Zheng, Y. Ma, Z. Huang, *Phys. Rev. Appl.* **2019**, *11*, 034041.



- [490] L. Gong, W. Zheng, Z. Huang, *Photon* **2020**, *14*, 115.
- [491] O. Tzang, D. Azoury, O. Cheshnovsky, *Opt. Express* **2015**, *23*, 17929.
- [492] M. Wang, C. Zhang, S. Yan, T. Chen, H. Fang, X. Yuan, *ACS Photonics* **2021**, *8*, 1801.
- [493] K. Watanabe, A. F. Palonpon, N. I. Smith, L. D. Chiu, A. Kasai, H. Hashimoto, S. Kawata, K. Fujita, *Nat. Commun.* **2015**, *6*, 10095.
- [494] C. Roeder, M. Ritsch-Marte, A. Jesacher, *Opt. Lett.* **2016**, *41*, 3825.
- [495] A. Diaz Tormo, D. Khalkenow, K. Saurav, A. G. Skirtach, N. L. Thomas, *Opt. Lett.* **2017**, *42*, 4410.
- [496] C. Qian, K. Miao, L. E. Lin, X. Chen, J. Du, L. Wei, *Nat. Commun.* **2021**, *12*, 3648.
- [497] S. M. Stranahan, K. A. Willets, *Nano Lett.* **2010**, *10*, 3777.
- [498] C. A. Casacio, L. S. Madsen, A. Terrasson, M. Waleed, K. Barnscheidt, B. Hage, M. A. Taylor, W. P. Bowen, *Quantum-enhanced nonlinear microscopy Nature* **2021**, *594*, 201.
- [499] A. T. Wassie, Y. Zhao, E. S. Boyden, *Nat. Methods* **2019**, *16*, 33.
- [500] C. G. Artur, T. Womack, F. Zhao, J. L. Eriksen, D. Mayerich, W. C. Shih, *Biomed. Opt. Express* **2018**, *9*, 603.
- [501] J. Shou, Y. Ozeki, *Opt. Lett.* **2021**, *46*, 2176.
- [502] S. Hell, E. H. K. Stelzer, *Opt. Commun.* **1992**, *93*, 277.
- [503] L. Schermelleh, R. Heintzmann, H. Leonhardt, *J. Cell Biol.* **2010**, *190*, 165.
- [504] M. Fernández-Suárez, A. Y. Ting, *Nat. Rev. Mol. Cell Biol.* **2008**, *9*, 929.
- [505] B. Huang, H. Babcock, X. Zhuang, *Cell* **2010**, *143*, 1047.
- [506] T. A. Klar, S. W. Hell, *Opt. Lett.* **1999**, *24*, 954.
- [507] M. Hofmann, C. Eggeling, S. Jakobs, S. W. Hell, *Proc. Natl. Acad. Sci. USA* **2005**, *102*, 17565.
- [508] M. G. L. Gustafsson, *Proc. Natl. Acad. Sci. USA* **2005**, *102*, 13081.
- [509] S. W. Hell, *Nat. Methods* **2009**, *6*, 24.
- [510] E. Rittweger, K. Y. Han, S. E. Irvine, C. Eggeling, S. W. Hell, *Nat. Photonics* **2009**, *3*, 144.
- [511] Z. Zalevsky, E. Saat, S. Orbach, V. Mico, J. Garcia, *Appl. Opt.* **2008**, *47*, A1.
- [512] Z. Zalevsky, E. Fish, N. Shachar, Y. Vexberg, V. Micó, J. Garcia, *J. Opt. A Pure Appl. Opt.* **2009**, *11*, 085406.
- [513] A. Gur, D. Fixler, V. Micó, J. Garcia, Z. Zalevsky, *Opt. Express* **2010**, *18*, 22222.
- [514] T. Ilovitsh, Y. Danan, R. Meir, A. Meiri, Z. Zalevsky, *Sci. Rep.* **2014**, *5*, 8244.
- [515] M. J. Rust, M. Bates, X. Zhuang, *Nat. Methods* **2006**, *3*, 793.
- [516] H.-Y. Tsai, S. W. Thomas, R. Menon, *Opt. Express* **2010**, *18*, 16014.
- [517] Y. Danan, T. Ilovitsh, Y. Ramon, D. Malka, D. Liu, Z. Zalevsky, *J. Nanophotonics* **2016**, *10*, 036015.
- [518] C. Cleff, P. Groß, C. Fallnich, H. L. Offerhaus, J. L. Herek, K. Kruse, W. P. Beeker, C. J. Lee, K.-J. Boller, *Phys. Rev. A* **2012**, *86*, 23825.
- [519] W. P. Beeker, P. Groß, C. J. Lee, C. Cleff, H. L. Offerhaus, C. Fallnich, J. L. Herek, K.-J. Boller, *Opt. Express* **2009**, *17*, 22632.
- [520] V. Raghunathan, E. O. Potma, *J. Opt. Soc. Am. A. Opt. Image Sci. Vis.* **2010**, *27*, 2365.
- [521] H. Pinhas, Y. Danan, A. Meiri, O. Wagner, A. Shahmoon, T. Ilovitsh, Y. Ramon, D. Malka, M. Danino, M. Sinvani, Z. Zalevsky, In: V. Astratov, (eds) *Label-Free Super-Resolution Microscopy. Biological and Medical Physics, Biomedical Engineering*, Springer, Cham **2019**.
- [522] H. Pinhas, Y. Danan, M. Sinvani, M. Danino, Z. Zalevsky, STED like microscopy based on plasma dispersion effect in silicon. *Prof. of Imaging and Applied Optics 2017 (3D, AIO, COSI, IS, MATH, pcAOP)*, OSA Technical Digest (online), Optical Society of America, **2017**, paper CTh3B.5.
- [523] M. Tiferet, H. Pinhas, O. Wagner, Y. Danan, M. Danino, Z. Zalevsky, M. Sinvani, Plasma dispersion effect based super-resolved imaging in silicon. Proc. of SPIE Conf. 10891, Nanoscale Imaging, Sensing, and Actuation for Biomedical Applications XVI, SPIE Photonics West, San Francisco, USA (Feb. 2019).
- [524] M. Tiferet, Z. Zalevsky, M. Sinvani, in *Imaging and Applied Optics 2019 (COSI, IS, MATH, pcAOP)*, OSA Technical Digest Optical Society of America, **2019**, paper p. JTh3D6.
- [525] N. Shabairou, M. Tiferet, Z. Zalevsky, M. Sinvani, Laser-Induced Focusing for Silicon nanoscopy. Proc. of OSA FiO conf. 2020, paper #FTu8B.6, **2020**.
- [526] N. Shabairou, M. Tiferet, Z. Zalevsky, M. Sinvani, Novel Beam Shaping Based All Optical Measurement Method for Free Charge Carriers Dynamics in Silicon. Proc. of OSA FiO conf. 2020, paper #JTu1A.17, **2020**.
- [527] T. J. Liu, R. Y. Xu, P. Yu, Z. M. Wang, J. Takahara, *Nanophotonics* **2020**, *9*, 1115.
- [528] T. Zhang, Y. Che, K. Chen, J. Xu, Y. Xu, T. Wen, G. Lu, X. Liu, B. Wang, X. Xu, Y.-S. Duh, Y.-L. Tang, J. Han, Y. Cao, B.-O. Guan, S.-W. Chu, X. Li, *Nat. Commun.* **2020**, *11*, 3027.
- [529] H.-Y. Wu, Y.-T. Huang, P.-T. Shen, H. Lee, R. Oketani, Y. Yonemaru, M. Yamanaka, S. Shoji, K.-H. Lin, C.-W. Chang, S. Kawata, K. Fujita, S.-W. Chu, *Sci. Rep.* **2016**, *6*, 24293.
- [530] Y. Sivan, S. W. Chu, *Nanophotonics-Berlin* **2017**, *6*, 317.
- [531] T. C. Jagadale, D. S. Murali, S.-W. Chu, *Beilstein J. Nanotechnol.* **2019**, *10*, 2182.
- [532] S.-W. Chu, T.-Y. Su, R. Oketani, Y.-T. Huang, H.-Y. Wu, Y. Yonemaru, M. Yamanaka, H. Lee, G.-Y. Zhuo, M.-Y. Lee, S. Kawata, K. Fujita, *Phys. Rev. Lett.* **2014**, *112*, 017402.
- [533] D. Denkova, M. Ploschner, M. Das, L. M. Parker, X. Zheng, Y. Lu, A. Orth, N. H. Packer, J. A. Piper, *Nat. Commun.* **2019**, *10*, 3695.
- [534] S. W. Chu, H.-Y. Wu, Y.-T. Huang, T.-Y. Su, H. Lee, Y. Yonemaru, M. Yamanaka, R. Oketani, S. Kawata, S. Shoji, K. Fujita, *ACS Photon* **2014**, *1*, 32.
- [535] X. Ouyang, F. Qin, Z. Ji, T. Zhang, J. Xu, Z. Feng, S. Yang, Y. Cao, K. Shi, L. Jiang, X. Li, *APL Photonics* **2018**, *3*, 110801.
- [536] B. Wang, Y. Che, X. Zhong, W. Yan, T. Zhang, K. Chen, Y. Xu, X. Xu, X. Li, *Photon. Res.* **2021**, *9*, 950.
- [537] K. C. Gwosch, J. K. Pape, F. Balzarotti, P. Hoess, J. Ellenberg, J. Ries, S. W. Hell, *Nat. Methods* **2020**, *17*, 217.
- [538] G.-J. Huang, H.-Y. Cheng, Y.-L. Tang, I. Hotta, J. Takahara, K.-H. Lin, S.-W. Chu, *Adv. Optical Mater.* **2022**, *10*, 2101711.
- [539] A. E. Miroshnichenko, A. B. Evlyukhin, Y. F. Yu, R. M. Bakker, A. Chipouline, A. I. Kuznetsov, B. Luk'yanchuk, B. N. Chichkov, Y. S. Kivshar, *Nat. Commun.* **2015**, *6*, 8069.
- [540] K. Koshelev, S. Kruk, E. Melik-Gaykazyan, J. H. Choi, A. Bogdanov, H. G. Park, Y. Kivshar, *Science* **2020**, *367*, 288.
- [541] A. Bag, M. Neugebauer, U. Mick, S. Christiansen, S. A. Schulz, P. Banzer, *Nat. Commun.* **2020**, *11*, 2915.
- [542] J. Yao, L. Wang, C. Li, C. Zhang, L. V. Wang, *Phys. Rev. Lett.* **2014**, *112*, 014302.
- [543] O. Tzang, A. Pevzner, R. E. Marvel, R. F. Haglund, O. Cheshnovsky, *Nano Lett.* **2015**, *15*, 1362.
- [544] S. K. Sundaram, E. Mazur, *Nat. Mater* **2002**, *1*, 217.
- [545] O. Cheshnovsky, O. Tzang, D. Hershkovitz, in *Label-Free Super-Resolution Microscopy*, (Ed.: V. Astratov), Springer Nature, Switzerland **2019** pp. 261–287.
- [546] O. Tzang, D. Hershkovitz, A. Nagler, O. Cheshnovsky, *Rev. Sci. Inst.* **2018**, *89*, 123102.
- [547] O. Tzang, O. Cheshnovsky, *Opt. Express* **2015**, *23*, 20926.
- [548] K. Isobe, H. Kawano, T. Takeda, A. Suda, A. Kumagai, H. Mizuno, A. Miyawaki, K. Midorikawa, *Biomed. Opt. Express* **2012**, *3*, 1594.
- [549] K. Isobe, H. Kawano, A. Kumagai, A. Miyawaki, K. Midorikawa, *Biomed. Opt. Express* **2013**, *4*, 1937.
- [550] M. A. A. Neil, R. Juškaitis, T. Wilson, Z. J. Laczik, V. Sarafis, *Opt. Lett.* **2000**, *25*, 245.
- [551] G. M. Lerman, U. Levy, *Opt. Express* **2008**, *16*, 4567.

- [552] L. Novotny, S. J. Stranick, *Annu. Rev. Phys. Chem.* **2006**, *57*, 303.
- [553] A. Chiuri, F. Angelini, *Sensors* **2021**, *21*, 2579.
- [554] E. E. Hoover, J. A. Squier, *Nat. Photonics* **2013**, *7*, 93.
- [555] Z. Zhang, J. C. de Munck, N. Verburg, A. J. Rozemuller, W. Vreuls, P. Cakmak, L. M. G. van Huizen, S. Idema, E. Aronica, P. C. de Witt Hamer, P. Wesseling, M. L. Groot, *Adv. Sci.* **2019**, *6*, 1900163.
- [556] M. Paar, C. Jüngst, N. A. Steiner, C. Magnes, F. Sinner, D. Kolb, A. Lass, R. Zimmermann, A. Zumbusch, S. D. Kohlwein, H. Wolinski, *J. Biol. Chem.* **2012**, *287*, 11164.
- [557] S. V. Plotnikov, A. C. Millard, P. J. Campagnola, W. A. Mohler, *Bio-phys. J.* **2006**, *90*, 693.
- [558] M. Zimmerley, P. Mahou, D. Débarre, M. C. Schanne-Klein, E. Beaufort, *Phys. Rev. X* **2013**, *3*, 011002.
- [559] L. Zhang, Y. Wu, B. Zheng, L. Su, Y. Chen, S. Ma, Q. Hu, X. Zou, L. Yao, Y. Yang, L. Chen, Y. Mao, Y. Chen, M. Ji, *Theranostics* **2019**, *9*, 2541.
- [560] S. Huang, A. A. Heikal, W. W. Webb, *Biophys. J.* **2002**, *82*, 2811.
- [561] M. Strupler, A.-M. Pena, M. Hernest, P.-L. Tharaux, J.-L. Martin, E. Beaufort, M.-C. Schanne-Klein, *Opt. Express* **2007**, *15*, 4054.
- [562] M. J. Huttunen, R. Hristu, A. Dumitru, I. Floroiu, M. Costache, S. G. Stanciu, *Biomed. Opt. Express* **2020**, *11*, 186.
- [563] N. V. Kuzmin, P. Wesseling, P. C. D. W. Hamer, D. P. Noske, G. D. Galgano, H. D. Mansvelter, J. C. Baayen, M. L. Groot, *Biomed. Opt. Express* **2016**, *7*, 1889.
- [564] J. H. Park, S.-W. Lee, E. S. Lee, J. Y. Lee, *Opt. Express* **2014**, *22*, 9854.
- [565] H. Kim, G. W. Bryant, S. J. Stranick, *Opt. Express* **2012**, *20*, 6042.
- [566] J. Hou, L. Zhang, W. Yin, S. Yao, Y. Zhao, W. Ma, L. Dong, L. Xiao, S. Jia, *Opt. Express* **2017**, *25*, 23024.
- [567] S. G. Stanciu, R. Hristu, G. A. Stanciu, D. E. Tranca, L. Eftimie, A. Dumitru, M. Costache, H. A. Stenmark, H. Manders, A. Cherian, M. Tark-Dame, E. M. M. Manders, *Proc. Natl. Acad. Sci.* **2022**, *119*, e2214662119.
- [568] I. Gregor, M. Spiecker, R. Petrovsky, J. Großhans, R. Ros, J. Enderlein, *Nat. Methods* **2017**, *14*, 1087.
- [569] K. Toda, K. Isobe, K. Namiki, H. Kawano, A. Miyawaki, K. Midorikawa, *Biomed. Opt. Express* **2018**, *9*, 1510.
- [570] P. Pradhan, T. Meyer, M. Vieth, A. Stallmach, M. Waldner, M. Schmitt, J. Popp, T. Bocklitz, *Biomed. Opt. Express* **2021**, *12*, 2280.
- [571] T. Wang, C. Wu, D. G. Ouzounov, W. Gu, F. Xia, M. Kim, X. Yang, M. R. Warden, C. Xu, *eLife* **2020**, *9*, e53205.
- [572] C. J. Rowlands, D. Park, O. T. Bruns, K. D. Piatkevich, D. Fukumura, R. K. Jain, M. G. Bawendi, E. S. Boyden, P. T. So, *Light Sci. Appl.* **2017**, *6*, e16255.
- [573] C. Macias-Romero, M. E. P. Didier, P. Jourdain, P. Marquet, P. Magistretti, O. B. Tarun, V. Zubkovs, A. Radenovic, S. Roke, *Opt. Express* **2014**, *22*, 31102.
- [574] M. J. Huttunen, A. Hassan, C. W. McCloskey, S. Fasih, J. Upham, B. C. Vanderhyden, R. W. Boyd, S. Murugkar, *J. Biomed. Opt.* **2018**, *23*, 066002.
- [575] A. Dilipkumar, A. Al-Shemmary, L. Kreiß, K. Cvecek, B. Carlé, F. Knieling, J. Gonzales Menezes, O.-M. Thoma, M. Schmidt, M. F. Neurath, M. Waldner, O. Friedrich, S. Schürmann, *Adv. Sci.* **2019**, *6*, 1801735.
- [576] J. Duboisset, D. Ait-Belkacem, M. Roche, H. Rigneault, S. Brasselet, *Phys. Rev. A-At. Mol. Opt. Phys.* **2012**, *85*, 043829.
- [577] V. Astratov, (Ed.), *Label-Free Super-Resolution Microscopy*, Springer Nature, Switzerland **2019**.
- [578] A. V. Zayats, I. I. Smolyaninov, *J. Opt. A: Pure Appl. Opt.* **2003**, *5*, S16.
- [579] T.-J. Huang, L.-Z. Yin, J. Zhao, C.-H. Du, P.-K. Liu, *ACS Photonics* **2020**, *7*, 2173.
- [580] I. I. Smolyaninov, Y. J. Hung, C. C. Davis, *Science* **2007**, *315*, 1699.
- [581] M. He, G. R. S. Iyer, S. Aarav, S. S. Sunku, A. J. Giles, T. G. Folland, N. Sharac, X. Sun, J. Matson, S. Liu, J. H. Edgar, J. W. Fleischer, D. N. Basov, J. D. Caldwell, *Nano Lett.* **2021**, *21*, 7921.
- [582] I. I. Smolyaninov, *PIER* **2021**, *170*, 177.
- [583] I. I. Smolyaninov, *Journal of Optics* **2021**, *23*, 095002.
- [584] A. Darafsheh, G. F. Walsh, L. Dal Negro, V. N. Astratov, *Appl. Phys. Lett.* **2012**, *101*, 141128.
- [585] R. P. Feynman, R. P. Leighton, M. Sands, *The Feynman Lectures on Physics*, Vol. II (Addison-Wesley, San Francisco, **2006**).
- [586] J. de Rosny, M. Fink, *Phys. Rev. Lett.* **2002**, *89*, 124301.
- [587] U. Leonhardt, T. G. Philbin, *Geometry and Light: The Science of Invisibility*, (Dover, Mineola, NY, **2010**).
- [588] C. Castro, *J. Appl. Math. Phys.* **2010**, *4*, 870.
- [589] L. Petruzzello, F. Wagner, *Phys. Rev. D* **2021**, *103*, 104061.
- [590] P. W. Carlin, *IEEE* **1964**, *52*, 1371.
- [591] R. K. Luneburg, *Mathematical Theory of Optics*, (University of California Press, Berkeley and Los Angeles, **1964**, reprinted 2021).
- [592] J. C. Maxwell, *Cambridge Dublin Math. J.* **1854**, *8*, 188.
- [593] U. Leonhardt, T. G. Philbin, *Phys. Rev. A* **2010**, *81*, 011804.
- [594] M. Born, E. Wolf, *Principles of Optics*, (Cambridge University Press, Cambridge, **1999**).
- [595] O. Bitton, R. Bruch, U. Leonhardt, *Phys. Rev. Appl.* **2018**, *10*, 044059.
- [596] S. T. Tyc, X. Zhang, *Nature (London)* **2011**, *480*, 42.
- [597] J. C. Minano, J. Sanchez-Dehesa, J. C. Gonzalez, P. Benitez, D. Grabovickic, J. Carbonell, H. Ahmadpanahi, *New J. Phys.* **2014**, *16*, 033015.
- [598] Y. G. Ma, S. Sahebdivan, C. K. Ong, T. Tyc, U. Leonhardt, *New J. Phys.* **2011**, *13*, 033016.
- [599] Y. G. Ma, S. Sahebdivan, C. K. Ong, T. Tyc, U. Leonhardt, *New J. Phys.* **2012**, *14*, 025001.
- [600] U. Leonhardt, S. Sahebdivan, A. Kogan, T. Tyc, *New J. Phys.* **2015**, *17*, 053007.
- [601] U. Leonhardt, S. Sahebdivan, *Phys. Rev.* **2015**, *92*, 053848.
- [602] S. He, F. Sun, S. Guo, S. Zhong, L. Lan, W. Jiang, Y. G. Ma, T. Wu, *Prog. Electromag. Res.* **2015**, *152*, 1.
- [603] S. Sahebdivan, *The Enigma of Imaging in the Maxwell Fisheye Medium*, PhD thesis, St Andrews, **2016**.
- [604] B. S. Luk'yanchuk, R. Paniagua-Dominguez, I. Minin, O. Minin, Z. Wang, *Opt. Mater. Express* **2017**, *7*, 1820.
- [605] Z. Wang, B. Luk'yanchuk, in *Label-Free Super-Resolution Microscopy*, (Ed.: V. Astratov), Springer, Switzerland **2019**, pp. 371–406.
- [606] Y. F. Lu, L. Zhang, W. D. Song, Y. W. Zheng, B. S. Luk'yanchuk, *JETP Lett.* **2000**, *72*, 457.
- [607] W. Guo, Z. B. Wang, L. Li, D. J. Whitehead, B. S. Luk'yanchuk, Z. Liu, *Appl. Phys. Lett.* **2007**, *90*, 243101.
- [608] M. W. Tang, X. W. Liu, Z. Wen, F. H. Lin, C. Meng, X. Liu, Y. G. Ma, Q. Yang, *Laser Photonics Rev.* **2020**, *14*.
- [609] L. Li, W. Guo, Y. Yan, S. Lee, T. Wang, *Light Sci. Appl.* **2013**, *2*, e104.
- [610] Y. Yan, L. Li, C. Feng, S. L. W. Guo, M. H. Hong, *ACS Nano* **2014**, *8*, 1809.
- [611] A. Darafsheh, N. I. Limberopoulos, J. S. Derov, D. E. Walker, V. N. Astratov, *Appl. Phys. Lett.* **2014**, *104*, 061117.
- [612] F. F. Wang, L. Q. Liu, H. B. Yu, Y. D. Wen, P. Yu, Z. Liu, Y. C. Wang, W. J. Li, *Nat. Commun* **2016**, *7*.
- [613] B. Yan, Y. Song, X. Yang, D. Xiong, Z. Wang, *Appl. Opt.* **2020**, *59*, 2641.
- [614] <https://www.lig-nanowise.com> and <https://phaostech.com>
- [615] A. Bekirov, B. Luk'yanchuk, A. Fedyanin, *JETP Lett.* **2020**, *112*, 341.
- [616] Z. Wang, B. Luk'yanchuk, L. Yue, B. Yan, J. Monks, R. Dhama, O. V. Minin, I. V. Minin, S. Huang, A. A. Fedyanin, *Sci. Rep.* **2019**, *9*, 20293.
- [617] Z. Wang, B. Luk'yanchuk, B. Wu, B. Yan, A. Assel, I. Yaminsky, H. Yu, L. Liu, *Mesophotonics: Physics and Systems at Mesoscale SPIE* **2022**, *12152*, 24.

- [618] X. Liu, C. Kuang, X. Hao, C. Pang, P. Xu, H. Li, Y. Liu, C. Yu, Y. Xu, D. Nan, W. Shen, Y. Fang, L. He, X. Liu, Q. Yang, *Phys. Rev. Lett.* **2017**, *118*, 076101.
- [619] A. Bezryadina, J. X. Li, J. X. Zhao, A. Kothambawala, J. Ponsetto, E. Huang, J. Wang, Z. W. Liu, *Nanoscale* **2017**, *9*, 14907.
- [620] J. N. Monks, B. Yan, N. Hawkins, F. Vollrath, Z. B. Wang, *Nano Lett.* **2016**, *16*, 5842.
- [621] C. L. Jiang, H. Y. Yue, B. Yan, T. J. Dong, X. Y. Cui, P. Chen, Z. B. Wang, *Biomed. Opt. Express* **2021**, *12*, 7113.
- [622] X. X. Chen, T. L. Wu, Z. Y. Gong, J. H. Guo, X. S. Liu, Y. Zhang, Y. C. Li, P. Ferraro, B. J. Li, *Light Sci. Appl.* **2021**, *10*, 242.
- [623] H. Zhu, W. Fan, S. Zhou, M. Chen, L. Wu, *ACS Nano* **2016**, *10*, 9755.
- [624] R. Dhama, B. Yan, C. Palego, Z. Wang, *Photonics* **2021**, *8*, 222.
- [625] Y. Y. Zhou, Z. L. Hao, P. F. Zhao, H. Y. Chen, *Phys. Rev. Appl.* **2022**, *17*.
- [626] C. J. Hu, S. W. Xue, Y. H. Yin, Z. L. Hao, Y. Y. Zhou, H. Y. Chen, *Appl. Phys. Lett.* **2022**, *120*.
- [627] V. Marx, *Nat. Methods* **2017**, *14*, 1133.
- [628] S. M. Kamali, E. Arbabi, A. Arbabi, Y. Horie, A. Faraon, *Laser Photonics Rev.* **2016**, *10*, 1002.
- [629] K. W. Allen, N. Farahi, Y. Li, N. I. Limberopoulos, D. E. Walker, A. M. Urbas, V. N. Astratov, *Opt. Express* **2015**, *23*, 24484.
- [630] H. Shroff, C. G. Galbraith, J. A. Galbraith, E. Betzig, *Nat. Methods* **2008**, *5*, 417.
- [631] B. Hein, K. I. Willig, S. W. Hell, *Proc. Natl. Acad. Sci. USA* **2008**, *105*, 14271.
- [632] A. Brettin, F. Abolmaali, K. F. Blanchette, C. L. McGinnis, Y. E. Nesmelov, N. I. Limberopoulos, D. E. Walker, Jr., I. Anisimov, A. M. Urbas, L. Poffo, A. V. Maslov, V. N. Astratov, *Appl. Phys. Lett.* **2019**, *114*, 131101.
- [633] H. Yang, R. Trouillon, G. Huszka, M. A. M. Gijs, *Nano Lett.* **2016**, *16*, 4862.
- [634] S. Yang, F. Wang, Y.-H. Ye, Y. Xia, Y. Deng, J. Wang, Y. Cao, *Opt. Express* **2017**, *25*, 27551.
- [635] Z. Chen, A. Taflove, V. Backman, *Opt. Express* **2004**, *12*, 1214.
- [636] Y. E. Geints, Z. A. Zemlyanov, E. K. Panina, *J. Opt. Soc. Am. B* **2012**, *29*, 758.
- [637] V. M. Sundaram, S.-B. Wen, *Appl. Phys. Lett.* **2014**, *105*, 204102.
- [638] T. X. Hoang, Y. Duan, X. Chen, G. Barbastathis, *Opt. Express* **2015**, *23*, 12337.
- [639] R. Heydarian, C. Simovski, *Photonics Nanostruct. – Fundam. Appl.* **2021**, *46*, 100950.
- [640] The Abbe Theory of Imaging, Chapter 21 in *Handbook of Optical Systems*, Vol. 2. Physical Image Formation. (Ed.: H. Gross) Wiley-VCH Verlag GmbH & Co. KGaA, Weinheim **2005**.
- [641] Y. Ben-Aryeh, *J. Opt. Soc. Am. A* **2016**, *33*, 2284.
- [642] Y. Ben-Aryeh, *Recent Progress in Materials* **2019**, *1*, 003.
- [643] A. V. Maslov, *Phys. Rev. A* **2014**, *90*, 033825.
- [644] R. Boudoukha, S. Perrin, A. Demagh, P. Montgomery, N.-E. Demagh, S. Lecler, *Photonics* **2021**, *8*, 73.
- [645] A. V. Maslov, V. N. Astratov, *Appl. Phys. Lett.* **2016**, *108*, 051104.
- [646] B. Jin, G. W. Bidney, I. Anisimov, N. I. Limberopoulos, K. W. Allen, A. V. Maslov, V. N. Astratov, *Proc. SPIE 11972, Label-free Biomedical Imaging and Sensing (LBIS)*, **2022**, 119720F.
- [647] V. N. Astratov, B. Jin, A. A. Erykalin, A. V. Maslov, *Proc. SPIE 12152, Mesophotonics: Physics and Systems at Mesoscale*, **2022**, 1215206.
- [648] J. Li, J. Garfinkel, X. Zhang, D. Wu, Y. Zhang, K. de Haan, H. Wang, T. Liu, B. Bai, Y. Rivenson, G. Rubinstein, P. O. Scumpia, A. Ozcan, *Light Sci. Appl.* **2021**, *10*, 233.
- [649] B. Acs, F. Shabbir Ahmed, S. Gupta, P. Fai Wong, R. D. Gartrell, J. Sarin Pradhan, E. M. Rizk, B. G. Rothberg, Y. M. Senger, D. L. Rimm, *Nat. Commun.* **2019**, *10*, 5440.
- [650] M. Antohe, R. I. Nedelcu, L. Nichita, C. G. Popp, M. Cioplea, A. Brinzea, A. Hodorogea, A. Calinescu, M. Balaban, D. A. Ion, C. Diaconu, C. Bleotu, D. Pirici, S. A. Zurac, G. Turcu, *Oncol Lett* **2019**, *17*, 4155.
- [651] D. N. Breslauer, R. N. Maamari, N. A. Switz, W. A. Lam, D. A. Fletcher, *PLoS One* **2009**, *4*, e6320.
- [652] H. Zhu, O. Yaglidere, T. Su, D. Tseng, A. Ozcan, *Lab Chip* **2011**, *11*, 315.
- [653] J. Smith, K. Chu, A. R. Espenson, M. Rahimzadeh, A. Gryshuk, M. Molinaro, D. M. Dwyre, S. Lane, D. Matthews, S. Wachsmann-Hogiu, *PLoS One* **2011**, *6*, e17150.
- [654] N. A. Switz, M. V. D.' Ambrosio, D. A. Fletcher, *PLoS One* **2014**, *9*, e95330.
- [655] E. McLeod, Q. Wei, A. Ozcan, *Anal. Chem.* **2015**, *87*, 6434.
- [656] K. W. Allen, N. Farahi, Y. Li, N. I. Limberopoulos, D. E. Walker, Jr., A. M. Urbas, V. Liberman, V. N. Astratov, *Ann. Phys. (Berlin)* **2015**, *527*, 513.
- [657] *Label-free super-resolution microscopy*, Ed. V. Astratov, (Springer, Cham) **2019**.
- [658] A. V. Maslov, B. Jin, V. N. Astratov, *Sci. Reports* **2023**, *13*, 6688.
- [659] B. Jin, A. R. Jean, A. V. Maslov, V. N. Astratov, *Laser Photon. Rev.* **2023**, 2300146.
- [660] D. Lange, C. W. Stornent, C. A. Conley, G. T. A. Kovacs, *Sensors and Actuators B-chemical* **2005**, *107*, 904.
- [661] X. Heng, D. Erickson, L. R. Baugh, Z. Yaqoob, P. W. Sternberg, D. Psaltis, C. Yang, *Lab Chip* **2006**, *6*, 1274.
- [662] J. Garcia-Sucerquia, W. Xu, S. K. Jericho, P. Klages, M. H. Jericho, H. J. Kreuzer, *Appl. Opt.* **2006**, *45*, 836.
- [663] D. Tseng, O. Mudanyali, C. Oztoprak, S. O. Isikman, I. Sencan, O. Yaglidere, A. Ozcan, *Lab Chip* **2010**, *10*, 1787.
- [664] M. V. Klibanov, N. A. Koshev, D.-L. Nguyen, L. H. Nguyen, A. Brettin, V. N. Astratov, *SIAM J. Imaging Sci.* **2018**, *11*, 2339.
- [665] U. Leonhard, S. Sahebdivan, *Phys. Rev. A* **2015**, *92*, 053848.
- [666] X. Liu, H. Lee, Y. Xiong, C. Sun, X. Zhang, *Science* **2007**, *315*, 1686.
- [667] T. Lee, J. B. Khurgin, *Optica* **2016**, *3*, 1489.
- [668] Y. Chen, C. Zhou, Q. Wei, D. Wu, X. J. Liu, *Appl. Phys. Lett.* **2013**, *103*, 224104.
- [669] R. Heydarian, C. Simovski, *JOSA A* **2022**, *39*, 1256.
- [670] S. Jiang, M. Guan, J. Wu, M. Guan, J. Wu, G. Fang, X. Xu, D. Jin, Z. Liu, K. Shi, F. Bai, S. Wang, P. Xi, *Adv. Phot.* **2020**, *2*, 036005.
- [671] R. Heydarian, C. Simovski, *JOSA A* **2022**, *39*, 2124.
- [672] S. Perrin, S. Lecler, P. Montgomery, *In Label-Free Super-Resolution Microscopy*, eds. V. Astratov, (Springer, Cham, **2019**).
- [673] S. Lecler, S. Perrin, A. Leong-Hoi, P. Montgomery, *Sci. Reports* **2019**, *9*, 4725.
- [674] S. Perrin, Y. J. Donie, P. Montgomery, G. Gomard, S. Lecler, *Phys. Rev. Applied* **2020**, *13*, 014068.
- [675] V. Abbasian, S. Rasouli, E. A.-R. Moradi, *J. of Opt* **2019**, *21*, 045301.
- [676] S. Zhou, Y. Deng, W. Zhou, M. Yu, H. P. Urbach, Y. Wu, *Appl. Phys. B* **2017**, *123*, 9.
- [677] A. V. Maslov, V. N. Astratov, *Appl. Phys. Lett.* **2017**, *110*, 261107.
- [678] G. Basset, A. Luu-Dinh, C. Schneider, D. Schlup, S. Perrin, W. Fangting, S. Lecler, *SPIE Photonics Europe*, *Proc. SPIE* **2020**, *11368*, 1136803.
- [679] Y. Yang, Y. Bi, L. Peng, B. Yang, S. Ma, H.-C. Chan, Y. Xiang, S. Zhang, *Optica* **2021**, *8*, 249254.

## Addendum

V. N. Astratov, B. Jin  
Department of Physics and Optical Science  
University of North Carolina at Charlotte  
Charlotte, NC 28223-0001, USA  
E-mail: astratov@charlotte.edu

Y. B. Sahel, Y. C. Eldar  
Department of Computer Science and Applied Mathematics  
Weizmann Institute of Science  
Rehovot 7610001, Israel  
E-mail: yair.bensahel@weizmann.ac.il

L. Huang, A. Ozcan  
Electrical and Computer Engineering Department  
University of California  
Los Angeles, CA 90095, USA  
E-mail: ozcan@ucla.edu

L. Huang, A. Ozcan  
Bioengineering Department  
University of California  
Los Angeles, CA 90095, USA

L. Huang, A. Ozcan  
California Nano Systems Institute (CNSI)  
University of California  
Los Angeles, CA 90095, USA

A. Ozcan  
David Geffen School of Medicine  
University of California  
Los Angeles, CA 90095, USA

N. Zheludev  
Optoelectronics Research Centre  
University of Southampton  
Southampton SO17 1BJ, UK  
E-mail: niz@orc.soton.ac.uk

N. Zheludev  
Centre for Disruptive Photonic Technologies  
The Photonics Institute  
School of Physical and Mathematical Sciences  
Nanyang Technological University  
Singapore 637371, Singapore

J. Zhao, Z. Burns, Z. Liu  
Department of Electrical and Computer Engineering  
University of California  
9500 Gilman Drive, La Jolla, San Diego, CA 92093, USA  
E-mail: zhaowei@ucsd.edu

Z. Liu  
Material Science and Engineering  
University of California  
9500 Gilman Drive, La Jolla, San Diego, CA 92093, USA

E. Narimanov  
School of Electrical Engineering, and Birck Nanotechnology Center  
Purdue University  
West Lafayette, IN 47907, USA  
E-mail: evgenii@purdue.edu

N. Goswami, G. Popescu<sup>†</sup>  
Quantitative Light Imaging Laboratory  
Beckman Institute of Advanced Science and Technology  
University of Illinois at Urbana-Champaign  
Champaign, IL 61801, USA  
E-mail: nehag4@illinois.edu

E. Pfizner, P. Kukura  
Department of Chemistry  
University of Oxford  
Oxford OX1 3QZ, UK  
E-mail: philipp.kukura@chem.ox.ac.uk

Y.-T. Hsiao, C.-L. Hsieh  
Institute of Atomic and Molecular Sciences (IAMS)  
Academia Sinica 1  
Roosevelt Rd. Sec. 4, Taipei 10617, Taiwan  
E-mail: clh@gate.sinica.edu.tw

B. Abbey  
Australian Research Council Centre of Excellence for Advanced Molecular  
Imaging  
La Trobe University  
Melbourne, Victoria 3086, Australia  
E-mail: b.abbey@latrobe.edu.au

B. Abbey  
Department of Chemistry and Physics  
La Trobe Institute for Molecular Science (LIMS)  
La Trobe University  
Melbourne, Victoria 3086, Australia

A. Diaspro, A. LeGratiet, P. Bianchini, B. S. Kariman  
Optical Nanoscopy and NIC@IIT, CHT  
Istituto Italiano di Tecnologia  
Via Enrico Melen 83B, Genoa 16152, Italy  
E-mail: diaspro@fisica.unige.it; paolo.bianchini@iit.it

A. Diaspro, P. Bianchini, B. S. Kariman  
DIFILAB, Department of Physics  
University of Genoa  
Via Dodecaneso 33, Genoa 16146, Italy

A. LeGratiet  
CNRS, Institut FOTON - UMR 6082  
Université de Rennes  
Lannion F-22305, France

N. T. Shaked  
Faculty of Engineering  
Department of Biomedical Engineering  
Tel Aviv University  
Tel Aviv 6997801, Israel  
E-mail: nshaked@tau.ac.il

B. Simon  
LP2N  
Institut d'Optique Graduate School  
CNRS UMR 5298  
Université de Bordeaux  
Talence 33405, France  
E-mail: bertrand.simon@institutoptique.fr

N. Verrier, M. Debailleul, O. Haeberlé  
IRIMAS UR UHA 7499  
Université de Haute-Alsace  
Mulhouse 68 093, France

S. Wang  
School of Physics and Technology  
Wuhan University  
Wuhan, Hubei Province China  
E-mail: shengwang16@whu.edu.cn

S. Wang  
Wuhan Institute of Quantum Technology  
Wuhan 430206, China

M. Liu  
Department of Physics and Astronomy  
Stony Brook University  
Stony Brook, NY 11794-3800, USA  
E-mail: mengkun.liu@stonybrook.edu

M. Liu  
National Synchrotron Light Source II  
Brookhaven National Laboratory  
Upton, NY 11973-5000, USA



Y. Bai, J.-X. Cheng  
Boston University Photonics Center  
Boston, MA 02215, USA  
E-mail: jxcheng@bu.edu

K. Fujita  
Department of Applied Physics and the Advanced Photonics and Biosensing Open Innovation Laboratory (AIST) and the Transdimensional Life Imaging Division Institute for Open and Transdisciplinary Research Initiatives Osaka University  
Osaka 565-0871, Japan  
E-mail: fujita@ap.eng.osaka-u.ac.jp

M. Sinvani, Z. Zalevsky  
Faculty of Engineering and the Nano-Technology Center Bar-Ilan University  
Ramat Gan 52900, Israel  
E-mail: Zeev.Zalevsky@biu.ac.il

X. Li  
Guangdong Provincial Key Laboratory of Optical Fiber Sensing and Communications Institute of Photonics Technology Jinan University  
Guangzhou 510632, China  
E-mail: xiangpingli@jnu.edu.cn

G.-J. Huang, S.-W. Chu  
Department of Physics and Molecular Imaging Center National Taiwan University  
Taipei 10617, Taiwan  
E-mail: swchu@phys.ntu.edu.tw

G.-J. Huang, S.-W. Chu  
Brain Research Center National Tsing Hua University  
Hsinchu 30013, Taiwan

O. Tzang, D. Hershkovitz, O. Cheshnovsky  
School of Chemistry The Sackler faculty of Exact Sciences and the Center for Light matter Interactions and the Tel Aviv University Center for Nanoscience and Nanotechnology Tel Aviv 69978, Israel  
E-mail: orich@tauex.tau.ac.il

M. J. Huttunen  
Laboratory of Photonics Physics Unit Tampere University  
Tampere FI-33014, Finland  
E-mail: mikko.huttunen@tuni.fi

S. G. Stanciu  
Center for Microscopy – Microanalysis and Information Processing National University of Science and Technology Politehnica Bucharest 313 Splaiul Independentei, Bucharest 060042, Romania

V. N. Smolyaninova  
Department of Physics Astronomy and Geosciences Towson University  
8000 York Rd., Towson, MD 21252, USA

I. I. Smolyaninov  
Department of Electrical and Computer Engineering University of Maryland College Park, MD 20742, USA  
E-mail: igor.smolyaninov@saltenna.com

U. Leonhardt  
Weizmann Institute of Science Rehovot 7610001, Israel  
E-mail: ulf.leonhardt@weizmann.ac.il

S. Sahebdivan  
EMTensor GmbH TechGate, Donau-City-Strasse 1 Wien 1220, Austria  
E-mail: sahar.sahebdivan@emtensor.com

Z. Wang  
School of Computer Science and Engineering Bangor University Bangor LL57 1UT, United Kingdom  
E-mail: z.wang@bangor.ac.uk

B. Luk'yanchuk  
Faculty of Physics Lomonosov Moscow State University Moscow 119991, Russia

L. Wu  
Department of Materials Science and State Key Laboratory of Molecular Engineering of Polymers Fudan University Shanghai 200433, China

A. V. Maslov  
Department of Radiophysics University of Nizhny Novgorod Nizhny Novgorod 603022, Russia  
E-mail: avmaslov@rf.unn.ru

C. R. Simovski  
Department of Electronics and Nano-Engineering Aalto University Espoo FI-00076, Finland  
E-mail: Konstantin.Simovski@aalto.fi

C. R. Simovski  
Faculty of Physics and Engineering ITMO University St-Petersburg 199034, Russia

S. Perrin, P. Montgomery, S. Lecler  
ICube Research Institute University of Strasbourg - CNRS - INSA de Strasbourg 300 Bd. Sébastien Brant, Illkirch 67412, France  
E-mail: sperrin@photonics-bretagne.com; sylvain.lecler@unistra.fr



**Vasily N. Astratov** is a professor in the Department of Physics and Optical Science at the University of North Carolina at Charlotte. He is a principal organizer of this Roadmap who devised its concept. He received his Ph.D. in experimental physics from the Ioffe Institute in St. Petersburg, Russia, in 1986. He pioneered studies of synthetic opals as 3D photonic crystals in his former group at the Ioffe Institute in the mid-90s. In the last decade, he developed the use of high-index microspheres for super-resolution imaging applications in his lab at UNC-Charlotte. His research subjects include superlens imaging, resonant light forces, and the optical properties of microresonator and photodetector arrays. He is also a Visiting Professor at University Paris Saclay, Center for Material Physics in San Sebastian, and Air Force Research Laboratory. He organized and chaired special sessions on Label-Free Super-Resolution Microscopy at such conferences as PQE, IEEE Photonics, and ICTON. He is an editor of a book on this subject.<sup>[149]</sup>



**Yair Ben Sahel** received his B.Sc. degree in physics from The Hebrew University of Jerusalem, Israel, in 2019. He is currently working toward his M.Sc. degree in mathematics and computer science at the Weizmann Institute of Science, Rehovot, Israel. His research interests include machine learning and computational biology, focusing on learning-based algorithms for super-resolution in biological imaging.



**Yonina Eldar** is a professor of electrical engineering at the Weizmann Institute of Science, Israel, where she heads the center for Biomedical Engineering. She is also a visiting professor at MIT, a visiting scientist at the Broad, a research collaborator at Princeton, and an adjunct professor at Duke. She is a member of the Israel Academy of Sciences and Humanities, an IEEE Fellow, a EURASIP Fellow, a Fellow of the Asia-Pacific Artificial Intelligence Association, and of the 8400 Health Network. She received many awards for excellence in research and teaching, including the IEEE Signal Processing Society Technical Achievement Award, the IEEE/AESS Fred Nathanson Memorial Radar Award, and the IEEE Kiyo Tomiyasu Award.



**Luzhe Huang** received his B.Sc. degree in optical science and engineering in Zhejiang, China, 2019. He is currently a Ph.D. candidate in Electrical and Computer Engineering Department, University of California, Los Angeles, USA. His research focus includes computer vision, microscopy, and computational imaging.



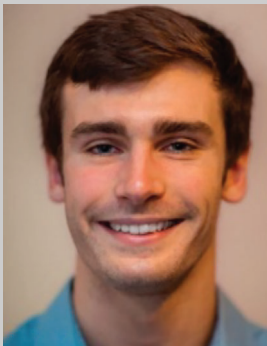
**Aydogan Ozcan** is the Chancellor's Professor and the Volgenau Chair for Engineering Innovation at UCLA and an HHMI Professor with the Howard Hughes Medical Institute. He is also the associate director of the California NanoSystems Institute. Dr. Ozcan is elected Fellow of the National Academy of Inventors (NAI) and holds >65 issued/granted patents in microscopy, holography, computational imaging, sensing, mobile diagnostics, nonlinear optics and fiber-optics, and is also the author of one book and the co-author of > 1000 peer-reviewed publications. Dr. Ozcan is elected Fellow of Optica, AAAS, SPIE, IEEE, AIMBE, RSC, APS, and the Guggenheim Foundation, and is a Lifetime Fellow Member of Optica, NAI, AAAS, and SPIE. Dr. Ozcan is listed as a Highly Cited Researcher by Web of Science.



**Nikolay Zheludev** FRS NAE, is Deputy Director of the Optoelectronics Research Centre, University of Southampton and directs the Centre for Disruptive Photonic Technologies at Nanyang Technological University, Singapore. He is also a fellow at the Halger Institute for Advanced Study, Texas A&M University, USA. His research interests are in nanophotonics, metamaterials and nonlinear optics. He is a fellow of the Royal Society of London, Member of the United States of America National Academy of Engineering. He is also a fellow of the European Physical Society, the Institute of Physics and the Optical Society of America (Optica) and American Physical Society. His personal awards include the IOP Thomas Young medal and Michael Faraday Gold medal, the President of Singapore Science and Technology Award and the IPS President Gold medal.



**Junxiang Zhao** received his bachelor's degree in electrical and computer engineering from the University of California, San Diego. He is currently a Ph.D. candidate in the Electrical and Computer Engineering department at the University of California, San Diego. He has conducted research in various topics including plasmonic-assisted super-resolution imaging, design of hyperbolic metamaterials, and metasurface-based quantitative phase imaging. Currently, his primary research activities focus on the use of plasmonic nanostructures and metamaterials to enhance the resolution of super-resolution microscopies beyond their conventional limits along with the corresponding image reconstruction methods.



**Zachary Burns** received his bachelor's degree in electrical engineering and engineering physics from the University of Michigan. He is currently a Ph.D. student in the Electrical and Computer Engineering department at the University of California, San Diego. His research focuses on the use of deep learning for image reconstruction in super-resolution microscopy. He is particularly interested in cases where knowledge of imaging physics can be incorporated into neural networks to reduce the need for labeled data and increase generalization capacity. He is a recipient of the NSF graduate research fellowship.



**Zhaowei Liu** is a professor in the Electrical and Computer Engineering department at the University of California, San Diego. He received his Ph.D. in mechanical engineering from UCLA in 2006. Dr. Liu was a pioneer in the field of optical hyperlens and super-resolution microscopy. His current research interest includes nanophotonics, imaging and sensing, bio-photonics, nonlinear optics, metamaterials, plasmonics, energy, ultrafast microscale light sources, and nanofabrication. He is a recipient of the 2010 SME Outstanding Young Manufacturing Engineer Award, the UCSD 2010 Hellman Faculty Fellowship Award, the 2013 ONR Young Investigator Award, and the 2013 DARPA Young Faculty Award. He has been elevated to OPTICA Fellow in 2016.



**Evgenii Narimanov** is Elmore Professor of Electrical and Computer Engineering at Purdue University. He is a Fellow of IEEE and Optics/OSA.



The late **Gabriel Popescu** (1971–2022) was an electrical and computer engineering professor at the University of Illinois at Urbana-Champaign (UIUC). He obtained his Ph.D. in optics in 2002 from the School of Optics, CREOL, University of Central Florida. Dr. Popescu was a postdoctoral researcher for Prof. Michael Feld in G. R. Harrison Spectroscopy Lab at M.I.T. He joined UIUC in August 2007. Prof. Popescu was a pioneer in the field of quantitative phase imaging. His most significant contributions include the invention of diffraction phase microscopy (DPM, 2006), spatial light interference microscopy (SLIM, 2011), and gradient light interference microscopy (GLIM, 2017).



**Philipp Kukura** is a professor of chemistry and fellow of Exeter College at the University of Oxford. He received an M.Chem. from the University of Oxford (2002) and a Ph.D. from the University of California, Berkeley (2006). After postdoctoral work at ETH Zurich, he joined the Chemistry Department at the University of Oxford as research fellow (2010) before becoming a lecturer (2011), and promotion to full professor (2016). Honours and awards include the Klung-Wilhelmy Science award in chemistry (2018), the Blavatnik Award for Young Scientists UK in chemistry (2019), the Emil Thomas Kaiser Ward by the Protein Society (2022), and the Sackler International Prize in biophysics (2023). He is the founder of Refeyn Ltd, which has commercialized and thereby enabled broad access to mass photometry. His current research focuses on the application of light microscopy combined with mass measurement at the single molecule level to study biomolecular structure and interactions.





**Chia-Lung Hsieh** is a principal investigator at Academia Sinica in Taiwan. He also holds a joint appointment with the Department of Physics at National Taiwan University. He received his Ph.D. degree in 2011 in electrical engineering from the California Institute of Technology, where he studied nonlinear optics in nano-sized particles for bioimaging under Prof. Demetri Psaltis. Before joining Academia Sinica in 2012, he worked on interferometric scattering (iSCAT) microscopy and single-particle tracking with Prof. Vahid Sandoghdar at Max Planck Institute for the Science of Light in Erlangen, Germany. Currently, his research interests lie in exploring nanoscale biological dynamics using advanced microscope techniques.



**Brian Abbey** received a Ph.D. in chemistry from Cambridge University in 2007. Over the past 16 years, he has been leading the development of new optical technologies for biological imaging employing techniques in coherent optics and nanotechnology. Prof. Abbey has received a number of prizes and awards for research excellence including the 2019 national Medtech's Got Talent award for his invention of a novel photonics-based diagnostic test for early-stage breast cancer. More recently, Brian was awarded both the 2022 Eureka prize for the innovative use of technology and the 2022 Victoria prize for Science and Innovation. He is currently deputy director of the La Trobe Institute for Molecular Science, Australia where he is a professor of physics in the field of Optics.



**Alberto Diaspro** is a full professor of applied physics at Department of Physics of Genoa University, research director in Nanoscopy and of the Nikon Imaging Center at the Istituto Italiano di Tecnologia, affiliate at the Institute of Biophysics of the National Research Council. He was president of OWLS and EBSA. AD research experience is related to optical, computational, and biophysical approaches applied to molecular oncology and neuroscience. SPIE and EOS fellow, IEEE and OSA senior. A.D. received the Emily M. Gray Award for mentoring in Biophysics in 2014. Since 2021, A.D. is president of the Italian Society of Pure and Applied Biophysics (SIBPA) and of the Assembly of the Italian node of Eurobioimaging. A.D. received the Gregorio Weber Award on 2022 for excellence in studies, theory, and application of fluorescence. <https://peerj.com/Diaspro/>



**Aymeric Le Gratiot** is an assistant professor at the University of Rennes, FOTON Institute (Lannion, France). He received his Ph.D. degree in 2016 in photonics from the University of Western Brittany (Brest, France). In 2017, he joined the Nanoscopy group led by Prof. Alberto Diaspro at the Istituto Italiano di Tecnologia (Genoa, Italy). His primary research activities involve the development of innovative optical microscopes based on manipulating the properties of light (wavelength, amplitude, phase, polarization, fluorescence). His main goal is to propose new multimodal optical methods for capturing numerous information through a deep-learning way about localized biological structures from macroscopic (small animals) down to sub-micrometric (tissues, cells, DNA) scales.



**Paolo Bianchini** is a researcher and technologist in the Nanoscopy and NIC@IIT research line at the Istituto Italiano di Tecnologia in Genoa, Italy. He is also an adjunct professor at the University of Parma and the University of Genoa. His research has focused on designing, realizing and utilizing conventional, confocal, multi-photon, and super-resolution fluorescence and label-free microscopy for biophysical applications. In particular, he developed original architectures for SHG, 2PE-STED, and pump-probe nanoscopy. He recently combined STED with Expansion microscopy and applied correlative AFM-STED microscopy. He is in charge of the scientific management of the Nikon Imaging Center and is a senior editor of the Microscopy Research and Technique journal.



**Natan T. Shaked** is a professor in the Department of Biomedical Engineering at Tel Aviv University, Israel, and currently the chair of the department. His research subjects include biomedical optical microscopy, nanoscopy, and interferometry. He is chairing the SPIE Label-Free Imaging and Sensing (LBIS) Conference in SPIE Photonics West, San Francisco, USA, a fellow in the Optical Society of America (now OPTICA), and a fellow in the SPIE.



**Bertrand Simon** is currently associate professor in optics at the Institut d'Optique Graduate School in France. He began his career at the Université de Haute-Alsace, where he focused on the development and characterization of tomographic diffraction microscopes as a tool for biological imaging. His research interests then shifted towards improving 3D resolution, specifically through the use of specimen rotation and fast reconstructions to achieve isotropic 3D resolution.



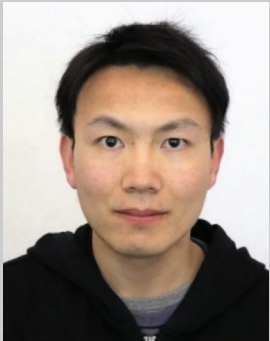
**Nicolas Verrier** is associate professor in electrical engineering at Université de Haute-Alsace (France). His main research topics focus on non-conventional and quantitative phase imaging. Among these techniques, he is developing tomographic diffraction microscopy allowing for 3D quantitative refractive index characterization. His main efforts are brought to the addition of new imaging contrasts, allowing to bring back content selectivity (e.g. chemical, structural, Doppler) to this marker-less technique.



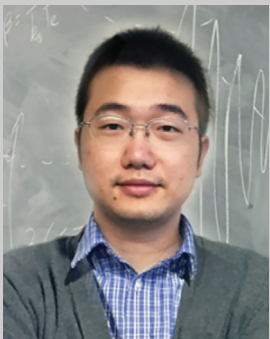
**Matthieu Debailleul** is a research engineer in physics and image processing at the Université de Haute-Alsace (France). Special skills include optical instrumentation, modeling in C++ and GPU computing. His main research topics are 3D microscopy and quantitative phase imaging. His current research focuses on the improvement of label-free techniques, and image formation models to enhance 3D reconstructions.



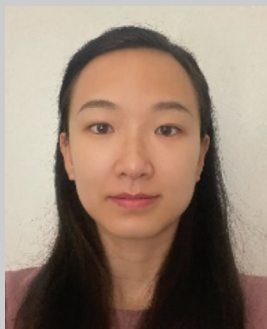
**Olivier Haerberlé** obtained his Ph.D. in electromagnetism in 1994 and joined the University of Haute-Alsace in 1998 as assistant professor at MIPS laboratory. He defended his Habilitation in 2004, to become a full professor in 2006. He has been director of the MIPS laboratory, then of the IRIMAS research institute, and he is now adjunct-director of the IRIMAS. His present work focuses on modeling of image formation mechanisms, and on developing new techniques for label-free microscopy, based on phase imaging and tomography, as well as on associated image reconstruction/processing.



**Sheng Wang** is a professor of Wuhan University in China. He obtained his B.Sc. degree from the University of Science and Technology of China in 2014 and his Ph.D. degree from the University of California, Berkeley in 2020. After working as a director's postdoctoral fellow at Los Alamos National Laboratory, he joined Wuhan University as a professor in November 2021. His research interests lie in nano- and quantum photonics, with an emphasis on probing the novel optical properties of low-dimensional materials at the nanoscale by scanning near-field optical microscopy.



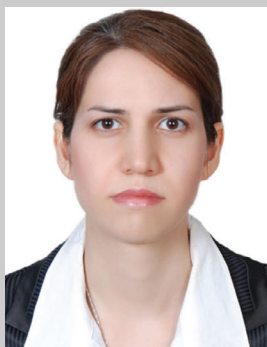
**Mengkun Liu** is an associate professor at the Department of Physics and Astronomy of Stony Brook University. He completed his Ph.D. in 2012 at Boston University and his post doc research was at UC San Diego from 2012–2014. His research interests include physics of correlated electron systems, low-dimensional quantum materials, infrared and terahertz nano-optics and ultrafast time-domain spectroscopy. Prizes include the NSF career award (2021) and Seaborg Institute Research Fellowships at Los Alamos National Lab (2009, 2010).



**Yeran Bai** is currently a postdoctoral researcher at the University of California Santa Barbara. She received her Ph.D. degree in Optical Engineering from the Chinese Academy of Sciences in 2019. Her research interests are novel vibrational spectroscopic imaging instrumentation for biomedical applications, with a special focus on mid-infrared photothermal imaging for neuroscience research.



**Ji-Xin Cheng** attended the University of Science and Technology of China (USTC) from 1989 to 1994. From 1994 to 1998, he carried out his Ph.D. study on bond-selective chemistry at USTC. As a graduate student, he worked as a research assistant at Universite Paris-sud (France) on vibrational spectroscopy and the Hong Kong University of Science and Technology (HKUST) on quantum dynamics theory. After postdoctoral training on ultrafast spectroscopy at HKUST, he joined Sunney Xie's group at Harvard University as a postdoc, where he spearheaded the development of CARS microscopy that allows high-speed vibrational imaging. Cheng joined Purdue University in 2003 as an assistant professor at Weldon School of Biomedical Engineering and Department of Chemistry, promoted to associate professor in 2009 and full professor in 2013. He joined Boston University as the Inaugural Theodore Moustakas Chair Professor in Photonics and Optoelectronics in summer 2017.



**Behjat Sadat Kariman** is currently a postdoctoral fellow under the supervision of Prof. Giulio Cerullo at the Department of Physics Politecnico di Milano, collaborating with IN2SIGHT project. She has completed her doctoral thesis entitled "Non-Linear Optical Process for the label-free microscope," under the supervision of Prof. Alberto Diaspro, and Prof. Paolo Bianchini at Istituto Italiano di Tecnologia in Genoa, Italy (2018–2022). Her research project focused on developing a multi-modal microscope, a custom-built femtosecond-pulsed near-infrared pump-probe microscope, that allows for simultaneous image acquisition from multiple optical imaging modalities to improve content information by label-free imaging. The microscope enables the following methods: multi-photon excitation fluorescence (MPEF), sum-frequency generation (SFG), second harmonic generation (SHG), pump-probe (PP), and saturated pump-probe (SPP). She did part of her PhD research abroad at Laboratory Nanoscale Biology led by Prof. Aleksandra Radenovic, at EPFL in 2021.



**Katsumasa Fujita** is a professor of applied physics at Osaka University. He received his B.Sc., M.Sc., and Ph.D. all in applied physics in 1995, 1997, and 2000, respectively, from Osaka University. After working as a JSPS postdoctoral fellow at Kyoto Prefectural University of Medicine and as a research associate at Frontier Research Center in Osaka University, he was appointed as an assistant professor member in Osaka University in 2002 and was promoted to full professor in 2018. His research interest includes optical microscopy, non-linear optics, vibrational spectroscopy, and their applications for biomedical sciences.





**Moshe Sinvani** was born in Israel. He received his Ph.D. in physics in 1979 on transport properties in Aluminum at liquid He temperatures. He was a postdoc at Caltech in 1980–1983 conducting research on absorption–desorption of He atoms on a solid surface at liquid He temperatures. He became a senior researcher at Soreq NRC in 1984–2010 conducting R&D on thermoelectric materials and coolers, R&D on Chalcogenide fiber optics for long IR laser beam delivery, and its physical characterization. He established the infrared and lasers laboratory, and developed research on interactions electro-optical sensors and materials. He retired from Soreq in 2010. From 2010 till date, he is a visiting professor at Bar-Ilan University, researching super-resolution and dynamics of fast laser-excited carriers in semiconductors.



**Zeev Zalevsky** received his B.Sc. and direct Ph.D. degrees in electrical engineering from Tel-Aviv University in 1993 and 1996, respectively. Zeev is currently a full professor and the dean of the faculty of engineering in Bar-Ilan University, Israel. His major fields of research are optical superresolution, biomedical optics, and nano-photonics. Zeev has published more than 600 peer review papers, 350 proceeding papers, nine books (6 authored and 3 as an editor), more than 30 book chapters, and about 100 patents. Zeev gave more than 600 conference presentations with more than 200 invited/keynote or plenary talks. He is a fellow of many large scientific societies such as SPIE, IEEE, Optica, AIMBE, NAI, and more, and for his research, he received many national and international awards.



**Xiangping Li** completed his Ph.D. at Swinburne University of Technology in 2009. His research is focused on nano-optics, superresolution, and meta-optics. Prof. Li has published over 120 internationally referred journal publications including *Science*, *Nature Photonics*, *Nature Nanotechnology*, and *Nature Communications*. Prof. Li is a recipient of a number of prestigious awards including the Australian Postdoctoral Fellow funded by Australian Research Council in 2011, Discovery Early Career Researcher Award by Australian Research Council in 2014, China's Young 1000 Talents Award in 2015, and Young Scholars from National Natural Science Foundation of China in 2015. He joined the Institute of Photonics Technology in Jinan University as a full professor and principle investigator in nanophotonic devices group in 2015.



**Guan-Jie Huang** completed his bachelor's degree in physics at the National Taiwan Normal University in 2017. Later, in 2023, he obtained his Ph.D. in physics from National Taiwan University. During his doctoral studies, he worked under the supervision of Prof. Shi-Wei Chu and conducted research in various fields, including nonlinear nanophotonics, instrumental development of pump-probe microscopy, and stimulated Raman scattering spectromicroscopy. Currently, he is a postdoctoral researcher at National Taiwan University and a Brain Research Center fellow at National Tsing-Hua University. His primary research activities involve the development of high-speed and multiplex imaging techniques for stimulated Raman scattering microscopy.



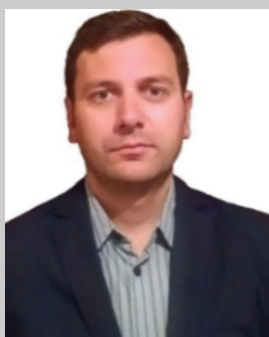
**Shi-Wei Chu** received his Ph.D. from National Taiwan University (NTU), and joined NTU Physics in 2006, promoted to associate professor and full professor in 2010 and 2014, respectively. His research interest lies in developing novel optical microscopic tools for nanophotonics and biomedical applications, with more than 70 journal publications. He had served as the deputy director in the Center of Teaching and Learning Development of NTU, and the vice dean of NTU D.School. Now he serves as the vice president of Student Affairs. He is currently on the board of directors in the Taiwan Physical Society, and on the editorial board of Biophysical Reports.



**Ori Cheshnovsky** is a professor (emeritus) at the School of Chemistry at Tel Aviv University, Israel. He studied gas-phase clusters, utilizing photoelectron new spectroscopy methods. Currently, he specializes in the spectroscopy (absorption, Raman, chirality, ultrafast dynamics) of nano-objects and develops label-free super-resolution microscopy methods. He chaired the School of Chemistry at TAU (2001-2001), and was a visiting scientist at the universities of Rice, Yale, Berkeley UC, Vienna, Basel, and CNRS. He is the recipient of The Weizmann Prize in Exact Sciences (2007) and is a fellow of the American Physical Society (since 2008). Since 1997 he promotes nanotechnology in Israel, initiated in TAU the first nano-center in Israel (2000), and headed it in 2004–2012.



**Mikko Huttunen** is a lecturer and group leader at the Physics department in Tampere University, Finland. His research interests include nonlinear plasmonics, metamaterials, waveguides, laser development, multiphoton microscopy, and machine learning.



**Stefan G. Stanciu** received the Ph.D. degree in electronic engineering and a Habilitation degree in physics, both from the University Politehnica of Bucharest (UPB), Bucharest, Romania, in 2011 and 2022, respectively. He is currently a senior researcher with the Center for Microscopy-Microanalysis and Information Processing, National University of Science and Technology Politehnica Bucharest, his research focusing, mainly, on optical microscopy & nanoscopy, biophotonics, advanced materials, and on Artificial Intelligence methods for high-resolution imaging. He authored >75 WOS Journal articles, and five book chapters. He edited three books on image processing, microscopy, and nanotechnology, and is currently a senior editor for IEEE Photonics Journal and an associate editor for Frontiers in Photonics. Among other Management Committee (MC) Roles in European COST Actions focused on bioimage analysis and advanced microscopies, Stefan serves as an MC Member, Grant Awarding Coordinator and Workgroup (6) Co-Leader in CA19118 EsSENce.



**Vera Smolyaninova** is a professor of physics in the Department of Physics, Astronomy, and Geosciences at Towson University. She received her Ph.D. in physics from the University of Maryland. She worked extensively in the areas of electromagnetic metamaterials and transport, magnetic and thermal properties of functional oxides. She is an expert in transformation optics, ferrofluid-based hyperbolic metamaterials, and metamaterial superconductors. Her work on transformation optics and metamaterials have been recognized as novel and extremely interesting through numerous publications in both professional and general news media, such as Physics World, MIT Technology Review, Extreme Tech, SPIE News Room, Superconductor Week, etc.



**Igor Smolyaninov** is the co-founder and CTO of Saltenna. He is a fellow of the Optical Society of America and a recipient of the Scientific American 50 Award. He received his Ph.D. in 1990 from the Kapitza Institute for Physical Problems. He has published more than 400 journal and conference papers and patents in various areas of low-temperature physics, wireless communications, quantum computing, plasmonics, electromagnetic metamaterials, and underwater communications. Science News magazine has recognized his research on hyperbolic metamaterials among the 2011 Science News of the Year.



**Ulf Leonhardt** received his Ph.D. in 1993 from Humboldt University Berlin on the quantum theory of simple optics instruments. From 2000 to 2012, he was a professor of theoretical physics at the University of St Andrews and since 2012 he holds the Murray B Koffler Professorial Chair of physics at the Weizmann Institute of Science. Currently, he is working on experiments with fiber-optical analogs of the event horizon and on the theory of quantum fluctuations in the expanding universe.



**Sahar Sahebdivan** received her Ph.D. in 2016 from the University of St Andrews in the field of transformation optics, with a focus on super-resolution and perfect imaging. As a researcher/postdoc, she joined the quantum optomechanics group at the University of Vienna from 2013 to 2018. Currently, she is working as a senior scientist in medical neuroimaging, utilizing microwave tomography to develop a novel modality for imaging the human brain. Besides imaging, she is interested in studying gravity and its encounter with quantum mechanics in low-energy regimes where testing some quantum aspects of gravity is expected to be possible in a quantum optomechanical setup.



**Zengbo Wang** is a professor at Bangor University, United Kingdom. He earned his Ph.D. from the National University of Singapore in laser and optical engineering. He is also a visiting professor at Northeastern University, Boston, USA. His research expertise spans laser-based manufacturing, nanophotonics, metamaterials, solar energy, fiber sensors, and machine learning. He is particularly known for his pioneering work on microsphere-based super-resolution microscopy, imaging and sensing. He was awarded the 2022 Leverhulme Trust Research Fellowship and is a senior member of Optica.



**Boris Luk'yanchuk** graduated in 1967 from the Faculty of Physics of Lomonosov Moscow State University (Department of Quantum Theory, supervisor - A.A. Abrikosov, later Nobel laureate). Boris got in 1978 a Ph.D. (physics and mathematics) from the P.N. Lebedev Physical Institute, Academy of Sciences of USSR, 1979. He also received a doctor of sciences degree (physics and mathematics) - a second doctorate (Habilitation) from the General Physics Institute, Academy of Sciences of USSR, 1991. Since 1992, he received a State Professor's Degree (physics and mathematics) from State Highest Certifying Committee of Russian Federation. Luk'yanchuk was working as a professor of General Physics Institute, he also was awarded the honorary professor of the Johannes Kepler University (Linz, Austria). Luk'yanchuk was a visiting professor in Austria, Italy, France, Japan, and Australia. Since 1999 till 2019 he was working in Data Storage Institute of Agency for Science, Technology and Research in Singapore. Luk'yanchuk was awarded a number of prestigious awards, including the President's Science Award in Singapore. He is a fellow of Optica (formerly OSA) and SPIE. At present, Luk'yanchuk is a professor of Physical Faculty Lomonosov Moscow State University.



**Limin Wu** is a professor at Fudan University in China. He obtained his Ph.D. from Zhejiang University in 1991, and studied at The Pennsylvania State University from October 1994 through April 1998, then joined Fudan University in May, 1998. He has published around 400 peer-reviewed papers in international journals and 60 patents. He is currently "Changjiang" distinguished professor appointed by Ministry of Education in China. His research interests are colloidal spheres, functional coatings, etc.



**Alexey V. Maslov** is an associate professor at the Department of Radiophysics, the University of Nizhny Novgorod (UNN), Russia. He earned a B.Sc. degree (1995) from UNN, and M.Sc. (1997) and Ph.D. (2001) degrees, all in physics, from Washington State University (Pullman, WA). He subsequently worked at the Georgia Institute of Technology (Atlanta, GA), NASA Ames Research Center (Moffett Field, CA), and Canon USA (Irvine, CA and Tucson, AZ) before joining UNN in 2014. His research interests include the optical properties of semiconductor nanostructures, semiconductor nanowire and quantum well lasers, wave transformation in nonstationary media, optical forces, radiation pressure, and optical super-resolution.





**Boya Jin** received her Ph.D. degree in optical science and engineering from the University of North Carolina at Charlotte, 2022. She is currently a postdoctoral associate in Peking University. Her primary research interests are in super-resolution microscopy including microsphere- and ball lens-assisted imaging and in the optical properties of mesoscale photonic structures.



**Constantin (Konstantin) R. Simovski** has worked in both industry and academy in several countries. Defended his Ph.D. thesis in 1986 in the Polytechnic University of Leningrad (USSR) and Habilitation (HDR) in 2000 in the same university which is presently Peter the Great Polytechnic University of St. Petersburg (Russian Federation). In 2001 became a full professor at ITMO University in St. Petersburg. Since 2008, he has been with Helsinki University of Technology, presently Aalto University (Finland). Full professor at the Dept. Electronics and Nano-Engineering of Aalto University since 2012. Recent research areas: plasmon-enhanced fluorescence, Raman scattering, light trapping in solar cells, thermophotovoltaic generation, electromagnetic characterization of metamaterials and metasurfaces, magnetic resonance imaging, wireless power transfer, label-free subwavelength imaging, optical trapping, metamaterials for detection of dark matter.



**Sylvain Lecler** is a professor at INSA Strasbourg, leader of the Instrumentation and Photonic Processes team of the ICube Laboratory in Strasbourg. He got his Ph.D. degree in 2005 at the Louis Pasteur University in Strasbourg. After a postdoctoral position at the University of Liège in Belgium, he became an associate professor at the University of Strasbourg and then a professor at INSA Strasbourg in 2019. His work concerns physical optics at mesoscale with main contribution concerning photonic jet theory and applications, and laser processes.